

Microfluidics at high-intensity X-ray sources: from microflow chips to microfluidic liquid jet systems

DOCTORAL THESIS (Dissertation)

to be awarded the degree of Doctor rerum naturalium (Dr. rer. nat.) at
the Faculty of Biology, Chemistry and Earth Sciences, University of Bayreuth

submitted by
Dipl. Chem. Martin Trebbin
from Hamburg
Bayreuth, 2013

The work described in this thesis was carried out at the Institute of Physical Chemistry at the University of Hamburg (August 2009 to September 2010) and the Department of Physical Chemistry I at the University of Bayreuth (October 2010 to September 2013) under the supervision of Prof. Stephan Förster.

This is a full reprint of the dissertation submitted to obtain the academic degree Doctor of Natural Sciences (Dr. rer. nat.) and approved by the Faculty of Biology, Chemistry and Geosciences of the University of Bayreuth.

Acting dean: Prof. Dr. Rhett Kempe

Thesis submitted: 13.09.2013

Date of Scientific Colloquium: 19.12.2013

Doctoral Committee:

Prof. Dr. Stephan Förster (1st reviewer)

Prof. Dr. Andreas Fery (2nd reviewer)

Prof. Dr. Hans-Werner Schmidt (Chairman)

Prof. Dr. Thomas Scheibel

**"If you want better results,
you have to ask yourself better questions."**

- unknown

Table of contents

Summary.....	13
Zusammenfassung	15
1 Introduction	17
1.1 Motivation	17
1.2 Microfocus X-ray sources	17
1.3 Introduction to microfluidics	20
2 Microfluidic devices as experimental platforms for X-ray studies	25
2.1 Introduction	25
2.2 X-ray compatible microfluidic device types	29
2.3 Outlook: new processing techniques and device materials	34
2.4 Microfluidic liquid jet devices for next generation X-ray sources	35
2.5 Conclusions	39
3 Theoretical Fundamentals	41
3.1 Self-organization of amphiphiles	41
3.2 Fluid dynamics fundamentals for microfluidics	43
3.2.1 Navier-Stokes equations	43
3.2.2 The No-Slip condition	45
3.2.3 Convection and Diffusion	46
3.3 Solution of non-linear problems	48
3.3.1 Fluid structure interaction	48
3.3.2 Shear forces and Non-Newtonian fluids	48
3.3.3 Two-phase systems and liquid jets	49
3.4 Small angle X-ray scattering	53
3.4.1 Preface	53
3.4.2 Introduction	53
3.4.3 The scattering vector	54
3.4.4 The scattering pattern	55
3.4.5 Form factor	58
3.4.6 Structure factor	59
3.4.7 Bragg reflexes	60
3.4.9 Model-based order analysis	63
3.4.10 Particle orientation distribution	64
4 Methods and Techniques	71
4.1 Photolithography	71
4.2 Molding Materials	75
5 Summary and Strategy	79

6 Individual contributions to joint publications	99
7 Publications	103
7.1 Anisotropic particles align perpendicular to flow- direction in narrow microchannels	105
7.2 Microfluidic SAXS for the high-throughput screening and correlation of complex fluid behavior with structural information	127
7.3 Microfluidic Liquid Jet System with compatibility for atmospheric and vacuum conditions	157
7.4 Lyotropic phase behavior of polymer-coated iron oxide nanoparticles.	187
7.5 Early development drug formulation on a chip: Fabrication of nanoparticles using a microfluidic spray dryer	199
7.6 Freestanding films of crosslinked gold nanoparticles prepared via layer- by-layer spin-coating	213
7.7 Adsorption of spherical polyelectrolyte brushes: from interactions to surface patterning	233
8 List of Publications	251
9 Conference presentations	255
10 Acknowledgements	259
11 Declaration / (Eidesstattliche) Versicherungen und Erklärungen	261

Summary

Microfluidics enables the precise control of liquids on the nanoliter scale. These very well defined flow conditions make this technology predestined for fundamental investigations at microfocused X-ray sources. With recent developments in synchrotron technology and with the advent of free electron lasers (FEL), very exciting possibilities arise, such as serial femtosecond X-ray nanocrystallography. This on-going technological progress also gives rise to the question of how to design and make sample environments that are compatible with the increasingly brilliant and highly intense X-ray beams.

By developing X-ray compatible microflow chips and microfluidic liquid jet devices, which are optimized for the combination of microbeam X-ray scattering and microfluidics, this thesis contributes crucially to the advent of a powerful experimental methodology that is suitable for the investigation of nanostructures, particle alignment, protein nanocrystals and the *in situ* study of kinetics.

After covering the fundamental details of microfocused X-rays and microfluidics individually, this thesis reviews the combination of these technologies extensively. This review includes the past and current device fabrication approaches, their up- and down-sides with respect to X-ray applications & processability as well as the related successful application examples.

Further, different types X-ray compatible microfluidic devices have been developed and produced by using soft lithography which gives precise and highly reproducible design control over features of the microchannel geometry. These developed types of X-ray compatible microfluidic devices include closed-microchannel systems and open liquid jet systems.

Devices of the first, closed type have already been operated successfully at the 3rd generation synchrotron PETRA III (DESY) at the Micro- and Nanofocus X-ray scattering beamline MiNaXS/P03.

One example of the microfluidic small-angle X-ray scattering (MF-SAXS) experiments revealed the striking effect, that after passing a narrow section, anisotropic wormlike particles are rotated perpendicular to the flow direction, keeping this orientation over the remaining length of the channel. This phenomenon has then been studied excessively using various techniques including MF-SAXS, microparticle image velocimetry and different kinds of microscopy such as scanning electron-, light-, polarization-, high speed video-, fluorescence-, confocal laser scanning-microscopy. Additionally, the microfluidic systems have been studied using computational fluid dynamics (CFD) simulations that help to understand the fluid flow, non-linear problems or enabled the optimization of the microchannel geometries.

As a result, the non-linear scientific problem of non-Newtonian fluids in confined geometries is now well understood and the related experimental control parameters have been identified and quantified. This flow-alignment of cylindrical, wormlike or fibrous structures is central to many processing steps such as in the production of fibers, during injection molding or the flow of cells and proteins through thin capillaries.

Another example of a closed system demonstrates the high sample efficiency of microfluidic grids. These devices are merely millimeters of size, shear-inducing and require only 2-5 μl of sample for the shearing and X-ray study of a polymer nanocomposite material.

The second microfluidic device type is based on an open nozzle geometry and produces small liquid jets with μm -diameters (0.9 to 5 μm) at very low flow rates (150 to 1000 $\mu\text{l h}^{-1}$) under atmospheric or vacuum conditions. The presented microfluidic liquid jet devices are based on the gas dynamic virtual nozzle (GDVN) design which enables reliable and essentially clogging-free jetting over long periods of time. Further, these devices are easy to produce using established soft-lithographical techniques which enable precise and reproducible microchannel design control that is critical for the liquid jet optimization at small flow rates. This design control is demonstrated by the easy integration of additional microfluidic features, such as jet-in-jet flow focusing or dense arrays of multiple adjacent liquid jet nozzles on a single device, without the need of additional production steps. The microfluidic liquid jet system has also been studied in great detail using various microscopic techniques (see above) as well as CFD-simulations. Along with the variation of experimental parameters and nozzle geometries, these analyses have lead to a better understanding of the fluid dynamic behavior of the liquid jet in microfluidic devices and to the control of jet diameters and droplet breakup types.

The mentioned features (reliability, small sample consumption, etc.) and the open geometry design make this microfluidic liquid jet system highly relevant for the establishment as a sample environment at X-ray FELs. These facilities deliver X-ray pulses that are ultrashort (fs-range) and so enormously intense that a full diffraction pattern is recorded from a single pulse while the sample explodes in the process and turns into a glowing plasma (ca. 60,000 K). Hence, static samples or closed flow geometries are incompatible with these next generation X-ray sources which underlines the importance of the liquid jet approach.

The broad scientific scope of microfluidic concepts and lithographic microfabrication techniques have also been demonstrated by creating solutions for other non-X-ray applications. The examples for this include the CFD-simulation of a non-linear scientific problem of a spray drying device, i.e. its internal fluid structure interaction, or the design & fabrication of microfeatured stamps for the microcontact printing of spherical polyelectrolyte brushes. Another example demonstrates the combination of nanotechnology and microstructuring techniques for developments towards sensoric applications.

Zusammenfassung

Mikrofluidik erlaubt es Flüssigkeiten nanoliter-genau zu kontrollieren. Durch diese präzise Strömungskontrolle ist diese Technologie prädestiniert für die Grundlagenforschung an mikrofokussierten Röntgenquellen. Die aktuellen Entwicklungen auf dem Gebiet der Synchrotron-Technologie sowie das Aufkommen von Freie-Elektronen-Lasern (FEL) eröffnen aufregende Möglichkeiten, wie z.B. Femtosekunden Röntgen Nanocrystallographie. Aus der stetigen technologischen Entwicklung ergibt sich die Frage, wie Probenumgebungen gestaltet und gefertigt sein müssen, um mit den zunehmend brillanten und hoch-intensiven Röntgenstrahlen kompatibel zu sein.

Durch die Entwicklung Röntgen-kompatibler Mikroflusszellen und mikrofluidischer Flüssigkeits-Strahl Systeme, die für die Kombination von Röntgenstreuung mit mikrofokussierten Strahlen und Mikrofluidik optimiert sind, trägt diese Dissertation wesentlich zum Aufstreben dieser machtvollen experimentellen Methode bei, welche für die Untersuchungen von Nanostrukturen, Partikelorientierungen, Proteinkristallen und *in situ* Studien von Kinetiken geeignet ist.

Nach der Beleuchtung der grundlegenden Details über mikrofokussierte Röntgenstrahlen und Mikrofluidik, wird die Kombination dieser Technologien ausführlich besprochen. Dabei wird auf die vergangenen und aktuellen Chip-Fertigungsansätze, deren Vor- und Nachteile in Bezug auf Röntgenanwendungen & Verarbeitung sowie auf relevante Anwendungsbeispiele eingegangen.

Darüber hinaus wurden verschiedene Röntgen-kompatible Mikrofluidik-Chips entwickelt und mittels Softlithographie hergestellt, wodurch eine präzise und reproduzierbare Kontrolle über die hergestellten mikrofluidischen Kanalgeometrien ermöglicht wird. Diese entwickelten Röntgen-kompatiblen Chips können in zwei Typen unterteilt werden: geschlossene Kanalsysteme und offene Flüssigkeits-Strahl Systeme.

Chips des ersten, geschlossenen Typs wurden bereits erfolgreich an dem Synchrotron der dritten Generation PETRA III (DESY) an der Mikro- und Nanofokus Röntgenstreuungs Beamline MiNaXS/P03 betrieben.

Zum Beispiel enthüllte ein mikrofluidisches Röntgenkleinwinkelstreuungs-Experiment (MF-SAXS) den erstaunlichen Effekt, dass sich anisotrope wurmartige Partikel nach dem Passieren einer Kanalverjüngung im Kanal quer stellen und diese Orientierung über die restliche Länge des Kanals beibehalten. Dieses Phänomen wurde daraufhin mit vielen Techniken, wie MF-SAXS, Mikropartikel-Velocimetrie oder verschiedensten mikroskopischen Methoden ausführlich untersucht; darunter Raster-Elektronen-, Licht-, Polarisations-, Hochgeschwindigkeitsvideo-, Fluoreszenz-, Konfokal-Laser-Scanning-Mikroskopie. Zudem wurden die mikrofluidischen System mittels der numerischen Strömungsmechanik (CFD) untersucht, welche dabei hilft den Fluid-Fluss sowie diese nicht-lineare Problemstellung zu verstehen oder die Kanalgeometrien zu optimieren.

Diese nicht-lineare wissenschaftliche Problemstellung nicht-Newtonischer Fluide in engen Geometrien ist nun gut verstanden und die relevanten Einflussgrößen wurden erkannt und

quantifiziert. Die Strömungsorientierung von zylindrischen, Wurm- und Fibrillen-artigen Strukturen ist von zentraler Bedeutung für die viele Prozesse, wie z. B. der Faserherstellung, den Spritzguss-Verfahren oder dem Fluss von Zellen und Proteinen durch dünne Kapillaren.

Ein weiteres Beispiel für geschlossene Kanäle demonstriert die hohe Probeneffizienz mikrofluidischer Rillen-Chips. Diese sind nur wenige Millimeter groß, scher-induzierend und benötigen lediglich 2-5 µl Probe für die Röntgenanalyse eines scher-orientierteren Polymer-Nanokomposit Materials.

Der zweite Typ von Mikrofluidik-Chips basiert auf einer offenen Düsen-Geometrie und produziert Flüssigkeits-Strahlen mit Mikrometer-Druchmessern (0.9 bis 5 µm) bei sehr geringen Flussraten (150 to 1000 µl h-1) unter Normaldruck- oder Vakuum-Bedingungen. Die vorgestellten mikrofluidischen Flüssigkeits-Strahl-Chips basieren auf dem Prinzip der gas-dynamischen virtuellen Düse (GDVN), welches der zuverlässigen und verstopfungsfreien Betrieb über lange Zeiten ermöglicht. Darüber hinaus sind diese Chips einfach und mittels softlithographischer Techniken herstellbar, welches ein präzises und reproduzierbares Mikrokanal-Design ermöglicht, dass kritisch für die Optimierung von Flüssigkeits-Strahlen bei kleinen Flussraten ist. Diese Design-Kontrolle wird demonstriert durch die einfache Integration zusätzlicher mikrofluidischer Elemente, wie z. B. ein Strahl-im-Strahl-Strömungsfokussierung oder dichter Gruppen vieler Düsen, ohne zusätzliche Herstellungsschritte. Das mikrofluidische Flüssigkeits-Strahl System wurde ebenfalls mittels einer Reihe mikroskopischer Methoden untersucht (s. oben) sowie CFD-Simulationen. Zusammen mit der Variation experimenteller Parameter sowie Kanalgeometrien, haben diese Untersuchungen zu einem besseren Verständnis des fluiddynamischen Verhaltens von Flüssigkeitsstrahlen in mikrofluidischen Chips sowie zu der Kontrolle des Strahldruckmessers und des Tropfenabbruch-Typs geführt.

Diese erwähnten Vorteile (Zuverlässigkeit, geringer Probenverbrauch, etc.) und die offene Kanalgeometrie machen dieser mikrofluidischen Flüssigkeits-Strahl Systeme höchst relevant für die Etablierung als Probenumgebung an Röntgen-FEL. Diese Einrichtungen generieren Röntgenblitze, die ultrakurz (fs-Bereich) und enorm intensiv sind und mit denen ein ganzes Streubild mit nur einem Lichtpuls aufgenommen werden kann. In diesem Prozess explodiert die Probe und wird in ein leuchtendes, ca. 60 000 K-heißes Plasma verwandelt. Deshalb sind statische Proben oder geschlossene Flusssysteme die diesen Röntgenquellen der nächsten Generation inkompatibel, was die Wichtigkeit des Ansatzes offener Flüssigkeits-Strahlen unterstreicht.

Der wissenschaftliche Weitblick des mikrofluidischen Konzepts und der lithographischen Mikrofabrikation wurde ebenfalls demonstriert, indem zusätzlich Lösungen für andere Röntgen-freie Anwendungen gefunden wurden. Die Beispiele hierfür umfassen CFD-simulationen für nicht-lineare wissenschaftliche Problemstellungen eines Sprühtrockners, genauer dessen interne Fluid-Struktur-Interaktion, oder die Gestaltung & Herstellung von Mikrostrukturen für den Mikro-Kontaktdruck, also das mikrometer-genaue Stempeln, kugelförmiger Polyelektrolyt-Bürsten. Ein weiteres Beispiel demonstriert die Kombination von Nanotechnologie und Mikrostrukturierungs-Techniken für Entwicklungen in Richtung sensorischer Anwendungen.

1 Introduction

1.1 Motivation

A wide range of nature's fundamental growth principles, like for example self-assembly or nucleation & growth, are governed by processes on the nanometer to micrometer length scale and their understanding is of great interest for modern material sciences and condensed matter physics.¹⁻³ The investigation of these elemental principles requires the combination of advanced analysis techniques that extend into the relevant length scales with sample environments that are capable of controlling the experimental physical and chemical conditions with very high precision.

From an analysis point of view, X-ray scattering techniques and microscopic methods offer a variety of tools to study these processes with great detail on all the relevant length scales. With the current developments in synchrotron technology and with the advent of free electron lasers (FEL), very exciting possibilities arise such as time-resolved experiments at highly brilliant synchrotron sources and serial femtosecond X-ray nanocrystallography at X-ray free electron lasers.⁴⁻⁷

With respect to the sample environment, the interdisciplinary scientific field of microfluidics is predestined for fundamental investigations because it focuses on the precise control and manipulation of very small fluid volumes in micrometer-sized geometries.⁸ The combination of microbeam X-ray scattering, microscopy and microfluidics is currently being developed into a powerful experimental methodology suitable for the *in situ* investigation of nanostructures, particle alignment and the *in situ* study of kinetics.⁹⁻¹⁴ This progress is enabled by creating X-ray compatible microflow chips and microfluidic liquid jet devices that allow new scientific approaches compared to traditional experiments on the macroscale because the sample's environmental conditions, like small scale concentration gradients or flow fields on the micron-scale, can be tailored to particular scientific questions.^{9,13,15}

The following chapters will provide an overview over this combination of technologies by covering its origins & challenges, the theoretical fundamentals as well as the involved methods and techniques.

1.2 Microfocus X-ray sources

Small-angle X-ray scattering (SAXS) allows to analyze the nanometer-sized internal structure of a sample. However, X-ray sources with traditional collimation systems are only capable to deliver beams which are typically millimeter-sized. This range of X-ray spot sizes prevents the precise analysis of small or heterogeneous samples due to the signal averaging over the illuminated area.

This situation improved tremendously with the greatly increased peak brilliance of state-of-the-art synchrotrons and with the advent of specialized techniques for the generation of microfocused X-rays.^{4,16} Due to the pioneering work at dedicated focused X-ray beamlines, a variety of focusing principles has been developed that involve components like Kirkpatrick-Baez (KB) crossed mirrors or -multilayers, capillaries, Fresnel optics, wave guides or compound refractive lenses (CRL) and together with advances in high-precision positioning systems, these techniques now enable X-ray foci down to the nanometer range.^{11,16-26} Consequently, samples can now be analyzed with a much higher spatial resolution and greater precision. This capability allows to distinguish between differently structured domains in a material of which the scattering signal previously had been averaged.

However, the focus spot size is not the only thing to consider for experiments with focused X-ray beams. It is also very important to consider the divergence of the beam as well as the overall photon flux.²⁰ The relation between these three parameters can be imagined as a triangle because all of them are interrelated. For example, it is possible to generate very small-sized X-ray beams using CRL-focusing optics. This also increases the photon flux at the focus position tremendously. However, this is only possible at the cost of a higher beam divergence and consequently a loss of resolution. It is also possible to have a small beam with low divergence for an increased resolution, but this might only be possible at the cost of photon flux which results in longer measurement times. If photon flux and divergence are both important, the minimum X-ray spot size has to be larger with a decrease of spatial resolution, although the beam size would still be in the low micrometer range. An example overview over the spot sizes and its influence on divergence and flux for different focusing techniques is shown in Fig. 1.

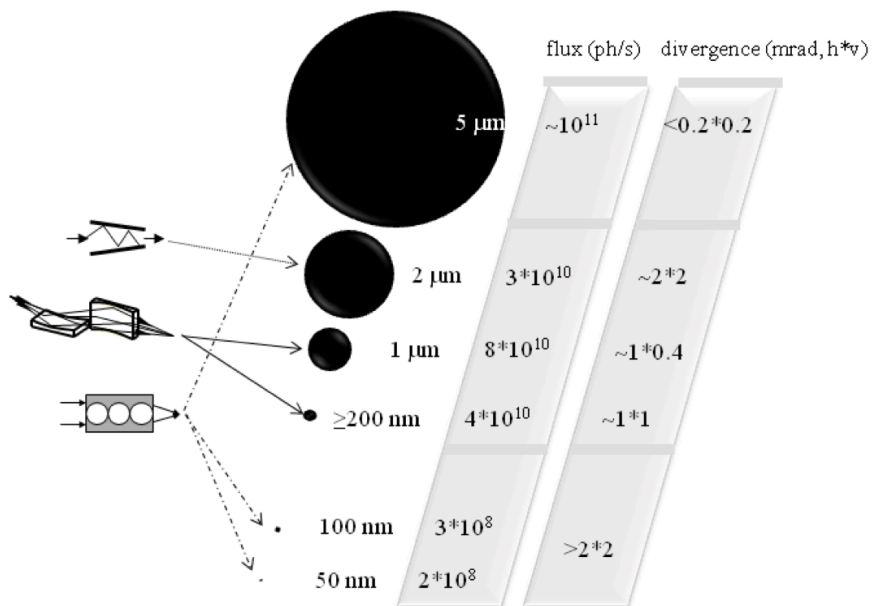


Figure 1 Comparison of different X-ray microfocusing techniques and their spot size-dependent influence on flux and divergence. The focusing types include capillaries (*top*), Kirkpatrick-Baez (KB) crossed mirrors (*middle*) and compound refractive lenses (CRL, *bottom*). (Figure from²⁰, Copyright IOP Publishing)

Today's dedicated microfocus X-ray beamlines at 3rd generation synchrotrons, like for example P03 (PETRA III at DESY, Hamburg, Germany) or ID13 (ESRF, Grenoble, France), also take the focusing distance from the optics to the sample into account. This leads to a lower divergence at a given focus spot size while a high photon flux is maintained. In the end, it is a question of the optimum combination of focusing settings for a given sample or experimental setup. In case of a microfluidic X-ray experiment, the maximum divergence of the microfocused beam is dictated by the channel height which typically ranges between 50 µm and 100 µm. In most of our microfluidic SAXS experiments, the X-ray beam size was adjusted to spot sizes around 10 µm by 10 µm to guarantee a low divergence and maintain a high photon flux.

An example which clearly demonstrates the benefits of the high spatial resolution of microfocused X-ray beams is the analysis of thin cellulose- or high-performance polymer fibers²⁷⁻²⁹. A fiber's structure can be mapped in great detail which also provides information about the fibers internal structure. Another very interesting example for a biological sample system are spider silk fibers.^{22,30-34} These in vitro and in vivo studies revealed how the spider silk fiber's nanostructure changes during the spinning process, during its elongation or under the influence of CO₂ and how this affects the fiber's tensile strength and micro-structural properties.

The smaller X-ray beam size is also important for grazing-incidence small-angle scattering (GISAXS) because the microfocus-illuminated area is much smaller compared to conventional X-ray beams, enabling better spatial scanning resolution.³⁵

Another example where the use of a microfocused X-ray beam greatly improves the spatial resolution is SAXS microtomography.³⁶⁻⁴⁰ This measurement technique reveals the internal three-dimensional structure of a sample, like for example a high performance polymer fiber, by rotating it during the detailed mapping with the X-ray beam. Due to the Nyquist-Shannon sampling theorem and the microfocused X-rays that enable the mapping of much smaller volumes, the sample scans require much less images (and therefore shorter scanning times) for a given resolution compared to tomographic scans with larger beams.^{41,42}

The ongoing development of X-ray sources leads to increasingly brilliant and intense beams.⁴ This can lead to new problems concerning the sample: the maximum X-ray dose before the sample degrades. Biological samples or soft matter are just two examples of sample systems which are susceptible to radiation damage.⁴³ A protein crystallographic case study demonstrated that it is possible to increase the sample's resilience to beam damages through freezing.⁴⁴ Obviously, this cryogenic approach is impractical for liquid samples or solutions that freeze below the targeted temperature, but it is a very useful method for protein crystals. However, this study also revealed that the successful collection of a crystallographic data set is only possible up to a certain X-ray dose because otherwise the sample degrades before the data set is obtained.⁴⁴ This maximum dose dictates a minimum crystal size in the micrometer

range which is very limiting for the protein-structure determination at traditional X-ray sources like synchrotrons or lab sources. The required minimal crystal size could be reduced by the use of microfocused X-rays in combination with motorized sample handling that enable precise crystal scans, but it is still an extremely challenging task to grow 'large' micrometer-sized protein single crystals in the first place.^{43,45}

One possible approach to avoid the beam damage for liquid samples or solutions is to use a continuous sample stream minimizing the sample residence time in the volume of the X-ray focus. This approach requires a sample environment that allows to control liquids with very high precision and reproducibility on the micrometer scale. If this was not the case, the possibly high sample consumption rates of macroscopic flow systems would make the required sample amounts impractical. This is where the combination of microfocused X-ray beams and X-ray compatible microfluidic devices becomes important and demonstrates its strengths.^{9,46-48} The challenges and benefits of X-ray compatible microfluidic sample environments as well as first examples of experiments will be discussed in further detail in the following chapter.

Another approach for overcoming the maximum dose limit of solid and liquid samples becomes available with the advent of X-ray free electron lasers (XFEL).⁴⁹⁻⁵¹ This next generation of X-ray sources solves the radiation damage problem by generating highly intense femtosecond X-ray pulses and applying the principle of 'diffraction before destruction'.^{6,52} Each generated X-ray pulse is so intense that a full diffraction pattern is collected with this single shot while its pulse length is so short (femtosecond range) that the diffraction pattern is generated before the sample is destroyed by Coulomb explosion. Consequently, the successful collection of diffraction patterns requires a fresh sample with each single pulse. However, the realization of an efficient and reliable way of generating a continuously replenishing sample stream is a very challenging task.^{53,54} This is where the microfluidic liquid jet devices, which are introduced in more detailed in chapter 7.3, offer great potential as a sample environment for XFELs and other pulsed laser experiments due to the flexible design control and fast fabrication routines of these devices.

1.3 Introduction to microfluidics

Microfluidics has become today's platform technology for the precise control and manipulation of fluids on the micrometer scale.⁸ The term 'microfluidics' originates from the combination of microfabrication techniques such as soft lithography with the fluid dynamics on the micrometer scale.^{10,55-57} Accordingly, small amounts of fluids (10^{-9} to 10^{-18} liters) are handled and manipulated using channels with dimensions of tens to hundreds of micrometers.⁵⁸ Hence, the biggest advantage of microfluidics lies in the micrometer dimensions of the channels and the related fluid dynamic implications for the samples such as laminar flow or diffusion-based mixing. These fundamental physical properties at the micron scale enabled the evolution of a variety of microfluidic tools. As an example, these tools can be highly

beneficial for the precise study of nucleation and growth processes and the fast and efficient screening of experimental conditions, like i.e. pH, ionic strength, species compositions, shear forces, cosolvents and concentration.⁵⁸

In the beginnings of this technology, the microfabrication of these small channels has been strongly influenced by the field of microelectromechanical systems (MEMS) that involves electronic circuits, sensors and micromechanical components.⁵⁸⁻⁶¹ This field offers a rich portfolio of available glass- and silicon-related fabrication techniques which stimulated the early development of microfluidics.⁵⁸ Today, the most used microfluidic device fabrication technique is soft lithography which is the combination of soft materials such as polydimethylsiloxane (PDMS) with photolithography.^{55,56,62,63} These fabrication methods and more device materials will be discussed in greater detail in the chapters 2 and 4.

The closely related terms ‘miniaturized total analysis systems’ (μ TAS) or ‘lab on a chip’ originate from the 1990s.⁶⁴ They describe the concept of combining the elements of microchemical ‘factories’ on a small, single chip which can incorporate functional elements such as pumps, valves, mixers, switches, heaters, multiplexers, electrodes and sensors.^{8,58,65-83} Consequently, the ‘lab on a chip’ concept aims towards the increase of mobility and the reduction of energy consumption, waste production and ultimately production costs by eliminating the need for traditional laboratory equipment.⁶⁴ This idea has been demonstrated for complicated chemical reactions and complex microchannel networks that combine multiple functional elements on a single chip.^{67,79} The concept of a micro reaction plant on a chip has also been demonstrated for complex reactions like the living anionic polymerization of block copolymers with direct on-chip DLS analysis of the resulting micelles. Another complicated reaction on a chip has been demonstrated for the synthesis of ¹⁸F-labeled organic compounds that are used in positron emission tomography (PET).^{58,81,84,85}

Additionally to the already-mentioned features of microfluidics that include low sample consumption, the beneficial features of microfluidics also include the integration of functional elements on a chip which enable small device footprints. Further, the fabrication costs are typically small, the waste production is minimized and it is also possible to run exothermic reactions while maintaining temperature control.^{86,87} This great temperature control is enabled by the small amounts of reacting mass combined with the high surface to volume ratio of the microchannel network. As a consequence, safe operation is guaranteed while the uniform heat transfer also gives great control over the reaction kinetics.^{86,87} Further examples include the production of microparticles and nanoparticles with a large diversity of morphologies and physicochemical properties with respect to size, shape, surface charge and amphiphilicity.⁸⁸⁻⁹⁶ Although the volumes of the handled fluids are typically small, the massive parallelization of microfluidic devices offers the potential of upscaling the processes to industrial scales.⁹⁷

Microfluidic technology also offers many advantages when it comes to sample analysis and, consequently, today's list of developed applications for microfluidic platforms is manifold.⁵⁸ For example, sample analysis related demonstrations include "separations coupled to mass spectroscopy, high-throughput screening in drug development, bioanalyses, examination and manipulation of samples consisting of a single cell or a single molecule".^{58,74,96,98-101} Further, applications include processes such as free-flow electrophoresis or blood sample analysis which have been improved and miniaturized.^{102,103} Together with the above-described functional elements, like valves and pumps, combinatoric experiments and high-throughput reaction screenings became possible.^{67,79,104,105} As an example, Quake *et al.* developed methods for the microfluidic large scale integration which is the microfluidic analogue to the technological jump from single transistors to microprocessors in electrical engineering.^{67,104} Through microfluidic valves, pumps, and multiplexers, this technology enables combinatorics and high-throughput screenings (HTS) for single cell analysis, deoxyribonucleic acid (DNA) synthesis, digital polymerase chain reaction (dPCR), genome sequencing, as well as and large scale genomics and proteomics.^{80,106-117} Furthermore, this HTS-approach also allows to find and optimize protein crystallization conditions while only requiring very small amounts of sample.¹¹⁸⁻¹²¹

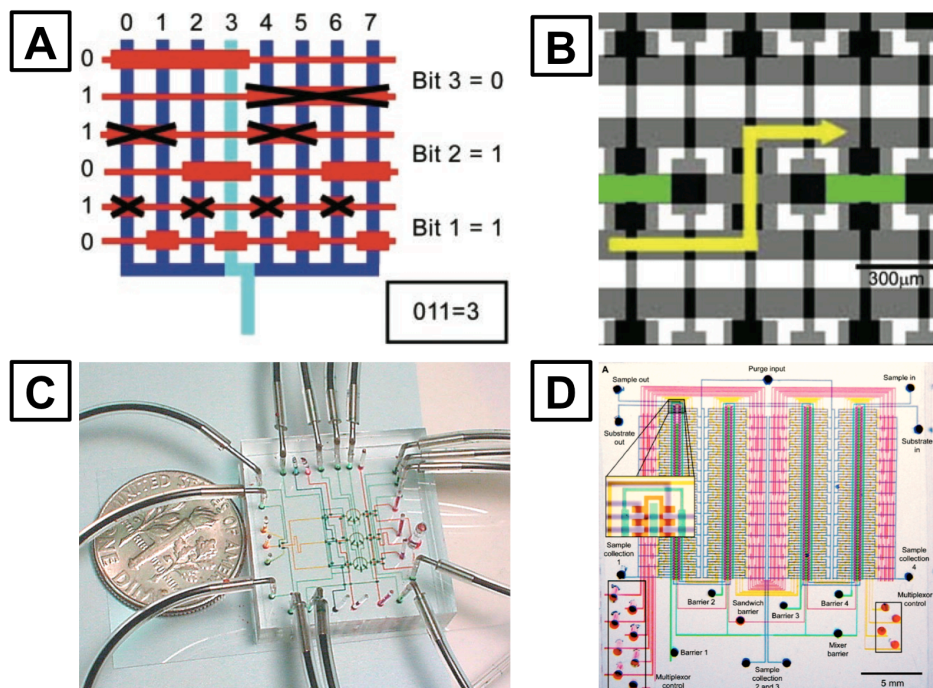


Figure 2 Illustration of the microfluidic large scale integration concept.^{67,79,104} (A,B) The flow and mixing of samples with nanoliter volumes are controlled using small valves and pumps. Accordingly, the resulting device footprint is very small (C) and the computer-controlled devices can handle very complex tasks such as the high-throughput screening of fluorescence-based single-cell assays (D). (Images from⁶⁷(A,B, Copyright Science),⁷⁹ (C, D, Copyright Nature))

Another example for microfluidic condition screening and combinatorics is the crystallization of single protein crystals. A wide range of microfluidic tools have been developed for this purpose due to this field's great importance for medicine and the life sciences.^{119,120,122-128} These examples show that it is possible to generate screening libraries for the automated crystallization of enzymes, proteins and other substances under defined conditions in droplets of individually addressable, on-chip microcompartments while only requiring very small amounts of sample.

All these examples demonstrate that microfluidics offers great control over fluids, reactions and experimental conditions by taking advantage of the fluid dynamics on the micrometer scale that enable laminar flow and diffusive mixing.¹⁰ In combination with the above-mentioned microfocus X-ray techniques, many new experimental opportunities arise which would not be possible with conventional macroscopic systems.

However, the transfer of microfluidic technology to X-ray experiments is technically very challenging due to the X-ray compatibility of the different device materials. In this ongoing transfer process, a variety of fabrication approaches and multiple device types have been developed. The next chapter will review these available X-ray compatible device types and describe the studies that have been performed at microfocus X-ray sources.

2 Microfluidic devices as experimental platforms for X-ray studies

2.1 Introduction

The combination of microfluidics and microfocused X-ray beams is a relatively young field of research that started with early experiments by Pollack *et al.* during the uprise of microfocused X-rays.⁴⁶⁻⁴⁸ These sample environments have been used for kinetic folding studies of biological systems such as RNA or proteins.⁴⁶⁻⁴⁸ Hence, this technology-combining approach links the benefits of small X-ray microbeams with the ones from microfluidics and, therefore, allows to study the sample system's response *in situ* and *in operando* with high precision and control.⁹⁻¹² The resulting opportunities as well as the first approaches and current developments of microfluidic sample environments for X-ray experiments will be reviewed over the course of this chapter.

As mentioned above, the turbulence-free flow conditions within the microchannels offer great control over the chemical and physical conditions. These experimental parameters, like concentration, pH, shear- and extensional forces, can be controlled precisely and reproducibly by adjusting flow, mixing and the microchannel geometry according to the sample system of interest. For example, reaction kinetics are diffusion-based due to the laminar flow. These fluid dynamic conditions enable detailed scans of the mixing area with microfocused X-ray beams and results in observable reaction time scales that extend over range from zero to several seconds.^{46-48,129-132}

Further, the earlier-mentioned problem of radiation damage (chapter 1.2) can be tackled by using sample environments that replenish the sample continuously and therefore reduce the X-ray dose to avoid beam damage of the sample. This is particularly important for fast-degrading systems, like for example biological samples. While the dose barrier for these samples is about 200 photons·Å⁻² for X-rays at an energy of 12 keV, the X-ray dose in a typical microfluidic continuous flow experiment is reduced to doses on the order of 0.1 photons·Å⁻² due to the very short sample residence times in the exposed volume.^{9,44,49} The experimental setup can be optimized even further by tuning the X-ray energy to maximize the transmission through the device's microchannel material and the liquid therein.¹³³

Next to the capability of successfully measuring fast-degrading and X-ray sensitive samples, microfluidic devices enable the study of precious samples that are only available in small amounts, like i.e. membrane proteins or deoxyribonucleic acid (DNA).^{46-48,130-132} Traditional experiments could prevent their analysis due to the limited sample availability and the experiment's minimum required sample quantity while microfluidic devices are highly sample efficient and consume only very small volumes in the range of micro- or even nanoliters per hour.^{67,79,118,134}

Another field where microfluidic devices offer a great potential is the analysis of (complex) fluids or anisotropic particles under defined shear and elongational conditions. Due to the well-controllable device design, various kinds of confined and well-defined geometries can be created. This design control enables the generation of specific shear fields which can be generated within the microchannels. This highly reproducible microchannel design allows deep insights into the non-linear dynamics of complex fluid because the experimental results from different methods can be correlated with each other. The experimental techniques which have been combined and correlated during this thesis include i.e. SAXS, micro particle image velocimetry (μ PIV), (polarisation-, confocal-, high speed video-) microscopy and computational fluid dynamics (CFD) simulations.^{13,135-137} As an example, our microfluidic SAXS experiments at the microfocus beamline P03 (PETRA III, DESY, see Fig.3) revealed the striking effect, that after passing a narrow section, wormlike particles are rotated perpendicular to the flow direction, keeping this orientation over the remaining length of the channel.¹³ The combination and correlation of multiple techniques lead to a detailed explanation of this phenomenon.^{13,135} The flow-alignment of cylindrical, wormlike or fibrous structures is central to many processing steps such as in the production of fibers, during injection molding or the flow of cells and proteins through thin capillaries. A recent publication, which underlines the scope of this effect, studied the orientation of carbon nanotubes (CNT) in melt-spun polymer fibers under different draw ratios. The results reveal a strong correlation between the CNT-orientation and the structural and mechanical properties of the fibers.¹³⁸ A more detailed analysis of the perpendicular orientation after narrow taperings demonstrates how the control over the nozzle geometry and other experimental conditions is a powerful tool for the precise tuning the perpendicular orientation which influences the mechanical properties of materials.¹³⁵

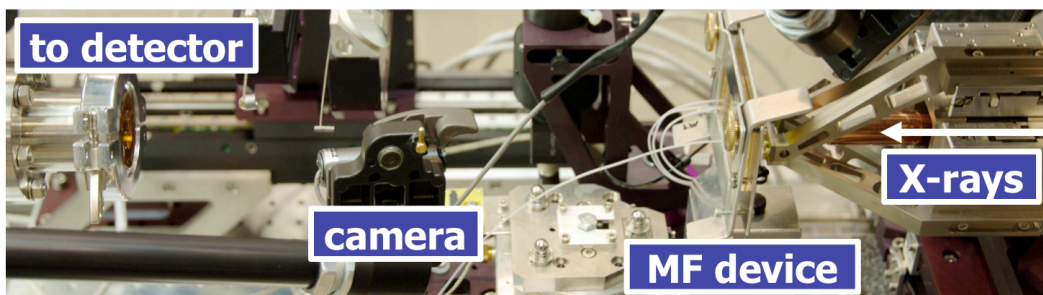


Figure 3 Photo of the setup at the P03 beamline at the PETRA III synchrotron (DESY, Hamburg, Germany). The microfocused X-rays pass the final slit collimation system (right) before the beam passes the microfluidic device that is monitored by a camera (middle). The scattered signal then passes the vacuum flight tube (left) and is recorded using a digital detector (Pilatus by Dectris, not shown).

The correct alignment between the focused X-ray spot and the microchannel is critical for an experiment and can be achieved in two ways. One method for the determination of measurement positions within the channels is based on the X-ray transmission scanning of the microfluidic device to identify the channel position and the device material. Typically, this routine is only possible with devices that offer sufficient contrast between the channel and the

wall material.^{25,130-132,139,140} Increasingly transparent and thinner devices show a much lower contrast for these types of scans and the correct alignment of the channel to the beam can become a very challenging task.¹⁴¹ In these cases it is much more convenient to rely on microscopic equipment that is available at modern microfocus beamlines. These beamlines offer special on-axis and off-axis microscopes that are aligned with the X-ray beam allowing the precise positioning of the X-ray spot in the microfluidic device.^{9,20,21,142} This microscope-based approach also allows to visually control the correct device operation during the experiment.

During this thesis, the microfluidic chips were usually aligned by scanning the microchannels (and integrated alignment structures) with the X-ray microbeam in x- and y-direction by moving the device along its plane. Next to the alignment step, a scan raster is chosen based on calibration design features that have previously been included in the microchannel design. This also allows the later correlation of the scanned scattering patterns to the channel geometry and other methods such as microscopy or particle image velocimetry. Once the area of interest is chosen and the device is aligned to the X-ray beam, the syringe pumps are started. As soon as the flow reached its steady state, the data collection begins by moving the microfluidic chip across the beam based on the previously programmed positions. The experiment is monitored using multiple video cameras and a software that handles and evaluates the scanned data in realtime (DPDAK, P03, DESY).¹⁴³

The continuous and reproducible steady-state nature of the fluid flow in the microchannels enables mapping experiments. These mapping scans allow to link the microfluidics-controlled experimental parameters at each of the scanned positions with the state of the sample system, like i.e. the time- and concentration-dependent reaction state in a kinetic experiment or the shear- and extensional force-induced orientation and structure of the sample.

Naturally, these mapping-type SAXS experiments can produce large amounts of data. Therefore, a question-driven and automated data reduction and -processing is of advantage to gain a quick, and at the same time detailed, overview over the location dependent SAXS-patterns.^{143,144} This approach of the fast data evaluation has been established during the course of this thesis and applied for generation color-coded pixel map that represent the location-dependent orientation of wormlike polymer micelles.¹³ As described above, the SAXS studies revealed an unexpected perpendicular orientation of anisotropic particles after passing narrow sections.^{13,135} As an example for the data reduction, color-coded pixel maps can be generated in real time during the scans giving a fast overview over the particle orientations. The live generation of pixel maps can also be used for other microfluidic experiments like the mapping of kinetic reactions with color-coding based on the advent or evolution of scattering features that indicate the progress of a reaction.^{25,130,132} In a second step, the results can be correlated to other methods like computational fluid dynamics simulations, microparticle image velocimetry or other microscopic techniques.^{13,130-132,135,140}

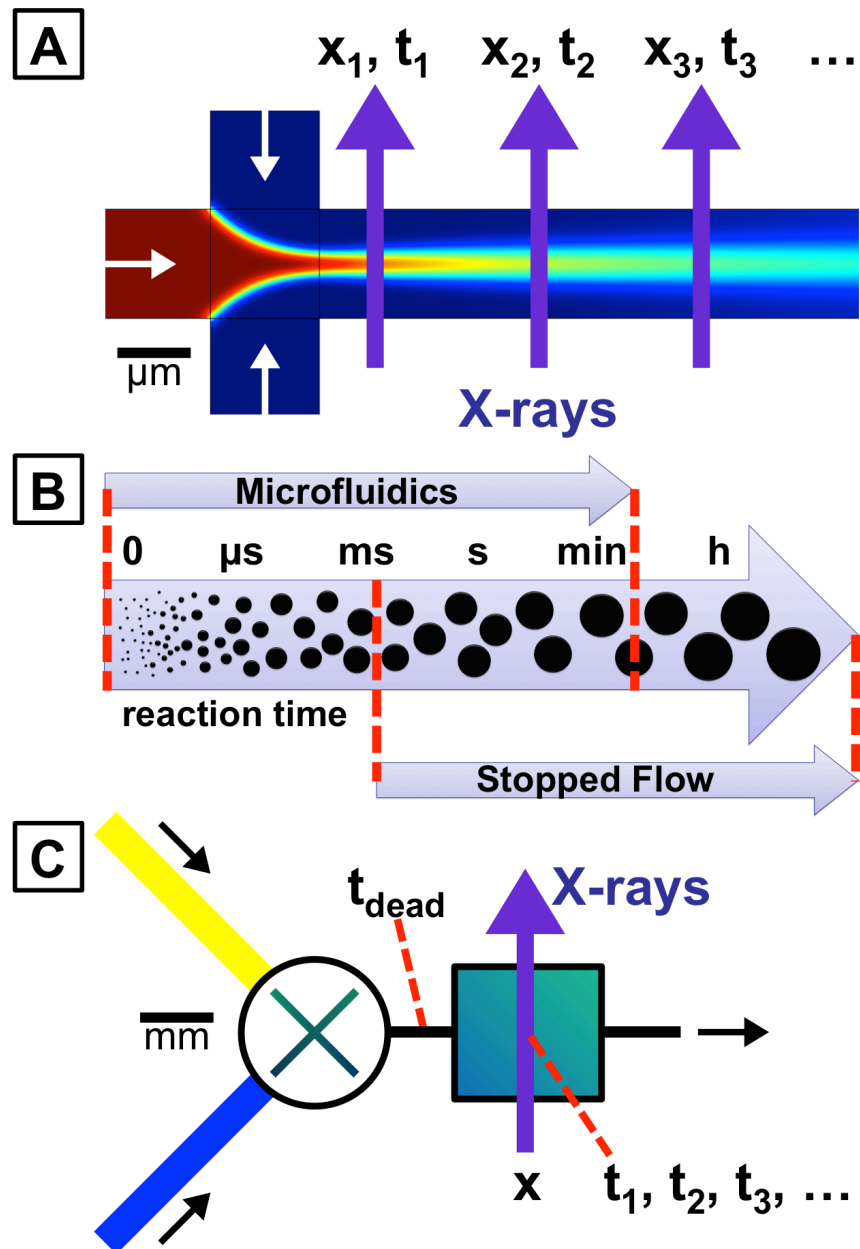


Figure 4 Illustration of time-resolved SAXS measurements of *in situ* nucleation and growth processes. (A) The controlled steady state flow in microfluidic channels enables precise scans with microfocused X-ray beams. (B) As a consequence, reaction kinetics down to very short time scales (μs -range) can be measured because the time resolution depends on the scan positions.¹²⁹ Stopped flow cells have a time-resolution down to a few milliseconds due to the experimental design. (C) The fluids are injected into a measurement cell at fast flow rates under turbulent mixing which involves a certain dead time. After the flow is stopped abruptly, the growth is monitored using highly intense X-ray beams and fast detector readout times which dictate the maximum time resolution.⁵

As pointed out above, the time-component of reaction kinetics are projected to a channel location due to the laminar continuous flow conditions in microfluidic devices whereas classical time-resolved X-ray studies require short exposure times and highly intense X-ray sources that are available at 3rd generation synchrotrons.^{145,146} The comparison of these two

methods is illustrated in Fig.4. Further, this mapping of a controlled steady state flow makes it possible to study the reaction kinetics down to very short time scales (starting at zero over microseconds up to seconds) and expose a single scanning spot longer while observing a constant reaction state. In contrast to microfluidics, the observable time range for time-resolved experiments in conventional stopped-flow cells is limited by the mixing times of the stopped flow cell and the minimum detector exposure- and readout times.^{5,129,145} The last aspect can be countered to a certain degree by binning the pixels of the detector for shorter readout times and reduced data noise, but at the cost of pixel resolution. Another alternative involves a smart fast shutter design that enables exposures with constant rates and variable time shifts.⁵ This setup improves the achievable time-resolution, but the experiments and measurements have to be repeated multiple times requiring large amounts of sample, more experimental time and the continual intervention of the experimentalist.

The weak X-ray scattering signal of low concentrated or weakly scattering samples requires longer X-ray exposure times for the collection of scattering data with a sufficient signal-to-noise ratio. The data quality can be critical for the data evaluation of SAXS patterns. As discussed above, this low scattering contrast can become a great problem for the static measurements of degrading samples because the maximum X-ray dose could be exceeded. Further, the sample's low signal could also prevent time-resolved experiments, even at 3rd generation synchrotrons, because the exposure times are too long for the time scale of a reaction.

The continuous flow of the microfluidic X-ray devices allows long measurement times at a single position due to the steady-state of the continuously flowing sample. Hence, the signal-to-noise ratio of the recorded scattering data can be improved while the time-resolution is maintained. By implication, this methodology makes kinetic experiments also accessible to lower intensity X-ray lab sources such as rotating anodes for example. Instead of relying on highly intense X-ray sources that enable short exposure times in the millisecond-range, the microfluidic time-resolved experiments can simply be performed by the measuring the steady-state system a fixed positions for a longer time while simultaneously offering a better time-resolution in the microsecond range.¹²⁹ This kind of SAXS-experiments requires specially designed and X-ray compatible microfluidic devices which will be reviewed in the following section of this chapter.

2.2 X-ray compatible microfluidic device types

The fabrication of X-ray compatible microfluidic devices has to meet multiple opposing challenges. On the one hand, the material has to be as transparent and as resistant to X-rays as possible. Simultaneously, it also has to be well processable for the fast, easy and reproducible fabrication of microfluidic devices that allow rapid prototyping of microchannel geometries that are based on computer aided design (CAD). The design and fabrication routines should also be compatible with the available microfluidic functional elements for fluid handling and -manipulations. Additionally, the fabrication routine has to provide an

interface to connect the microchannels to the elements of the macroscopic world like tubings and syringes or pressure control.

On the other hand, the material has to provide the necessary mechanical properties to withstand the applied pressures for handling the fluids while its resistance to solvents, chemicals and elevated temperatures is equally important. These requirements usually interfere with the material processability, the device-sealing bonding steps and/or microchannel surface modifications. Obviously, the X-ray compatibility and low background signal are also key factors for the use of microfluidic devices at synchrotrons and other X-ray sources.⁹ If there is any background scattering signal from the material that is not interfering with the measurements, distinct and also well defined, then it could be subtracted from the measurement data.

From the mentioned requirements, the solvent compatibility of the microfluidic device materials is a critical and potentially limiting factor for the range of possible experiments.¹⁴⁷⁻¹⁵⁰ Additionally the device material should be inert to the studied samples and chemicals as well as resistant to their adsorption to the channel walls. In many cases it is also highly desirable that the material allows visible light microscopy for the visual control of experiments.

Table 1 Comparison of different microfluidic device types for X-ray applications. The marks (+ = good / o = neutral / - = bad) are based on experience and the cited publications of the following device review.

	glass	silicon-PDMS	PDMS	Kapton	Kapton-steel	Kapton-PDMS	NOA81	COC	THV
X-ray resistance	+	+	-	+	+	+	o	+	+
X-ray transparency	-	o	-	+	+	+	+	+	o
Background signal	-	o	-	+	+	+	+	+	o
Fabrication speed	-	-	+	-	o	o	+	+	+
Design flexibility	o	o	+	+	-	+	+	o	o
Interface/Connection	-	-	+	o	-	+	+	o	-
Mechanical properties	+	o	-	+	+	-	+	+	+
Functional elements	-	-	+	-	-	o	o	o	-
Chemical resistance	+	o	o	+	o	o	-	o	+
Solvent resistance	+	-	-	+	o	-	o	-	+
Temperature resistance	+	+	o	+	+	o	o	-	o

Facing these challenges, a variety of device types has been developed over the past years which are based on different materials or hybrid variants thereof.⁹ Although no material has been suggested so far that meets *all* criterions at the same time, each of these X-ray compatible devices offers characteristics that are well suited for specific cases of sample systems or applications. An overview over the different available device types is shown in Fig.5 which are described in more detail in Tab.1. These device types and their applications will be reviewed over the course of this chapter.

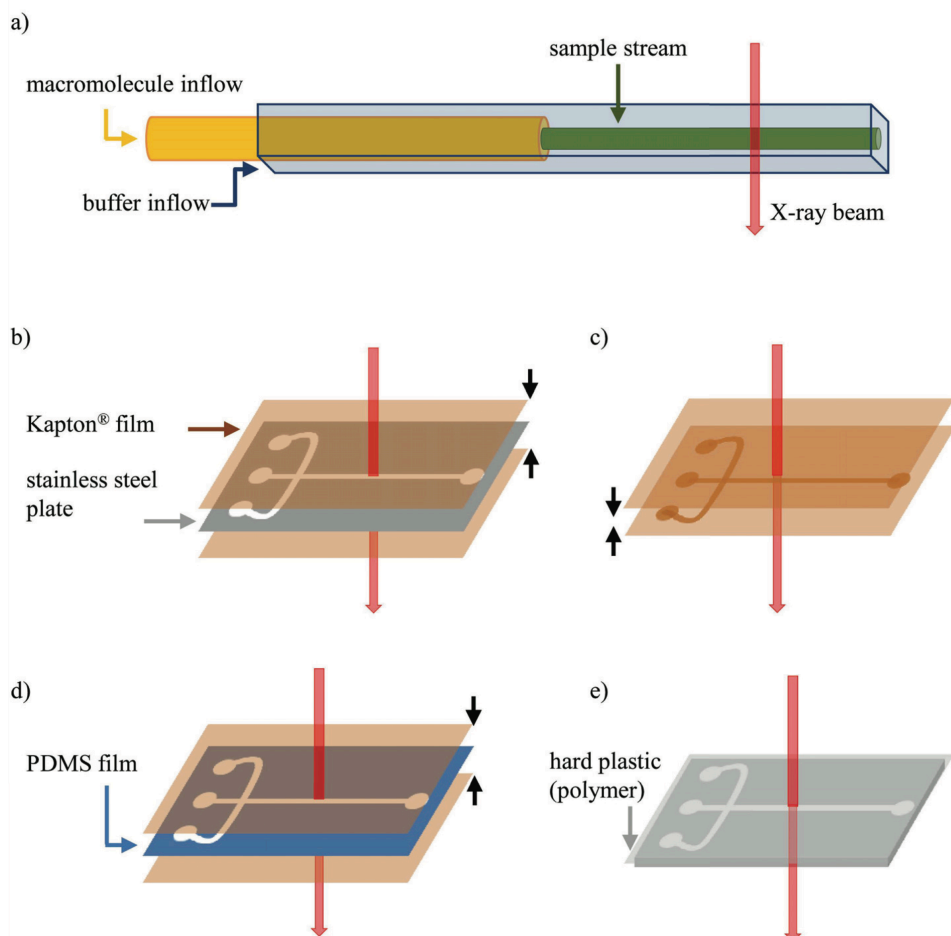


Figure 5 Illustration of different X-ray compatible microfluidic device types. (A) Glass capillary coflow device where the round inner capillary exactly matches the squared outer capillary for decreasing wall contact of the sample. Further, different hybrid or polymer-based devices are shown, including (B) Kapton-Steel, (C) Kapton, (D) Kapton-PDMS and (E) other polymers (NOA81, COC, THV, etc.). (Image from⁹, Copyright World Scientific Publishing Company)

As mentioned above, the first X-ray experiments with microfluidic devices have been performed by Pollack *et al* who investigated the folding of ribonucleic acid (RNA) and proteins.⁴⁶⁻⁴⁸ However, the used devices were mainly based on microstructured silicon which involves complicated, resource- and time-consuming fabrication steps.⁴⁶ Due to the use of cured silicone rubber (RTV 615) as a sealing layer, the solvent compatibility of these devices is limited.^{46,47,129,147}

Since the soft lithographic replication using polydimethylsiloxane (PDMS) is so easy to learn, it has become one of today's most used fabrication technique for microfluidic devices.⁵⁸ During the microstructure replication the curing PDMS shrinks less than 1% which results in very precise replicas that can be used for example as stamps in micro contact printing.¹⁵¹⁻¹⁵⁴ These open replicas can also be sealed to create closed microchannels. This is typically achieved by activating the PDMS using air plasma and then binding it covalently to glass slides which results in very pressure resistance microchannels.⁵⁷ This combination of PDMS that is bonded glass is typically the material combination of choice when it comes to microscopy-related applications of microfluidics due to its excellent optical transparency from 240 nm to 1000 nm and its low toxicity.⁵⁸ Additionally, the elasticity of PDMS can be controlled by the ratio between oligomer the cross-linker while this material's gas permeability is beneficial for cell cultures or microevaporation.^{9,15,58}

PDMS also has two significant drawbacks: the limited compatibility with solvents and the device fouling from the unspecific adsorption of biomolecules.^{9,34,147} However, PDMS offers a wide range of surface modification possibilities which enables to minimize these drawbacks or avoid the negative effects all together.¹⁵⁵⁻¹⁵⁹ The modification routines include sol-gel glass coatings for improved solvent resistance, layer-by-layer deposition of polyelectrolytes for permanently hydrophilic channel walls, the covalent deposition of fluorinated repellants against device fouling and UV-controlled photochemistry or grafting reactions on the channel surface for wettability tuning.¹⁵⁵⁻¹⁵⁹

PDMS can also be used for the measurement for SAXS directly if the devices are very thin. This has been demonstrated at the Diamond light source in for the orientation analysis of lamellae in microchannels.¹⁶⁰ Thin PDMS-based devices also allow microevaporation that can be used for the generation of concentration gradients in non-flowing samples.¹⁵ Although showing a stronger background signal, these devices' material homogeneity typically allows to extract the sample's signal through background subtraction. However, this process can decrease the signal quality and eventually the ability to evaluate the obtained scattering patterns. This decreased signal-to-noise ratio of the sample can result from factors like the subtraction-induced reduction of the signal and added detector readout noise from combining multiple files.¹⁶¹ Additionally to the X-ray background signal, the solvent compatibility of this material is also very limited.¹⁴⁷

A much better solvent compatibility is provided by glass-only-based microfluidic devices. As an example, glass capillary devices with tube-in-tube geometries have been successfully operated at synchrotrons for the study of *in situ* spider silk fiber formation.²² This device type also offers the benefit of reduced or no wall clogging due to the coaxial liquid sheath of the outer capillary.¹⁶² Further, the glass capillaries can also be etched down to thicknesses around 50 µm for improved X-ray transmission. The main downside of this device type is its fabrication procedure because it is complex, involves precise manual capillary alignment skills and lastly, the design variations of the channel geometry are limited.^{22,162}

When it comes to X-ray transmission experiments, glass and PDMS or their combination is counterproductive because of the material's own strong small angle scattering signal.¹⁶³

Alternatively, microfluidic devices can be directly fabricated through laser ablation.¹⁴¹ The microstructures are written directly into Kapton film which is then sealed with another Kapton film to yield the closed microchannel. The resulting devices are very thin, solvent resistant and they show good mechanical properties. Further, Kapton is an excellent material for X-ray applications because of its high radiation resistance and low absorption. It has also been shown that the laser ablation approach can be applied to other materials such as poly(methyl methacrylate) (PMMA), polystyrene (PS) and cyclic olefin copolymers (COC).¹⁶⁴ However, the major drawback of this laser-based approach is the low machining speed which can lead to long processing times due to the typically wide-spreading microchannel patterns.¹⁴¹

Another variant of stable microfluidic devices with Kapton as the only window material have been described by Pfohl *et al.*^{23,130,139,140} In these examples, open microchannels are spark eroded into stainless steel plates which are then sealed at the top and bottom using self-adhesive Kapton film. The minimum channel size is restricted to about 60-100 µm due to the resolution of the spark eroding technique.⁹ While this minimum channel size can be sufficient for many microfluidic experiments, the main drawback of this technique is the limited design flexibility because it is only possible to create relatively simple structures like straight lines.⁹

This design flexibility can be increased by choosing a channel wall material that is suitable for rapid prototyping.⁵⁷ A widely used process is called soft lithography and it involves microchannel templates that are fabricated by microstructuring a photoresist on a silicon wafer using UV lithography.⁵⁶ A thin layer of moldable material, such as PDMS, is then casted on this template by doctorblading or spin coating to generate open microchannels. These channels are then sealed with Kapton films from top and bottom, similar to the steel-based devices that have been described above.^{13,130,131,139,165} This combination offers great design flexibility through rapid prototyping while maintaining good X-ray properties by using Kapton windows. However, the X-ray signal could be influenced by the adhesive layer of the sealing kapton tape and the use of PDMS also limits the solvent compatibility of these devices.¹⁴⁷

A different routine that takes advantage of moldable materials and rapid prototyping is the fabrication of microfluidic devices made of an UV-curable optical adhesive by Nordland (NOA81).^{14,132,166,167} Originally used for the glueing of optical components such as lenses, this thiol-ene-based material is cured by a radical mechanism that allows surface chemistry modification and which is initiated by a UV-sensitive initiator.^{149,168} This material also allows to fabricate very thin devices with window thicknesses of a few tens to hundreds of microns while the small angle background signal is also much lower compared to PDMS.^{9,132,135} Furthermore, it provides a much better resistance to a wide range of solvents compared to

PDMS.^{147,149} It has also been demonstrated that this material is suitable for the fabrication of microfluidic three-dimensional flow geometries by aligning and sealing two microstructured layers.¹³² Each side is fabricated by multilayer lithography which yields a flow focusing geometry that minimizes or prevents clogging of the sample to the microchannel wall.^{9,132,162} However, the exact alignment of the two halves with micrometer precision can be very challenging. A general downside of this material is the observable beam damage of this material, especially for higher X-ray intensities, which can be observed as a brownish spot on the yellow-white translucent material. However, this beam damage does not interfere with the flowing samples on the timescale of typical microfluidic experiments.^{9,132}

2.3 Outlook: new processing techniques and device materials

New ways to fabricate microfluidic devices arise with the advent of new materials, new processing techniques or the recombination of existing components. As mentioned earlier, so far no material or routine has been studied yet that matches all criterions simultaneously, but many good routines have been described for the specific experiments.

Materials which allow rapid prototyping, like PDMS or NOA81, can take advantage the great design flexibility that is enabled through soft lithography.⁵⁷ Other rigid or hard materials, in terms of material properties or ease of processing (i.e. silicon, glass, Kapton), usually rely on fabrication processes that can be complicated or do not allow the same design flexibility as soft lithography.

The relatively young combination of soft lithography with casting-, (microinjection) molding- and hot-embossing-approaches offer multiple processing paths for the fabrication of microfluidic devices.¹⁶⁹⁻¹⁷⁴ This makes a wider range of (polymeric) materials accessible to microfluidics and offers great potential for the fabrication of microfluidic devices with material properties tailored to the specific experimental needs while maintaining the great design flexibility of rapid prototyping. As an example, rapid-prototyping-based PDMS-stamps and -templates can be used to emboss the microchannel structures into a wide range of thermoplastic materials such as polystyrene (PS), poly(methyl methacrylate) (PMMA), cyclic olefin copolymers (COC) and THV (fluorinated terpolymer: tetrafluoroethylene, hexafluoropropylene and vinylidene fluoride).^{148,150,175-182} Further, the use of fabrication techniques that are based on microinjection molding or hot embossing can greatly increase the production speed of microfluidic devices to industrial scales due to the relatively fast embossing step in the template replication process.^{163,169,170,172,183,184}

Next to Kapton with its great properties for X-ray applications, a number of X-ray compatible window materials have been tested including polymethylmethacrylate (PMMA), cyclic olefin copolymers (COC), negative photo resist SU-8 (MicroChem) or polypropylene (PP). It is possible to fabricate thin (ca. 250 µm or less) and microstructured films out of these materials of which the background scattering is very similar to air.^{9,163} From these

examples, thermoplasts like PMMA or COC can easily be structured by soft- or hot embossing while SU-8 can be microstructured directly by UV-lithography.^{9,184,185}

Multiple uses of COC as a material for microfluidic devices have been demonstrated.¹⁸⁴ COC-based microfluidic devices also offer a great potential when it comes to the integration of functional elements into the device. These integrated features of COC devices are manifold and include Au-electrodes for electrochemistry, elements for electrochromatography, or PDMS-based control layers for the screening of lyotropic phases.¹⁸⁶⁻¹⁸⁸ Further, the surface chemistry of COC-based devices can be modified by UV-grafting procedures and therefore optimized for the particular experimental needs.¹⁸⁹

Among the X-ray-related examples is a computer-coupled high throughput screening setup by Arleth *et al.* that uses microfluidic devices for the fast SAXS analysis of protein-folding under the influence of changing buffer conditions.^{176,179} Further, the automatization potential of microfluidic devices is demonstrated by using X-ray-CDs that are combined with automated sample positioning at synchrotron beamlines (PETRA III, DESY, Hamburg). These ‘SAXS-LabDiscs’ are rotational microfluidic devices that are based on centrifugal flow principles for the combinatoric mixing and screening of samples.^{125,180,190-194} It has also been shown that COC-based microfluidic devices are suitable for microfluidic grazing-incidence small-angle X-ray scattering (GISAXS) experiments.³⁵

However, a downside if this polymeric material is the limited solvent compatibility and, based on its thermoplastic nature, the lack of resistance against higher temperatures.^{163,177,180,184,189,195}

As described above, the advent of new techniques and materials offers new paths for the fabrication of microfluidic devices that are tailored to the experimental requirements. A different device fabrication approach will be discussed in the next section with the generation of liquid jets that avoid any materials in the X-ray beam path.

2.4 Microfluidic liquid jet devices for next generation X-ray sources

Today’s developments in synchrotron technology continually push the peak brilliance of the X-rays, enabling fast measurements as well as time-resolved *in situ* experiments.⁷ Consequently, radiation-induced sample degradation and the maximum X-ray dose start to become the limiting factors for experiments at these facilities. As described above, one way to avoid the dose problem is to scan different spatial position with microfocused beams, or use (microfluidic) continuous flow systems. However, each of these alternatives is limited to certain sample types.^{45,142}

Another path for overcoming the X-ray dose problems becomes available with the advent of highly intense and ultrashort-pulsed X-ray free electron lasers (XFEL).^{6,49} These free-

electron laser sources currently generate X-ray pulses at rates up to 120 Hz (LCLS, SLAC, Stanford, USA) while future facilities will even generate up to ca. 27,000 pulses per second that are bundled in 10Hz bunch trains (European XFEL, Hamburg, Germany, in 2015/2016). These X-ray pulses are so intense that a full diffraction pattern of nanometer-sized crystals is collected within a single shot and that the X-ray beams “are capable of destroying anything in their path”.^{6,50,196} During the illumination with a single light pulse, the sample explodes and turns into a glowing plasma (ca. 60,000 K).¹⁹⁶ Due to the ultrashort femtosecond pulse length however, the X-ray pulses outrun the explosion process, ‘freezing’ the atom positions in space.^{49,50} An analogue example from the macroscopic world for this ‘freezing’ principle is the highspeed flash photography work done by Harold Edgerton (MIT, Cambridge, USA). For example, his photograph “Cutting the Card Quickly” (1964, 1 µs exposure) shows how a bullet-separated play card levitates in air at its original position.

This concept of ‘diffraction before destruction’ is of great importance for the study of ultrafast processes and the characterization of a wide range of X-ray sensitive samples.⁴⁹ As an example, the structure determination of transmembrane proteins is important for medicine and the life sciences because this information can help to understand the signalling of cells or mechanisms of diseases.⁶ However, the structure determination of proteins is a very challenging task because these and many other biological samples are only available in small amounts and/or tend not to form single crystals of sufficient dimensions for traditional X-ray (micro-)crystallography.⁶ It is much easier to grow nanometer-sized protein crystals, but these cannot be analyzed at tradionional X-ray sources due to their small size and the discussed dose limit. The relation between the average intensity of a diffraction peak and the crystal volume is approximately proportional.⁴⁵ Hence, the required beam intensity of a 20 µm crystal is 1000-fold higher than for a 200 µm crystal.⁴⁵ Theoretical and experimental results show that the critical dose for a successful structural evaluation is mainly dictated by the crystal size, despite cryogenic attempts of measuring protein crystals that are cooled below 100 K.⁴⁵

Recently, femtosecond X-ray protein nanocrystallography has been demonstrated for the high-resolution characterization of photosystem I&II and the model protein lysozyme, showing that the X-ray dose limit can be overcome as described above.^{6,197-199} As a consequence of the enormous X-ray pulse intensity, statically mounted samples or experimental environments for flowing samples that are based on closed geometries are incompatible with these 4th generation X-ray sources. Therefore, special sample environments are required that deliver the samples in mid-air and under vacuum conditions while being as sample efficient as possible.^{53,200} These kinds of sample environments for XFELs and how microfluidics offers great potential for the adequate delivery of samples will be discussed in this chapter.

Currently, continuously replenishing sample streams are generated using aerodynamic lens particle injectors or liquid jets using a glass-based capillary-in-capillary design.^{53,200} Since the

glass capillaries are widely used and suitable for liquid samples, this chapter will focus only on these. The principle for the generation of liquid jet is based on a gas sheath which shapes a liquid stream and has first been demonstrated in a plate-orifice geometry.^{201,202} Later, this concept has been transferred to glass capillaries which run essentially clogging free due to their gas-dynamic virtual nozzle design (GDVN).⁵³ In other words, the pressured gas forms a liquid stream and avoids any wall contact of the liquid.⁵³ This results in a very stable and reliable system for the generation of nano- or micrometer-sized liquid jets that require only small amounts of sample (down to ca. 100 $\mu\text{l h}^{-1}$).^{203,204}

The main drawback of this glass capillary design is the complex fabrication process that involves steps like flame polishing of the tip, its grinding as well as alignment of the inner and outer capillary.^{53,203-205} These steps require the manual skills and attention of a lab worker which intrinsically results in geometric variations of the nozzles. It is therefore very hard or impossible to exactly reproduce a targeted design or even automate the process. This is a major issue because the generated fluid dynamics of the liquid jet and, hence, minimum flow rates and liquid jet diameters strongly depend on the geometric and experimental parameters.²⁰⁵⁻²⁰⁷

The fabrication procedure is one key point where microfluidic devices shine, due to their fast and easy fabrication and highly reproducible design which is based on established soft-lithographical techniques.⁵⁵⁻⁵⁷ In this thesis, microfluidic chip-based devices are presented that produce liquid jets with μm -diameters (20 down to 2 μm , or even 940 nm) at very low flow rates (down to 150 $\mu\text{l h}^{-1}$) under atmospheric or vacuum conditions. These microfluidic liquid jet devices are also based on the gas dynamic virtual nozzle (GDVN) design which enables reliable and essentially clogging-free jetting over long periods of time.⁵³

The flexibility in microchannel design control is demonstrated by the easy integration of additional microfluidic features, such as jet-in-jet flow focusing, which could enable new *in situ* experiments at XFELs, or dense arrays of multiple adjacent liquid jet nozzles on a single device, without the need of additional production steps. Hence, the potential of simplifying and up-scaling the fabrication of micro-nozzles for the generation of liquid jets is demonstrated. The microfluidic liquid jet system is highly relevant for the establishment of microfluidics at XFELs because these devices deliver the sample continuously, reliably and efficiently in atmospheric or under vacuum conditions, as illustrated in Fig.6.¹³⁶

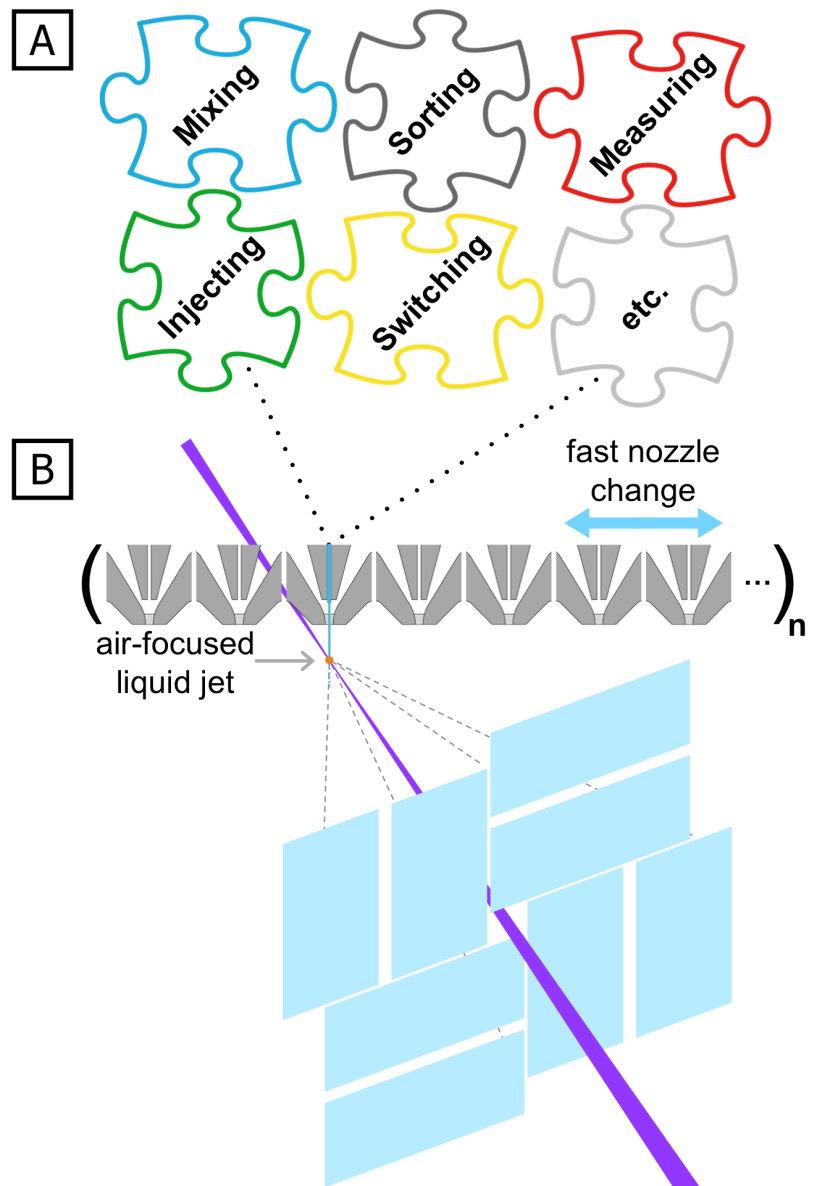


Figure 6 Combining the liquid jet principle with microfluidics. (A) Illustration of the building block principle of functional microfluidic tools that can be combined and stacked using the microfluidic liquid jet device principle. (B) The X-ray beam hits the liquid jet in this illustration of the experimental setup. Microfluidic devices are advantageous because each liquid jet device contains a dense array multiple microfluidic GDNV-nozzles which enable fast nozzle changes and, consequently, reduce (expensive) downtimes at the X-ray free electron lasers. (Image adapted and extended from ⁶)

2.5 Conclusions

In conclusion, the combination of microfluidics with microfocussed X-rays is a valuable experimental methodology for the study of fast *in situ* experiments. While this field is still emerging, a wide range of device types is already available. The on-going development of microfabraction techniques and advent of materials for the production of X-ray compatible microfluidic devices add to the great potential and this technique's future applications. Additionally, the variety of other X-ray imaging and spectroscopic techniques could extend the experimental opportunities of microfluidics at X-ray sources even further. Future developments of microfluidic systems and highly brilliant X-ray sources, such as synchrotrons or XFELs, could soon lead to the fundamental understanding of nucleation and growth processes or integration of the high-throughput screening of proteins that yields full three-dimensional as well as dynamics information about these species or even whole cells; with important insights for the natural and life sciences.

3 Theoretical Fundamentals

3.1 Self-organization of amphiphiles

One of nature's fundamental principles is self-assembly.²⁰⁸ While technical systems are typically organized by men, the self-organization of natural systems is based on internal processes on the very small scale. This bottom-up approach begins with single functional molecules that build up and organize themselves to larger structural elements. The self-organization of a system induces properties that it did not have before, like i.e. order, and this process can be described by the theory of spontaneous symmetry breaking.^{208,209} For example, this mechanism can be observed in nature with the formation of lipid double membranes of cells or the self-assembly of micelles and liquid crystals.²⁰⁹⁻²¹¹

For molecules to be able to form such assemblies of higher order, their structure and functional elements need to meet certain molecular prerequisites.²⁰⁸ These molecules need to possess (and unite) both long range repulsive and short range attractive forces in order to be capable of forming structured domains, as illustrated in Fig.7.

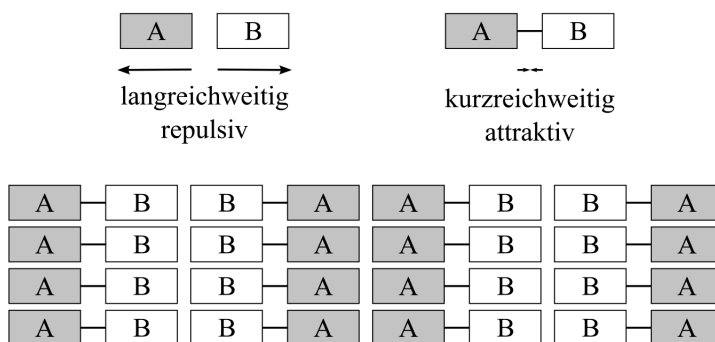


Figure 7 Illustration of amphiphile building blocks with long range repulsive and short range attractive forces and their self-assembly. (from²⁰⁸, Copyright WILEY-VCH)

Long range repulsive forces can appear as Coulomb repulsion, chemical incompatibility or hydrophobic interactions while covalent bonds or the local conservation of electroneutrality are examples of short range attractive forces.²⁰⁸ These prerequisites are met by molecules such as lipids or amphiphilic block copolymers of which the latter can form a wide variety of superstructures as illustrated in Fig8.^{1,208}

Continuous phases are formed in bulk or in lyotropic phases, and colloids like spherical or cylindrical micelles or vesicles are typically formed by microphase separation in dilute solutions.^{1,208}

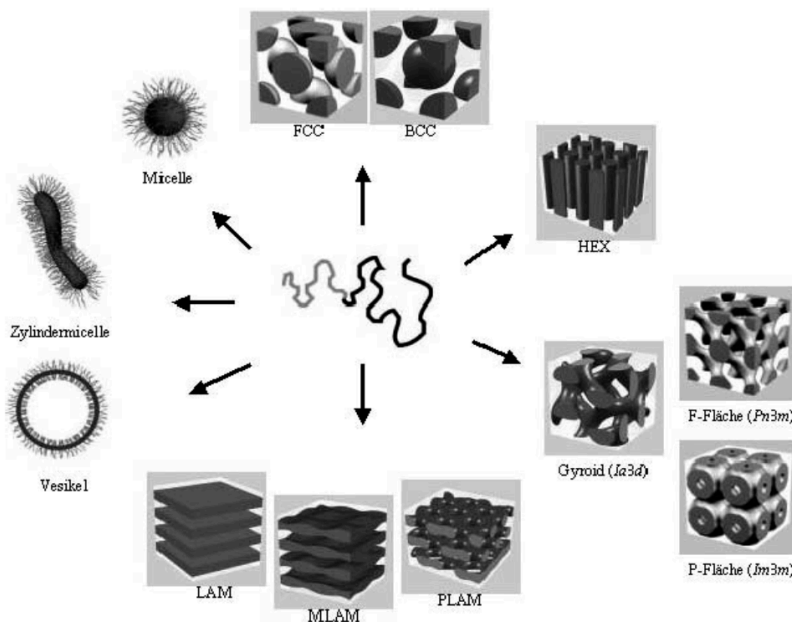


Figure 8 The self-organizational principle of amphiphile molecules, such as block copolymers or surfactants, leads to the formation of multiple topologies which are illustrated above. (Image from ²⁰⁸, Copyright WILEY-VCH)

These ordered domains are formed due to the minimization of interaction between the blocks of opposing forces. In an aqueous solution the hydrophobic chains of amphiphile molecules form molecular clusters or micelles and the hydrophilic chains of these molecules orient outwards towards the solvent. These clusters or micelles are formed above a certain concentration which is called the critical micelle concentration (CMC). Furthermore, the temperature has to be above the Krafft-temperature, below which the amphiphile's solubility decreases abruptly due to its increasing crystallinity.

It is also possible to predict the topologies and symmetries of the superlattices by the size of the hydrophobic domain (or tecton) relative to the hydrophilic domain which determines the curvature of the hydrophobic-hydrophilic interface.¹ This interface is described by the mean curvature H and its Gaussian curvature K that are defined by the two radii of curvature R_1 and R_2 based on the following equations and as shown in Fig.9.¹

$$H = \frac{1}{2} \left(\frac{1}{R_1} + \frac{1}{R_2} \right)$$

$$K = \frac{1}{R_1 R_2}$$

The resulting interface curvature is related to the dimensionless packing parameter P by¹

$$P = \frac{v}{a \cdot l} = 1 - H \cdot l + \frac{K \cdot l^2}{3}$$

with the hydrophobic volume v of the amphiphile, the interfacial area a and the chain length l normal to the interface.¹

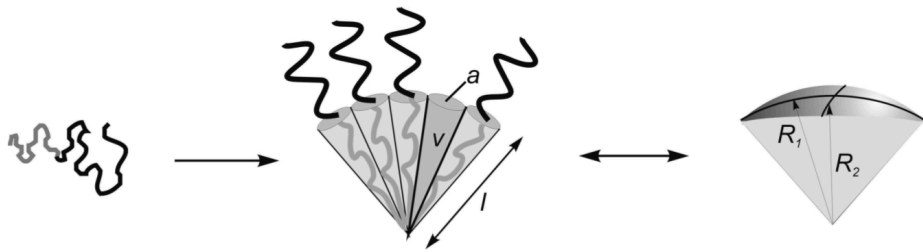


Figure 9 Illustration of the packing parameter P and the related geometric parameters. (Images from ^{1,212}, Copyright WILEY-VCH)

Simple shapes such as spheres, cylindrical micelles or bilayers can be characterized by certain values of the packing parameter and the curvature which are summarized in Tab.2.¹

Table 2 Overview over the packing parameter P and its related parameters: the curvature H and the Gaussian curvature K that are defined by the two radii of curvature R_1 and R_2 .¹

Shape	$v/a \cdot l$	R_1	R_2	H	K
Sphere	$\frac{1}{3}$	R	R	$\frac{1}{R}$	$\frac{1}{R^2}$
Cylinder	$\frac{1}{2}$	R	∞	$\frac{1}{2R}$	0
Bilayer	1	∞	∞	0	0

Aqueous solutions of amphiphile block copolymers that have the right block length ratio, in the range of intermediate packing parameters ($P=1/2$), are capable of forming cylinders or wormlike micelles. These anisotropic colloids are used to study the particle orientation in microfluidic channels after narrow taperings.^{13,135}

3.2 Fluid dynamics fundamentals for microfluidics

3.2.1 Navier-Stokes equations

The precise microfluidic design control enables to fabricate exactly-reproducible microfluidic channel from computer-designed photo masks.⁵⁷ These designs can be optimized prior to the actual device fabrication by predicting the fluid flow by computational fluid dynamics (CFD) and therefore enabling simulation-based rapid prototyping.¹³¹

The description of the dynamics of Newtonian fluids are based on the conservation of energy, mass and momentum.^{213,214} This leads to a set of two partial differential equations (PDE), the so-called Navier-Stokes equations.^{215,216} These PDEs can be solved numerically by computational fluid dynamics (CFD) simulations.²¹⁷ For this task, the finite element methods (FEM) is the most common tool that enables highly accurate modeling by handling complex meshes to describe the fluid dynamics within the flow geometry.²¹⁸⁻²²⁰ These analyses have been performed using the software COMSOL Multiphysics (v4.2a).

Assuming isotropic conditions, i.e. omnidirectional forces, a system of second degree non-linear partial differential equations can be established, the Navier-Stokes equations.^{215,216}

$$\rho \frac{\partial \mathbf{u}}{\partial t} + \rho(\mathbf{u} \cdot \nabla) \mathbf{u} = -\nabla \cdot \left(-p \mathbf{I} + \eta \left(\nabla \mathbf{u} + (\nabla \mathbf{u})^T \right) \right) + \mathbf{F}$$

$$\rho \nabla \cdot \mathbf{u} = 0$$

Which contains the density ρ , the dynamic viscosity η , the velocity vector \mathbf{u} , the volume force vector \mathbf{F} (i.e. gravity), the absolute temperature T and the pressure p .²¹⁴

The first equation describes the velocity field of an incompressible Newtonian fluid in a finite element.²¹⁴ The second equation is the continuity equation which is yielded by assuming an incompressible fluid and taking the conservation of mass into account. This approximation is in good agreement with reality when the temperature variation are small and the density ρ is constant or nearly constant.²¹⁴ This is the case for liquids in a microfluidic channel. Consequently, the fluid mass that enters a finite volume element in a given time Δt is exactly equal to the exiting fluid mass.^{214,221}

The flow in microfluidic devices is laminar which is why stationary conditions can be assumed. The Navier-Stokes equations for this case is given by

$$\rho(\mathbf{u} \cdot \nabla) \mathbf{u} = \eta \nabla^2 \mathbf{u} - \nabla p + \mathbf{F}$$

$$\rho \nabla \cdot \mathbf{u} = 0$$

The term $\eta \nabla^2 \mathbf{u} - \nabla p$ reflects the stress forces per volume unit due to the pressure gradient ∇p and the viscosity $\eta \nabla^2 \mathbf{u}$.²²² The expression $\rho(\mathbf{u} \cdot \nabla) \mathbf{u}$ represents the inertial term. The *Reynolds* number (Re) is a fundamental dimensionless number that describes the ratio between these inertial and viscous forces.^{10,214,222} It is very useful for the prediction of fluid flow and defined by:

$$Re = \frac{|\rho(\mathbf{u} \cdot \nabla) \mathbf{u}|}{|\eta \nabla^2 \mathbf{u}|} = \frac{\rho U L}{\eta}$$

with a velocity scale U , the characteristic length of the geometry L , the density ρ , the time t and the viscosity of the fluid η .

The flow is laminar at low *Reynolds* numbers ($Re < 1$) which is typically the case for example at very small geometries, very low flow rates and/or high viscosities.¹⁰ The flow becomes turbulent in the opposite case, i.e. with larger geometries, increasing flow rates and/or decreasing viscosities.^{10,213} The laminar flow at low Reynolds numbers is time-symmetrical which is reflected by the absence of a time variable in the Navier-Stokes equations in contrast to the above Navier-Stokes equations.

The dimensionless *Weber* (We) number is the ratio between the inertia of the fluid compared to its surface tension.^{10,213} It is expressed by the following expression:

$$We = \frac{\rho v^2 l}{\sigma}$$

with the density of the fluid ρ , the velocity v , characteristic length l (i.e. droplet diameter) and the surface tension σ .

The *Deborah* (De) number is the dimensionless ratio that expresses elastic effects by relating the polymer relaxation time τ_p to the relevant flow time scale τ_{flow} .¹⁰ It is given by

$$De = \frac{\tau_p}{\tau_{flow}}$$

The Deborah number is very useful for the characterization of a fluid's response to a stimulus of a given duration. The time scale of such a stimulus could be given by the fluid's flow through a microchannel tapering, or its passing of a tight nozzle geometry, at a given flow rate.¹⁰

The relation between the Reynolds and Deborah number is defined as the *Elasticity* (El) number that describes the relative importance of elastic to inertial effects and is given by¹⁰

$$El = \frac{De}{Re} = \frac{\tau_p \eta}{\rho h^2}$$

with the shortest dimension h that sets the shear rate and expresses the. Consequently, this dimensionless number depends only on the material properties and the geometry, but it is flow rate independent.¹⁰

The equivalent pressure P of the surface tension is given by the Laplace equation.²²³

$$P = \frac{2\gamma \cos\theta}{r}$$

with the contact angle θ between the fluid and the surface and the channel diameter r . This shows that the surface tension is inversely proportional to the microchannel dimension.

3.2.2 The No-Slip condition

The surface to volume ratio in microfluidic channels is very high which is why surface properties have a great influence on the fluid dynamics.^{224,225} These hydrodynamic interaction between solids and liquids can be described using the no-slip condition.^{226,227} The velocity vector \mathbf{u} of a flowing fluid is assumed to be zero at the wall. This condition remains valid in the sub-micron range which has been shown by molecular dynamic calculations that assumed a hydrodynamic wall that corresponds to a monomolecular layer of fluid molecules resting on a solid wall.^{228,229} The no-slip condition is also in good agreement with aqueous samples that flow in PDMS-based microfluidic channels which have been studied in this thesis.²³⁰⁻²³²

Microscale particle image velocimetry- (μ PIV) and surface force apparatus (SFA) experiments have shown that the velocity close to the wall is not exactly zero, a velocity

component remains, when hydrophilic species are in contact with strongly hydrophobic or nanostructured materials.^{231,233}

This is why a slip length δ is defined that considers this velocity deviation.^{225,227,232} This slip length δ is a depth below the wall surface when extrapolating the linear velocity component v_x . A δ -value of infinity corresponds to perfect slip, while a value of zero corresponds to the no-slip condition. Depending on the experimental conditions, this depth δ corrects the deviation and it can range between a few molecule diameters up to multiple micrometers.²²⁸

3.2.3 Convection and Diffusion

A widely used principle for the fast and diffusive mixing of species is hydrodynamic focusing.^{46,129,132,134,140,234,235} This can be achieved in a cross-like channel geometry similar to Fig.10 which shows a CFD simulation of a hydrodynamically focused stream of a given concentration (red) with another miscible fluid with the concentration zero (blue).

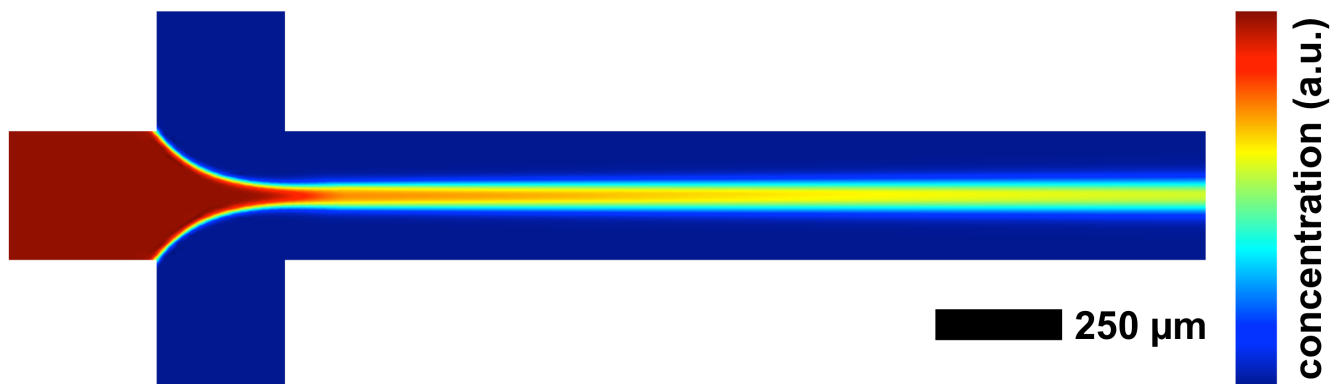


Figure 10 Example of hydrodynamic flow focusing. The CFD-simulation (*COMSOL Multiphysics v4.2a*) shows convective transport of a species due to the laminar flow of a Newtonian fluid that is coupled with the diffusive species transport. The color bar describes the transition from high (red) to low (blue) concentrations of the species.

The mixing time depends on the diffusion coefficient of the species and the width of the focused stream which can be controlled by adjusting the flow rate ratio between main and side channels. The mixing is diffusion based because of the laminar flow profile inside the small microchannels. The diffusion of a species with the concentration of the species c for the general non-conservative case is given by

$$\frac{\partial c}{\partial t} + \mathbf{u} \cdot \nabla c = \nabla \cdot (D \nabla c) + R$$

with diffusion coefficient D , the reaction rate expression for the species R and the velocity vector \mathbf{u} .²¹⁴ The mixing and diffusion times are given by the equations:

$$t_{\text{convection}} = \frac{1}{v} \quad \text{with} \quad v = \frac{\eta}{\rho}$$

$$t_{\text{diffusion}} = \frac{l^2}{D}$$

with the kinematic viscosity ν which is the ratio of the (dynamic) viscosity η and the density ρ . These equations also show the characteristic length l linearity to the mixing time $t_{\text{convection}}$ and proportionality to the square of the diffusion time $t_{\text{diffusion}}$.

While the diffusive species exchange is not effective on the centimeter scale, the small microfluidic channels enable effective diffusion based experiments at very low Reynolds numbers within very short times (10 μs).^{129,226,236}

A very important ratio for the description of transport phenomena is the dimensionless *Péclet* (Pe) number. It describes the ratio between advective transport (i.e. fluid flow) and diffusive transport (i.e. diffusion) and is defined as¹⁰

$$\text{Pe} = \frac{UL}{D} = \text{Re} \cdot \text{Sc}$$

with the characteristic length L , the characteristic velocity U and the diffusion coefficient D . The *Péclet* number is the product of the dimensionless *Reynolds* (Re) and *Schmidt* (Sc) numbers of which the latter is defined by the ratio between the viscous diffusion rate and the molecular (mass) diffusion rate. The Schmidt number is given by:¹⁰

$$\text{Sc} = \frac{\nu}{D_m} = \frac{\mu}{\rho D_m}$$

with the kinematic viscosity ν and the mass diffusivity D_m .

Experiments in microfluidic take advantage of the laminar and non-turbulent flow conditions that are enabled through the small channel dimensions which results in low Reynolds and *Péclet* numbers.^{9,10} This fact leads to advantageous experimental conditions such as laminar diffusion-based hydrodynamic focusing and stationary continuous flow which projects dynamic processes to a fixed position along the flow direction. This fact makes even very fast kinetics or the shearing of samples locally stable and time-symmetric. The resulting steady state condition enables mapping scans of reactions or shear profiles with suitable *in situ* probing techniques like, i.e. small-angle X-ray scattering.^{9,13,46,129,135,230} The microchannel design remains adjustable, due to rapid prototyping and computer aided design, to the experimental needs which can range from single molecules to cell studies (see chapter 1.3).^{131,237,238}

As an example, fast reactions kinetics can be controlled with great precision due to the microchannel design.^{92,239} Another example describes actin fibers that can be fully elongated by suppressing Brownian motion which is of high interest for the modeling of *in vivo* processes of semiflexible biopolymers (i.e. DNA or proteins) or dilute solutions of block copolymers.²⁴⁰

Next to defined mixing scenarios and concentration gradients on the micron scale,^{9,15} microfluidic devices are also well-suited for the generation of defined shear and elongational force profiles.^{13,241-246}

3.3 Solution of non-linear problems

For linear systems, the input is proportional to the output. Most systems which are of interest for science and their applications are non-linear due to the complexity of nature. Their successful simulation is of great interest because precious resources such as material costs, man-power and development time can be saved. Further, these systems can lead to interesting non-linear scientific problems of which a few examples will be discussed below.

3.3.1 Fluid structure interaction

As mentioned earlier, PDMS is a soft polymeric material that deforms elastically under force, like i.e. high pressures. Depending on the application, the mechanical properties of this elastomer can also be beneficial or a down side. On the one hand, the deformation under high pressures and high flow rates can result in rounded channels and reduced the wall contact of a hydrodynamically focused liquid stream.¹³⁷ On the other hand, this pressure-induced deformation (at >2-3 bar) can alter the microchannel geometry which could make the prediction of flow condition more complicated. With the help of computer-based CFD simulations (COMSOL Multiphysics v4.2a) it is possible to solve these problems numerically based on the finite element method. This approach couples the microchannel geometry deformation with the fluid flow field which are incrementally affecting each other in a non-linear way. This routine results in the dynamically stable state of this problem. The theoretical background as well as the solved models, which are good agreement with the real experimental demonstrations, are described in one of the publications of this thesis (see chapter 7.5).¹³⁷

3.3.2 Shear forces and Non-Newtonian fluids

Another non-linear problem occurs when one has to predict the flow of non-Newtonian fluids. These fluids change viscosity under the influence of forces like shear or elongation. Generally speaking, the viscosity of non-Newtonian fluids can increase (shear thickening, dilatant) or decrease (shear thinning, pseudoplastic). The wormlike polymeric micelle solutions which have been used in this thesis are examples of shear thinning non-Newtonian fluids. Their change of viscosity η under shear can be described by the Cole-Cole- (or Cross-) equation which is given by:²⁴⁷⁻²⁴⁹

$$\eta = \eta_\infty + \frac{\eta_0 - \eta_\infty}{1 + (\tau_c \dot{\gamma})^n}$$

with the zero shear viscosity η_0 , the high-shear viscosity η_∞ , the internal relaxation time τ_c and the power law exponent n characterizing the shear thinning between η_0 and η_∞ .^{13,135} The fluid flow of non-Newtonian fluids can now be calculated by coupling this equation with the above-described Navier-Stokes equations of an incompressible fluid and running the FEM-based CFD-simulation. As described in the publications of this thesis (see chapter 7.1 & 7.2), the simulated flow and predicted shear and extensional forces are also in good agreement with the experimental results (SAXS, μ PIV, polarization microscopy) and can be

applied i.e. for the prediction of perpendicular particle orientation in confined geometries.^{13,135}

3.3.3 Two-phase systems and liquid jets

Another example of a non-linear system, which has been studied in this thesis, is the fluid flow of two-phase systems (see chapter 7.3).¹³⁶ The gas-dynamic virtual nozzle principle is a two-phase flow system which uses a pressured-gas sheath for the generation of liquid jets.⁵³ This design prevents wall contact of the liquid and nozzles of this type run essentially clogging-free while consuming only small amounts of sample.^{53,54}

The non-linearity of this system lies in the coupled flow fields of each fluid. When the liquid enters the nozzle geometry, where the gas is already flowing, the liquid's surface shape is affected by the gas flow. At the same time, its presence alters the gas flow dynamics, etc. The theoretical background and the simulation are described in a paper of this thesis.¹³⁶ In this paper, a time-resolved model enables to begin the simulation with easily definable starting conditions. The CFD-simulation of this coupled interaction incrementally leads to a stable equilibrium state and a stable gas-shaped liquid jet.^{54,207} The resulting simulated liquid jet shape and diameter are found to be in good agreement with the experimental results from high speed video microscopy.¹³⁶ This CFD-model allows the very detailed analysis of the whole system, including jet shape, pressure gradients, shear rates, velocities at every simulated position of each fluid.

If one only needs to estimate the liquid jet diameter, there is also an alternative, analytical approach which has been described for a plate-orifice configuration, as illustrated in Fig.11.²⁰¹

Assuming cylindrical coordinates (r,z) for the axis of the liquid jet, the cusplike meniscus at the inlet is pulled towards the nozzle orifice by the pressure gradient that is generated by the gas stream.²⁰¹ This pressure difference ΔP_g and tangential viscous stress τ_s of the gas sheath leads to the formation of a thin liquid thread with the radius $r = \xi$ as illustrated in Fig.11.^{201,206} The averaged momentum equation for this case is given by:²⁰¹

$$\frac{d}{dz} \left(P_l + \frac{\rho_l Q^2}{2\pi^2 \xi^4} \right) = \frac{2\tau_s}{\xi} \quad \text{with } P_l = P_g + \frac{\gamma}{\xi}$$

with the flow rate Q , the liquid pressure P_l and the surface tension stress γ/ξ . The liquid evaporation will be neglected as well as the viscous extensional term which is negligible compared to the kinetic energy term. This holds true for many flow rates of stable liquid threads.²⁰¹ Thus, the above averaged momentum equation can be simplified to:

$$\frac{d}{dz} \left(\frac{\rho_l Q^2}{2\pi^2 \xi^4} \right) = - \frac{dP_g}{dz} + \frac{2\tau_s}{\xi}$$

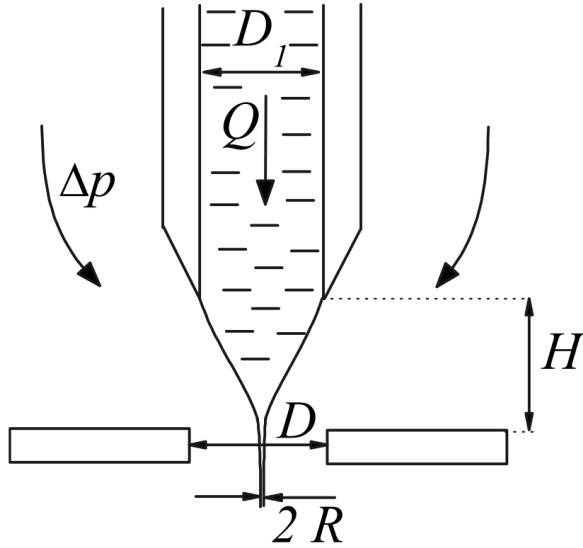


Figure 11 Illustration of a general plate-orifice nozzle design for the generation of liquid jets and the involved geometric parameters. The liquid exits the capillary with the diameter D_1 at a flow rate of Q . It is shaped by the pressured gas sheath (Δp , left & right arrows) along the path H towards the nozzle and as it passes the nozzle with the diameter D . The diameter $2R$ and the stability of the resulting liquid jet depend on the given geometric parameters as well as other fluid dynamic properties such as fluid density ρ , viscosity η or surface tension σ . (Image from²⁰⁶, Copyright American Institute of Physics).

Assuming high pressure gradients towards the nozzle and that the confining nozzle aperture is of the order or thinner than its diameter, this equation can be integrated.²⁰¹ This integration yields a simple and universal expression for the jet diameter that is given by

$$d_j \approx \left(\frac{8\rho_1}{\pi^2 \Delta P_g} \right)^{\frac{1}{4}} Q^{\frac{1}{2}}$$

This formula is independent of the geometrical parameters (like i.e. inlet- and outlet diameters, inlet-to-outlet-distance, etc.), liquid-gas surface tension and liquid and gas viscosities.²⁰¹ The validity of this expression has been demonstrated experimentally for plate-orifice configurations and glass capillary setups.^{201,206} Our experimental results show that there is also a good agreement of this formula with the liquid jet diameters that are generated in microfluidic gas-dynamic virtual nozzles (see chapter 7.3).¹³⁶

When it comes to the lowest possible flow rate however, the nozzle shape has a decisive effect.²⁰⁶ It has been demonstrated that the minimum flow rate for stable jetting can be controlled by adjusting the geometry.²⁰⁶ For three different nozzle diameters (D), the following graph (Fig.12) shows the minimum flow rates (Q_{min}) which are plotted against the distance (H) between the liquid inlet and the nozzle aperture. This graph clearly shows that this H/D -ratio is very sensitive. Consequently, a precise and reproducible nozzle design control is essential for the optimization of liquid jet system and their integration as a sample environment at high intensity X-ray sources.⁶

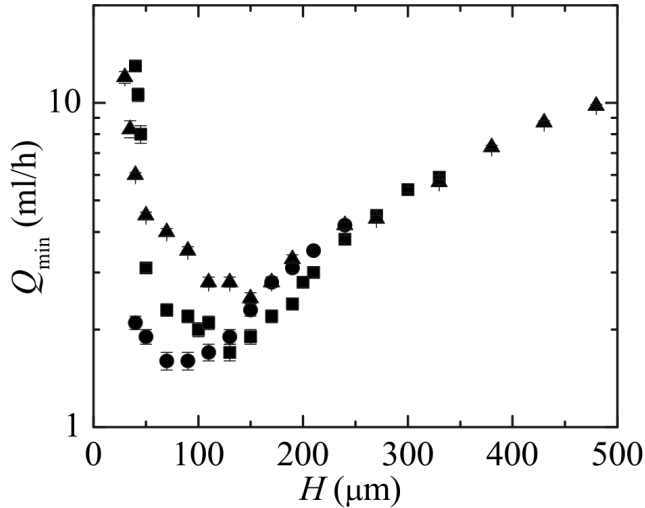


Figure 12 The minimum flow rate for stable jetting of water at different combinations of nozzle distance H and nozzle diameters with $D = 100\text{ }\mu\text{m}$ (circles), $200\text{ }\mu\text{m}$ (squares) and $400\text{ }\mu\text{m}$ (triangles). The pressure difference was set to 250 mbar. (Image from²⁰⁶, Copyright American Institute of Physics).

The regimes for stable liquid jets (steady jetting) can be mapped out using Reynolds- and Weber number diagrams as illustrated in Fig.13.²⁰⁶ The breakup transition lines depend on the specific nozzle geometries & fluid properties and are therefore only valid for a specific case, as indicated in Fig.13 *bottom*. The careful mapping of a scenario's jet-breakup parameter combinations allows to identify its breakup type.

In case of a plate-orifice configuration, the following equations can be used for the parameter conversion:²⁰⁶

$$\text{Re} = \frac{\rho Q}{\pi R \eta} \text{ and } \text{We} = \frac{\rho Q^2}{\pi^2 R^3 \sigma} \text{ with } R = \sqrt[4]{\frac{\rho Q^2}{2\pi^2 \Delta p}}$$

with the density of the fluid ρ , the flow rate Q , the jet radius R , the viscosity η , the surface tension σ and the pressure difference Δp .

These equations can also be combined in a radius-independent form if the *exact* value of the pressure difference is known:

$$\text{Re} = \frac{\sqrt[4]{2\rho^3 \Delta p} \sqrt{Q}}{\eta \sqrt{\pi}} \text{ and } \text{We} = \frac{\sqrt[4]{8\rho \Delta p^3} \sqrt{Q}}{\sigma \sqrt{\pi}}$$

As described above, the Reynolds number describes the ratio between inertial and viscous forces while the Weber number is the ratio between the inertia of the fluid compared to its surface tension.^{10,213}

A stable jet is observed if the fluid outruns the instabilities convectively.^{201,206,207,250,251}

If the gas flow is too high for a given liquid stream for example, the jet turns into a spray which corresponds to a local&global stability- to local&global instability-transition. This 'right-to-left' transition is marked as a blue intersected line in Fig.13.^{201,206,207,250,251}

If the gas pressure at a given flow rate is lowered slowly ('top-to-bottom'), the breakup corresponds to a local stability- to local instability-transition while being globally stable. In this case a continuous droplet train at a constant frequency is observed with a steady liquid column in the range of the nozzle opening. This breakup type is marked by the red dotted line in Fig.13 and is also known as the Leib-Goldstein limit.^{250,251} Further lowering of the pressure finally leads the global instability (Fig.13 *bottom*).^{201,206,207,250,251}

Under certain conditions when the nozzle geometries become very small, as in microfluidic liquid jet devices and very small jets, the relative influences of the fluid's surface tension and of the shear from fast-flowing gas streams on the liquid surface increase. Hence, the underlying assumptions (see momentum equation discussion above) are not neglectable anymore and the Re- and We-number conversions can become inaccurate.^{201,206} It is therefore preferable to rely on qualitative results for the identification of breakup types. This can be achieved by recording the jet breakup transition using highspeed cameras. This has been demonstrated in the attached paper on microfluidic liquid jet systems, i.e. for the column-length of liquid jets or droplet trains in the local instability regime (see chapter 7.3).¹³⁶

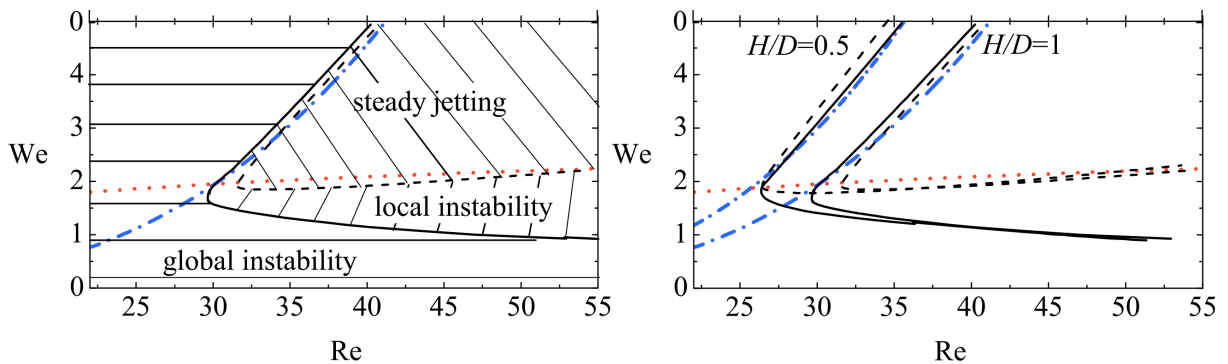


Figure 13 Reynolds- and Weber number diagrams and jet breakup types at minimum flow rates. The liquid jets are observed in the steady jetting regime. The red dotted line describes the Leib-Goldstein transition (local stability to local instability).^{250,251} The blue intersected line marks the global stability to instability transition. The *top* diagram marks the different jet breakup transition regions. Spraying can typically be observed in the global instability regime while a continuous droplet streams can be an example for the local instability breakup type. The *bottom* graph illustrates how the curves in the Re-We-space shift with changing nozzle geometries. (Images from²⁰⁶, Copyright American Institute of Physics).

3.4 Small angle X-ray scattering

3.4.1 Preface

Small angle X-ray scattering (SAXS) is one of today's most important experimental techniques for the characterization of soft condensed matter and colloidal systems. This chapter will give an overview over its theoretical background and describe the fundamental X-ray scattering principles. A more detailed description can be found in the original, cited literature on which this chapter is based.^{12,252-263}

3.4.2 Introduction

The scattering of electromagnetic waves is a very helpful tool for the characterization of colloids and polymers. The fundamental setup of a scattering experiment is illustrated in Fig. 14.

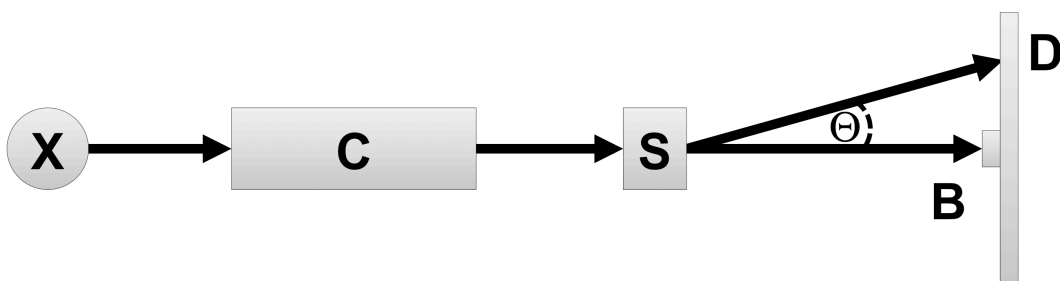


Fig. 14 Illustration of the fundamental elements of a scattering experiment. The X-ray source (X) emits light which passes a collimation system (C). The X-rays then hit the sample (S) and the scattering pattern is recorded using a detector (D) while the primary beam is absorbed by the beamstop (B). (Image adapted from²⁵⁸)

The X-rays, which should be as monochromatic as possible, are emitted from a source (X), like a synchrotron or rotating anode. The X-rays pass a collimation system (C) before they hit the sample (S). This interaction causes the sample's electrons to resonate and the induced dipoles emit secondary waves of the same frequency. This scattering process is considered to be elastic because the incident photons have the same energy as the scattered ones. The scattered X-rays are coherent and the phases of these secondary waves differ from each other due to the different spatial positions of the scattering electrons. Consequently, interference of these secondary waves occurs and the resulting scattering patterns are then recorded using 2D digital detectors (i.e. Pilatus, FReLoN, MarCCD) or alternative recording techniques such as 1D counting devices or image plates.

The interference of the scattered X-rays and therefore the scattering pattern is characteristic for the given sample's structure. The fundamental principle of the waves' interference can be described by the Bragg equation.²⁵³

$$2d \sin(\Theta) = n\lambda$$

A scattering reflex, which is an intensity maximum, can be found where the waves' path difference $\Delta = \bar{s}t + \bar{t}u$ is an integer multiple of the wavelength λ which leads to constructive

interference. This principle is illustrated in Fig. 15, which clearly shows that the path difference is determined by the scattering angle 2Θ and the distance of the scattering planes d .

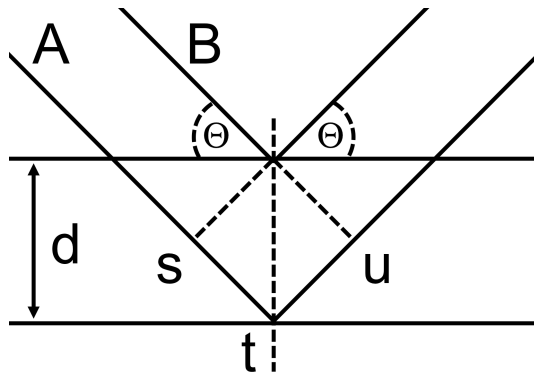


Fig. 15 Illustration of the Bragg equation with the incident X-rays A and B, the lattice distance d and the half scattering angle Θ . The path difference of the wave is given by $\Delta = \bar{s} + \bar{t}$. (Image adapted from ²⁶³)

The resulting scattering pattern of a sample is an angle-dependent intensity distribution that is characteristic for the sample's structure. Given by the range of the (small) scattering angles of this method, the size range of structures that are studied by SAXS typically lies between 1 nm and 100 nm. This is also why this experimental technique has become very popular for the characterization of sample systems such as polymers, colloids, soft condensed matter and nanomaterials.

3.4.3 The scattering vector

For a better understanding of the interference phenomena one can imagine the interaction between the X-ray beam and two scattering electrons at the positions \vec{r}_1 and \vec{r}_2 . The vector which describes the distance between them is given by $\vec{r} = \vec{r}_1 - \vec{r}_2$ as illustrated in Fig. 16.

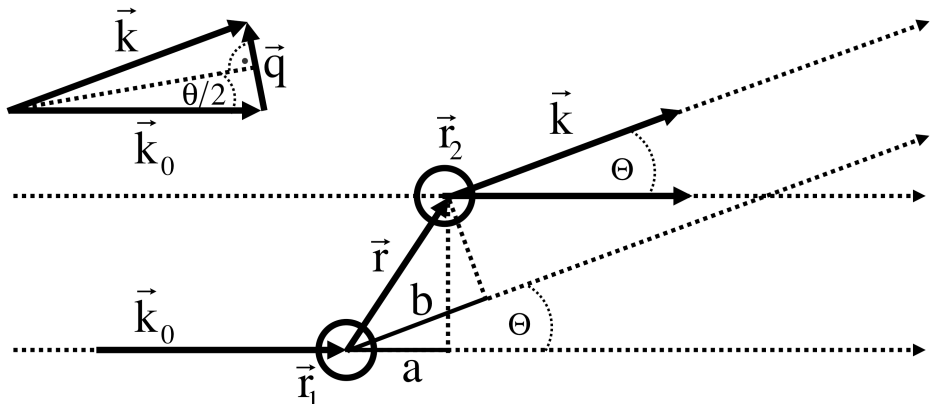


Fig. 16 Phase relation between the two scattering centers \vec{r}_1 and \vec{r}_2 and the geometric construction of the scattering vector \vec{q} . (Image adapted from ²⁵⁸)

All interferences of waves that originate from scattering events sum up with respect to their amplitude and phase. Due to the equality of electrons when it comes to X-ray scattering, only

the location-dependent phase difference ξ needs to be considered which is given by

$$\xi = -\frac{2\pi}{\lambda} \cdot \vec{r} \cdot (\vec{k} - \vec{k}_0)$$

This equation contains the wave vectors which are given by

$$\vec{k}_0 = \frac{2\pi}{\lambda} \cdot \vec{s}_0$$

for the incident wave, while the scattered wave is described by

$$\vec{k} = \frac{2\pi}{\lambda} \cdot \vec{s}$$

with the unit vectors (\vec{s}, \vec{s}_0) in \vec{k}, \vec{k}_0 -direction.

The absolutes of these vectors are given by

$$k = |\vec{k}_0| = |\vec{k}| = \frac{2\pi}{\lambda}$$

Considering the angle of the X-rays Θ , the wave vectors can be combined to construct the scattering vector \vec{q} which is given by

$$\vec{q} = \vec{k} - \vec{k}_0$$

The geometric representation of this relation is shown in Fig. 16. The phase shift ξ can be described by the multiplication of this vector \vec{q} with $-\vec{r}$.

$$\xi = -\vec{q} \cdot \vec{r}$$

The scattering curve is received by plotting the measured intensity against the scattering vector's absolute value q which is given by

$$q = |\vec{q}| = \frac{4\pi}{\lambda} \sin\left(\frac{\Theta}{2}\right)$$

The absolute value of q can also be expressed as s which is based on the following equation where the relation between s, q and Θ has a similarity to the Bragg equation.

$$s = \frac{q}{2\pi} = \frac{2}{\lambda} \sin\left(\frac{\Theta}{2}\right)$$

3.4.4 The scattering pattern

The coherent scattered X-ray waves interfere with each other and the amplitude $E(\vec{q})$ of the resulting wave is given by

$$E(\vec{q}) = b \cdot e^{-i\vec{r}(\vec{k}-\vec{k}_0)} = b \cdot e^{-i\vec{r}\vec{q}}$$

with the scattering length b . For SAXS the scattering length of an electron is given by²⁵⁵

$$b_e \approx \frac{e_0^2}{m_e c^2} \approx 2.82 \cdot 10^{-15} \text{ m}$$

with the elementary charge e_0 , the electron's mass m_e and the speed of light c . Consequently, the scattering length of an atom with the ordering number Z is given by

$$b = Z \cdot b_e$$

The cumulative scattering of a sample is the sum of all scattered waves. Therefore, the collective scattering amplitude $E(\vec{q})$ is received by integration and the scattering length b of a single pair of scattering centers is replaced by the density distribution of all scattering centers $\rho(\vec{r})$. This is described by the following formula.

$$E(\vec{q}) = \text{const} \cdot \int_V \rho(\vec{r}) \cdot e^{-i\vec{q}\vec{r}} d\vec{r}$$

Since this equation's mathematical form is a Fourier transformation, the scattering amplitude $E(\vec{q})$ and the scattering center density distribution $\rho(\vec{r})$ are a pair of Fourier transforms. Further, this equation links the real space (with the vector \vec{r}) to the reciprocal space (with the scattering vector \vec{q}). However, the scattering amplitude $E(\vec{q})$ is experimentally not accessible because only the scattering intensity $I(\vec{q})$ is measured. Their relation is defined as

$$I(\vec{q}) = \langle |E(\vec{q})|^2 \rangle$$

In other words, the scattering intensity $I(\vec{q})$ is the time-averaged square of the absolute value of the scattering amplitude $E(\vec{q})$. It is time-averaged, as indicated by the pointed brackets $\langle \dots \rangle$, because the measurement is long compared to the system's dynamics.

Another relevant mathematical operation is the convolution of two functions and it is given by

$$f(\vec{r}) * g(\vec{r}) = \int f(\vec{r}') \cdot g(\vec{r}-\vec{r}') d\vec{r}'$$

It is commonly known that a convolution of $f(\vec{r})$ and $g(\vec{r})$ in the real space corresponds to the multiplication of their Fourier transforms $F(\vec{q})$ and $G(\vec{q})$ in the reciprocal space:²⁶³

$$f(\vec{r}) * g(\vec{r}) \xleftarrow{\text{F.T.}} F(\vec{q}) \cdot G(\vec{q})$$

The application of this convolution theorem on the complex scattering amplitude and the scattering intensity yields

$$I(\vec{q}) = E(\vec{q}) \cdot E^*(\vec{q}) \xleftarrow{\text{F.T.}} \rho(\vec{r}) * \rho(\vec{r}) \equiv \rho^{*2}(\vec{r}) \equiv p(\vec{r})$$

As briefly described above, the scattering amplitude $E(\vec{q})$ and the scattering center density $\rho(\vec{r})$ are a pair of Fourier transforms. The above convolution theorem also shows that this is also true for the scattering intensity $I(\vec{q})$ and the pair correlation function $p(\vec{r})$. The scattering intensity $I(\vec{q})$ results from the square of the absolute value of the scattering amplitude $E(\vec{q})$ while the pair distribution function $p(\vec{r})$ results from the self-convolution of the scattering center density $\rho(\vec{r})$.

In the form of a Fourier transform $I(\vec{q})$ can also be written as²⁶⁴

$$I(\vec{q}) = \left\langle |E(\vec{q})|^2 \right\rangle = \left\langle \int_V \gamma(\vec{r}) e^{-i\vec{q}\cdot\vec{r}} d\vec{r} \right\rangle = 4\pi \int_0^\infty \gamma(r) r^2 \frac{\sin(qr)}{qr} dr = 4\pi \int_0^\infty p(r) \frac{\sin(qr)}{qr} dr$$

which is the spatially averaged intensity of a statistically isotropic system without any long range order, such as dilute particles. Here, $\gamma(\vec{r})$ is the auto-correlation function which is given by

$$\gamma(\vec{r}) = \left\langle \int_V \rho(\vec{r}_i) \rho(\vec{r}_i - \vec{r}) d\vec{r}_i \right\rangle$$

and the following equation highlights the relation between the pair distribution function $p(\vec{r})$ and the auto-correlation $\gamma(\vec{r})$

$$p(\vec{r}) = \vec{r}^2 \cdot \gamma(\vec{r})$$

The following Fig. 17 illustrates these relations between real and reciprocal space graphically.

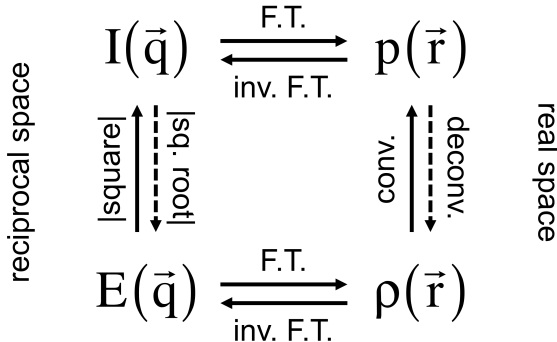


Fig. 17 Graphical representation of the mathematical operations that link the scattering amplitude $E(\vec{q})$, the scattering center density $\rho(\vec{r})$, the scattering intensity $I(\vec{q})$ and the pair correlation function $p(\vec{r})$. (Image adapted from²⁵⁸)

The Fourier-transformation is fully reversible in both directions while the square of the absolute value and the self-convolution are not. The wanted scattering center density $\rho(\vec{r})$ is not extractable from the experimentally measured scattering intensity $I(\vec{q})$ because the phase information is missing; this is also known as the phase problem.

This is why two different approaches have been developed to receive the scattering center density $\rho(\vec{r})$. The so-called indirect method is based on the modeling of the scattering center density $\rho(\vec{r})$ using spline functions.²⁶⁵⁻²⁷⁰ The splines are transformed to the measurement space and fitted to the scattering curve. The desired scattering center density $\rho(\vec{r})$ is finally received by the deconvolution of these fitted spline functions.^{271,272}

Another approach is the model-based or direct method. This approach uses a given structure with a known scattering center density $\rho(\vec{r})$ that is Fourier-transformed to receive the

scattering amplitude $E(\vec{q})$. This function's square yields an analytical expression that can be fitted to the experimentally obtained scattering curve to receive the desired parameters.²⁷³

3.4.5 Form factor

The model-based or direct method describes the scattering curve as a function in the basic form of

$$I(q) = I_0 \cdot P(q)$$

with I_0 as the intensity of the incident beam at an angle of 0° and the form factor $P(q)$.²⁷⁴

Corresponding to its name, the form factor describes the particle's form and shape. One of these simpler equations is the form factor of spherical particles with the radius R and homogenous shapes that have a constant scattering length distribution. These can be described by an analytical expression that is given by^{273,275,276}

$$P(q) = \rho^2 V^2 \left(3 \frac{\sin(qR) - qR \cdot \cos(qR)}{(qR)^3} \right)^2$$

An example of simple anisotropic particles, cylinders can be described by the following formula which uses the parameter R to describe the cylinder radius and the parameter L for the cylinder length L ^{252,277,278}

$$P(q) = \frac{L\pi}{q} \cdot P_c(q)$$

with

$$P_c(q) = 4\rho^2 R^2 \left(\frac{\sin(qR)}{qR} \right)^2$$

This formula is valid for rigid cylinders, but it has to be modified to describe flexible wormlike micelles which have been investigated in this thesis. The wormlike chain model by Kratky and Porod introduced the following form factor²⁷⁹

$$P(q) = \int_0^L (L-r) \cdot e^{-q^2 C^2} \frac{\sin Bq}{Bq} dr$$

with

$$B^2 = \langle R \rangle^2 \eta$$

$$C^2 = \langle R \rangle^2 \frac{1-\eta}{6}$$

$$2\eta^2 = 5 - 3 \frac{\langle R^4 \rangle}{\langle R^2 \rangle^2}$$

$$\langle R \rangle^2 = l_k^2 \left(y - \frac{1}{2} (1 - e^{-2y}) \right)$$

$$\langle R^4 \rangle = l_k^4 \left(\frac{5}{3} y^2 - \frac{26}{9} y - \frac{1 - e^{-6y}}{54} + 2(1 - e^{-2y}) - ye^{-2y} \right)$$

$$y = \frac{2}{l_k}$$

$$l_k = 2l_p$$

In this sequence of equations l_k is the Kuhn length and l_p is the persistence length. The variables r and s indicate the direct distance between two segments and their dividing contour length. The contour length of the worm-chain is L .

Further form factors for various particle shapes are compiled in the articles of Pedersen and Förster.^{252,275}

Homogeneous particles have a constant density and their scattering length can be described using Heaviside functions where the step corresponds to the particle's radius. This is not the case for inhomogenous particles, such as self-assembled micelles. However, it is possible to model these systems using core-shell-models which combine the form factors of a homogenous sphere with a homogenous hollow sphere which are blended using density profiles. The approach by Förster and Burger describes the scattering amplitudes using hypergeometric functions, which can be solved analytically in many cases.²⁸⁰ A typical core-shell-structure with a $r^{-\alpha}$ -dependent density profile yields the following expression

$$P_d(q) = \left(\frac{\sum_{i=1}^3 \rho_i R_{i-1}^{-\alpha_i} V(a_i, R_i) {}_1F_2(a_i, R_i) - \rho_{i+1} R_i^{-\alpha_{i+1}} V(a_{i+1}, R_i) {}_1F_2(a_{i+1}, R_i)}{\sum_{i=1}^3 \rho_i R_{i-1}^{-\alpha_i} V(a_i, R_i) - \rho_{i+1} R_i^{-\alpha_{i+1}} V(a_{i+1}, R_i)} \right)$$

with

$$V(\alpha, R) = \frac{2\pi^{\frac{d}{2}} R^{d+\alpha}}{\Gamma(\frac{d}{2}(d+a))}$$

and the hypergeometric functions

$${}_1F_2(\alpha, R) = {}_1F_2\left(\frac{d+\alpha}{2}, \frac{d}{2}, \frac{d+2+\alpha}{2}; -\frac{q^2 R^2}{4}\right)$$

with $d=1$ for spheres, $d=2$ for cylinders and $d=3$ for lamellae.

3.4.6 Structure factor

So far, this chapter has only covered the diffusive scattering of diluted systems. With raising concentrations, one also has to consider interparticular relations which complicate the mathematical description of the system.^{281,282} This leads to the introduction of the structure factor $S(q)$ which appears as an additional factor in the scattering intensity formula

$$I(q) = I_0 \cdot P(q) \cdot S(q)$$

with

$$S(q) = 1 + \int_0^{\infty} [g(r) - 1] \frac{\sin(qr)}{qr} 4\pi r^2 dr$$

This expression is also valid for isotropic systems that form cubic lattices such as spheres. For increasing concentrations and more ordered systems, this factor $S(q)$ generates peaks that decay exponentially. This is indicated by an intensity drop at low q -values along with the raising of a first peak. The peak intensity increases with higher concentrations and higher order of the scattering system. However, strongly diluted or disordered systems will be described solely by the form factor because the structure factor $S(q)$ becomes 1. This trend is also shown in the graph of Fig. 18.

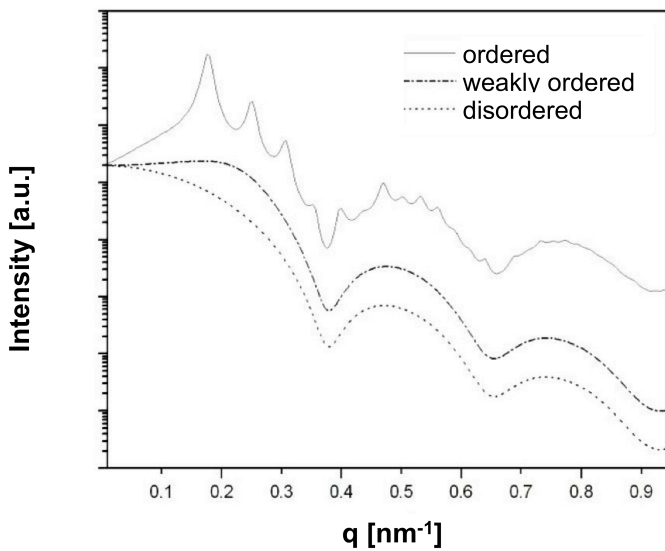


Fig. 18 Simulated scattering curves for spherical particles of varying concentrations. These particles are disordered at the lowest concentration and are solely described by the form factor. Raising concentrations lead to increasing particle interactions and the resulting scattering of weakly ordered particles (without long-range order) is described by the structure factor. Highly concentrated particles lead to defined scattering peaks from the long-range ordered lattice that is body-centered cubic in this example. (Image from ²⁵⁸, Copyright M. Konrad)

3.4.7 Bragg reflexes

When a scattering system starts to form long-range ordered structures that are similar to lattices in crystals, like in the case of liquid crystalline or lyotropic samples, Bragg peaks can be observed in the scattering pattern. Then the principles of classical crystallography can be applied for this system's description while the above-described scattering principles are also valid for these systems of higher order.²⁸⁵ In this context, it can be beneficial to use s as the scattering vector's absolute value because a peak position's reciprocal value ($1/s$) directly equals the corresponding lattice plane distance. The particle scattering that has been outlined so far can be applied to extended, periodic structures because they can be viewed as a successive array of interfering scattering centers with the periodic distance a . The density

profile $\rho(x)$ can be expressed using a corresponding delta function.²⁵⁵

$$\rho(x) = \sum_{n=-\infty}^{+\infty} \delta(x - na)$$

The Fourier transformation yields the scattering amplitude

$$E(s_x) = \sum_{n=-\infty}^{+\infty} e^{2\pi s_x n} = \frac{1}{a} \sum_{n=-\infty}^{+\infty} \delta\left(s_x - \frac{n}{a}\right)$$

which shows that a delta function is also obtained in the reciprocal space. The intensity yields discrete lines with a distance of $1/a$ and spatially limited periodicity results in peaks with finite width. The delta function approach is also valid for the structure factor $S(\vec{s})$ while applying the principles of classical crystallography. Peaks are only generated for discrete values of \vec{s}

$$S(\vec{s}) = \left(\sum_{hkl} \delta(\vec{s} - \vec{H}_{hkl}) \right)^2$$

with

$$\vec{H}_{hkl} = h\vec{a}^* + k\vec{b}^* + l\vec{c}^*$$

where h , k and l are the Miller indices of the crystal planes and \vec{a}^* , \vec{b}^* and \vec{c}^* are the reciprocal vectors of the unit cell.

3.4.8 Crystallographic description of lyotropic mesophases

Similar to the formalism of crystallography, lyotropic phases and their periodic structures can be described using unit cells. The translation of a unit cell reconstructs the whole lattice and a unit cell is defined by its edge lengths (a , b and c) and the corresponding angles (α , β and γ). A general unit cell is illustrated in Fig. 19.

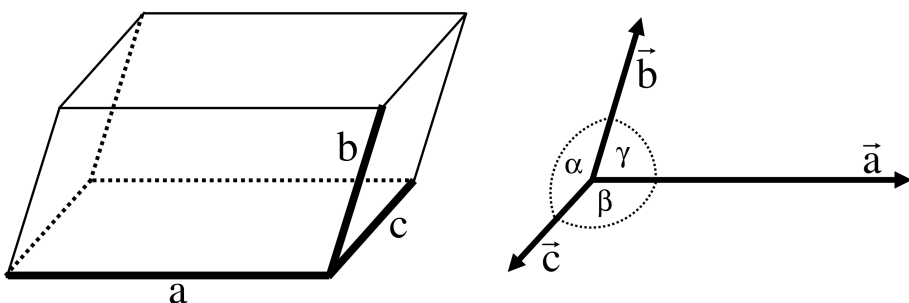


Fig. 19 Unit cell as parallelepiped with its corresponding coordinate system. Both are defined by the edge lengths (a , b and c) and the corresponding angles (α , β and γ). (Image adapted from²⁵⁸)

The planes of the crystal lattice which is defined by the unit cell can be uniquely identified by the Miller indices h , k and l . The indices denote the planes orthogonal to a direction in the basis of the reciprocal lattice vectors while their greatest common divisor should be 1. The unit cell coordinate system of a cubic lattice is orthogonal with $a = b = c$ as illustrated in

Fig. 20. This figure shows examples of lyotropic mesophases: a body-centered cubic (bcc) lattice of long-range ordered spherical micelles (A), closest packed cylinders (B) and a lamellar phase (C).



Fig. 20 Examples of common lyotropic mesophases: body-centered cubic (A), hexagonally closest packed (B) and lamellar (C). (Image from²⁵⁸, Copyright M. Konrad)

The lattice plane distance d_{hkl} for orthogonal unit cells is given by

$$\frac{1}{d_{hkl}^2} = \frac{h^2}{a^2} + \frac{k^2}{b^2} + \frac{l^2}{c^2} = h^2 (\vec{a}^*)^2 + k^2 (\vec{b}^*)^2 + l^2 (\vec{c}^*)^2$$

where \vec{a}^* , \vec{b}^* and \vec{c}^* are the so-called reciprocal vectors which are defined as

$$\vec{a}^* = \frac{\vec{b} \times \vec{c}}{V_{EZ}}, \quad \vec{b}^* = \frac{\vec{c} \times \vec{a}}{V_{EZ}}, \quad \vec{c}^* = \frac{\vec{a} \times \vec{b}}{V_{EZ}}$$

with V_{EZ} as the unit cells volume.

The simple cubic lattice ($a=b=c$) represents a special case where the lattice plane distance d_{hkl} is given by

$$d_{hkl} = \frac{a}{\sqrt{h^2 + k^2 + l^2}}$$

with the peak positions of the lattice

$$s_{hkl} = \frac{\sqrt{h^2 + k^2 + l^2}}{a}$$

In case of a hexagonal lattice with $a=b$ and $\gamma=120^\circ$, only the planes that are parallel to the c-axis (=hk0) are of interest. This allows the reduction of the three-dimensional problem to a two-dimensional one and the point lattice can be visualized two-dimensionally as shown in Fig. 21.

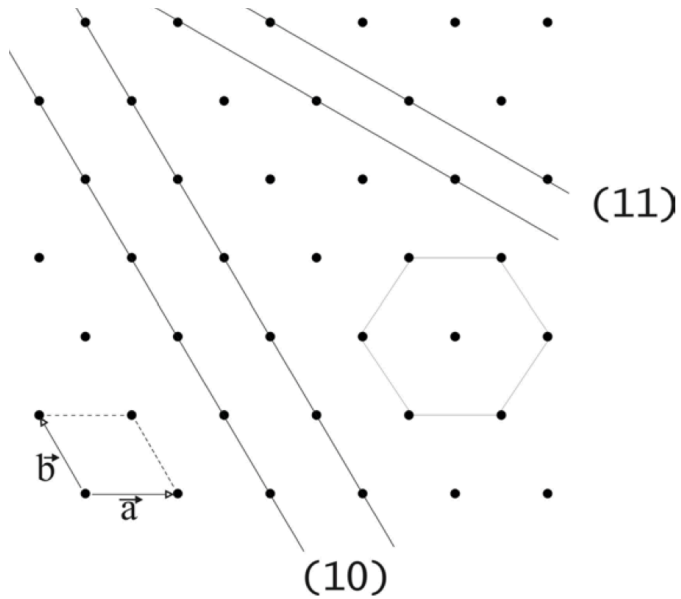


Fig. 21 Point lattice projection (hk) of the hexagonal packing. The six-fold symmetry and the (10) and (11) lattice planes are indicated by the lines. (Image from²⁵⁸, Copyright M. Konrad)

The calculation of lattice plane distance d_{hk} of this two-dimensional lattice is given by

$$d_{hk} = \frac{\sqrt{3}}{2} a \frac{1}{\sqrt{h^2 + hk + k^2}}$$

with the corresponding peak positions

$$s_{hk} = \frac{2}{\sqrt{3} \cdot a} \sqrt{h^2 + hk + k^2}$$

3.4.9 Model-based order analysis

The model-based analysis of experimental scattering data from ordered systems requires additional parameters. The complete structure factor for ordered systems is given by²⁵⁸

$$S(q) = 1 + \left(\frac{(2\pi)^{d-1}}{c_d V_d n_0} \sum_{hkl} \left(m_{hkl} |F_{hkl}|^2 \frac{L_{hkl}(q)}{q_{hkl}^{d-1}} \right) - 1 \right) E(q)$$

with the number of structure elements n_0 (spheres, cylinders or lamellae) per unit cell, the dimensionality d (3 for spheres, 2 for cylinders and 1 for lamellae) and the dimension-dependent volume V_d . The parameter c_d has a value of 1 for lamellae, 2π for cylinders and 4π for spheres. The factor m_{hkl} considers the multiplicity of peaks that stem from lattice plane multitudes with identical peak positions while the factor F_{hkl} contains any extinction rules.

The profile $L_{hkl}(q)$, which determines the peaks shapes and locations, is normalized:

$$\int_0^\infty L_{hkl}(q) dq = 1$$

and its general equation is given by²⁸⁰

$$L_{hkl}(q) = \frac{2}{\pi\delta} \prod_{n=0}^{\infty} \left(1 + \frac{4\gamma^2(q - q_{hkl})^2}{\delta^2 \left(\frac{n+v}{2} \right)^2} \right)$$

with

$$\gamma_v = \pi^{\frac{1}{2}} \frac{\Gamma \frac{v+1}{2}}{\Gamma \frac{v}{2}}$$

This profile shape smoothly transitions from a Lorentz peak shape at very small v -values

$$\lim_{v \rightarrow 0} L_{hkl}(q) = \frac{2\delta}{\pi(\delta^2 + 4(q - q_{hkl})^2)}$$

to a Gauß shape at large values of v

$$\lim_{v \rightarrow \infty} L_{hkl}(q) = \frac{1}{\sqrt{\pi}\delta} \cdot e^{-\frac{(q - q_{hkl})^2}{\delta^2}}$$

The peak width δ is determined by the domain size D which is given by

$$D = \frac{2\pi}{\delta}$$

The correlation function $E(q)$ is given by

$$E(q) = e^{-\frac{q^2 \langle u - u_0 \rangle^2}{3}}$$

which also describes the deviation, known as the Debye-Waller factor, from the ideal lattice position based on the following equation

$$\langle u - u_0 \rangle^2 = \frac{\Delta^2}{\bar{a}^2}$$

In this formula Δ is the mean square deviation and \bar{a} is the nearest neighbor distance.

3.4.10 Particle orientation distribution

In the above discussion, the orientation of anisotropic particles, such as cylindrical micelles or wormlike micelles, has been assumed to be isotropic. This results in ring-like, isotropic scattering patterns on two-dimensional detectors which can simply be represented as radially averaged scattering curves. If the particles in a sample are oriented however, the resulting scattering patterns are also anisotropic and both components of the scattering vector (q_x and q_y) need to be considered in the analysis.

A good experimental example for anisotropic scattering patterns are small angle X-ray scattering studies of shear-oriented wormlike micelles in small microfluidic channel geometries, as illustrated in Fig. 22.

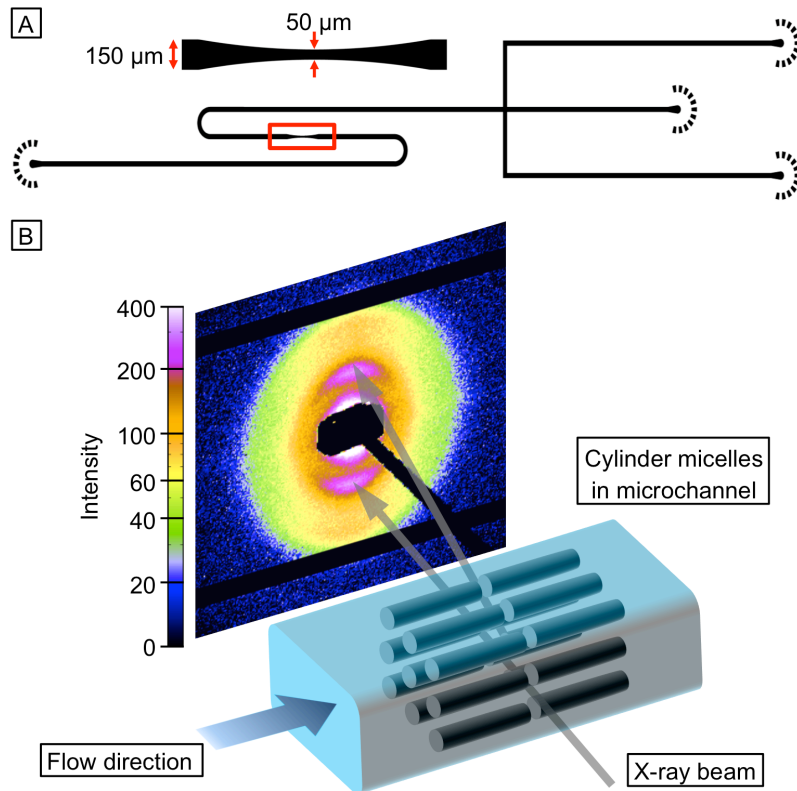


Fig. 22 (A) The sample is flowing though the microchannel geometry and passes a narrow section (red box). (B) 3D illustration of the X-ray microbeam that passes the microchannel of flowing wormlike micelles (hexagonal closest packing, determined by SAXS) and the resulting SAXS-pattern which is captured using a digital detector (Pilatus 300K, Dectris). The parallel or perpendicular orientation of the wormlike micelles is controlled by varying the experimental parameters, such as the channel geometry, the flow rate or the sample concentration.(Adapted from ¹³, Copyright PNAS)

The wormlike micelles in the microchannel are oriented according to the flow-induced shear and extensional forces which are controlled by the experimental parameters such as microchannel geometry, flow speed and particle concentration. Due to the highly reproducible flow conditions, this setup enables the correlation between structural- and orientation information from SAXS studies with fluid dynamic studies from other methods like high speed video analysis, particle image velocimetry or polarization microscopy.

Instead of splitting the scattering vector into its components (q_x and q_y) it is more beneficial to use the polar coordinate system.²⁵² Here, the scattering vector is described by its absolute value and the angle β between cylinder axis and the scattering vector. This results in the following equation for the scattering intensity of oriented cylindrical micelles²⁵⁸

$$I(q_x, q_y) = N \int S(q, \beta) P(q, \beta) h(\beta) d\beta$$

with the form factor P , the structure factor S , the fraction of micelles $h(\beta)$ with the angle β and the number of micelles N . The form factor is further defined by

$$P(q, \beta) = \int_0^{\frac{\pi}{2}} \langle F_R^2(q, R, \beta) \rangle \langle F_L^2(q, L, \beta) \rangle h(\delta) \sin \delta d\delta$$

The distribution function $h(\delta)$ describes the cylindrical micelle orientation with the angle δ between the cylinder axis with the base vector \vec{r} and the director \vec{D} which defines the direction of the shear field.

The expressions F_R and F_L are yielded from the factorization of the scattering amplitude into its cross section- and length-contribution. The pointed brackets indicate the averaging across the corresponding size distributions of cylinders and radii. As described above, it is possible to express F_R for typical block copolymers, that have a core-shells-structure and a density-profile of $r^{-\alpha}$, by using hypergeometric functions. F_R is given by

$$F_R(x_R) = \frac{\frac{\rho}{2} {}_0F_1\left(2; -\frac{p^2 x_R^2}{4}\right) + \frac{1}{(2-\alpha)p^{2-\alpha}} {}_1F_2\left(\frac{2-\alpha}{2}, 1, \frac{4-\alpha}{2}; -\frac{x_R^2}{4}\right) - \frac{1}{2-\alpha} {}_1F_2\left(\frac{2-\alpha}{2}, 1, \frac{4-\alpha}{2}; -\frac{p^2 x_R^2}{4}\right)}{\frac{\rho}{2} + \frac{1}{(2-\alpha)p^{2-\alpha}} - \frac{1}{2-\alpha}}$$

with $x_R = qR \cos \beta$ and the ratios of the radii (p) and densities (ρ) compared to the shell. These are given by

$$p = \frac{R_c}{R}$$

$$\rho = \frac{\rho_c}{\rho_s}$$

The form factor $P(q, \beta)$ calculation requires a definition for the relation between the angles β and δ , as shown in Fig. 23.

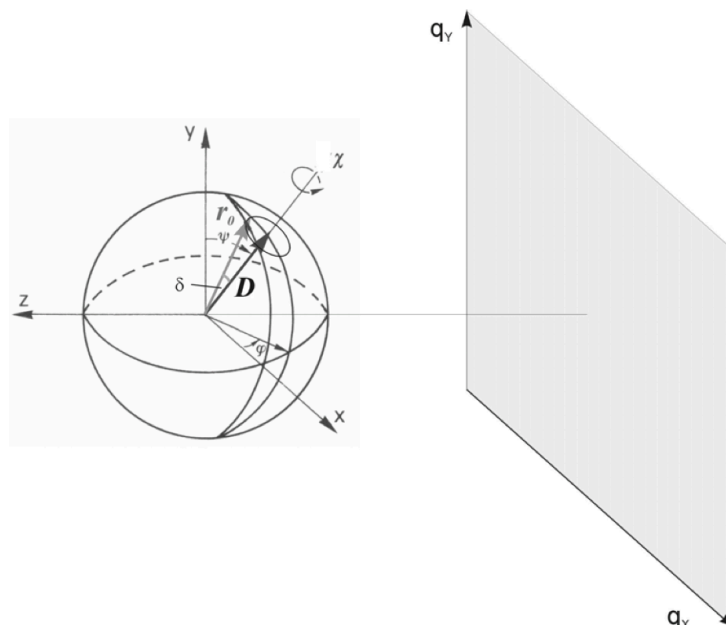


Fig. 23 Three-dimensional illustration of the vector sphere. (Image from ^{252,258}, Copyright Elsevier).

In this figure the director \vec{D} is determined by the angles ψ and φ . The base vectors \vec{r} of the cylinder axes are positioned on a cone that is directed towards \vec{D} . Therefore, the range of angles of χ is given by $0 \leq \chi < 2\pi$ and the integration of the function $f(\delta)$ leads to

$$f(\delta) = \int_0^{\frac{\pi}{2}} f(\delta) h(\delta) \sin \delta d\delta = \int_0^{\frac{\pi}{2}} \int_0^{2\pi} f(\delta, \chi) h(\delta) d\chi d\delta$$

The vector \vec{r} is calculated by using the rotation matrix \mathbf{R}_{rot} based on the following equation

$$\vec{r} = \mathbf{R}_{\text{rot}} \vec{r}_0$$

The vectors \vec{D} and \vec{r} are given by

$$\vec{D} = \begin{pmatrix} \sin(\psi) \cos(\varphi) \\ \cos(\psi) \\ -\sin(\psi) \sin(\varphi) \end{pmatrix}$$

and

$$\vec{r}_0 = \begin{pmatrix} \sin(\psi - \delta) \cos(\varphi) \\ \cos(\psi - \delta) \\ -\sin(\psi - \delta) \sin(\varphi) \end{pmatrix}$$

The rotation matrix is defined by

$$\mathbf{R}_{\text{rot}}(\chi) = \begin{pmatrix} c\chi + (1 - c\chi)s^2\psi c^2\varphi & -s\psi s\varphi s\chi + (1 - c\chi)c\psi s\psi c\varphi & -c\psi s\chi - (1 - c\chi)s^2\psi c\varphi s\varphi \\ s\psi s\varphi s\chi + (1 - c\chi)c\psi s\psi c\varphi & c\chi + (1 - c\chi)c^2\psi & s\psi c\varphi s\chi - (1 - c\chi)c\psi s\psi s\varphi \\ c\psi s\chi - (1 - c\chi)s^2\psi c\varphi s\varphi & -s\psi c\varphi s\chi - (1 - c\chi)c\psi s\psi s\varphi & c\chi - (1 - c\chi)s^2\psi s^2\varphi \end{pmatrix}$$

with

$$c(z) = \cos(z)$$

$$s(z) = \sin(z)$$

$$0 \leq \varphi < 2\pi$$

$$0 \leq \psi < \pi$$

Lastly, β is given by

$$\beta = \cos^{-1}(\vec{r} \cdot \vec{q}) = \cos^{-1}(r_x q_x + r_y q_y + r_z q_z)$$

The orientation of anisotropic particles can be described by a range of distribution functions $h(\delta)$ that are given by

$$h(\delta) = \begin{cases} e^{-\frac{\sin \delta}{\bar{\delta}}} & \text{Onsager} \\ e^{-\frac{\delta}{\bar{\delta}}} & \text{Boltzmann} \\ e^{\left(\frac{\cos \delta}{\bar{\delta}}\right)^2 - 1} & \text{Maier-Saupe} \\ e^{-\left(\frac{\delta}{\bar{\delta}}\right)^2} & \text{Gauß} \\ \sum_{k=0}^{k_{\max}} \left(\frac{\delta}{\bar{\delta}}\right)^{2k} \frac{e^{-\left(\frac{\delta}{\bar{\delta}}\right)^2}}{k!} & \text{Laguerre} \\ \Theta(\delta - \bar{\delta}) & \text{Heaviside} \end{cases}$$

with the parameter $\bar{\delta}$ which can take on values between zero and infinity. The graphs of these different distribution functions are shown in Fig. 24.

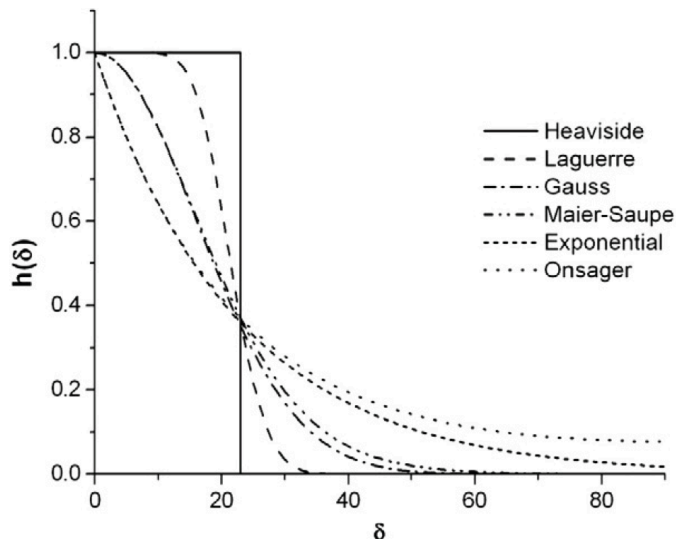


Fig. 24 The graphs of different distribution functions. (Image from ²⁵², Copyright Elsevier).

Among these functions, the Onsager and Maier-Saupe distributions can be pointed out because they are very important for the description of particle orientations in lyotropic and thermotropic liquid-crystalline systems. The distribution functions are normalized using the following factor

$$\frac{1}{c_h} = \int_0^{\frac{\pi}{2}} h(\delta) \sin \delta d\delta$$

The resulting mean deviation angle between cylinders and the director, which can take on values between 0° and 90° , is given by

$$\langle \delta \rangle = c_h \int_0^{\frac{\pi}{2}} \delta h(\delta) \sin \delta d\delta$$

A very general function is the Laguerre distribution which changes from a Gauß function (at

$k = 0$) to a Heaviside function (at very large k).

The order parameter S can take on values between 0 and 1. For a known distribution function it is given by

$$S = \langle P_2(\vec{r}\vec{D}) \rangle = \langle P_2(\cos\delta) \rangle = \left\langle \frac{3\cos^2\delta - 1}{2} \right\rangle$$

The above equations are valid for diluted systems and with raising concentrations it becomes necessary to take the structure factor into account as described by van-der-Schoot²⁸⁴

$$S(\vec{qL}) = \frac{P^2(\vec{qL})}{P(\vec{qL}) + 2cP^2(\vec{qL}) - 5cG^2(\vec{qL})}$$

$$\vec{qL} = qL \cos\beta$$

with the cylinder concentration c and with

$$G(\vec{qL}) = \frac{3}{4} \frac{(1 - J_0(2\vec{qL}))}{(\vec{qL})^2} - \frac{1}{2} P(\vec{qL})$$

$$\vec{qL} = qL \cos\beta$$

4 Methods and Techniques

4.1 Photolithography

Early materials that have been used for the fabrication of microfluidic devices include glass or silicon.⁷⁸ These materials were used because a wide range of microstructuring techniques were readily available from the field of semiconductor technology and because these materials offer resistance against a wide range of solvents. While glass is additionally optically transparent, silicon is opaque which limits microscopic applications for the latter material. A downside of both materials is the need for expensive clean room environments during their processing and the use of aggressive chemicals which makes it an expensive and resource intensive process.^{57,285}

The fast and effective fabrication of microfluidic devices in a short time became possible through the progress in the areas of photo- and soft lithography.⁵⁶ Polymer-based materials offer more application friendly properties which is why they have gained importance during the past years.^{230,286} One example for these are photoresists like SU-8 which are used in photolithography.²⁸⁷ This technology enables the creation of microstructures based on specific technical drawings which are created using computer aided design (CAD) software. By using the computer-designed photo masks, photo resists are selectively exposed for the generation of microstructures.⁵⁶ These microstructures are then replicated using soft materials such as polymers to create microstructured stamps or microfluidic devices which is why this technology is called soft lithography.⁵⁵ Due to the precise control over design features and the shortened system optimization feedback loop, this process enables (simulation-based) rapid prototyping.⁵⁷ Furthermore, the replication templates, also called masters, can be re-used multiple times without quality loss enabling mass production and low fabrication costs.²⁸⁸

The microstructuring of the photo resist happens by selective exposure using photo masks.⁵⁷ In case of a negative photoresist like SU-8, the non-cross-linked areas of the photoresist remain soluble and will be removed in the development stage of the lithographic process. The development bath typically contains 80 to 100% 2-methoxy-1-methylethyl acetate solution and is, similar to the photo resists, commercially available (mr-DEV 600, Microchem). Only the insoluble cross-linked areas of the photoresist remain on the substrate, typically a polished flat silicon wafer, and will be used as a master template for the subsequent replication steps.^{55,56} The resolution of soft lithography is limited by diffraction and, hence, dependent on the wave length of the light source.⁵⁶ The range of available photo resist materials is only small due to the specific processing requirements.

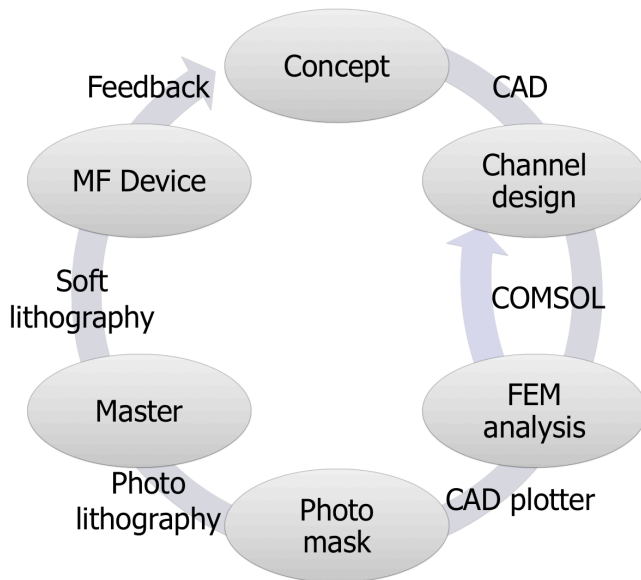


Figure 25 Illustration of the rapid prototyping concept which describes the short design-feedback-loop that enables the fast optimization of microfluidic systems. (Image adapted and modified from ⁵⁶)

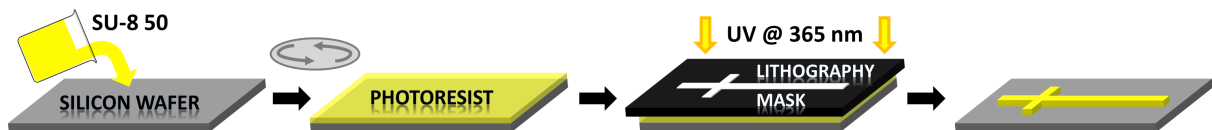


Figure 26 Fabrication of SU-8 master templates. A polished silicon wafer is spin coated using the negative photo resist SU-8. Using selective UV-exposure with an emulsion film mask, the microchannel geometry (i.e. mixing cross for hydrodynamic focusing) is received after the development process which removes the non-cross-linked material. (Image from ¹³, Copyright PNAS)

The photo resist EPON SU-8 is a material that is widely used for the fabrication of microfluidic devices. Developed by Shell Chemicals, this highly-functionalized monomer (69% in γ -butyrolactone) is capable of intermolecular cross-linking which enables the formation of three-dimensional structures with nanometer resolution.²⁸⁹⁻²⁹²

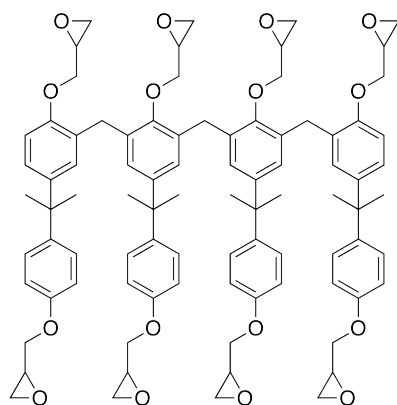


Figure 27 Structural formula of EPON SU-8.^{222,293,294}

The mechanism of this cross-linking is a cationic ring opening polymerization (ROMP) of the epoxide that is started by photo-initiated aryl sulfonium salts.

The lithographic process involves a UV-exposure step that leads to the formation of fluoroantimonic acid (HSbF_6). This is a strong Lewis acid that is formed in the presence of triarylsulfonium hexafluoroantimonate (3.3% solution in propylene carbonate, 4-Methyl-1,3-dioxolan-2-one) and proton donors like the organic solvent.²⁹⁵⁻²⁹⁷ This reaction mechanism is illustrated in Fig.28.

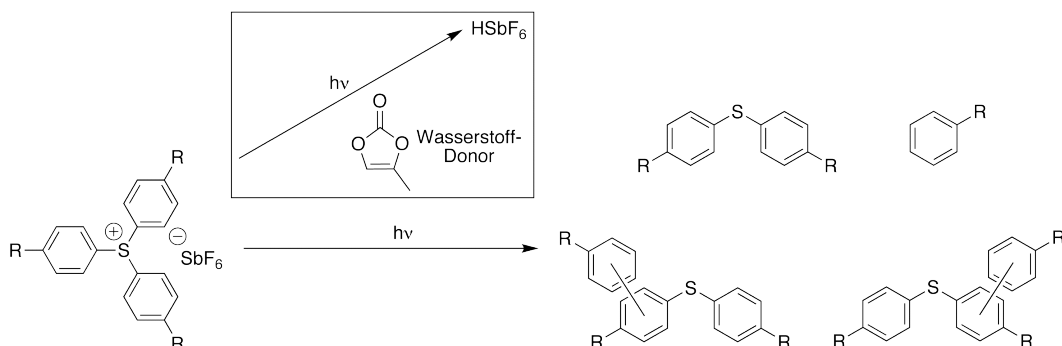


Figure 28 Photochemical pathways during the generation of fluoroantimonic acid (HSbF_6).^{297,298}

Since the photo initiator is consumed in an alternative reaction path during the UV-exposure, it is critically important to adjust the light dose accordingly. Otherwise, the required initiator is not available in sufficient amounts for the acid-induced epoxide cross-linking during the subsequent “post exposure bake” step, which is the heating of the exposed photoresist. The reaction mechanism of the cationic ring opening polymerization of the SU-8 photo resist is shown in Fig.29.

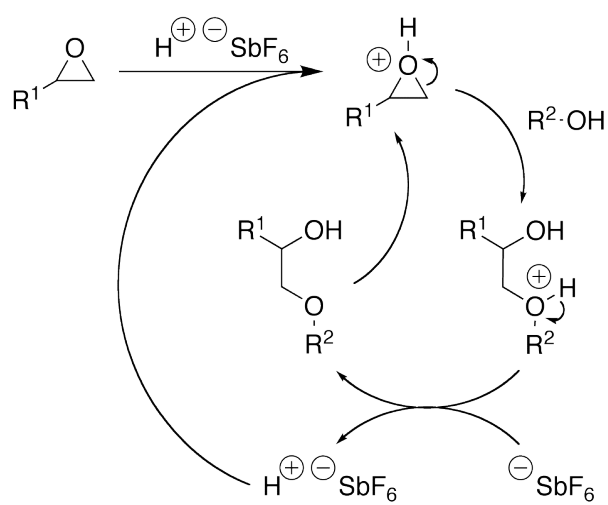


Figure 29 Catalytic reaction mechanism during the cross-linking of SU-8.²⁹⁹

The epoxide group is protonated and the nucleophilic attack of the hydroxyl group of another SU-8 molecule leads to the opening of the epoxide ring. The catalyst is regenerated by the elimination of a proton and the cycle repeats itself which leads to a cross-linked network.

Although PDMS would also be suitable for the replication of three-dimensional templates, photolithography is typically limited to planar substrates, such as silicon wafers or glass plates. However, it is also possible to generate three-dimensional microstructures. As an outlook, the ongoing advances in 3D-printing make this technology more affordable while the resolution improves continuously and range of processable material keeps growing.³⁰⁰⁻³⁰⁸

A possible approach for the generation of three-dimensional microstructures is based on modern technologies such as direct laser writing.³⁰⁹⁻³¹³ In this ultrashort-pulsed laser process, the laser passes the photoresist without altering its chemistry. Photo-induced reaction only occurs in case of multi-photon absorption, such as two-photon absorption. The probability of this absorption type is greatly increased by creating a small laser focus spot using microscopic lenses with high numeric apertures ($NA > 1.3$). This laser spot is moved three-dimensionally through the photo resist using piezo-stages with nanometer precision based on the 3D-CAD-model which is converted into a sequence of positions and exposures. During this movement process the intense pulsed laser spot induces multi-photon absorption. This absorption leads to chemical modifications and cross-linking of the photo resist in the subsequent post exposure baking process.³⁰⁹⁻³¹¹

However, a downside of this process is the slow writing speed because millimeter-sized structures could take days of writing time due to the small focus spot size.³¹⁴ Therefore, this approach could be combined with conventional photolithography for the microchannel feature refinement and post-integration of three-dimensional elements. Another downside is that the required equipment is still very expensive due to its relatively early development stage. Although this technology enables the generation of arbitrarily complicated three-dimensional structures, not all 3D-design features would be suitable for the replication using soft materials. The molded replica needs to remain removable from the template after curing which would not be the case with certain three-dimensional structures of the template, like i.e. tunnels or gyroid networks.

Another path for the generation of three-dimensional microchannels, which has been used in this thesis, is the stacking of multiple layers that are generated using conventional photolithography. This so-called “2.5D”-approach is based on open, pyramid-like microchannel assemblies that are based on multiple layers of microstructured photoresist. A matching pair of these is then combined to form a closed three-dimensional microchannel geometry.

A critical step in this technology is the precise and correct alignment of these matching microchannel structures. During this thesis, an alignment routine has been created and it is now possible to easily align the top and bottom half of the microfluidic device in a “click”-like routine (see chapter 7.3).¹³⁶ Compared to the previous manual alignment under the microscope, which could lead to layer shifts and errors, the micrometer-precise alignment is now as easy as putting Lego® building blocks together. The new interlocking triangular

structures are integrated into the microchannel (CAD-)design. After a short oxidizing air plasma treatment, these alignment structures snap into each other and lock the aligned position of the two matching PDMS-halves during their covalent bonding process. This process is described in one of the following papers (see chapter 7.3).¹³⁶

This multi-layer design also enables to precisely control the material heights during device fabrication, which is important for (i.e. NOA81-based) X-ray-compatible microfluidic chips. The liquid and uncured channel material is pushed away by laying a flat block on the surface of the microchannel template. This block is bridged by a spacer structure that is placed next to the microchannel of interest. The spacer is one spin-coating layer higher and therefore enables to precise control the material thickness of the scanning window above the channel of interest. This routine results in very thin microfluidic devices with a homogenous window thickness across the whole scanning area of the device. The photo resists which were used in this thesis are SU-8 50 and SU-8 100 which are suitable for different ranges of layer heights (30 µm to 250 µm) during spin coating due to their different viscosities. This process is described in one of the following papers (see chapter 7.2).¹³⁵

4.2 Molding Materials

The molding materials which were used in this thesis are poly(dimethylsiloxane) (Sylgard® 184 PDMS) and Nordland Optical Adhesive 81 (NOA81). The general molding concept and different variations thereof are described in the following papers.^{13,135,136}

Sylgard® 184 is a set of two components, the monomer and the cross-linker, which contain the molecules which are listed in Fig.30.

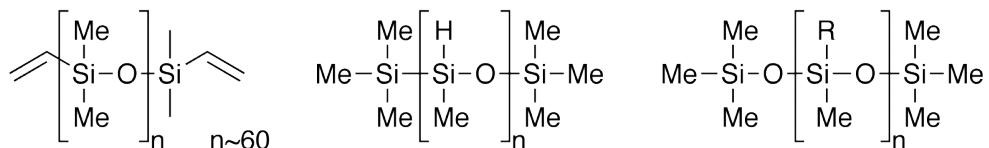


Figure 30 Structural formulas of the Sylgard® 184 compounds: dimethyl siloxane (oligomer), hydrogenmethyl siloxane (cross-linker), crosslinked PDMS.^{315,316}

The first component mainly consists of dimethylsiloxane (60%) which carries two terminal vinyl groups while the reactive compound of the cross-linker is hydrogenmethylsiloxane (40 to 70%). Furthermore one of the components contains organic platinum molecules such as dihydrogenhexachloroplatinat(VI) that catalyses the hydrosilylation of the terminal vinyl group of the dimethylsiloxane with the hydrogen-containing cross-linker.^{317,318} This two-component set results in a homogenous elastomeric material which is important for microfluidic components and devices, especially in combination with optical setups. This is not the case for conventional RTV-based silicon elastomers because their reaction is based on a condensation reaction mechanism. The vulcanization or curing of Sylgard 184 PDMS can be increased with increasing temperatures without weight loss or noteworthy volume

shrinkage (~1%).³¹⁹ Therefore the replicated microfluidic channel structures and consequently the intended flow conditions are not altered which makes predictive computational fluid dynamics (CFD) simulations possible. Hence, the elastomer PDMS has become an important material for the fabrication of microfluidic devices. This material offers a decent replication resolution, is optically transparent, non-toxic and has much lower costs per volumes compared to silicon.^{55,56,78,320,321} Due to the latter fact, the fabrication is still cost-efficient at low quantities which is important for rapid prototyping and often-changing microstructures. PDMS can be used for a wide range of temperatures (-50 up to 250 °C) and for common solvents such as water, acetone, methanol and ethanol.^{147,181}

However, PDMS swells easily when it is in contact with many organic solvents.¹⁴⁷ Further, the softness of PDMS limits the design freedom when it comes to high aspect ratios between channel height and width. The height to width ratio of microstructures has to be within a ratio of 0.2 and 8 for well-formed microchannels.⁵⁵ Exceeding this range can lead to two extreme cases, pairing or sagging, which are illustrated in Fig.31.

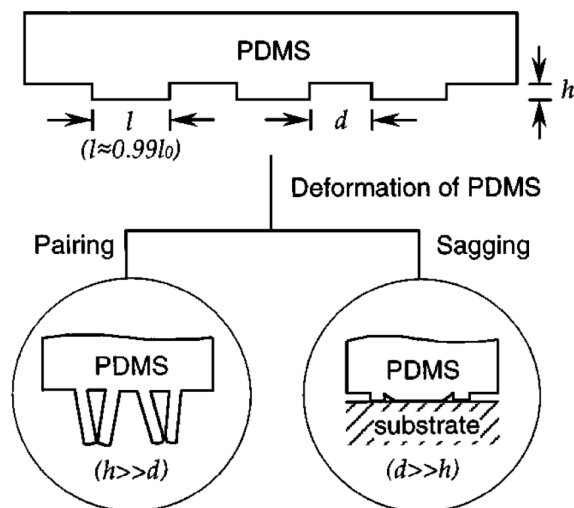


Figure 31 Illustration of the consequences of exceeding the height to width ratio when designing PDMS-based microfluidic devices. (Image from⁵⁵, Copyright Annual Reviews)

While PDMS is widely used as a material for microfluidic devices, it also serves as a template for the transfer of microfeatures into other polymeric materials such as a wide range of thermoplasts or UV-curable adhesives.^{148,150,163,175,181}

Nordland optical adhesive 81 (NOA81, Nordland Products) is a commercially available UV-curable glue for optical components and its composition is not clearly defined.^{168,322} However, the main components of this material have been determined by NMR and FT-Raman.¹⁶⁸ NOA81 mainly contains a mixture of allyl- and thiol-compounds which are cross-linked in a radical polymerization mechanism. These compounds and the steps of this mechanism are illustrated in Fig.32.

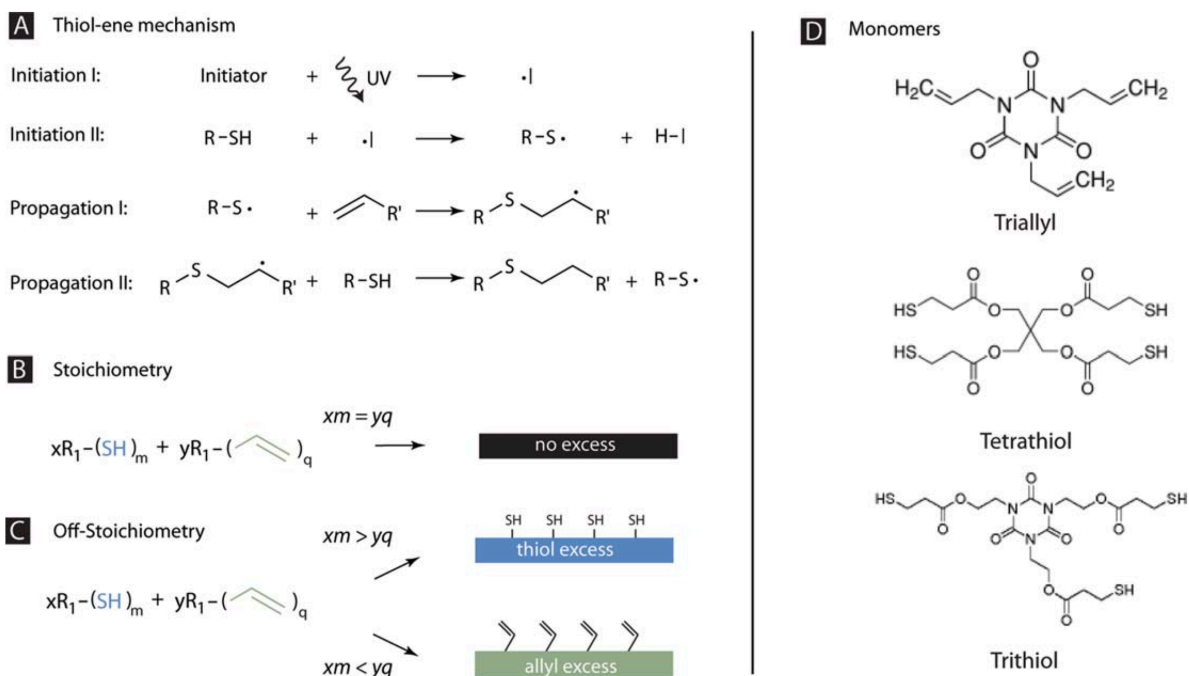


Figure 32 (D) Structural formulas of the NOA81-compounds, (A) their radical polymerization mechanism and (B, C) options for controlling the material's surface chemistry. (Image from ¹⁶⁸, Copyright The Royal Society of Chemistry).

The reaction is initiated by an UV-sensitive initiator which transfers its UV-generated radical to a thiol group. Maintaining the radicals, the thiol-radicals attack the allyl-groups (and vice versa) in the radical propagation steps which leads to the three-dimensional cross-linking of the molecules. This process is used to replicate the PDMS microstructure template. Due to the gas-permeability of PDMS, the NOA81 at the PDMS-interface remains uncured which allows the sealing of the open channel in the subsequent steps.¹³²

By tuning the composition ratio of the initial compounds it is possible to control the distribution of available functional groups at the surface.¹⁶⁸ Therefore, it is possible to control the microchannel surface wettability or cover the channel walls with coatings.^{149,168} and, as a result, control the functionalization chemistry. Additionally, the above cross-linking chemistry allows to control the mechanical properties, i.e. towards PDMS, by integrating thiol- or allyl-functionalized additives into the polymer network.¹⁶⁸

NOA81 has a very good solvent capability for a wide range of unpolar solvents which are unaccessible for PDMS-based devices.¹⁴⁹ Further, the material offers more rigid mechanical properties compared to PDMS which makes NOA81 very interesting for developments towards high pressured flow applications.

In summary, polymeric molding materials and lithographic tools are highly beneficial for the fabrication of microfluidic devices. Furthermore, these materials enable great design flexibility on the micron scale and can be tailored to specific needs by taking advantage of the materials' rich portfolio for modifying the surface and composition chemistry. The different fabrication techniques and -variations for microfluidic devices which have been used in this thesis are outlined in the following papers.^{13,14,155,136}

5 Strategy and Summary

As pointed out by Whitesides, a technological revolution requires two essential components: many different application-specific subsystems as well as the possibility to integrate these into complete, functional systems.⁵⁸ For the growth of a technology to gain momentum, it must also be as simple, understandable and easy to use as possible for being picked up and adapted by non-experts.⁵⁸

As an example, microfluidics can be an overwhelming field because it offers such a broad range of interesting applications, tools and functional elements. If at all, microfluidic applications are seldomly found at synchrotrons or free electron lasers, which also represent broad and complex fields of research.

Therefore, the primary goal of this thesis is the development of an integrated platform technology, that combines microfluidics & microfocused X-ray scattering techniques, for establishing of a powerful experimental methodology that is suitable for the investigation of nanostructures, particle alignment, protein nanocrystals and the *in situ* study of kinetics. This has been achieved by the development and fabrication of different types of X-ray compatible devices: closed systems and an open-/liquid jet-based system.

Next to microfluidic liquid jet systems, which are described further below, this thesis presents different examples of the first (closed) microfluidic device type: Kapton-PDMS- or NOA81-based.

The first one of these two device types was used to demonstrate the capabilities that are offered by X-ray compatible microfluidic devices and their operation at a microfocus beamline. As outlined in the summary at the beginning of this thesis, the detailed SAXS-mapping scans of well-defined microchannels revealed perpendicularly oriented wormlike micelles after passing narrow taperings. These results were enabled by soft lithography-based microfluidic devices that originate from a published device design (Kapton-PDMS).¹³⁹ These devices have a very low scattering background due to the use of Kapton as a window material. These devices have a major flaw however: the tubing interface, or lack thereof, which is crucial for connecting the microchannels to the macroscopic world. In the very early experiments, the described clamps which are connected to the tubing have been used. Unfortunately, these were either too loose (& leaking) or too tight, deforming or even closing the microchannel geometry. Therefore, a new approach has been developed that combines this fundamental device type with a PDMS-based approach for the tubing-connection. This resulted in well-sealed and more pressure resistant devices, capable of pumping viscous samples, such as the described wormlike micelles and enabling the described microfluidic SAXS experiments and studies of the re-orientation phenomenon.

A key benefit of the microstructuring technique called soft lithography is its precise control of the microchannel geometries. It is therefore possible to combine different experimental techniques in a complementary way. Consequently, the exact reproduction of microchannel geometries is crucial for the combined use of different experimental techniques. Accordingly, microfocus SAXS-studies, microscopic experiments, such as polarization microscopy or microparticle image velocimetry (μ PIV), and computational fluid dynamics (CFD) simulations have been used in an integrated approach that has been applied in the successful explanation of the perpendicular re-orientation effect (see chapter 7.1). We could show by polarization microscopy, μ PIV-experiments and additional CFD simulations that the perpendicular orientation of wormlike micelles is the result of the interplay between the x-orienting shear- and y-orienting extensional forces; with x along the flow direction and y along the widening of the tapering.

The re-orientation of anisotropic particles has been investigated in further detail in the following paper (see chapter 7.2). The established system of just-described complementary analysis methods has been applied for a systematic parameter screening, including the tapering ratios (-width, -length), the flow speeds and concentrations. Further, the rheological parameters have been varied systematically using CFD-simulation that are based on the sample's experimentally measured rheological parameters. The system's response to these parameter variations has been analyzed and quantified carefully. A relative ranking of the described system-controlling parameters could be derived from the combined experimental and theoretical results. The results of this work (chapters 7.1 & 7.2), and the perpendicular re-orientation effect in general, are of great importance for application that require orientation control, such as injection molding, fiber spinning or processing of composite materials.

The second (chapter 7.2) paper also describes an improved version of the closed-channel X-ray compatible microfluidic device that is based on a recently published paper.¹³² These devices are made of the UV-curable adhesive NOA81 (see chapter 2.1 and 4.2) as the device material. However, the published design also has two weak points. The first is related the tubing-interface which glues PDMS onto the flat NOA81-device, punches a hole through the complete structure and seals it again the self-adhesive Tape. This reduces the pressure resistance as well as the solvent compatibility of the device (see chapter 2.1). The second flaw is the lack of the device's height control. Since a correct background subtraction is essential for SAXS-experiments, especially for dilute or weakly-scattering samples, a homogenous device height is of great importance, as is the overall material thickness of the microfluidic device.

The improved fabrication of NOA81-devices is described in the experimental section while its illustration is presented in the supplemental section of this paper (chapter 7.2). The first improvement involves the integration of bridging structures that are used of controlling the device height by adjusting the photoresist layer height through spin-coating. This leads to very even and extremely thin and stable microfluidic chips, reducing the X-ray background

signal and improving the signal transmission. The second improvement is related to the tubing interface. During the molding or replication step, a tubing is punched through the (PDMS-)microstructure and serves as a temporary template, enabling the direct connection of the tubing to the finished replica. As a consequence, the solvent compatibility of NOA81 is fully maintained and many polar and unpolar solvents, which are incompatible with PDMS, can now be used in this purely NOA81-based devices without issues. Additionally the pressure resistance of these devices is improved and can even be enhanced by glueing tubing to the device. Further, these improved devices run more reliably, have a smaller device footprint enabling denser arrays of microchannels, better optical properties and lower background signal compared to PDMS-Kapton-devices. Above all, the fabrication is easier due to the precise height control and much quicker due to the fast UV-exposure times (under one minute) compared to tens of minutes, or even hours, for thermally cured PDMS.

Another microfluidic device that is also made of this material (NOA81) is described in chapter 7.4. This variation is closed and not actively flowing, but therefore only very small sample amounts are required for the SAXS-measurement of sheared samples. With only 2-5 µl of fluid volume, the nanoparticle lyotropic gel sample is applied to a millimeter-sized patch of the microstructured grid (14 µm spacing) while being sheared in the process. The microgrid is then sealed against evaporation using Kapton tape. Hence, this device demonstrates the high sample efficiency and ease of use when it comes to experiments at synchrotrons. Additionally, this work was essential for the improvement and optimization of soft lithographic fabrications techniques related to NOA81 that lead to the successful fabrication of high-resolution NOA81-based X-ray compatible microflow devices which are presented in chapter 7.2.

The next paper describes a microfluidic liquid jet system (see chapter 7.3). As an example of an open microfluidic sample environment, it is designed for experiments at highly brilliant X-ray sources or X-ray free electron lasers. The liquid jet is generated based on the gas-dynamic virtual nozzle design (GDVN) which represents the current state of the art at XFELs.⁶ For this reason this microfluidic device runs essentially clogging-free and highly reliable over long periods of time.⁵³

The goal of this paper was to create a microfluidic liquid jet design that is easy and fast to fabricate, since the current glass capillary fabrication is a complex and manually challenging procedure. The creation of glass-based nozzles requires a skilled producer because the fabrication involves manual steps like grinding, flame-polishing and alignment of the capillaries. In contrast, the here presented microfluidic liquid jet nozzles can easily be replicated by using standard PDMS-device fabrication steps which are very fast to learn. The microfluidic devices further offer the benefit of a parallelized nozzle design which enables to create complex jet-in-jet-focusing geometries or complete arrays of multiple nozzle simultaneously in one fabrication sequence. Consequently the device footprint is very small which enables fast nozzle changes by simply switching to the adjacent nozzles.

The fabrication of these microfluidic liquid jet devices became possible due to our advances in multi-layered soft lithography. This enables the fabrication of 3D-microchannels by sealing two matching halves of microstructured PDMS that are treated with an air plasma. Since the micrometer-precise alignment would be manually challenging, the replication templates already incorporate alignment structures by design. These snap-in alignment structures could be integrated through the multi-layered microstructure design and they work similarly to Lego® building blocks, locking the microstructures of the two PDMS-halves in their right position during the sealing step.

A key benefit of this microfluidic device over the state of the art glass capillaries is the highly reproducible design that is enabled through soft lithography. This micrometer-precise control over the nozzle geometries is critically important for the optimization of the liquid jets, especially at small flow rates. As described in chapter 2.4, the geometric parameters strongly affect the minimum flow rate for stable jetting which is the key factor for the high sample efficiency of these devices.

Taking advantage of this design control, the relevant parameters, such as liquid flow rate and pressure difference, were varied to study the liquid jet dynamics. We found that the microfluidic liquid jet diameters can adjusted with great control by varying the pressures & flow rates and that they are in good agreement with available analytical expressions for the prediction of jet diameters in plate-orifice geometries.²⁰¹ This has also been verified by *in-situ* environmental scanning electron microscopy of the liquid jet exiting the nozzle. Furthermore, the variations of the above parameters allowed to control the jet breakup type. These jet breakup transitions have been studied using highspeed video microscopy and we also found that the stable jet's column length can be controlled over a wide length scale.

The jet shape could be predicted successfully by using time-resolved non-linear 3D CFD-simulations that describe the two-phase flow of fluids. The simulated shape of this theoretical liquid jet is in good agreement with the experimental microscopic results.

The jet's 3D shape was also studied by using confocal laser scanning microscopy. Since this study involved an enhanced design that incorporated a jet in jet hydrodynamic focusing geometry, before the liquid jet is shaped by the gas sheath, the fluid flow within the liquid jet could also be studied using in these experiments. Interestingly, we find that the flow of the two dye solutions (rhodamine B and fluorescein) is inverted and the inner focused liquid stream can be observed at the outside of the liquid jet as it exits the nozzle geometry. This inversion might originate from the inversion of speeds at the outer boundaries of the liquid that lead to the generation of vortices counteracting the liquid flow.²⁰⁷ The velocity profile is parabolic inside the microchannel, therefore fastest in the liquid stream's center and slowest close to the walls, this scenario changes quickly as the liquid exits the microchannel. Suddenly, the fastest liquid velocity can be found at the outside where the fast-flowing gas is in contact with the liquid. This kind of diffusion-controlled mixing inside the liquid jet could

enable new kinds of experiments at XFELs, such as the femtosecond-pulse diffraction of *in situ* nucleation and growth processes.

The microfluidic concepts and lithographic microfabrication techniques have also been used for creating solutions for applications that are not related to X-ray experiments.

As presented in chapter 7.5, a CFD-model has been created which describes non-linear interaction between the fluid and the microchannel walls under high pressures and high flow rates. The CFD-simulations showed how PDMS-microchannels with high aspect ratios deformed under these unusual conditions towards a rounded shape. This round shape was in good agreement with the microscopic images. We further found that this round shape of microchannel reduces the wall contact of flowing species which were mixed by hydrodynamic focusing before entering this round passage. Therefore, clogging of the device can be strongly reduced or eliminated.

The creation of this CFD-model have lead to deeper insights about the simulation software and its capabilities and laid a foundation for the other non-linear CFD-models described above.

Soft lithography is essential for the work of the presented papers for which the foundation has been laid with the following two papers.

The paper described in chapter 7.6 describes the combination of nanotechnology and microstructuring techniques for developments towards sensoric applications. This work required the creation of deep, high aspect ratio, SU-8 microchannels. The optimization the parameters during the UV-lithographic process lead to better-defined and improved microchannel wall geometries for all microfluidic devices of this thesis.

The work described in chapter 7.7 focuses on increasing the soft lithographic resolution of microstructured templates and an optimized replication thereof. This optimization resulted in very small and well-defined letters of high resolution that served as a micro contact printing stamp for the defined deposition of spherical polyelectrolyte brushes. This increased lithographic resolution lead to the capability of fabricating very small microfluidic features, such as narrow taperings (chapter 7.1 & 7.2), narrow grids (chapter 7.4) and small nozzles (chapter 7.3).

Hence, the lithographic developments of these two papers played a crucial role for the successful application of soft lithography in the other papers by increasing the quality of high aspect ratio microchannel walls as well as the increasing resolution of very small microstructures.

The following chapter will describe the authors' contribution to these papers, followed by the papers in the subsequent chapter.

References

1. M. Antonietti and S. Förster, *Advanced Materials*, 2003, **15**, 1323–1333.
2. S. Förster, *Topics in Current Chemistry*, 2003, **226**, 1–28.
3. S. Förster, B. Berton, H. P. Hentze, E. Krämer, M. Antonietti, and P. Lindner, *Macromolecules*, 2001, **34**, 4610–4623.
4. I. Robinson, G. Gruebel, and S. Mochrie, *New J. Phys.*, 2010, **12**.
5. T. Narayanan, *Curr Opin Colloid In*, 2009.
6. H. N. Chapman, P. Fromme, A. Barty, T. A. White, R. A. Kirian, A. Aquila, M. S. Hunter, J. Schulz, D. P. DePonte, U. Weierstall, R. B. Doak, F. R. N. C. Maia, A. V. Martin, I. Schlichting, L. Lomb, N. Coppola, R. L. Shoeman, S. W. Epp, R. Hartmann, D. Rolles, A. Rudenko, L. Foucar, N. Kimmel, G. Weidenspointner, P. Holl, M. Liang, M. Barthelmess, C. Caleman, S. Boutet, M. J. Bogan, J. Krzywinski, C. Bostedt, S. Bajt, L. Gumprecht, B. Rudek, B. Erk, C. Schmidt, A. Hömke, C. Reich, D. Pietschner, L. Strüder, G. Hauser, H. Gorke, J. Ullrich, S. Herrmann, G. Schaller, F. Schopper, H. Soltau, K.-U. Kühnel, M. Messerschmidt, J. D. Bozek, S. P. Hau-Riege, M. Frank, C. Y. Hampton, R. G. Sierra, D. Starodub, G. J. Williams, J. Hajdu, N. Timneanu, M. M. Seibert, J. Andreasson, A. Rocker, O. Jönsson, M. Svenda, S. Stern, K. Nass, R. Andritschke, C.-D. Schröter, F. Krasniqi, M. Bott, K. E. Schmidt, X. Wang, I. Grotjohann, J. M. Holton, T. R. M. Barends, R. Neutze, S. Marchesini, R. Fromme, S. Schorb, D. Rupp, M. Adolph, T. Gorkhover, I. Andersson, H. Hirsemann, G. Potdevin, H. Graafsma, B. Nilsson, and J. C. H. Spence, *Nature*, 2011, **470**, 73–77.
7. D. H. Bilderback and P. Elleaume, *Journal of Physics B: ...*, 2005.
8. H. A. Stone, A. D. Stroock, and A. Ajdari, *Annu. Rev. Fluid Mech.*, 2004, **36**, 381–411.
9. S. Köster and T. Pfohl, *Mod. Phys. Lett. B*, 2012, **26**, 1230018.
10. T. Squires and S. Quake, *Rev. Mod. Phys.*, 2005, **77**, 977–1026.
11. J. Als-Nielsen and D. McMorrow, *Elements of Modern X-ray Physics*, Wiley, Chichester, 2011.
12. O. Glatter and O. Kratky, *Academic Press*, 1982.
13. M. Trebbin, D. Steinhauser, J. Perlich, A. Buffet, S. V. Roth, W. Zimmermann, J. Thiele, and S. Förster, *PNAS*, 2013, **110**, 6706–6711.
14. S. M. Taheri, S. Fischer, M. Trebbin, S. With, J. H. Schröder, J. Perlich, S. V. Roth, and S. Förster, *Soft Matter*, 2012, **8**, 12124.
15. L. Daubersies, J. Leng, and J.-B. Salmon, *Lab Chip*, 2013, **13**, 910.
16. C. Riek, P. Engström, and C. Martin, *J. of Macromolecular Sc., Part B*, 1998, **B37**, 587–599.
17. R. J. Davies, M. Burghammer, and C. Riek, *Synchrotron Radiation in Natural Science*, 2006, **5**, 96–99.
18. S. V. Roth, R. Döhrmann, M. Dommach, M. Kuhlmann, I. Kröger, R. Gehrke, H. Walter, C. Schroer, B. Lengeler, and P. Müller-Buschbaum, *Rev. Sci. Instrum.*, 2006, **77**, 085106.

19. A. Timmann, R. Döhrmann, T. Schubert, H. Schulte-Schrepping, U. Hahn, M. Kuhlmann, R. Gehrke, S. V. Roth, A. Schropp, C. Schroer, and B. Lengeler, *Rev. Sci. Instrum.*, 2009, **80**, 046103.
20. C. Riekel, M. Burghammer, and R. Davies, *IOP Conf. Ser.: Mater. Sci. Eng.*, 2010, **14**, 012013.
21. A. Buffet, A. Rothkirch, R. Döhrmann, V. Körstgens, M. M. Abul Kashem, J. Perlich, G. Herzog, M. Schwartzkopf, R. Gehrke, P. Müller-Buschbaum, and S. V. Roth, *J. Synchrotron Rad. (2012)*, 2012, **19**, 647–653 [[doi:10.1107/S0909049512016895](https://doi.org/10.1107/S0909049512016895)], 2012, 1–7.
22. A. Martel, M. Burghammer, R. Davies, E. DiCola, P. Panine, J.-B. Salmon, and C. Riekel, *Biomicrofluidics*, 2008, **2**, 024104.
23. A. Otten, S. Köster, B. Struth, A. Snigirev, and T. Pfohl, *J. Synchrotron Rad.*, 2005, **12**, 745–750.
24. A. Snigirev, V. Kohn, I. Snigireva, and B. Lengeler, *Nature*, 1996.
25. B. Struth, AIP, 2004, vol. 705, pp. 804–807.
26. C. G. Schroer and B. Lengeler, *Phys. Rev. Lett.*, 2005, **94**, 054802.
27. M. Müller, C. Riekel, R. Vuong, and H. Chanzy, *Polymer*, 2000, **41**, 2627–2632.
28. C. Riekel and R. J. Davies, *Curr Opin Colloid in*, 2005, **9**, 396–403.
29. R. J. Davies, M. Burghammer, and C. Riekel, *Macromolecules*, 2007, **40**, 5038–5046.
30. A. Martel, M. Burghammer, R. J. Davies, E. Di Cola, C. Vendrely, and C. Riekel, *J. Am. Chem. Soc.*, 2008, **130**, 17070–17074.
31. C. Riekel, M. Rossle, D. Sapede, and F. Vollrath, *Naturwissenschaften*, 2004, **91**, 30–33.
32. C. Riekel, B. Madsen, D. Knight, and F. Vollrath, *Biomacromolecules*, 2000, **1**, 622–626.
33. C. Riekel, M. Müller, and F. Vollrath, *Macromolecules*, 1999, **32**, 4464–4466.
34. M. E. Kinahan, E. Filippidi, S. Köster, X. Hu, H. M. Evans, T. Pfohl, D. L. Kaplan, and J. Wong, *Biomacromolecules*, 2011, **12**, 1504–1511.
35. J. F. Moulin, S. V. Roth, and P. Müller-Buschbaum, *Rev. Sci. Instrum.*, 2008, **79**, 015109.
36. N. Stribeck, A. A. Camarillo, U. Nöchel, C. Schroer, M. Kuhlmann, S. V. Roth, R. Gehrke, and R. K. Bayer, *Macromolecular Chemistry and Physics*, 2006, **207**, 1139–1149.
37. N. Stribeck, U. Nöchel, and A. Almendarez-Camarillo, *Macromolecular Chemistry and Physics*, 2008, **209**, 1976–1982.
38. J. M. Feldkamp, M. Kuhlmann, S. V. Roth, A. Timmann, R. Gehrke, I. Shakhverdova, P. Paufler, S. K. Filatov, R. S. Bubnova, and C. G. Schroer, *Phys. Status Solidi (a)*, 2009, **206**, 1723–1726.
39. C. G. Schroer, M. Kuhlmann, S. V. Roth, R. Gehrke, N. Stribeck, A. Almendarez-Camarillo, and B. Lengeler, *Appl. Phys. Lett.*, 2006, **88**, 164102–164102–3.
40. M. Kuhlmann, J. M. Feldkamp, S. V. Roth, and C. G. Schroer, 2008, pp. 570–573.
41. J. M. Feldkamp, *Dissertation*, 2009, 1–136.
42. A. C. Kak and M. Slaney, *IEEE Press*, 1988.
43. A. Gonzalez and C. Nave, *Acta Crystallogr D Biol Crystallogr*, 1994, **50**, 874–877.
44. R. Henderson, *Proceedings of the Royal Society B: Biological Sciences*, 1990, **241**, 6–8.

45. S. Cusack, H. Belrhali, A. Bram, M. Burghammer, A. Perrakis, and C. Riekel, *Nat. Struct. Biol.*, 1998, **5**, 634–637.
46. L. Pollack, M. Tate, N. Darnton, J. Knight, S. Gruner, W. Eaton, and R. Austin, *PNAS*, 1999, **96**, 10115–10117.
47. L. Pollack, M. W. Tate, A. C. Finnefrock, C. Kalidas, S. Trotter, N. C. Darnton, L. Lurio, R. H. Austin, C. A. Batt, S. M. Gruner, and S. Mochrie, *Phys. Rev. Lett.*, 2001, **86**, 4962–4965.
48. R. Russell, I. S. Millettt, M. W. Tate, L. W. Kwok, B. Nakatani, S. M. Gruner, S. Mochrie, V. Pande, S. Doniach, D. Herschlag, and L. Pollack, *Proceedings of the National Academy of Sciences*, 2002, **99**, 4266–4271.
49. R. Neutze, R. Wouts, D. van der Spoel, E. Weckert, and J. Hajdu, *nature*, 2000, **406**, 752–757.
50. L. Lomb, T. Barends, S. Kassemeyer, A. Aquila, S. Epp, B. Erk, L. Foucar, R. Hartmann, B. Rudek, D. Rolles, A. Rudenko, R. Shoeman, J. Andreasson, S. Bajt, M. Barthelmess, A. Barty, M. Bogan, C. Bostedt, J. Bozek, C. Caleman, R. Coffee, N. Coppola, D. DePonte, R. B. Doak, T. Ekeberg, H. Fleckenstein, P. Fromme, M. Gebhardt, H. Graafsma, L. Gumprecht, C. Hampton, A. Hartmann, G. Hauser, H. Hirsemann, P. Holl, J. Holton, M. Hunter, W. Kabsch, N. Kimmel, R. Kirian, M. Liang, F. R. N. Maia, A. Meinhart, S. Marchesini, A. Martin, K. Nass, C. Reich, J. Schulz, M. M. Seibert, R. Sierra, H. Soltau, J. C. Spence, J. Steinbrener, F. Stellato, S. Stern, N. Timneanu, X. Wang, G. Weidenspointner, U. Weierstall, T. White, C. Wunderer, H. Chapman, J. Ullrich, L. Strüder, and I. Schlichting, *Phys. Rev. B*, 2011, **84**, 214111.
51. A. Barty, C. Caleman, A. Aquila, N. Timneanu, L. Lomb, T. A. White, J. Andreasson, D. Arnlund, S. Bajt, T. R. M. Barends, M. Barthelmess, M. J. Bogan, C. Bostedt, J. D. Bozek, R. Coffee, N. Coppola, J. Davidsson, D. P. DePonte, R. B. Doak, T. Ekeberg, V. Elser, S. W. Epp, B. Erk, H. Fleckenstein, L. Foucar, P. Fromme, H. Graafsma, L. Gumprecht, J. Hajdu, C. Y. Hampton, R. Hartmann, A. Hartmann, G. Hauser, H. Hirsemann, P. Holl, M. S. Hunter, L. Johansson, S. Kassemeyer, N. Kimmel, R. A. Kirian, M. Liang, F. R. N. C. Maia, E. Malmerberg, S. Marchesini, A. V. Martin, K. Nass, R. Neutze, C. Reich, D. Rolles, B. Rudek, A. Rudenko, H. Scott, I. Schlichting, J. Schulz, M. M. Seibert, R. L. Shoeman, R. G. Sierra, H. Soltau, J. C. H. Spence, F. Stellato, S. Stern, L. Strüder, J. Ullrich, X. Wang, G. Weidenspointner, U. Weierstall, C. B. Wunderer, and H. N. Chapman, *Nature Photon*, 2011, **6**, 35–40.
52. J. Ullrich, A. Rudenko, and R. Moshammer, *Annu Rev Phys Chem*, 2012, **63**, 635–660.
53. D. P. DePonte, U. Weierstall, K. Schmidt, J. Warner, D. Starodub, J. C. H. Spence, and R. B. Doak, *J. Phys. D: Appl. Phys.*, 2008, **41**, 195505.
54. A. M. Gañán-Calvo, D. P. DePonte, M. A. Herrada, J. C. H. Spence, U. Weierstall, and R. B. Doak, *Small*, 2010, **6**, 822–824.
55. Y. Xia and G. M. Whitesides, *Annual review of materials science*, 1998, **28**, 153–184.
56. G. M. Whitesides and Y. Xia, *Angew. Chem. Int. Ed.*, 1998, **37**, 550–575.

57. D. C. Duffy, J. C. McDonald, O. J. A. Schueller, and G. M. Whitesides, *Anal. Chem.*, 1998, **70**, 4974–4984.
58. G. M. Whitesides, *Nature*, 2006, **442**, 368–373.
59. C.-M. Ho and Y.-C. Tai, *Annu. Rev. Fluid Mech.*, 1998, **30**, 579–612.
60. A. Groisman, M. Enzelberger, and S. Quake, *Science*, 2003, **300**, 955–958.
61. J. Thiele, University of Bayreuth, 2011.
62. G. M. Whitesides and A. D. Stroock, *Physics Today*, 2001, **54**, 42.
63. A. Stroock and G. M. Whitesides, *Electrophoresis*, 2002, **23**, 3461–3473.
64. A. Manz, N. GRABER, and H. M. WIDMER, *Sensors and Actuators B: Chemical*, 1990, **1**, 244–248.
65. A. R. Abate, M. B. Romanowsky, J. J. Agresti, and D. A. Weitz, *Appl. Phys. Lett.*, 2009, **94**, 023503.
66. A. R. Abate, T. Hung, P. Mary, J. J. Agresti, and D. A. Weitz, *Proceedings of the National Academy of Sciences*, 2010, **107**, 19163–19166.
67. T. Thorsen, S. J. Maerkl, and S. R. Quake, *Science*, 2002, **298**, 580–584.
68. Y.-C. Tan, V. Cristini, and A. P. Lee, *Sensors and Actuators B: Chemical*, 2006, **114**, 350–356.
69. W. Xu and S. J. Muller, *Lab Chip*, 2011, **11**, 435–442.
70. T. Pfohl, *Analyse, Manipulation und Aggregation von biologischen Makromolekülen im mikrofluidischen Scherfluss*, De Gruyter, 2010.
71. T. Franke and A. Wixforth, *Phys. Unserer Zeit*, 2007, **38**, 88–94.
72. A. R. Abate, J. J. Agresti, and D. A. Weitz, *Appl. Phys. Lett.*, 2010, **96**, 203509.
73. D. Therriault, S. R. White, and J. A. Lewis, *Nat. Mater.*, 2003, **2**, 265–271.
74. S. K. Sia and G. M. Whitesides, *Electrophoresis*, 2003, **24**, 3563–3576.
75. C. Xi, D. L. Marks, D. S. Parikh, L. Raskin, and S. A. Boppart, *Proceedings of the National Academy of Sciences*, 2004, **101**.
76. D. S. Kim, S. H. Lee, T. H. Kwon, and C. H. Ahn, *Lab Chip*, 2005, **5**, 739.
77. S. Hardt, K. S. Drese, V. Hessel, and F. Schönfeld, *Microfluid Nanofluid*, 2005, **1**, 108–118.
78. S. Quake and A. Scherer, *Science*, 2000, **290**, 1536–1540.
79. J. W. Hong and S. R. Quake, *Nature biotechnology*, 2003, **21**, 1179–1183.
80. J. W. Hong, V. Studer, G. Hang, W. F. Anderson, and S. R. Quake, *Nature biotechnology*, 2004, **22**, 435–439.
81. C. Lee, G. Sui, A. Elizarov, C. Shu, and Y. Shin, *Science*, 2005, **310**, 1793–1796.
82. J.-C. Baret, O. J. Miller, V. Taly, M. Ryckelynck, A. El-Harrak, L. Frenz, C. Rick, M. L. Samuels, J. B. Hutchison, J. J. Agresti, D. R. Link, D. A. Weitz, and A. D. Griffiths, *Lab Chip*, 2009, **9**, 1850.
83. H. Shafiee, M. B. Sano, E. A. Henslee, J. L. Caldwell, and R. V. Davalos, *Lab Chip*, 2010, **10**, 438.
84. T. Q. Chastek, K. Iida, E. J. Amis, M. J. Fasolka, and K. L. Beers, *Lab Chip*, 2008, **8**, 950.

85. K. Iida, T. Q. Chastek, K. L. Beers, K. A. Cavigchi, J. Chun, and M. J. Fasolka, *Lab Chip*, 2009, **9**, 339.
86. C. Hany, H. Lebrun, C. Pradere, J. Toutain, and J.-C. Batsale, *Chemical Engineering Journal*, 2010, **160**, 814–822.
87. H. Pennemann, P. Watts, S. J. Haswell, V. Hessel, and H. Lowe, *Org. Process Res. Dev.*, 2004, **8**, 422–439.
88. S. Seiffert and D. A. Weitz, *Polymer*, 2010, **51**, 5883–5889.
89. E. Tumarkin and E. Kumacheva, *Chem. Soc. Rev.*, 2009, **38**, 2161.
90. C. Priest, A. Quinn, A. Postma, A. N. Zelikin, J. Ralston, and F. Caruso, *Lab Chip*, 2008, **8**, 2182.
91. Y. Morimoto, W.-H. Tan, Y. Tsuda, and S. Takeuchi, *Lab Chip*, 2009, **9**, 2217–2223.
92. Y. Song, J. Hormes, and C. S. S. R. Kumar, *Small*, 2008, **4**, 698–711.
93. Y. Song, H. Modrow, L. L. Henry, C. K. Saw, E. E. Doomes, V. Palshin, J. Hormes, and C. S. S. R. Kumar, *Chem. Mater.*, 2006, **18**, 2817–2827.
94. A. Jahn, J. Reiner, W. Vreeland, and D. DeVoe, *Journal of Nanoparticle Research*, 2008.
95. P. Kallio and J. Kuncova, *TEKES Technology review*, 2004.
96. P. S. Dittrich and A. Manz, *Nat Rev Drug Discov*, 2006, **5**, 210–218.
97. W. Li, J. Greener, D. Voicu, and E. Kumacheva, *Lab Chip*, 2009, **9**, 2715.
98. R. S. Ramsey and J. M. Ramsey, *Anal. Chem.*, 1997, **69**, 1174–1178.
99. J. Pihl, M. Karlsson, and D. T. Chiu, *Drug Discov. Today*, 2005, **10**, 1377–1383.
100. A. R. Wheeler, W. R. Throndset, and R. J. Whelan, *Analytical ...*, 2003.
101. A. A. Werdich, E. A. Lima, B. Ivanov, I. Ges, M. E. Anderson, J. P. Wikswo, and F. J. Baudenbacher, *Lab Chip*, 2004, **4**, 357.
102. R. T. Turgeon and M. T. Bowser, *Anal Bioanal Chem*, 2009, **394**, 187–198.
103. I. K. Dimov, L. Basabe-Desmonts, J. L. Garcia-Cordero, B. M. Ross, A. J. Ricco, and L. P. Lee, *Lab Chip*, 2011, **11**, 845–850.
104. J. Melin and S. R. Quake, *Annual review of biophysics and biomolecular structure*, 2007, **36**, 213–231.
105. M. A. Unger, H. P. Chou, T. Thorsen, A. Scherer, and S. R. Quake, *Science*, 2000, **288**, 113–116.
106. Y. Huang, P. Castrataro, C.-C. Lee, and S. R. Quake, *Lab Chip*, 2006, **7**, 24.
107. C. Zhang, J. Xu, W. Ma, and W. Zheng, *Biotechnol. Adv.*, 2006, **24**, 243–284.
108. E. A. Ottesen, J. W. Hong, S. R. Quake, and J. R. Leadbetter, *Science*, 2006, **314**, 1464–1467.
109. I. P. G. Marshall, P. C. Blainey, A. M. Spormann, and S. R. Quake, *Applied and Environmental Microbiology*, 2012, **78**, 8555–8563.
110. S. J. Pamp, E. D. Harrington, S. R. Quake, D. A. Relman, and P. C. Blainey, *Genome Res.*, 2012, **22**, 1107–1119.
111. J. Wang, H. C. Fan, B. Behr, and S. R. Quake, *Cell*, 2012, **150**, 402–412.
112. F. E. Dewey, S. Pan, M. T. Wheeler, S. R. Quake, and E. A. Ashley, *Circulation*, 2012, **125**, 931–944.
113. D. Pushkarev, N. F. Neff, and S. R. Quake, *Nature biotechnology*, 2009, **27**, 847–850.

114. H. C. Fan, Y. J. Blumenfeld, Y. Y. El-Sayed, J. Chueh, and S. R. Quake, *YMOB*, 2009, **200**, 543.e1–543.e7.
115. R. A. White, P. C. Blainey, H. C. Fan, and S. R. Quake, *BMC Genomics*, 2009, **10**, 116.
116. M. Meier, R. Sit, W. Pan, and S. R. Quake, *Anal. Chem.*, 2012, **84**, 9572–9578.
117. M. Meier, R. V. Sit, and S. R. Quake, *Proceedings of the National Academy of Sciences*, 2013, **110**, 477–482.
118. C. L. Hansen, E. Skordalakes, J. M. Berger, and S. R. Quake, *Proceedings of the National Academy of Sciences*, 2002, **99**, 16531.
119. C. Hansen and S. R. Quake, *Current opinion in structural biology*, 2003, **13**, 538–544.
120. B. Zheng, J. D. Tice, and R. F. Ismagilov, *Advanced Materials*, 2004, **16**, 1365–1368.
121. C. L. Hansen, S. Classen, J. M. Berger, and S. R. Quake, *J. Am. Chem. Soc.*, 2006, **128**, 3142–3143.
122. B. Zheng, J. Tice, L. Roach, and R. Ismagilov, *Angewandte Chemie (International ed. in English)*, 2004, **43**, 2508.
123. J. D. Ng, P. J. Clark, R. C. Stevens, and P. Kuhn, *Acta Cryst (2008). D64*, 189–197 [[doi:10.1107/S0907444907060064](https://doi.org/10.1107/S0907444907060064)], 2008, 1–9.
124. J. Leng and J.-B. Salmon, *Lab Chip*, 2009, **9**, 24.
125. S. Emamzadah, T. J. Petty, V. De Almeida, T. Nishimura, J. Joly, J.-L. Ferrer, and T. D. Halazonetis, *Acta Cryst (2009). D65*, 913–920 [[doi:10.1107/S0907444909021489](https://doi.org/10.1107/S0907444909021489)], 2009, 1–8.
126. L. Li and R. F. Ismagilov, *Annu. Rev. Biophys.*, 2010, **39**, 139–158.
127. S. L. P. A. S. P. S. K. N. A. P. J. A. K. S Guha, 2011, 1–3.
128. M. Maeki, S. Yoshizuka, H. Yamaguchi, M. Kawamoto, K. Yamashita, H. Nakamura, M. Miyazaki, and H. Maeda, *Anal Sci*, 2012, **28**, 65.
129. J. B. Knight, A. Vishwanath, J. P. Brody, and R. H. Austin, *Phys. Rev. Lett.*, 1998, **80**, 3863–3866.
130. T. Pfohl, A. Otten, S. Köster, R. Dootz, B. Struth, and H. M. Evans, *Biomacromolecules*, 2007, **8**, 2167–2172.
131. S. Köster, H. M. Evans, J. Y. Wong, and T. Pfohl, *Biomacromolecules*, 2008, **9**, 199–207.
132. M. E. Brennich, J.-F. Nolting, C. Dammann, B. Nöding, S. Bauch, H. Herrmann, T. Pfohl, and S. Köster, *Lab Chip*, 2011, **11**, 708.
133. C. Reich, M. B. Hochrein, B. Krause, and B. Nickel, *Rev. Sci. Instrum.*, 2005, **76**, 095103.
134. T. Pfohl, F. Mugele, R. Seemann, and S. Herminghaus, *ChemPhysChem*, 2003, **4**, 1291–1298.
135. M. Trebbin, S. With, A. Mark, C. Hanske, A. Buffet, G. Santoro, S. Yu, J. Perlich, S. V. Roth, and S. Förster, *in preparation*, 2013.
136. M. Trebbin, K. Krüger, D. DePonte, J. Schulz, S. V. Roth, H. N. Chapman, and S. Förster, *in preparation*, 2013.
137. J. Thiele, M. Windbergs, A. R. Abate, M. Trebbin, H. C. Shum, S. Förster, and D. A. Weitz, *Lab Chip*, 2011, **11**, 2362.

138. T. Vad, J. Wulfhorst, T.-T. Pan, W. Steinmann, S. Dabringhaus, M. Beckers, G. Seide, T. Gries, W. F. C. Sager, M. Heidelmann, and T. E. Weirich, *Macromolecules*, 2013, 130705124618000.
139. H. M. Evans, R. Dootz, S. Koester, B. Struth, and T. Pfohl, *Bull Pol Acad Sci-Te*, 2007, **55**, 217–227.
140. R. Dootz, A. Otten, S. Köster, B. Struth, and T. Pfohl, *J. Phys.: Condens. Matter*, 2006, **18**, S639–S652.
141. R. Barrett, M. Faucon, J. Lopez, G. Cristobal, F. Destremaut, A. Dodge, P. Guillot, P. Laval, C. Masselon, and J.-B. Salmon, *Lab Chip*, 2006, **6**, 494–499.
142. C. Riekel, *J Synchrotron Rad*, 2004, **11**, 4–6.
143. Benecke, G. Li, C. Roth, S. V. Körstgens, V. Müller-Buschbaum, P. Gehrke, R. Rothkirch, A. Kracht, T. Paris, O. Aichmayer, B. Gourrier, A. Burghammer, M. Thiele, J. Trebbin, M. With, S. Körstgens, V. Rawolle, M. Herzog, G. Schwartzkopf, M. Buffet, A. Perlich, J. Müller-Buschbaum, P. Förster, S. R. C. Fratzl, and P., *DESY HASYLA Photon Science Report*, 2011, 1–2.
144. S. Förster, L. Apostol, and W. Bras, *J. Appl. Cryst.* (2010). **43**, 639–646 [[doi:10.1107/S0021889810008289](https://doi.org/10.1107/S0021889810008289)], 2010, 1–8.
145. D. Pontoni, J. Bolze, N. Dingenouts, T. Narayanan, and M. Ballauff, *J. Phys. Chem. B*, 2003, **107**, 5123–5125.
146. B. Abécassis, F. Testard, and O. Spalla, *Phys. Rev. Lett.*, 2008, **100**.
147. J. N. Lee, C. Park, and G. M. Whitesides, *Anal. Chem.*, 2003, **75**, 6544–6554.
148. S. Begolo, G. Colas, J.-L. Viovy, and L. Malaquin, *Lab Chip*, 2011, **11**, 508.
149. P. Wägli, A. Homsy, and N. F. de Rooij, *Sensors and Actuators B: Chemical*, 2011, **156**, 994–1001.
150. E. Sollier, C. Murray, P. Maoddi, and D. Di Carlo, *Lab Chip*, 2011, **11**, 3752.
151. A. Perl, D. N. Reinhoudt, and J. Huskens, *Advanced Materials*, 2009, **21**, 2257–2268.
152. D. C. Trimbach, H. Stapert, J. van Orselen, K. D. Jandt, C. W. M. Bastiaansen, and D. J. Broer, *Adv. Eng. Mater.*, 2007, **9**, 1123–1128.
153. J. Foley, H. Schmid, R. Stutz, and E. Delamarche, *Langmuir*, 2005, **21**, 11296–11303.
154. J. Tien, C. Nelson, and C. Chen, *Proceedings of the National Academy of Sciences*, 2002, **99**, 1758–1762.
155. H. Song, D. Chen, and R. Ismagilov, *Angewandte Chemie (International ed. in English)*, 2006.
156. A. R. Abate, S. Seiffert, A. S. Utada, A. Shum, R. Shah, J. Thiele, W. J. Duncanson, A. Abbaspourad, M. H. Lee, and I. Akartuna, 2007.
157. A. R. Abate, D. Lee, T. Do, C. Holtze, and D. A. Weitz, *Lab Chip*, 2008, **8**, 516.
158. A. R. Abate, D. Lee, C. Holtze, A. Krummel, and W. D. Do T, *Lab-on-a-Chip Technology: Fabrication and Microfluidics*, Caister Academic Press, 2009.
159. W.-A. C. Bauer, M. Fischlechner, C. Abell, and W. T. S. Huck, *Lab Chip*, 2010, **10**, 1814.
160. H. P. Martin, N. J. Brooks, J. M. Seddon, N. J. Terrill, P. F. Luckham, A. J. Kowalski, and J. T. Cabral, *J. Phys.: Conf. Ser.*, 2010, **247**, 012050.

161. B. Chu and B. S. Hsiao, *Chem. Rev.*, 2001, **101**, 1727–1762.
162. A. S. Utada, E. Lorenceau, D. R. Link, P. D. Kaplan, H. A. Stone, and D. A. Weitz, *Science*, 2005, **308**, 537–541.
163. K. Dhouib, C. Khan Malek, W. Pfleging, B. Gauthier-Manuel, R. Duffait, G. Thuillier, R. Ferrigno, L. Jacquemet, J. Ohana, J.-L. Ferrer, A. Théobald-Dietrich, R. Giegé, B. Lorber, and C. Sauter, *Lab Chip*, 2009, **9**, 1412.
164. R. Suriano, A. Kuznetsov, S. M. Eaton, R. Kiyan, G. Cerullo, R. Osellame, B. N. Chichkov, M. Levi, and S. Turri, *Applied Surface Science*, 2011, **257**, 6243–6250.
165. R. Dootz, H. Evans, S. Köster, and T. Pfohl, *Small*, 2007, **3**, 96–100.
166. D. Bartolo, G. Degré, P. Nghe, and V. Studer, *Lab Chip*, 2008, **8**, 274–279.
167. P. Wägli, A. Homsy, and N. F. de Rooij, *Procedia Engineering*, 2010, **5**, 460–463.
168. C. F. Carlborg, T. Haraldsson, K. Öberg, M. Malkoch, and W. van der Wijngaart, *Lab Chip*, 2010, **11**, 3136.
169. H. Becker and C. Gärtner, *Electrophoresis*, 2000, **21**, 12–26.
170. H. Becker and U. Heim, *Sensors and Actuators A: Physical*, 2000, **83**, 130–135.
171. D. A. Mair, E. Geiger, A. P. Pisano, J. M. J. Fr chet, and F. Svec, *Lab Chip*, 2006, **6**, 1346.
172. H. Becker and C. Gärtner, *Anal Bioanal Chem*, 2007, **390**, 89–111.
173. S. Miserere, G. Mottet, V. Taniga, S. Descroix, J.-L. Viovy, and L. Malaquin, *Lab Chip*, 2012, **12**, 1849.
174. R. Mukhopadhyay, *Anal. Chem.*, 2007, **79**, 3248–3253.
175. E. W. K. Young, E. Berthier, D. J. Guckenberger, E. Sackmann, C. Lamers, I. Meyvantsson, A. Huttenacher, and D. J. Beebe, *Anal. Chem.*, 2011, **83**, 1408–1417.
176. J. P. Lafleur, D. Snakenborg, S. S. Nielsen, M. Moller, K. N. Toft, A. Menzel, J. K. Jacobsen, B. Vestergaard, L. Arleth, and J. P. Kutter, *J. Appl. Cryst. (2011)*. **44**, 1090–1099 [[doi:10.1107/S0021889811050068J](https://doi.org/10.1107/S0021889811050068)], 2011, 1–10.
177. F. Bundgaard, G. Perozziello, and O. Geschke, *Proceedings of the Institution of Mechanical Engineers, Part C: Journal of Mechanical Engineering Science*, 2006, **220**, 1625–1632.
178. T. S. Hansen, D. Selmeczi, and N. B. Larsen, *J. Micromech. Microeng.*, 2009, **20**, 015020.
179. K. N. Toft, B. Vestergaard, S. S. Nielsen, D. Snakenborg, M. G. Jeppesen, J. K. Jacobsen, L. Arleth, and J. P. Kutter, *Anal. Chem.*, 2008, **80**, 3648–3654.
180. J. Steigert, S. Haeberle, T. Brenner, C. Müller, C. P. Steinert, P. Koltay, N. Gottschlich, H. Reinecke, J. Rühe, R. Zengerle, and J. Ducrée, *J. Micromech. Microeng.*, 2007, **17**, 333–341.
181. K. Ren, W. Dai, J. Zhou, J. Su, and H. Wu, *Proceedings of the National Academy of Sciences*, 2011, **108**, 8162.
182. G. S. Fiorini, R. M. Lorenz, J. S. Kuo, and D. T. Chiu, *Anal. Chem.*, 2004, **76**, 4697–4704.
183. G. S. Fiorini and D. T. Chiu, *Biotech.*, 2005, **38**, 429–446.
184. P. S. Nunes, P. D. Ohlsson, O. Ordeig, and J. P. Kutter, *Microfluid Nanofluid*, 2010, **9**, 145–161.

185. V. Sunkara, D.-K. Park, H. Hwang, R. Chantiwas, S. A. Soper, and Y.-K. Cho, *Lab Chip*, 2011, **11**, 962.
186. X. Illa, O. Ordeig, D. Snakenborg, A. Romano-Rodríguez, R. G. Compton, and J. P. Kutter, *Lab Chip*, 2010, **10**, 1254.
187. O. Gustafsson, K. B. Mogensen, and J. P. Kutter, *Electrophoresis*, 2008, **29**, 3145–3152.
188. D. Khvostichenko, E. Kondrashkina, S. L. Perry, A. Pawate, K. Brister, and P. J. A. Kenis, *Analyst*, 2013.
189. R. K. Jena and C. Y. Yue, *Biomicrofluidics*, 2012.
190. G. L. Hura, A. L. Menon, M. Hammel, R. P. Rambo, F. L. Poole II, S. E. Tsutakawa, F. E. Jenney Jr, S. Classen, K. A. Frankel, R. C. Hopkins, S.-J. Yang, J. W. Scott, B. D. Dillard, M. W. W. Adams, and J. A. Tainer, *Nat Meth*, 2009, **6**, 606–612.
191. V. V. Volkov and D. I. Svergun, *J Appl Crystallogr*, 2003, **36**, 860–864.
192. M. V. Petoukhov and D. I. Svergun, *Current opinion in structural biology*, 2007, **17**, 562–571.
193. G. David and J. Pérez, *J Appl Crystallogr*, 2009, **42**, 892–900.
194. Z. Noroozi, H. Kido, R. Peytavi, R. Nakajima-Sasaki, A. Jasinskas, M. Micic, P. L. Felgner, and M. J. Madou, *Rev. Sci. Instrum.*, 2011, **82**, 064303.
195. Q. Pu, O. Oyesanya, B. Thompson, S. Liu, and J. C. Alvarez, *Langmuir*, 2007, **23**, 1577–1583.
196. H. N. Chapman, A. Barty, M. J. Bogan, S. Boutet, M. Frank, S. P. Hau-Riege, S. Marchesini, B. W. Woods, S. Bajt, and W. H. Benner, *Nature Physics*, 2006, **2**, 839–843.
197. J. Kern, R. Alonso-Mori, J. Hellmich, R. Tran, J. Hattne, H. Laksmono, C. Glockner, N. Echols, R. G. Sierra, J. Sellberg, B. Lassalle-Kaiser, R. J. Gildea, P. Glatzel, R. W. Grosse-Kunstleve, M. J. Latimer, T. A. McQueen, D. DiFiore, A. R. Fry, M. Messerschmidt, A. Miahnahri, D. W. Schafer, M. M. Seibert, D. Sokaras, T. C. Weng, P. H. Zwart, W. E. White, P. D. Adams, M. J. Bogan, S. Boutet, G. J. Williams, J. Messinger, N. K. Sauter, A. Zouni, U. Bergmann, J. Yano, and V. K. Yachandra, *PNAS*, 2012, **109**, 9721–9726.
198. S. Boutet, L. Lomb, G. J. Williams, T. R. M. Barends, A. Aquila, R. B. Doak, U. Weierstall, D. P. DePonte, J. Steinbrener, R. L. Shoeman, M. Messerschmidt, A. Barty, T. A. White, S. Kassemeyer, R. A. Kirian, M. M. Seibert, P. A. Montanez, C. Kenney, R. Herbst, P. Hart, J. Pines, G. Haller, S. M. Gruner, H. T. Philipp, M. W. Tate, M. Hromalik, L. J. Koerner, N. van Bakel, J. Morse, W. Ghonsalves, D. Arnlund, M. J. Bogan, C. Caleman, R. Fromme, C. Y. Hampton, M. S. Hunter, L. C. Johansson, G. Katona, C. Kupitz, M. Liang, A. V. Martin, K. Nass, L. Redecke, F. Stellato, N. Timneanu, D. Wang, N. A. Zatsepin, D. Schafer, J. Defever, R. Neutze, P. Fromme, J. C. H. Spence, H. N. Chapman, and I. Schlichting, *Science*, 2012, **337**, 362–364.
199. A. Aquila, M. S. Hunter, R. B. Doak, R. A. Kirian, P. Fromme, T. A. White, J. Andreasson, D. Arnlund, S. Bajt, T. R. M. Barends, M. Barthelmess, M. J. Bogan, C. Bostedt, H. Bottin, J. D. Bozek, C. Caleman, N. Coppola, J. Davidsson, D. P. DePonte, V. Elser, S. W. Epp, B. Erk, H. Fleckenstein, L. Foucar, M. Frank, R.

- Fromme, H. Graafsma, I. Grotjohann, L. Gumprecht, J. Hajdu, C. Y. Hampton, A. Hartmann, R. Hartmann, S. Hau-Riege, G. Hauser, H. Hirsemann, P. Holl, J. M. Holton, A. Hömke, L. Johansson, N. Kimmel, S. Kassemeyer, F. Krasniqi, K.-U. Kühnel, M. Liang, L. Lomb, E. Malmerberg, S. Marchesini, A. V. Martin, F. R. N. C. Maia, M. Messerschmidt, K. Nass, C. Reich, R. Neutze, D. Rolles, B. Rudek, A. Rudenko, I. Schlichting, C. Schmidt, K. E. Schmidt, J. Schulz, M. M. Seibert, R. L. Shoeman, R. Sierra, H. Soltau, D. Starodub, F. Stellato, S. Stern, L. Strüder, N. Timneanu, J. Ullrich, X. Wang, G. J. Williams, G. Weidenspointner, U. Weierstall, C. Wunderer, A. Barty, J. C. H. Spence, and H. N. Chapman, *Optics Express*, 2012, **20**, 2706–2716.
200. M. J. Bogan, W. H. Benner, S. Boutet, U. Rohner, M. Frank, A. Barty, M. M. Seibert, F. Maia, S. Marchesini, S. Bajt, B. Woods, V. Riot, S. P. Hau-Riege, M. Svenda, E. Marklund, E. Spiller, J. Hajdu, and H. N. Chapman, *Nano Lett.*, 2008, **8**, 310–316.
201. A. M. Gañán-Calvo, *Phys. Rev. Lett.*, 1998, **80**, 285–288.
202. A. J. Acero, C. Ferrera, J. M. Montanero, and A. M. Gañán-Calvo, *J. Micromech. Microeng.*, 2012, **22**, 065011.
203. D. P. DePonte, R. B. Doak, M. Hunter, Z. Liu, U. Weierstall, and J. C. H. Spence, *Micron*, 2009, **40**, 507–509.
204. U. Weierstall, J. C. H. Spence, and R. B. Doak, *Rev. Sci. Instrum.*, 2012, **83**, 035108.
205. J. M. Montanero, A. M. Gañán-Calvo, A. J. Acero, and E. J. Vega, *J. Micromech. Microeng.*, 2010, **20**, 075035.
206. E. J. Vega, J. M. Montanero, M. A. Herrada, and A. M. Gañán-Calvo, *Phys. Fluids*, 2010, **22**, 064105.
207. M. A. Herrada, A. M. Gañán-Calvo, A. Ojeda-Monge, B. Bluth, and P. Riesco-Chueca, *Phys. Rev. E*, 2008, **78**, 036323.
208. S. Förster and T. Plantenberg, *Angew. Chem. Int. Ed.*, 2002, **41**.
209. D. L. Stein and P. W. Anderson, *Self-organizing systems*, Plenum Press, New York, 1987.
210. J. Falbe and M. Regnitz, *Römpf Lexikon Chemie*, Thieme, Stuttgart, 1996.
211. *Lexikon der Biologie*, Spektrum, Heidelberg, 2000.
212. S. Domes, University of Hamburg, 2007.
213. M. Baerns, A. Behr, A. Brehm, J. Gmehling, H. Hofmann, U. Onken, and A. Renken, *Technische Chemie*, 2006.
214. *COMSOL Multiphysics CFD Module User's Guide v4.2a*, COMSOL, Göttingen, 2011.
215. V. Girault and P. RAVIART, *Berlin and New York*, 1986.
216. J. Hulin, L. Petit, C. Mitescu, and E. Guyon, *Oxford University Press*, 2001.
217. T. J. Chung, *Computational Fluid Dynamics*, Cambridge University Press, 2002.
218. G. Kammel, H. Franeck, and H. G. Recke, *Einführung in die Methode der finiten Elemente*, Carl Hanser Verlag, 1990.
219. P. Wesseling, *Principles of Computational Fluid Dynamics*, Springer, 2000.
220. O. C. Zienkiewicz and R. L. Taylor, *The Finite Element Method*, Butterworth Heinemann, 2000.
221. T. Kunze, *Hauptseminar, Technische Universität Dresden*, 2006, 1–1.

222. J. Thiele, University of Bayreuth, 2011.
223. G. K. Batchelor, *An Introduction to Fluid Dynamics*, Cambridge University Press, 1967.
224. D. J. Beebe, G. A. Mensing, and G. M. Walker, *Annu. Rev. Biomed. Eng.*, 2002, **4**, 261–286.
225. C. Cottin-Bizonne, J. Barrat, L. Bocquet, and E. Charlaix, *Nat. Mater.*, 2003, **2**, 237–240.
226. J. Brody, P. Yager, R. Goldstein, and R. Austin, *Biophys. J.*, 1996, **71**, 3430–3441.
227. E. Lauga, M. P. BRENNER, and H. A. Stone, *arXiv preprint cond-mat/0501557*, 2005.
228. J. Baudry, E. Charlaix, A. Tonck, and D. Mazuyer, *Langmuir*, 2001, **17**, 5232–5236.
229. L. Bocquet and J. Barrat, *Phys. Rev. E: Stat. Phys.*, 1994.
230. R. Dootz, Georg-August-Universität zu Göttingen, 2008.
231. C. Cottin-Bizonne, S. Jurine, J. Baudry, J. Crassous, F. Restagno, and E. Charlaix, *Eur. Phys. J. E*, 2002, **9**, 47–53.
232. C. Neto, D. R. Evans, E. Bonaccurso, H.-J. Butt, and V. S. J. Craig, *Rep. Prog. Phys.*, 2005, **68**, 2859–2897.
233. D. Tretheway and C. Meinhart, *Phys. Fluids*, 2002, **14**, L9.
234. T. Thorsen, R. W. Roberts, F. H. Arnold, and S. R. Quake, *Phys. Rev. Lett.*, 2001, **86**, 4163–4166.
235. L. Locascio, W. Vreeland, A. Jahn, and M. Gaitan, *Lab-on-Chips for Cellomics: Micro and Nanotechnologies for ...*, 2007.
236. D. Gräßner, M. Gradzielski, and I. Grillo, 2001, 74–75.
237. S. Köster, J. Leach, B. Struth, T. Pfohl, and J. Wong, *Langmuir*, 2007, **23**, 357–359.
238. B. Weinhausen and S. Köster, *Lab Chip*, 2012, **13**, 212.
239. I. Shestopalov, J. D. Tice, and R. F. Ismagilov, *Lab Chip*, 2004, **4**, 316–321.
240. S. Köster, D. Steinhauser, and T. Pfohl, *J. Phys.: Condens. Matter*, 2005, **17**, S4091–S4104.
241. L. E. Rodd, T. P. Scott, D. V. Boger, J. J. Cooper-White, and G. H. McKinley, *Journal of Non-Newtonian Fluid Mechanics*, 2005, **129**, 1–22.
242. M. S. N. Oliveira, M. A. Alves, F. T. Pinho, and G. H. McKinley, *Exp Fluids*, 2007, **43**, 437–451.
243. M. S. N. Oliveira, L. E. Rodd, G. H. McKinley, and M. A. Alves, *Microfluid Nanofluid*, 2008, **5**, 809–826.
244. C. J. Pipe and G. H. McKinley, *Mechanics Research Communications*, 2009, **36**, 110–120.
245. S. J. Haward, T. J. Ober, M. S. N. Oliveira, M. A. Alves, and G. H. McKinley, *Soft Matter*, 2011, **8**, 536.
246. M. Cromer, L. P. Cook, and G. H. McKinley, *Journal of Non-Newtonian Fluid Mechanics*, 2011, **166**, 180–193.
247. K. S. Cole and R. H. Cole, *J. Chem. Phys.*, 1941, **9**, 341.
248. K. S. Cole, *J. Chem. Phys.*, 1942, **10**, 98.
249. M. M. Cross, *J Coll Sci Imp U Tok*, 1965, **20**, 417–437.
250. S. J. Leib and M. E. Goldstein, *Phys. Fluids*, 1986, **29**, 952–954.
251. S. J. Leib and M. E. Goldstein, *J. Fluid Mech.*, 1986, **168**, 479–500.

252. S. Förster, S. Fischer, K. Zielske, C. Schellbach, M. Sztucki, P. Lindner, and J. Perlich, *Advances in Colloid and Interface Science*, 2011, **163**, 53–83.
253. P. Lindner and T. Zemb, *Neutrons, X-rays and Light. Scattering Methods applied to Soft Condensed Matter*, Elsevier, 2002.
254. H. C. Hulst, *Light Scattering of Small Particles*, Wiley, New York, 1969.
255. L. A. Feigin and G. I. Svergun, *Structure Analysis by Small-Angle X-ray and Neutron Scattering*, Plenum Press, New York, 1987.
256. J. S. Higgins and H. Benoit, *Polymers and Neutron Scattering*, Clarendon Press, Oxford, 1994.
257. A. Guinier and G. Fournet, *Small-Angle Scattering of X-rays*, Wiley, Ney York, 1955.
258. M. Konrad, University of Hamburg, 2003.
259. M. Dulle, University of Graz, 2012.
260. K. Zielske, University of Hamburg, 2009.
261. S. Fischer, University of Hamburg, 2009.
262. U. Lipprandt, University of Hamburg, 2004.
263. T. Plantenberg, University of Hamburg, 2001.
264. P. Debye, *Ann. Phys.*, 1915, **351**, 809–823.
265. D. I. Svergun, *J Appl Crystallogr*, 1991, **24**, 485–492.
266. O. Glatter, *J Appl Crystallogr*, 1980, **13**, 7–11.
267. O. Glatter, *J Appl Crystallogr*, 1980, **13**, 577–584.
268. O. Glatter, *J Appl Crystallogr*, 1979, **12**, 166–175.
269. O. Glatter, *J Appl Crystallogr*, 1977, **10**, 415–421.
270. O. Glatter, *Acta Physica Austriaca*, 1977, **47**, 83–102.
271. O. Glatter and B. Hainisch, *J Appl Crystallogr*, 1984, **17**, 435–441.
272. O. Glatter, *J Appl Crystallogr*, 1981, **14**, 101–108.
273. S. Förster, MPI für Kolloid- und Grenzflächenforschung, 1999.
274. W. Burchard, *Polymer Characterization: Rheology, Laser Interferometry, Electrooptics*, 1983, **48**, 1–124.
275. J. S. Pedersen, *Advances in Colloid and Interface Science*, 1997, **70**, 171–210.
276. L. Rayleigh, 1914.
277. O. Kratky and G. Porod, *J Coll Sci Imp U Tok*, 1949, **4**, 35–70.
278. T. Neugebauer, *Ann. Phys.*, 1943, **434**, 509–533.
279. O. Kratky and G. Porod, *Recueil Des Travaux Chimiques Des Pays-Bas-Journal of the Royal Netherlands Chemical Society*, 1949, **68**, 1106–1122.
280. S. Förster and C. Burger, *Macromolecules*, 1998, **31**, 879–891.
281. B. Weyerich, J. Brunner-Popela, and O. Glatter, *J Appl Crystallogr*, 1999, **32**, 197–209.
282. J. Brunner-Popela and O. Glatter, *J Appl Crystallogr*, 1997, **30**, 431–442.
283. C. Giacovazzo, *Fundamentals of Crystallography*, Oxford University Press, 1992.
284. P. Van der Schoot, *Macromolecules*, 1992, **25**, 2923–2927.
285. J. Voldman, M. Gray, and M. Schmidt, *Annu. Rev. Biomed. Eng.*, 1999, **1**, 401–425.
286. K. Raiber, Universität Hamburg, 2005.
287. Y. Xia, Harvard University, 1996.

288. M. E. Sandison and H. Morgan, *J. Micromech. Microeng.*, 2005, **15**, S139–S144.
289. K. Y. Lee, *J. Vac. Sci. Technol. B*, 1995, **13**, 3012.
290. M. M. A. A. K. Mohamed, 2010, 1–26.
291. J. Simčič, P. Pelicon, Z. Rupnik, M. Mihelič, A. Razpet, D. Jenko, and M. Maček, *Nuclear Instruments and Methods in Physics Research Section B: Beam Interactions with Materials and Atoms*, 2005, **241**, 479–485.
292. C. G. Khan Malek, *Microelectronics Journal*, 2002, **33**, 101–105.
293. J. Zhang, K. Tan, G. Hong, L. Yang, and H. Gong, *J. Micromech. Microeng.*, 2001, **11**, 20–26.
294. J. Zhang, K. Tan, and H. Gong, *Polym. Test.*, 2001, **20**, 693–701.
295. Y. Wang, M. Bachman, C. Sims, G. Li, and N. Allbritton, *Langmuir*, 2006, **22**, 2719–2725.
296. J. Dektar and N. Hacker, *J. Am. Chem. Soc.*, 1990, **112**, 6004–6015.
297. *MicroChem NANOTM SU-8 Organic Resin Solution, MSDS, 12.12.2001, www.cise.columbia.edu/clean/msds/su-8resist.pdf (1.07.2013)*, 2009.
298. Y. Wang, J.-H. Pai, H.-H. Lai, C. E. Sims, M. Bachman, G. P. Li, and N. L. Allbritton, *J. Micromech. Microeng.*, 2007, **17**, 1371–1380.
299. Guerin, L. *The SU-8 homepage, http://www.geocities.com/guerinlj/ (17.07.2008)*. 2009.
300. X. Yan and P. Gu, *Computer-Aided Design*, 1996.
301. E. Sachs, S. Allen, H. Guo, and B. Banos, 1997.
302. E. Sachlos and J. T. Czernuszka, *Eur Cell Mater*, 2003.
303. C. M. Cheah, C. K. Chua, C. W. Lee, C. Feng, and K. Totong, *Int J Adv Manuf Technol*, 2004, **25**, 308–320.
304. A. Khademhosseini, *PNAS*, 2006, **103**, 2480–2487.
305. C. J. Campbell, S. K. Smoukov, K. J. M. Bishop, E. Baker, and B. A. Grzybowski, *Advanced Materials*, 2006, **18**, 2004–2008.
306. P. J. Kitson, M. H. Rosnes, V. Sans, V. Dragone, and L. Cronin, *Lab Chip*, 2012, **12**, 3267–3271.
307. K. B. Anderson, S. Y. Lockwood, R. S. Martin, and D. M. Spence, *Anal. Chem.*, 2013, **85**, 5622–5626.
308. V. Dragone, V. Sans, M. H. Rosnes, P. J. Kitson, and L. Cronin, *Beilstein J Org Chem*, 2013, **9**, 951–959.
309. Y. Liao, J. Song, E. Li, Y. Luo, Y. Shen, D. Chen, Y. Cheng, Z. Xu, K. Sugioka, and K. Midorikawa, *Lab Chip*, 2012, **12**, 746.
310. A. D. Campo and C. Greiner, *J. Micromech. Microeng.*, 2007, **17**, R81–R95.
311. S. Jeon, J. U. Park, R. Cirelli, S. Yang, C. E. Heitzman, P. V. Braun, P. J. A. Kenis, and J. A. Rogers, *Proceedings of the National Academy of Sciences*, 2004, **101**, 12428.
312. J. A. Lewis and G. M. Gratson, *Materials Today*, 2004, **7**, 32–39.
313. Y. L. Zhang, Q. D. Chen, H. Xia, and H. B. Sun, *Nano Today*, 2010.
314. B. Zimmer, *Nanoscribe GmbH*, 2013, 1–14.
315. *MSDS: Sylgard(R) 184 silicone elastomer kit (base), DOW Corning, v1.5, 2008*, 2008.
316. *MSDS: Sylgard(R) 184 silicone elastomer kit (curing agent), DOW Corning, v1.8, 2007*, 2007.

317. H. Finkelmann and G. Rehage, *Macromol. Rapid Commun.*, 1980, **1**.
318. B. Krucke, H. Zaschke, S. Kostromin, and V. Shibaev, *Acta Polym.*, 1985, **36**.
319. 2007, 1–3.
320. E. Delamarche, A. Bernard, H. Schmid, A. Bietsch, B. Michel, and H. Biebuyck, *J. Am. Chem. Soc.*, 1998, **120**, 500–508.
321. G. M. Whitesides, E. Ostuni, S. Takayama, X. Jiang, and D. Ingber, *Annu. Rev. Biomed. Eng.*, 2001, **3**, 335–373.
322. N. B. Cramer, J. P. Scott, and C. N. Bowman, *Macromolecules*, 2002, **35**, 5361–5365.

6 Individual contribution to joint publications

The results which are presented in the scientific papers of this thesis are based on the collaborative work with others. The contribution of every co-author will be specified in further detail below and the corresponding author will be indicated with an asterisk (*).

Chapter 7.1

This work is *published* in *PNAS*, 2013, **110**, 6706–6711 and featured as a “Technical Highlight” in DESY Photon Science 2011 and on the front pages of the DESY- and Uni Bayreuth web pages; entitled:

“Anisotropic particles align perpendicular to the flow direction in narrow microchannels”.

by Martin Trebbin, Dagmar Steinhauser, Jan Perlich, Adeline Buffet, Stephan V. Roth, Walter Zimmermann, Julian Thiele*, and Stephan Förster*. (shared corresponding authorship)

I performed most of the experiments & data analysis, created the non-linear non-Newtonian flow CFD-simulation model; and wrote the manuscript together with Julian Thiele and Stephan Förster. Dagmar Steinhauser and Julian Thiele helped with the experiments at the synchrotron beamlines at which Jan Perlich, Adeline Buffet and Stephan V. Roth provided the technical support. Walter Zimmermann was involved in scientific discussions and helped with the correction of the manuscript. Further, Stephan Förster supervised the project.

Chapter 7.2

This work is prepared as a manuscript that is *ready for submission*; entitled:

“Microfluidic SAXS for the high-throughput screening and correlation of complex fluid behavior with structural information”.

by Martin Trebbin, Sebastian With, Andres Mark, Christoph Hanske, Adeline Buffet, Gonzalo Santoro, Shun Yu, Jan Perlich, Stephan V. Roth, and Stephan Förster*.

I performed most of the experiments & data analysis, created the non-linear non-Newtonian flow CFD-simulation model and wrote the manuscript. Sebastian With was involved in the device fabrication and helped with the experiments at the synchrotron beamlines at which Adeline Buffet, Gonzalo Santoro, Shun Yu, Jan Perlich, Stephan V. Roth provided the technical support. Andreas Mark was involved in the μ PIV-experiments and their analysis. Christoph Hanske provided the tracer particles for the μ PIV-experiments. Stephan Förster supervised the project and corrected the manuscript.

Chapter 7.3

This work is prepared as a manuscript that is *ready for submission*; entitled:
"Microfluidic Liquid Jet System with compatibility for atmospheric and high-vacuum conditions".
by Martin Trebbin, Kilian Krüger, Daniel DePonte, Stephan V. Roth, Henry N. Chapman, and Stephan Förster*.

I performed most of the experiments & data analysis, created the non-linear two-phase flow CFD-simulation model and wrote the manuscript. Kilian Krüger was involved in the device fabrication, scientific discussions and helped with the experiments. Daniel DePonte, Stephan V. Roth and Henry N. Chapman were involved in scientific discussions and helped with the correction of the manuscript. Further, Daniel DePonte was involved in the ESEM-experiments. Stephan Förster supervised the project and corrected the manuscript.

Chapter 7.4

This paper is *published* in *Soft Matter* 2012, **8**, 12124; entitled:
"Lyotropic phase behavior of polymer-coated iron oxide nanoparticles".
by Sara Mehdizadeh Taheri*, Steffen Fischer, Martin Trebbin, Sebastian With, Jan H. Schröder, Jan Perlich, Stephan V. Roth and Stephan Förster*.

I designed and fabricated the grid-based static microfluidic device using soft lithography. Sara Mehdizadeh Taheri performed most of the experiments & data analysis and wrote the manuscript with Stephan Förster. Further, I helped, together with Sebastian With, Jan H. Schröder with the experiments at the synchrotron beamlines at which Jan Perlich, Stephan V. Roth provided the technical support. Steffen Fischer was involved in the synthesis of polymers and scientific discussions. Stephan Förster supervised the project and corrected the manuscript.

Chapter 7.5

This paper is *published* in *Lab Chip*, 2011, **11**, 2362 and featured in *Chemistry World*; entitled:
"Early development drug formulation on a chip: Fabrication of nanoparticles using a microfluidic spray dryer".
by Julian Thiele, Maike Windbergs, Adam R. Abate, Martin Trebbin, Ho Cheung Shum, Stephan Förster, and David A. Weitz*.

I developed the non-linear FEM-based CFD-simulation model and contributed to the simulation-related writing of the manuscript. Julian Thiele performed most of the experiments and wrote the manuscript. Adam Abate was involved in scientific discussions. Maike Windbergs performed the spray experiments in bulk and was involved in scientific discussions. Ho Cheung Shum conducted the SEM analysis of the drug. Stephan Förster

corrected the manuscript. David Weitz supervised the project. Parts of this work have been submitted for patenting.

Chapter 7.6

This paper is *published* in Nanotechnology 2011, **22**, 305303; entitled:
"Freestanding films of crosslinked gold nanoparticles prepared via layer-by-layer spin-coating".
by Hendrik Schlicke, Jan H. Schröder, Martin Trebbin, Alexey Petrov, Michael Ijeh, Horst Weller and Tobias Vossmeyer*.

I designed and fabricated the microstructures using computer aided design and photolithography, was involved in their microscopy as well as the scientific discussion. Jan H. Schröder performed most of the experiments and wrote the manuscript together with Tobias Vossmeyer. Hendrik Schlicke and Alexey Petrov were involved in the experiments related to the films and the scientific discussions. Michael Ijeh was involved in ligand synthesis. Horst Weller corrected the manuscript. Further, Tobias Vossmeyer supervised the project.

Chapter 7.7

This paper is *published* in *Z. Phys. Chem.* 2012, **226**, 569–584; entitled:
"Adsorption of spherical polyelectrolyte brushes: from interactions to surface patterning".
by Christoph Hanske, Johann Erath, Christin Kühr, Martin Trebbin, Christian Schneider, Alexander Wittemann, and Andreas Fery*.

I produced a specially designed stamp for micro contact printing using soft lithography. Christoph Hanske performed adsorption experiments, the micro contact printing, analyzed these experiments, was involved in scientific discussions, and wrote the manuscript. Johann Erath performed the AFM interaction measurements, analyzed these experiments, was involved in scientific discussions, wrote parts of the manuscript, and corrected the manuscript. Christin Kühr synthesized the SPBs. Christian Schneider synthesized the model particles for SPBs. Alexander Wittemann developed the synthesis protocol for the SPBs, was involved in scientific discussions, wrote parts of the manuscript, and helped correcting the manuscript. Andreas Fery analyzed the results, helped with discussions, and corrected the manuscript.

7 Publications

7.1 Anisotropic particles align perpendicular to flow-direction in narrow microchannels

Martin Trebbin,¹ Dagmar Steinhauser,^{2,3} Jan Perlich,⁴ Stephan V. Roth,⁴
Walter Zimmermann,⁵ Julian Thiele,^{6*} and Stephan Förster^{1*}

¹⁾ Physical Chemistry I, University of Bayreuth, D-95447 Bayreuth, Germany

²⁾ Max-Planck-Institute for Dynamics and Self-Organization, D-37073 Göttingen, Germany

³⁾ Deutsches Institut für Kautschuktechnologie, D-30519 Hannover, Germany

⁴⁾ HASYLAB/DESY, D-22607 Hamburg, Germany

⁵⁾ Theoretical Physics I, University of Bayreuth, D-95447 Bayreuth, Germany

⁶⁾ Radboud University Nijmegen, Institute for Molecules and Materials, NL-6525 AJ, Nijmegen, The Netherlands

The flow orientation of anisotropic particles in narrow channels is of importance in many fields ranging from the spinning and molding of fibers to the flow of cells and proteins through thin capillaries. It is commonly assumed that anisotropic particles align parallel to the flow direction. When flowing through narrowed channel sections one expects the increased flow rate to improve the alignment. Here we show by microfocus synchrotron X-ray diffraction and polarized optical microscopy for the first time that, after passing a narrow channel section, anisotropic colloidal particles align *perpendicular* to the flow-direction. We find this to be a general behaviour of anisotropic colloids, also observed for disk-like particles. The perpendicular alignment is stable, extending throughout the remaining part downstream the channel. We show by micro particle image velocimetry and finite element computational fluid dynamic simulations that the perpendicular orientation is due to the velocity field having large perpendicular gradients in the expansion zone after the narrow section. Shear-thinning, a typical property of anisotropic particles, promotes perpendicular extensional and orientation. Our discovery has important consequences when considering the flow orientation of polymers, micelles, fibers, proteins or cells through narrow channels, pipes or capillary sections. An immediate consequence for the production of fibers is the necessity for realignment by extension in flow direction. For fibrous proteins, reorientation and stable plug-flow are likely mechanisms for protein coagulation.

The flow orientation of anisotropic particles in narrow channels is an issue of relevance in many fields ranging from the spinning and molding of fibers to the flow of cells or proteins through thin capillaries.[1-3] It is commonly assumed that anisotropic particles align parallel to the flow direction.[4] When flowing through thin channel sections one expects the increased flow rate to improve the alignment. We investigated the alignment of anisotropic colloids, i.e. cylindrical micelles, flowing through thin sections of microchannels using synchrotron microfocus small-angle X-ray diffraction and polarized optical microscopy. We surprisingly find that anisotropic colloids orient *perpendicular* to the flow direction after passing through narrow channel sections. The perpendicular alignment is surprisingly stable, extending throughout the remaining part downstream the channel. Ongoing studies indicate that this is generally the case for any anisotropic cylindrical or disk-like colloids. We show by micro particle image velocimetry and finite element numerical computational fluid dynamics simulations that the perpendicular flow orientation is induced by perpendicular extensional flow in the expansion zone after the narrow section. Only close to the channel walls shear flow dominates leading to parallel flow orientation of anisotropic particles.

In-situ investigations of the flow orientation of colloids in solution under very well defined flow conditions have recently become possible with the development of X-ray transparent microfluidic devices and high-brilliance microfocused X-ray beams at dedicated synchrotron beam lines. [5-8] Due to the small channel dimensions, fluid flow in microchannels is mostly laminar even for high flow rates. Under laminar flow conditions there is a well-defined flow velocity profile within the channels. Such conditions are ideal to perform detailed investigations of the flow orientation of anisotropic colloids in various channel geometries.

There are many different types of anisotropic particles that are of high relevance for such studies, including semi-flexible polymer chains, carbon nanotubes, fibrous proteins, rod-like nanoparticles or DNA. [9-13] For our first experiments we chose a particularly well-suited model system for investigating the shear orientation of anisotropic particles, i.e. cylindrical polymer micelles. [14] They possess large axial ratios and their thickness can be adjusted over a wide range from 5 to 50 nm by tailoring the polymer molecular weight. In addition, their bending modulus can be varied and their contour lengths can range from nano- to micrometers. Their orientational distribution can be determined *in-situ* using small-angle X-ray scattering (SAXS) or neutron scattering (SANS) and has been correlated to their rheological properties measured simultaneously using rheo-SANS experiments. [15-17] These studies were performed under Couette-flow. In most cases of technological relevance, however, anisotropic particles are transported using pressure-driven flow. [18,19]

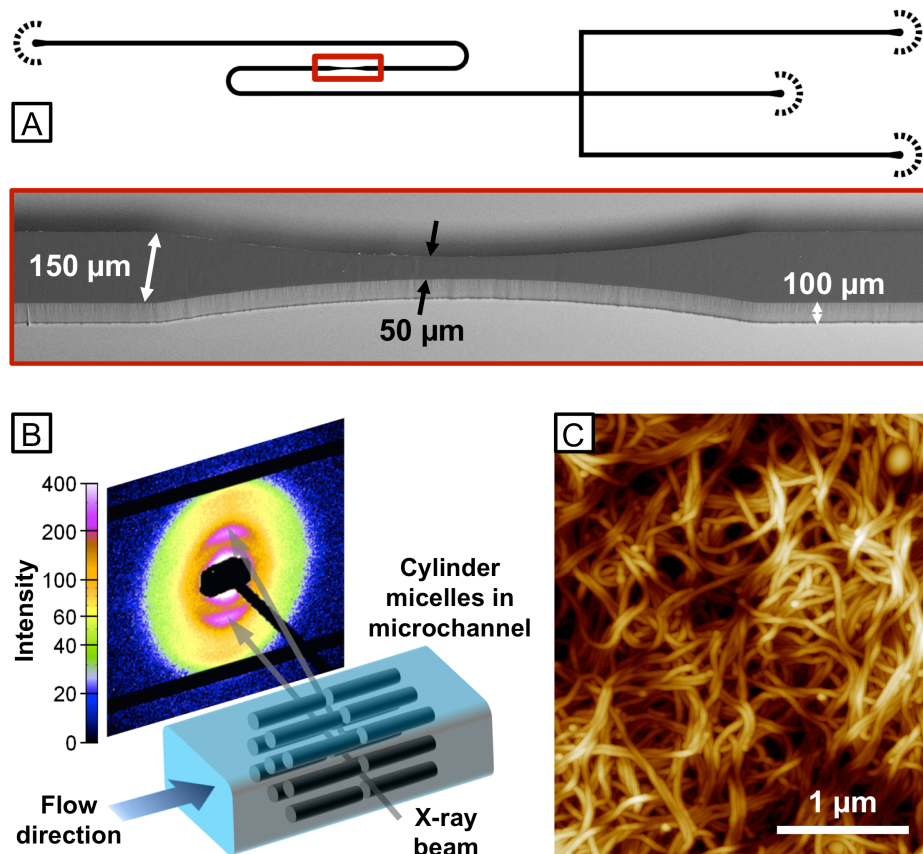


Figure 1. Schematic experimental setup for studying the orientation of cylindrical micelles in microchannels using SAXS. (A) Inverse black/white image of the microfluidic device drawn in AutoCAD 2011 together with an SEM image showing the actual dimensions of the narrow microchannel section. (B) X-ray beam alignment and SAXS pattern measured for a flowing stream of cylindrical micelles in a microchannel. (C) AFM image of an isotropic assembly of the cylindrical micelles used in the present study.

In the present study, we investigate the shear orientation of aqueous solutions of cylindrical block copolymer micelles under pressure-driven flow using specially designed Kapton®- and poly(dimethylsiloxane) PDMS-based X-ray transparent microfluidic devices. We use cylindrical micelles of different types of amphiphilic block copolymers, poly(isoprene-*b*-ethylene oxide) (PI-PEG) and poly(ethylenebutylene-*b*-ethylene oxide) (PEB-PEG), in water at concentrations between 5 - 30 % w/w. In this concentration range the flow orientation of the cylindrical micelles within the channels can be well investigated using polarized optical microscopy and microfocus (20 μm x 30 μm) synchrotron small-angle X-ray scattering (SAXS) as shown in Figure 1. The microfluidic chip design comprises a flow-focusing cross-junction as well as narrow and curved channel sections. The cylindrical micelles have diameters of 25 nm and contour lengths of several micrometers as shown by the AFM-image in Figure 1C.

In our studies we were interested in the orientation behavior of the cylindrical micelles when flowing through channel cross-junctions and narrow as well as curved sections. Figure 2A shows a polarized optical microscopy image of a flowing solution of cylindrical micelles giving

an overview of the observed orientational behavior. Using a quarter wave plate enables us to distinguish between cylindrical micelles oriented horizontally (blue) from vertically oriented micelles (yellow). The orientational distribution of the micelles when passing the T-junction at the beginning of the channel indicates that the development length for complete reorientation is very small, being less than 10 mm. Figures 2B and 2C show the measured X-ray scattering patterns in the curved and narrow sections of the channel. For all scattering patterns, we observe pronounced first-order reflections together with weak second-order reflections corresponding to mutual parallel alignment of the micelles, typical for nematic or hexagonal order. From the radial position of the reflections the average center-to-center distance between adjacent micelles is determined to be 58 nm.

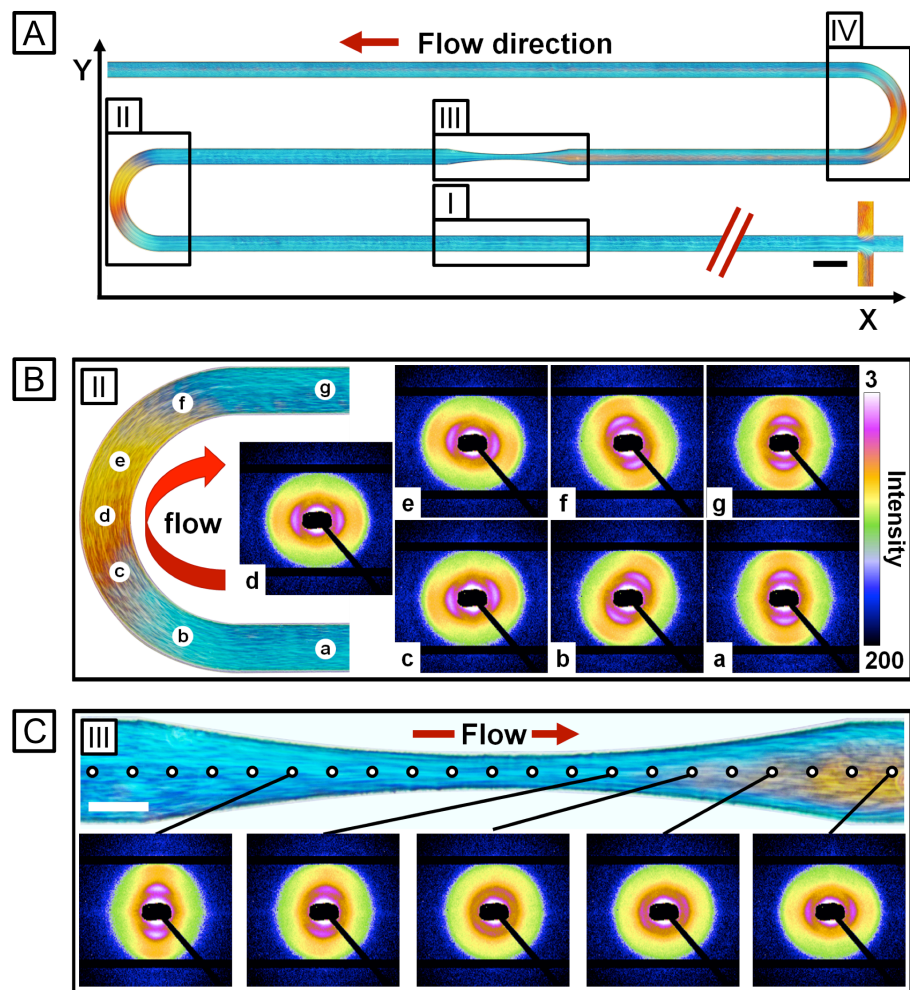


Figure 2. Orientation of cylindrical micelles in curved and narrow sections of a microfluidic device. Upper panel (A): Alignment of an aqueous solution of PI-PEG cylindrical micelles (20 % w/w) at a flow rate of $32.4 \mu\text{m h}^{-1}$ visualized using polarization microscopy. Blue areas indicate orientation of cylindrical micelles parallel to the x -axis, yellow areas indicate orientation parallel to the y -axis. Middle panel (B): Curved microchannel section with measured SAXS-patterns at different channel positions. Lower panel (C): Narrowed microchannel section with measured SAXS-patterns along the center line, showing the surprising *perpendicular* orientation of the cylindrical micelles after passing through the channel tapering. Scale bars denote 100 μm .

In the first straight section I of the microchannel, shown in Figure 2 A, we observe the expected parallel alignment of the cylindrical micelles with respect to the flow direction. When flowing through the curved section II, the micelles remain oriented parallel to the flow direction. This results in a blue → yellow → blue change of the birefringence interference color and a 180° rotation of the azimuthal angle of the first-order Bragg peak, as shown in Figure 2 B. When flowing further into the contraction zone of the narrow section III, the micelles remain aligned in flow direction as indicated by the blue birefringence interference color and the azimuthal positions of the Bragg-peaks, which appear on the meridian of the detector. The azimuthal peak widths become smaller, indicating improved alignment of the micelles in flow direction, as expected.

When scanning with the X-ray beam further downstream into the channel expansion zone, we observe a surprising behavior. First, in a region directly at the exit of the microchannel narrowing, there is no preferred orientation as apparent from the observed Debye-Scherrer rings (Fig. 2 C). Further downstream, the micelles become oriented *perpendicular* to the flow direction. We observe an interference color change from blue to yellow in the polarized microscopy image, and the Bragg-reflections now appear on the equator of the detector. This orientation is stable along the remaining part of the channel and does not even change in the subsequent curved section IV. Only at the channel walls, the wormlike micelles are aligned parallel to the flow direction, as indicated by the blue interference color close to the channel walls. There is a stable, relatively sharp interface between parallel and perpendicular aligned micelles in the remaining downstream part of the channel. When the wormlike micelles are subjected to planar extensional flow in x-direction in a subsequent narrow channel section, they again become aligned in flow direction in the contraction zone and perpendicularly aligned in the expansion zone (see Fig. S5 in the Supporting Information).

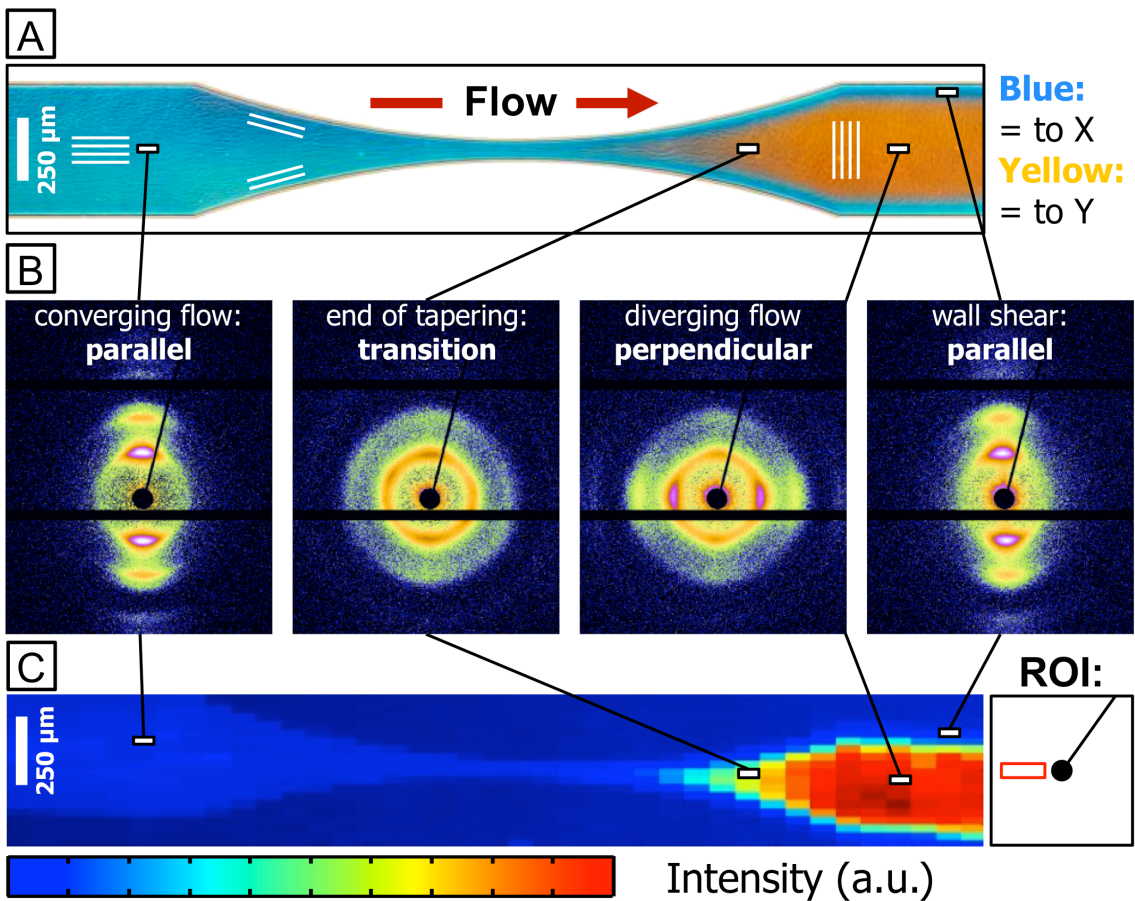


Figure 3. Orientation of PEB-PEG cylindrical micelles determined by scanning microfocus X-ray diffraction. Upper panel (A): Alignment of cylindrical micelles in the narrow section visualized by polarized optical microscopy. Middle panel (B): X-ray diffraction patterns measured at the positions indicated in the upper and lower panels. Lower panel (C): Pixel map of the equatorial intensity of the diffraction patterns at different positions in the channel tapering. The high intensity in the expansion zone corresponds to micelles with orientation perpendicular to the flow direction.

We performed additional synchrotron X-ray measurements to scan the complete contraction/expansion zone of the narrow section to map the orientation of the cylindrical micelles. The results are shown in Figure 3 together with a polarized optical micrograph of the channel section. We indeed find the cylindrical micelles to be oriented parallel to the flow orientation in the expansion zone close to the channel walls (Figure 3B). Here the azimuthal position of the Bragg-reflections is located on the meridian of the diffraction pattern, whereas in the central part of the expansion zone the Bragg-reflections are located on the equator. To compare the results of the microfocus X-ray diffraction scanning experiments to the polarized optical micrographs, we mapped the diffracted intensity on the equatorial region of the diffraction patterns onto the corresponding position of the X-ray beam (Figure 3C). Regions with high equatorial intensity correspond to regions where the micelles are oriented perpendicular to the flow direction. The observed intensity map corresponds very well to the birefringence interference colors in Figure 3A.

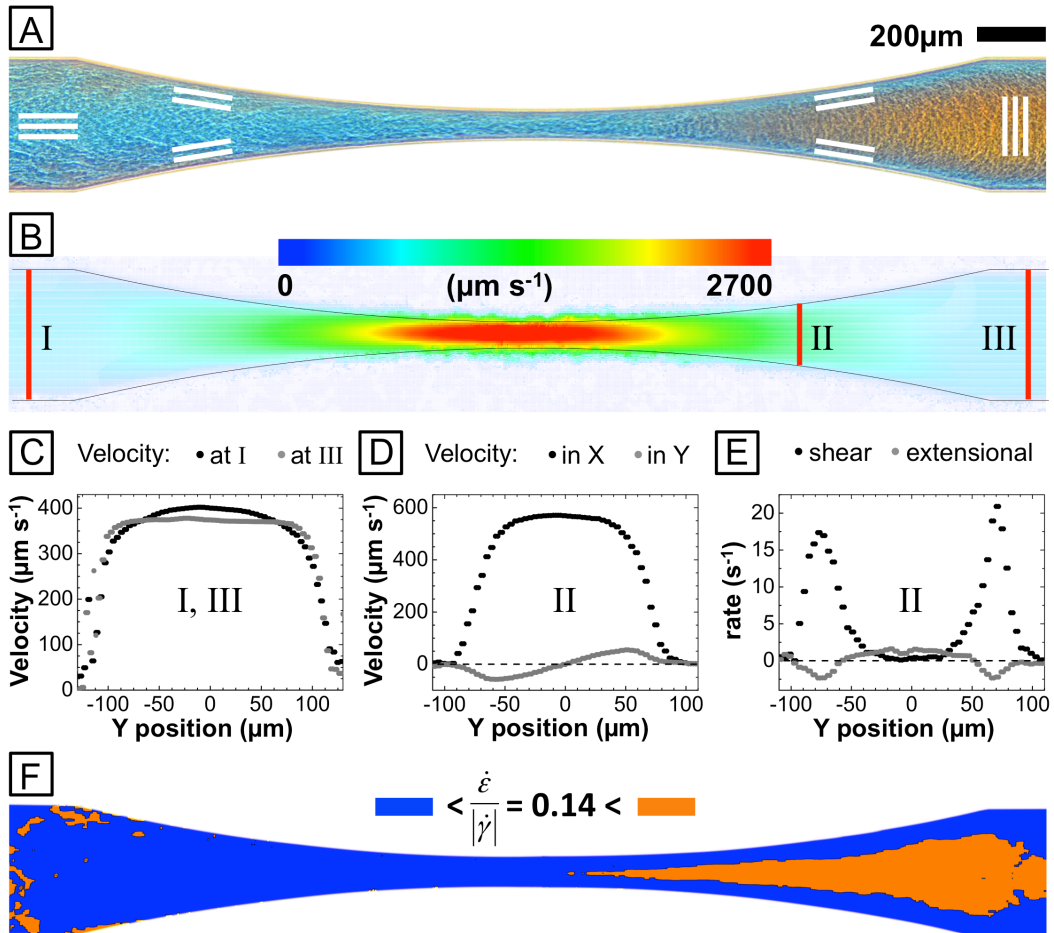


Figure 4. Velocity field $v(x, y)$ of cylindrical micelles measured by micro particle image velocimetry. Upper panel (A): Alignment of cylindrical micelles in the narrow section visualized by polarized optical microscopy. Panel (B): Measured particle velocity in the wide and narrow channel section. (C): Velocity profile $v_x(y)$ in the pre-tapering zone I (●) and post-tapering zone III (○). (D) Velocity profiles $v_x(y)$ (●) and $v_y(y)$ (○) in the expansion zone II. (E) Shear rate $|\dot{\gamma}(y)|$ (●) and extensional rate $\dot{\epsilon}(y)$ (○) in the expansion zone II. (F) Map of the ratio $\dot{\epsilon}/|\dot{\gamma}|$ in the wide and narrow channel section. In the orange regions $\dot{\epsilon}/|\dot{\gamma}| > 0.14$, whereas in the blue regions $\dot{\epsilon}/|\dot{\gamma}| < 0.14$. The resulting color map shows good agreement with polarized optical micrograph in panel (A) and the X-ray intensity map in Fig. 3 C.

We have reproduced this behavior for wormlike polymer micelles of different block copolymers, many different concentrations (5 – 30 % w/w) and different width ratios of the main channel and narrow section diameter (10:1 - 2.5:1) and always found the same behavior. Ongoing experiments on cylindrical micelles with much higher bending rigidity, on disk-like micelles and very flexible surfactant wormlike micelles show that this phenomenon is generally occurring. We have searched the literature for similar observations to find that only recently authors have observed a similar behavior for SDS/CTAC lamellae in a microfluidic test experiment at the Diamond synchrotron light source (U.K.). [8]

If reorientation in perpendicular direction in a channel expansion zone is a general property of anisotropic colloids, it should have its cause in the hydrodynamic flow pattern. Using micro particle image velocimetry we determined the velocity profile $v(x, y)$ in the narrow section as shown in Fig. 4. Entering the channel section, there is first a contraction zone with planar extensional flow in flow (x -) direction, followed by an expansion zone with planar extensional flow in perpendicular (y -) direction. Fig. 4 A shows the polarized optical micrograph of the channel section indicating zones with parallel (blue) and perpendicular (yellow) flow orientation. Fig. 4B shows the measured flow velocity, obtained from velocimetry measurements of added $3.3 \mu\text{m}$ diameter tracer particles. As expected, the flow velocimetry is largest in the narrow section of the channel. Fig. 4 C shows the measured velocity profiles across the channel at position I before entering the contraction zone, and at position III after the expansion zone. The velocity profiles are both non-parabolic, a consequence of the shear-thinning, non-Newtonian flow behavior of the micelles. Both are hydrodynamically stable states, yet having different velocity profiles. The pre-tapering velocity profile at position I has a broad, but clearly noticeable maximum, whereas the post-tapering velocity profile at position III is completely flat, indicating plug flow. The velocity profiles can be switched back and forth in subsequent narrow channels as shown in Fig. S5 (Supporting Information).

Fig. 4 D shows the measured velocity components v_x and v_y across the channel at position II in the expansion zone. From the velocity components the shear rates $\dot{\gamma} = \nabla_y v_x$ and the extensional rates $\dot{\epsilon} = -\nabla_y v_y$ can be calculated and are displayed in Fig. 4 E. We observe that in the middle part of the cross section the extensional rate $\dot{\epsilon}$ is either larger, or at least of comparable magnitude to the shear rate $\dot{\gamma}$. Extensional flows are much more effective in orienting and aligning anisotropic particles compared to shear flows.^[20,21] They lead to reorientation if the extensional rates become comparable to the shear rates. With an internal relaxation time of the cylindrical micelles of $\tau \approx 400 \text{ s}$ as determined from the rheological measurements and extensional rates of $\dot{\epsilon} \approx 2 \text{ s}^{-1}$ (see Figure 4 E), values of the Deborah number are $De = \tau \dot{\epsilon} = 800 \gg 1$. Under these conditions the micelles are highly susceptible for flow-induced alignment. In Fig. 4 F we mapped regions where $\dot{\epsilon}/|\dot{\gamma}| \geq 0.14$ in yellow, and regions where $\dot{\epsilon}/|\dot{\gamma}| < 0.14$ in blue for comparison with the flow birefringence pattern in Fig. 4 A. We note that the near-zero values of v_y in the regions before the contraction zone and after the expansion zone of the channel lead to some scatter of the data. Yet, we observe that by choosing a threshold of $\dot{\epsilon}/|\dot{\gamma}| = 0.14$, regions of high extensional rates in Fig. 4 F agree well with regions of perpendicular orientation in Figs. 3 C and 4 A. At the channel walls shear flow dominates such that $\dot{\epsilon}/|\dot{\gamma}| < 0.14$ and micelles remain oriented in flow-direction as observed experimentally. The beginning of the sharp rise of the shear rate $\dot{\gamma}$ close to the channel wall (see Figure 4 E) defines a relatively sharp transition with a stable interface between zones of perpendicular and parallel cylinder orientation.

To distinguish features of the flow pattern specifically related to particle anisotropy from features related to just channel geometry, we performed numerical computational fluid dynamic (CFD) simulations to calculate shear rates and extensional rates in the contraction/expansion zone. The calculations were done for Newtonian liquids, but also for non-Newtonian, shear-thinning liquids such as solutions of wormlike micelles. Shear-thinning was accounted for by measuring the shear-rate dependent viscosity of the micellar solution using a cone-plate rheometer and fitting the measured flow curve to the Cross equation (see Supporting Information). This equation well describes the measured data und serves to parameterize the flow curve in terms of its high- and low-shear viscosity, the relaxation time and a power-law exponent, which can be implemented in the CFD-simulations. Details of the simulations and the experiment are described in the Supplementary Information. Figure 5 A shows the calculated velocity field $v(x,y)$ for a shear-thinning solution in the contraction/expansion zone for a typical channel geometry and flow rate used in the experiments.

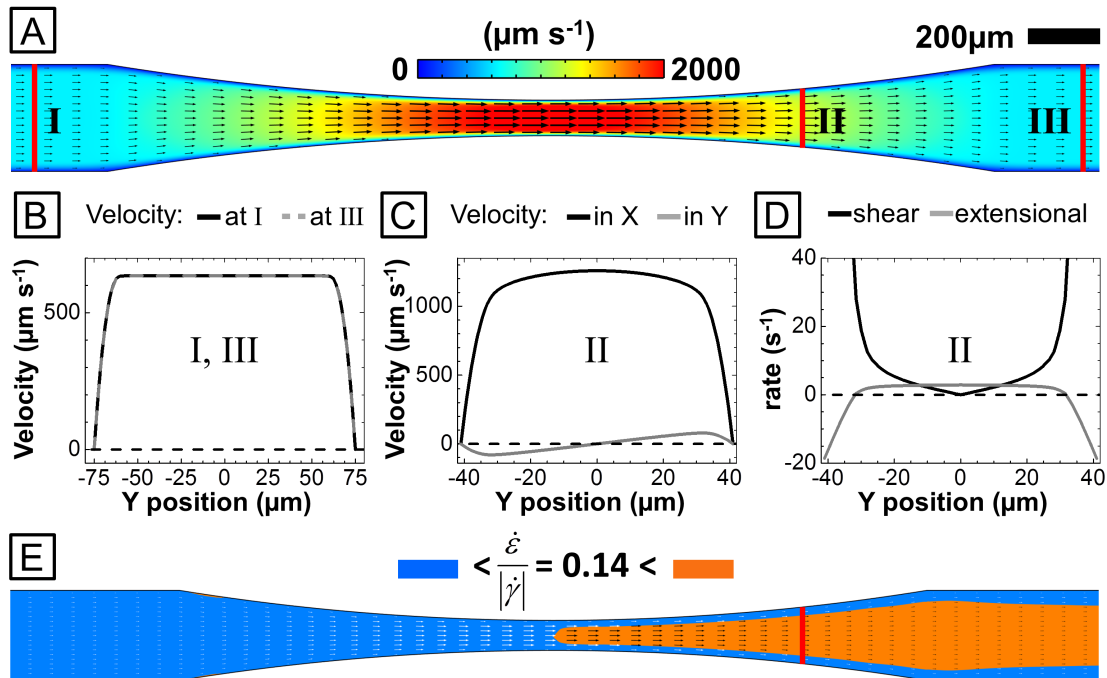


Figure 5. Velocity field $v(x,y)$ for cylindrical micelles calculated by CFD simulations. Upper panel (A): Calculated velocity in the wide and narrow channel section. (B): Calculated velocity profiles $v_x(y)$ in the pre-tapering zone I (■■■) and post-tapering zone III (■■■). (C): Velocity profiles $v_x(y)$ (■■■) and $v_y(y)$ (■■■) in the expansion zone indicated in (A). (D) Shear rate $|\dot{\gamma}(y)|$ (■■■) and extensional rate $\dot{\varepsilon}(y)$ (■■■) in the expansion zone. (E) Map of the ratio $\dot{\varepsilon}/|\dot{\gamma}|$ in the wide and narrow channel section. In the orange regions $\dot{\varepsilon}/|\dot{\gamma}| > 0.14$, whereas in the blue regions $\dot{\varepsilon}/|\dot{\gamma}| < 0.14$. The resulting color map shows good agreement with the polarized optical micrographs in Fig. 3A, the X-ray intensity map in Fig. 3 C, and the measured velocity map in Fig. 4 F.

Fig. 5 B shows the calculated velocity profiles across the channel at position I before entering the contraction zone, and at position III after the expansion zone. The velocity profiles are both non-parabolic, with an almost constant flow velocity in the central part of the channel and a strongly decreasing flow velocity close to the channel walls, a consequence of the shear-thinning, non-Newtonian flow behavior. This is different for Newtonian fluids where the flow velocity has a continuously varying parabolic profile as shown by micro particle image velocimetry and CFD calculations in the Supporting Information. Figure 5 C shows the calculated velocity components v_x and v_y , and Figure 5 D the corresponding shear rate $\dot{\gamma} = \nabla_y v_x$ and extensional rate $\dot{\epsilon} = -\nabla_y v_y$ along the line across the expansion zone indicated in Figure 5 A. We observe, as in the experimental data in Fig. 4, that over the major central part of the cross section the extensional rate $\dot{\epsilon}$ is larger or at least of the same order of magnitude as the shear rate $\dot{\gamma}$. Figure 5 E shows the calculated ratio $\dot{\epsilon}/|\dot{\gamma}|$ over the contraction/expansion zone with a color scale adjusted such as yellow color indicates the zone where $\dot{\epsilon}/|\dot{\gamma}| > 0.14$, whereas blue color indicates the zone with $\dot{\epsilon}/|\dot{\gamma}| < 0.14$. A comparison with Figure 2, 3A, 3C, and 4 A shows that choosing a threshold of $\dot{\epsilon}/|\dot{\gamma}| = 0.14$ also in the calculations nearly quantitatively reproduces the yellow zone with perpendicular alignment and the blue zone with parallel alignment in our experiment. CFD simulations show that with decreasing flow rate and diameter of the tapered cross-section the area of the perpendicular oriented zone increases, which is in agreement with our experimental observations. The calculations do not reproduce the difference observed in the two stable pre- and post-tapering velocity profiles shown in Fig. 4 C. To account for this difference the effect of anisotropic colloids on the shear field has to be modeled in more detail, which in the present calculations has only indirectly been accounted for via the resulting shear-thinning behavior.

In conclusion, we show that cylindrical micelles orient either parallel to the flow direction or, after passing through a narrow channel section, perpendicular to the flow direction. Both orientations are stable downstream the channel. Experiments with cylindrical micelles of different type and recent literature indicate that the reorientation in perpendicular direction is generally occurring for anisotropic cylindrical and disk-like colloids. The perpendicular orientation is caused by the velocity field having large perpendicular gradients in the expansion zone after the narrow section. Shear-thinning, a typical property of anisotropic particles, promotes perpendicular extensional and orientation. This phenomenon has important implications when considering the flow orientation of polymers, fibers, proteins or cells through narrow sections such as dies, molds or tapered capillaries. An immediate consequence for the production of fibers is the necessity to subsequently apply extensional forces to re-align polymers of fibrils in flow-direction for optimal fiber mechanical properties. For fibrous proteins reorientation and stable plug-flow are mechanisms for protein or cell coagulation with possible relations to thrombosis.^[22] Current experiments indicate that perpendicular flow-orientation can be utilized to orient cylindrical micelles perpendicular to surfaces, which is of relevance for applications involving electrical or thermal transport perpendicular to a surface such as in hybrid solar cells.

Materials and Methods

Fabrication of microfluidic devices:

The microchannel master of the microfluidic device was fabricated using optical lithography.^[23] The microchannel network was designed in AutoCAD 2011 and printed on a mask foil with an UV-absorbent ink (Zitzmann GmbH). An inverse black-white image of the device design is shown in Figure 1A. To pump fluids into the device, inlet ports are interfaced with tubing. Their punch location is surrounded with polygons that scatter light, making it easy to see and accurately punch the corresponding PDMS replica that are fabricated using soft lithography, as described in detail in the supplemental part to this publication.^[24,25] Stable tubing interfaces are an important prerequisite for long-term *in-situ* scanning experiments at the synchrotron beam line.

Preparation of cylindrical micelle solution:

Poly(isoprene-*b*-polyethylene oxide) (PI₁₁₀-PEG₁₉₈, mean M_w 16,200 g mol⁻¹) was prepared by sequential living anionic polymerization, yielding a block copolymer with narrow polydispersity M_w/M_n = 1.02, where M_w and M_n are the weight- and number-averaged molecular weights. The synthesis and characterization of PI-PEG is described in detail elsewhere.^[26] Poly(ethylenebutylene-*b*-polyethylene oxide) (PEB₃₉-PEO₁₀₂, mean M_w 7,700 g mol⁻¹, MW/M_n = 1.06) was obtained from EVONIK and lyophilized before use. The dry polymers were dissolved in Millipore-quality water with a resistivity of 18.1 MΩ cm⁻¹ before use. The solutions were homogenized using an UltraTurrax T8 (IKA Werke GmbH) and stored to allow the copolymer to swell in the water for three weeks at room temperature. Before the microfluidic experiments, the solutions are filtered through a PTFE filter with 5 μm pore size.

Device operation at the beamline:

The experiments were performed at the beamline BW4 and P03 at HASYLAB/DESY. The microfluidic device was connected to high precision syringe pumps (Cetoni GmbH, Nemesys system) and positioned in the X-ray beam. After collecting the necessary background data of an empty microchannel, the syringe pumps are set to typical flow rates of 32.4 μL h⁻¹ corresponding to a mean stream velocity of 360 μm s⁻¹. After 15 min. of equilibration time, measurements along the flow direction are performed with a microfocused X-ray beam at a wavelength of λ = 0.1381 nm. At both beamlines the beam was 20 μm in width and 30 μm in height. X-ray scattering patterns were recorded with step sizes of 70 μm at a distance of 3.128 m behind the microfluidic device using a Pilatus 300K detector (Dectris Ltd.) with a pixel size of 172 μm by 172 μm. The integration time is 240 s.

References

- [1] Yang HH, Allen SR (2000) in *Advanced fiber spinning technology*, (Ed: Nakajima T), Woodhead Publ., Abington, England, Ch. 6.
- [2] Cuculo JA, Hotter JF, Zhou Q (2001) in *Structure Formation in Polymeric Fibers*, (Ed: D. R. Salem), 1st edn., Hanser Gardner Pubns., Ch. 3.
- [3] Bouxsein NF, Hirst LS, Li Y, Safinya CR, Samah ZA, MacDonald NC, Pynn R (2004) Alignment of filamentous proteins and associated molecules through confinement in microchannels. *Appl Phys Lett* 85:5775.
- [4] P. Butler P (1999) Shear induced structures and transformations in complex fluids. *Curr Opin Colloid Interface Sci* 4:214.
- [5] Squires TM, Quake SR (2005) Microfluidics: fluid physics at the nanoliter scale. *Rev Mod Phys* 77:977.
- [6] Stone HA, Stroock AD, Ajdari A (2004) Engineering flows in small devices: microfluidics toward a lab-on-a-chip. *Annu Rev Fluid Mech* 36:381.
- [7] Barrett P, Faucon M, Lopez J, Cristobal G, Destremaut F, Dodge A, Guillot P, Laval P, Masselon C, Salmon JB (2006) X-ray microfocussing combined with microfluidics for on-chip X-ray scattering measurements. *Lab Chip* 6:494.
- [8] Martin HP, Brooks NJ, Seddon JM, Terrill NJ, Luckham PF, Kowalski AJ, Cabral JT (2010) Complex fluids under microflow probed by SAXS: rapid microfabrication and analysis. *J Phys Conf Ser* 247:012050.
- [9] Li S, Liu N, Chan-Park MB, Yan Y, Zhang Q (2007) Aligned single-walled carbon nanotube patterns with nanoscale width, micron-scale length and controllable pitch. *Nanotechnol* 18:455302.
- [10] Hesse HC, Beck R, Ding C, Jones JB, Deek J, MacDonald NC, Li Y, Safinya CR (2008) Direct imaging of aligned neurofilament networks assembled using in situ dialysis in microchannels. *Langmuir* 24:8397.
- [11] Rammensee S, Slotta U, Scheibel T, Bausch AR (2008) Assembly mechanism of recombinant spider silk proteins. *Proc. Natl. Acad. Sci. U.S.A.* 105:6590.
- [12] Sun B, Sirringhaus H (2006) Surface tension and fluid flow driven self-assembly of ordered ZnO nanorod films for high performance field effect transistors. *J Am Chem Soc* 128:16231.
- [13] Dimalanta ET, Lim A, Runnheim R, Lamers C, Churas C, Forrest DK, De Pablo JJ, Graham MD, Coppersmith SN, Goldstein S, Schwartz DC (2004) A microfluidic system for large DNA molecule arrays. *Anal Chem* 76:5293.
- [14] Cates ME, Candau SJ (1990) Statics and dynamics of worm-like surfactant micelles. *J Phys Cond Mat* 2:6869.
- [15] Förster S, Konrad M, Lindner P (2005) Shear thinning and orientational ordering of wormlike micelles. *Phys Rev Lett* 94:017803.
- [16] Richtering W (2001) Rheology and shear induced structures in surfactant solutions. *Curr Opin Colloid Interface Sci* 6:446.

- [17] Waton G, Michels B, Steyer A, Schossele F (2004) Shear-induced demixing and shear-banding instabilities in dilute triblock copolymer solutions. *Macromolecules* 37:2313.
- [18] Gao C, Kulkarni SD, Morris JF, Gilchrist JF (2010) Direct investigation of anisotropic suspension structure in pressure-driven flow. *Phys Rev E* 81:041403.
- [19] Cromer M, Cook LP, McKinley GH (2011) Pressure-driven flow of wormlike micellar solutions in rectilinear microchannels. *J Non-Newtonian Fluid Mech* 166:180.
- [20] Singh AP, Rey AD (1995) Computer simulation of dynamics and morphology of discotic mesophases in extensional flows. *Liquid Crystals* 18:219.
- [21] Oliveira MSN, Alves MA, Pinho FT, McKinley GH (2007) Newtonian fluid flow through microfabricated hyperbolic contractions. *Exp Fluids* 43:437.
- [22] Liu Q, Mirc D, Fu BM (2008) Mechanical mechanisms of thrombosis in intact bent microvessels of rat mesentery. *J. Biomechanics* 41:2726.
- [23] Nguyen NT, Wereley S (2002), *Fundamentals and Applications of Microfluidics*, 1st edn., Artech House, Ch. 3.
- [24] Xia Y, Whitesides GM (1998) Soft lithography. *Annu Rev Mater Sci* 28:153.
- [25] Quake SR, Scherer A (2000) From micro- to nanofabrication with soft materials. *Science* 290:1536.
- [26] Förster S, Krämer E (1999) Synthesis of PB-PEO and PI-PEO block copolymers with alkyl lithium initiators and the phosphazene base *t*-BuP₄. *Macromolecules* 32:2783.

Supporting Information

Fabrication of Kapton-PDMS-Kapton microfluidic devices (Figure S1):

A negative photoresist (SU-8 50, Microchem Co.) is spin-coated onto a silicon wafer. A mask aligner (Süss Mikro Tec) is used to impart the microchannel structure into the photoresist. We optimize the master device fabrication to obtain microchannels with a very uniform height of 100 µm. Although PDMS is widely applied to replicate the microchannel master device using soft lithography, PDMS scatters and absorbs X-rays. To fabricate X-ray compatible microfluidic devices involving PDMS, we modified the conventional fabrication procedure, based on the work of Evans and Dootz.^[S1, S2] After pouring PDMS pre-polymer (Sylgard 184, Dow Corning) on the master device, excess pre-polymer is removed from the master device with a razor blade. The remaining PDMS is cured and a small piece of self-adhesive polyimide tape (DuPont™ Kapton®) is used to cover the area of interest of the microchannel network including the curved and tapered microchannel sections. A second layer of PDMS is cured onto the previous layers. The PDMS replica is removed from the master device and inlet ports are punched into the polymer using a biopsy punch needle (Harris Uni-Core™ 0.75 mm). The bottom of the device is sealed with Kapton tape and a window is cut into the top PDMS layer. Thus, the microchannels in the area of interest are solely sealed with X-ray transparent Kapton tape.

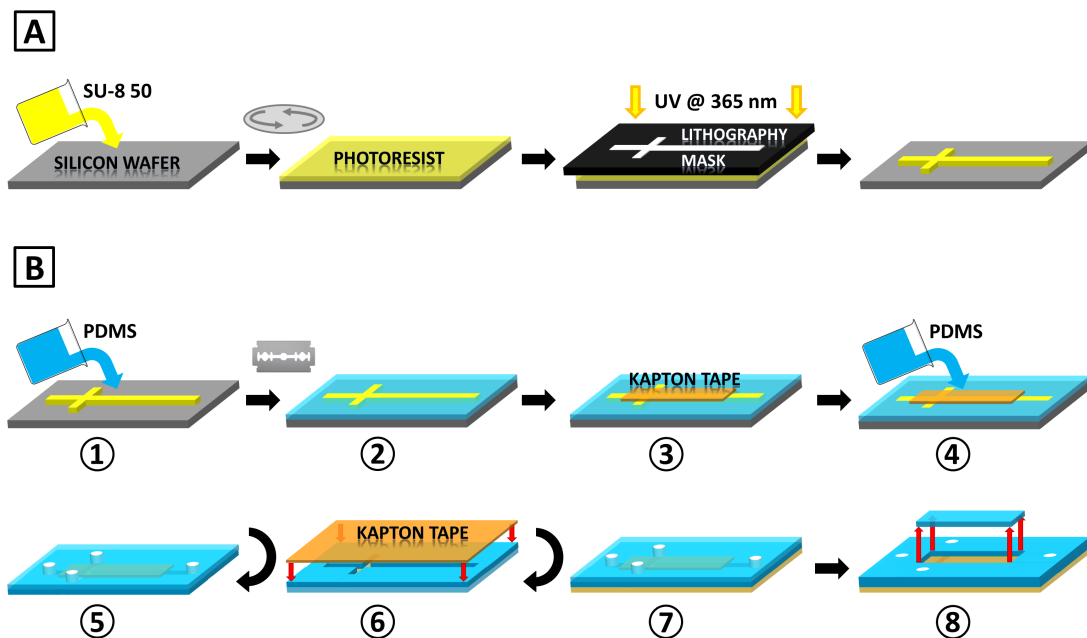


Figure S1. Fabrication of microfluidic devices with X-ray analysis capability based on PDMS. (A) Master device fabrication using photolithography. (B) Fabrication of X-ray transparent microfluidic Kapton-PDMS-Kapton sandwich devices. (B1) PDMS is poured on a master device, (B2) and excess PDMS is cut-off the microchannel structure. (B3) Self-adhesive Kapton tape is used to seal the area of interest, (B4) and a second layer of PDMS is grafted on top. (B5) The PDMS replica is peeled off the master device, and inlet ports for fluids are added. (B6) The bottom is sealed with Kapton tape, (B7, B8) before a window is cut into the top PDMS layer with similar dimensions as the Kapton window in B3.

Computational Fluid Dynamics Simulations (CFD):

The fluid dynamics calculations are based on the Navier-Stokes equations assuming an incompressible fluid, i.e. $\rho = \text{const.}$ ^[S3],

$$\begin{aligned} \rho \nabla \cdot \mathbf{u} &= 0 \\ \rho \frac{\partial \mathbf{u}}{\partial t} + \rho (\mathbf{u} \cdot \nabla) \mathbf{u} &= \nabla \cdot [-p \mathbf{I} + \mu (\nabla \mathbf{u} + \nabla \mathbf{u}^T)] + \mathbf{F} \end{aligned}$$

with the density of the fluid ρ , the pressure p , the identity matrix \mathbf{I} , the dynamic viscosity of the fluid μ , the velocity field \mathbf{u} and the volume force \mathbf{F} .

Solutions of anisotropic particles exhibit pronounced shear-thinning. To model the resulting flow profile, we used the software package COMSOL Multiphysics v4.2a, which allows one to import CAD-designed microchannel geometries and takes into account Non-Newtonian flow behavior in computational fluid dynamics simulations.^[S3] To integrate non-linear flow behavior in the CFD-model, experimental data are employed obtained by rheometry using a Bohlin Gemini 200 which was used to measure the shear-rate dependence of the viscosity. The measured flow curve can be well described by the Cross equation:^[S4, S5]

$$\eta = \eta_\infty + \frac{\eta_0 - \eta_\infty}{1 + (\tau_c \dot{\gamma})^n}$$

where the viscosity η is described by the zero-shear viscosity η_0 , the high-shear viscosity η_∞ , the internal relaxation time τ_c and the power-law exponent n characterizing the shear thinning between η_0 and η_∞ . This equation well reproduces the experimental data as shown in Fig. S2. The values of the parameters obtained by fitting the equation to the measured flow-curve are then used in the CFD-calculations.

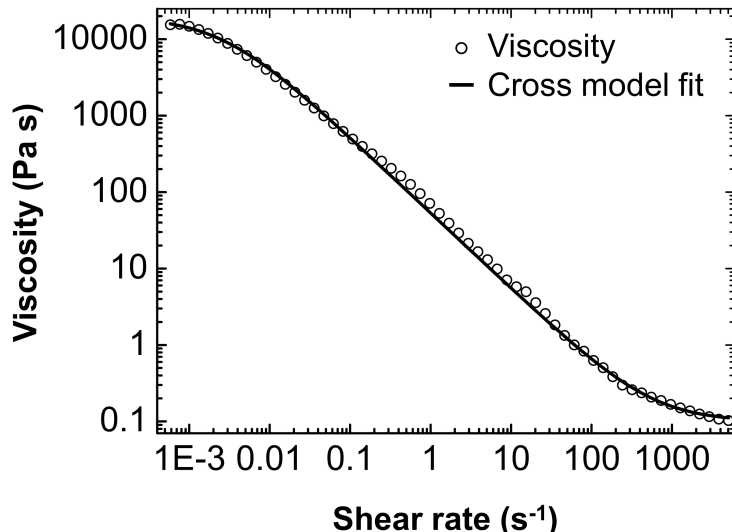


Figure S2. Experimental rheological data: viscosity (η) as a function of the shear rate ($\dot{\gamma}$) is described by the Cross equation.

The simulations yield the velocity field $v(x, y)$ from which the shear- and extensional rates can be calculated. A mean shear rate^[S3]

$$\dot{\gamma} = \sqrt{\frac{4u_x^2 + 2(u_y + v_x)^2 + 4v_y^2}{2}}$$

with the corresponding x- or y-components of u (velocity in x-direction) and v (velocity in y-direction) is used to map the local velocity on the microchannel.

The model is solved for 1412784 finite elements and 1072212 degrees of freedom using a multifrontal massively parallel solver (MUMPS). The average element quality of the mesh is 0.9889 on a scale from 0 to 1, where 1 is the highest quality; the minimal element quality is 0.6923. Using a Windows 7 x64 machine with two quad-core Intel® Xeon® E5440-processors operating at 2.83 GHz and an internal memory of 32 GB RAM. All relevant parameters, which are used in the simulations, are summarized in Table S1.

Table S1. Material properties used in the simulation model.

Figure 3 & S3	Non-Newtonian	Newtonian
Flow rate v_{flow}	32.4 $\mu\text{L h}^{-1}$	32.4 $\mu\text{L h}^{-1}$
Flow speed v	18.52 mm s^{-1}	18.52 mm s^{-1}
zero-shear viscosity η_0	19522 Pa s	-
high-shear viscosity η_∞	0.1 Pa s	-
internal relaxation time τ_c	388.5 s	-
power-law exponent n	0.99	-
Viscosity η [S6]	-	1.002 · 10 ⁻³ $\text{kg m}^{-1} \text{s}^{-1}$
Density ρ [S6]	998.2 kg m^{-3}	998.2 kg m^{-3}
Temperature T	293.15 K	293.15 K

Calculated velocity field for water

The calculated velocity field for the wormlike micelles has been discussed in the main part of the publication. Here we present the same calculations for water as a Newtonian fluid. This provides insight to what extent the shear-thinning behavior causes the observed reorientation behavior. We calculated the velocity field for water under the same experimental conditions as for wormlike micelles. The results are shown in Fig. S3, which is organized similar to Figure 5 in the main section of the manuscript for comparison.

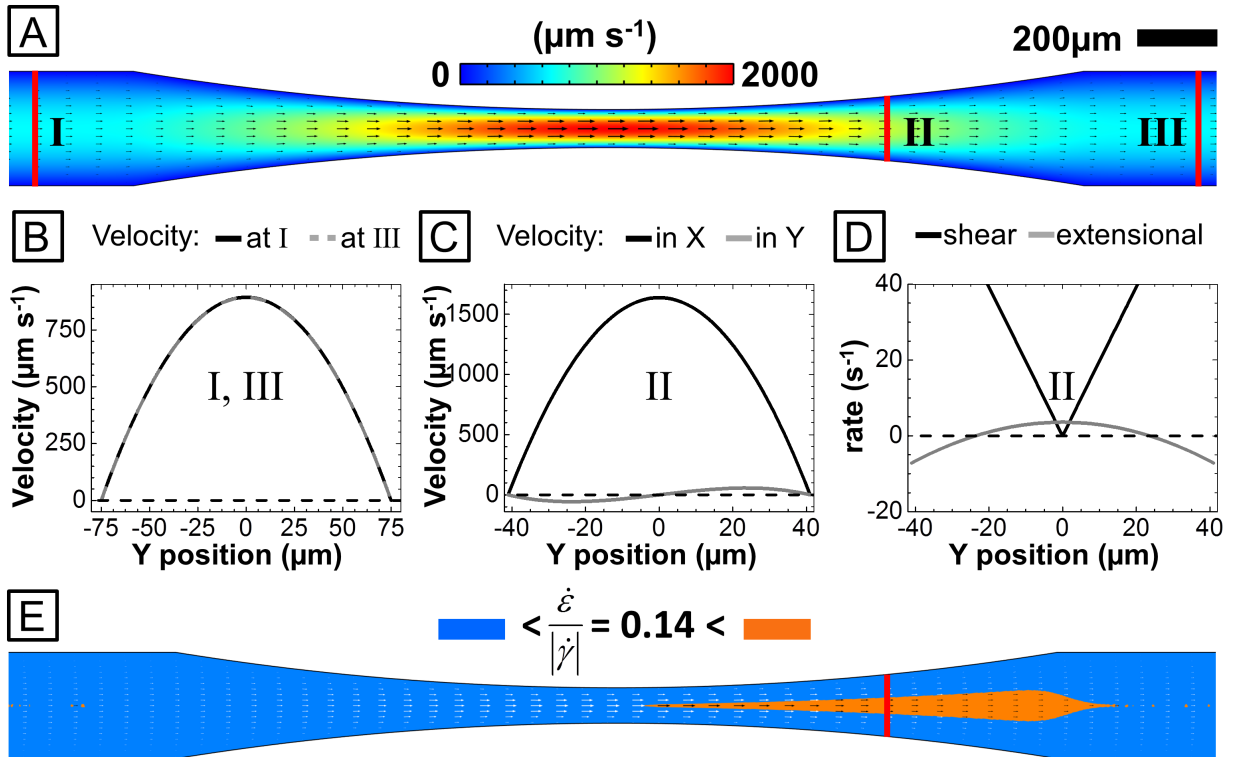


Figure S3. Calculated velocity field $v(x,y)$ of water (A) across the contraction/expansion region in the narrow channel section. (B): Calculated velocity profiles $v_x(y)$ in the pre-tapering zone I (■■■) and post-tapering zone III (■■■■■). (C): Velocity profiles $v_x(y)$ (■■■) and $v_y(y)$ (■■■■■) in the expansion zone indicated in red in (A). (D) Shear rate $|\dot{\gamma}(y)|$ (■■■) and extensional rate $\dot{\varepsilon}(y)$ (■■■■■) in the expansion zone. (E) Map of the ratio $\dot{\varepsilon}/|\dot{\gamma}|$ in the wide and narrow channel section. In the orange regions $\dot{\varepsilon}/|\dot{\gamma}| > 0.14$, whereas in the blue regions $\dot{\varepsilon}/|\dot{\gamma}| < 0.14$.

For water the expected parabolic flow profiles $v_x(y)$ is observed as shown in Figs. S3 B and C with the corresponding linear increase of the shear rate $\dot{\gamma}(y)$ towards the channel walls (Fig. S3 D). The extensional rate $\dot{\varepsilon}(y)$ smoothly decreases from small positive values in the central part of the channel to small negative values close to the channel walls. For comparison with the color maps in the main manuscript, we visualize zones with high extensional rates $\dot{\varepsilon}/|\dot{\gamma}| > 0.14$ in orange and zones with high shear rates $\dot{\varepsilon}/|\dot{\gamma}| < 0.14$ in blue, using the same threshold value of $\dot{\varepsilon}/|\dot{\gamma}| = 0.14$ as shown in Fig. S3 E. In case of a Newtonian fluid, such as water, the high extensional rate zone (orange) is limited to a small region in the central part of the channel. Thus, a high perpendicular extensional rate zone is also present in Newtonian fluids, but becomes larger and more pronounced in non-Newtonian, shear-thinning fluids.

Micro particle image velocimetry (μ PIV) and measured velocity fields of water

To obtain the velocity flow profiles $v(x, y)$ experimentally we used micro particle image velocimetry (μ PIV). The setup involves an Olympus IX71 inverse microscope, a phantom v9.1 high-speed camera, and highly intense, focused light source. This setup allows exposures down to 2 μ s and frame rates up to 150 000 s $^{-1}$. The narrow depth of focus of the setup enables precise vertical position control within the microchannel. The obtained high speed image sequence is auto-correlated and analyzed using the open-source software package JPIV.^[S6] Measurements were made in pure water and in aqueous solutions of cylindrical micelles at 25% w/w. Each solution contained 2% w/w of monodisperse polystyrene tracer particles (3.3 μ m diameter) which were coated with polyacrylic acid to avoid wall adhesion. Each solution is pumped through a 250 μ m channel with a height of 110 μ m at a flow rate of 2000 μ l h $^{-1}$. The channel's tapering had a width ratio of 5:1 and a length of 500 μ m.

The results for the shear-thinning wormlike micelle solutions were already discussed in the main article. Here we present the comparison to the flow behavior of pure water, a Newtonian fluid. The analysis shows that the key features of the velocity fields obtained from CFD simulations agree well with the experimentally determined velocity fields. The expected nearly parabolic flow profile $v_x(y)$ is observed in all channel sections as shown in Fig. S4 B, C. As shown Fig. S4 D, in the expansion zone the extensional rate $\dot{\epsilon}(y)$ smoothly decreases from small positive values in the central part of the channel to small negative values close to the channel walls. For comparison with the color maps in the main manuscript, we visualize zones with high extensional rates $|\dot{\epsilon}| > 0.14$ in orange and zones with high shear rates $|\dot{\gamma}| < 0.14$ in blue, using the same threshold value of $|\dot{\epsilon}| = 0.14$ as shown in Fig. S4 E. Similar as in the CFD-simulations, in case of a Newtonian fluid such as water, the high extensional rate zone (orange) is limited to a smaller region in the central part of the channel.

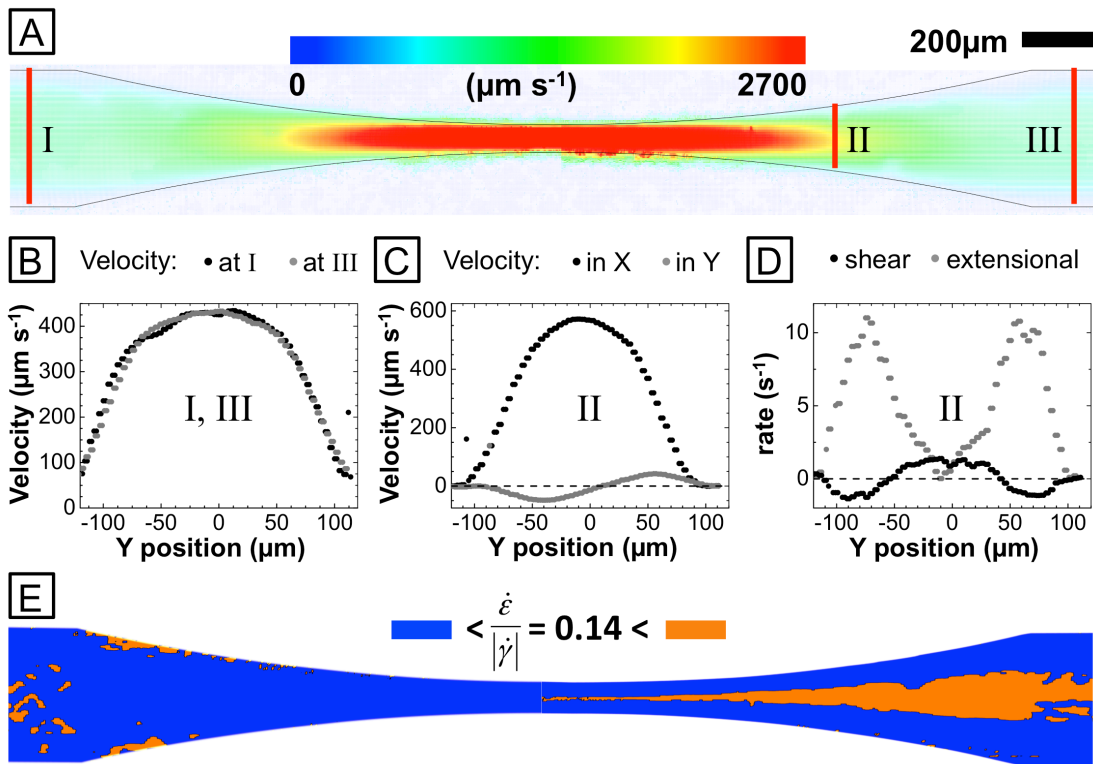


Figure S4. Velocity flow profiles $v(x,y)$ of water measured by micro particle image velocimetry. Upper panel (A): Measured particle velocity in the wide and narrow channel section. (B) Velocity profile $v_x(y)$ in the pre-tapering zone I (●) and post-tapering zone III (○). (C) Velocity profiles $v_x(y)$ (●) and $v_y(y)$ (○) in the expansion zone II. (D) Shear rate $\dot{\gamma}(y)$ (●) and extensional rate $\dot{\varepsilon}(y)$ (○) in the expansion zone II. (E) Map of the ratio $\dot{\varepsilon}/|\dot{\gamma}|$ in the wide and narrow channel section. In the orange regions $\dot{\varepsilon}/|\dot{\gamma}| > 0.14$, whereas in the blue regions $\dot{\varepsilon}/|\dot{\gamma}| < 0.14$, respectively. The resulting color map shows that even for pure water there is a region with considerable perpendicular extensional forces in the expansion zone.

Microchannels with double tapering:

The flow behavior of wormlike micelles in consecutive taperings is studied in a 250 μm channel with a 5:1 tapering ratio. In the expansion zone of the first tapering the micelles (30% w/w) orient perpendicularly to the flow direction, which is indicated by the yellow birefringence interference colors. This orientation is switched back to the parallel alignment when entering compression zone of the subsequent tapering, as indicated by the blue birefringence interference colors in Figure S5.

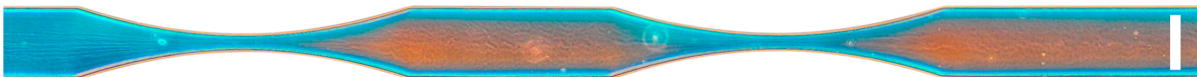


Figure S5. Polarisation microscopy reveals the flow behavior of PEB-PEO micelles (30% w/w in water) in consecutive taperings. In this example, the micelles are pumped though a 250 μm channel with two 250 μm taperings at a rate of 300 $\mu\text{l}/\text{h}$. The flow orientation is from left to right. The scale bar denotes 200 μm .

References

- [S1] H. M. Evans, R. Dootz, S. Köster, B. Struth, T. Pfohl, Bull. Pol. Acad. Sci., Tech. Sci. **2007**, *55*, 217.
- [S2] R. Dootz, H. Evans, S. Köster, T. Pfohl, Small **2007**, *3*, 96.
- [S3] User's Guide for COMSOL Multiphysics v4.2a, COMSOL AB, **2011**, 612-627.
- [S4] M. Cross, *J. Coll. Sci.* **1965**, *20*, 417–437.
- [S5] M. Konrad, P. Lindner, S. Förster, *Phys. Rev. Lett.* **2005**, *94*, 017803.
- [S6] R. Weast, M. Astle, *Handbook of Chemistry and Physics*, 60th edition, CRC Press, Boca Raton, **1979**, F-11, F-49.
- [S6] JPIV v1.0: open source software package for particle image velocimetry. <http://www.jpiv.vennemann-online.de/> (accessed Oct 02, 2012).

7.2 Microfluidic SAXS for the high-throughput screening and correlation of complex fluid behavior with structural information

Martin Trebbin,¹ Sebastian With,¹ Andres Mark,² Christoph Hanske,² Adeline Buffet,³ Gonzalo Santoro,³ Shun Yu,³ Jan Perlich,³ Stephan V. Roth,³ and Stephan Förster^{1,*}.

¹Physical Chemistry I, University of Bayreuth, D-95447 Bayreuth, Germany

²Physical Chemistry I, University of Bayreuth, D-95447 Bayreuth, Germany

³HASYLAB/DESY, D-22607 Hamburg, Germany

This work presents a fundamental study of the re-orientation of anisotropic particles in confined geometries for a wide range of experimental conditions. The screening of the experimental parameters, which control the re-orientation of wormlike polymeric micelles after passing microfluidic taperings, are studied in great detail using complementary analysis methods. These techniques involve microfocus small-angle X-ray scattering, polarization microscopy and microparticle image velocimetry in microfluidic channels, along with detailed CFD-simulations. A relative ranking according to the effectiveness for perpendicular alignment of anisotropic particles is derived as: *tapering ratio* (y-orienting extensional rate) > *concentration* (plug-flow and non-Newtonian behavior) > *length ratio* (wall shear surface) > *flow speed* (wall shear intensity). Further, the regions for perpendicular orientation were influenced by the rheological properties of the fluid, namely the zero shear viscosity and the internal relaxation time, as CFD-simulations show. Consequently, the perpendicular orientation of anisotropic particles can be controlled and predicted which has important implications for injection molding of anisotropic composite materials, the crystallinity of fibers during the spinning process or other applications that involve anisotropic electrical or thermal transport, as in isolating materials or hybrid solar cells.

Introduction

Microfluidic SAXS experiment. Microfluidics enables the precise control of liquids on the nanoliter scale.¹ These very well defined flow conditions make this technology predestined for fundamental investigations at microfocused X-ray sources. The basic idea of this experimental setup is to utilize the very well defined continuous flow conditions of the microchannel to scan it with a X-ray microbeam and record the small-angle X-ray scattering (SAXS) pattern of each measured position. This mapped data then allows to get a fast and detailed overview over the flow experiment within the microchannel. The combination of microbeam X-ray scattering and microfluidics is currently being developed into a powerful experimental methodology suitable for the investigation of nanostructures, particle alignment and the *in situ* study of kinetics by creating X-ray compatible microflow chips and microfluidic liquid jet devices.²⁻¹⁰

The sample is pumped through the microchannels of a X-ray compatible device and the microfocused X-ray beam passes the flowing sample; in this case anisotropic wormlike micelles. The scattered X-rays, which contain the structural information, are recorded using a 2D digital detector (Piltatus 1M, Dectris). The typical experimental setup at the microfocus beamline P03 (PETRA III, DESY) is shown in the supplemental information in Fig.S1.¹¹

Recently, microfluidic SAXS scanning experiments at the P03 and BW4 beamlines (DESY, Hamburg) revealed the striking effect, that after passing a narrow section, wormlike particles are rotated perpendicular to the flow direction, keeping this orientation over the remaining length of the channel.² The flow-alignment of cylindrical, wormlike or fibrous structures is central to many processing steps such as in the production of fibers, during injection molding or the flow of cells and proteins through thin capillaries.¹²⁻¹⁶

In this paper, this perpendicular orientation will be investigated in more detail to understand the influence of experimental parameters on the orientation effect. For this task, we create X-ray compatible microfluidic devices which are made of NOA81 (Nordland Optical Adhesive 81) for the SAXS analysis.^{9,17-19} A redesigned NOA81-fabrication routine now allows the production of very thin devices for high X-ray transmission while also maintaining the material's very good solvent compatibility. The resulting microfluidic device is shown in Fig.1B while its detailed fabrication routine is explained in the experimental section. This routine is soft lithography-based because it uses inverted PDMS-microchannels as a molding template.^{20,21} Therefore, the high microfluidic design flexibility is maintained which is important for rapid prototyping.¹ With this given design control from soft lithography, we vary the geometric parameters of the microchannel like channel width (250 to 500 µm) tapering ratios (1:10 to 1:2.5; w. r. t. channel width) and -lengths (9:1 to 2:1; w. r. t. channel width), as illustrated in Fig.1A. Further, we vary the sample concentration (30 to 0% w/w) and flow speeds (100 to 2000 µl h⁻¹).

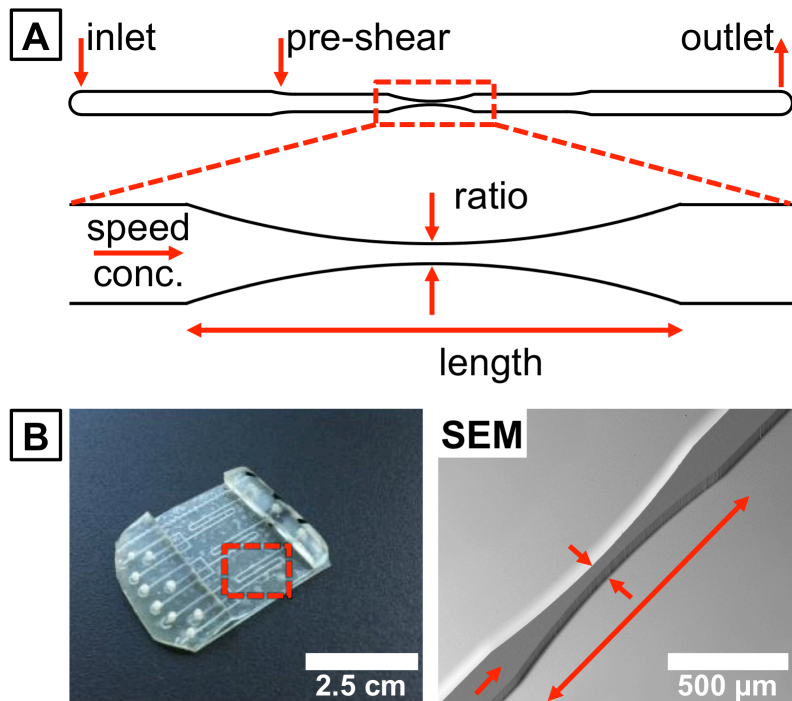


Figure 1 (A) The CAD-based design and use of high resolution photo masks (128 kdpi, JD Photo, UK) enable precise control over the microchannel geometries. In this case the shear field is controlled by smooth taperings with varying ratios (1:10 to 1:2.5) and lengths (9:1 to 2:1) with respect to the original channel widths (250 to 500 μm) at a constant channel height of 100 μm . Further, the varied relevant experimental parameters include flow speed and sample concentration. (B) The resulting NOA81-device and a typical electron micrograph of the SU-8 replication template (tapering ratio 3:1, channel width 150 μm).

Results and Discussion

SAXS pattern analysis. The microfluidic SAXS scanning setup enables fast sample screening of the varying experimental conditions. Each obtained SAXS pattern of a given position contains various structural information about the cylindrical micelles, like i.e. particle size, unit cell dimensions and orientational distribution; an example SAXS pattern is shown in Fig.2. The vertically-positioned crescents in this anisotropic SAXS pattern indicate a parallel orientation of wormlike micelles in respect to the (horizontal) flow direction. Additionally, the azimuthal peak width contains information about the micelles' orientation distribution. After the radial averaging of this SAXS pattern, the fits and projections can be calculated using the analysis software *Scatter* which yields further structural information about the sample.^{22,23} This sample contains hexagonally closest packed micelles ($\text{PEB}_{39}-b-\text{PEO}_{102}$, 30% w/w in pure water) which are oriented parallel to the (horizontal) flow direction. Their radius is 10.0 nm with varying lengths up to the micron range and a unit cell size of 40.9 nm (1 nm displacement, Laguerre distribution with $d_\beta=14$).²³ This software also allows the calculation of the micelle's 2D scattering patterns based on the 3D model of hexagonally closest-packed cylinders as shown in the image inlay in Fig.2.²³ The fitting parameters are listed in the following Tab.1.

Table 1 List of fitting parameters for the SAXS-pattern calculation using the analysis software *Scatter*.²²

Parameter	Value
Model	Hexagonally packed cylinders (P6/mm)
Micelle radius r , nm	10.0
Relative standard distribution σ_r , nm	0.15
Cylinder length L , nm	73.2
Relative standard distribution σ_L , nm	0.1
Unit cell dimensions a , nm	40.9
Displacement a_d , nm	1.0
Radial domain size a_{azi} , nm	213
Radial domain size a_{rad} , nm	65
Distribution function type	Laguerre
Distribution function parameter	14
d_β	

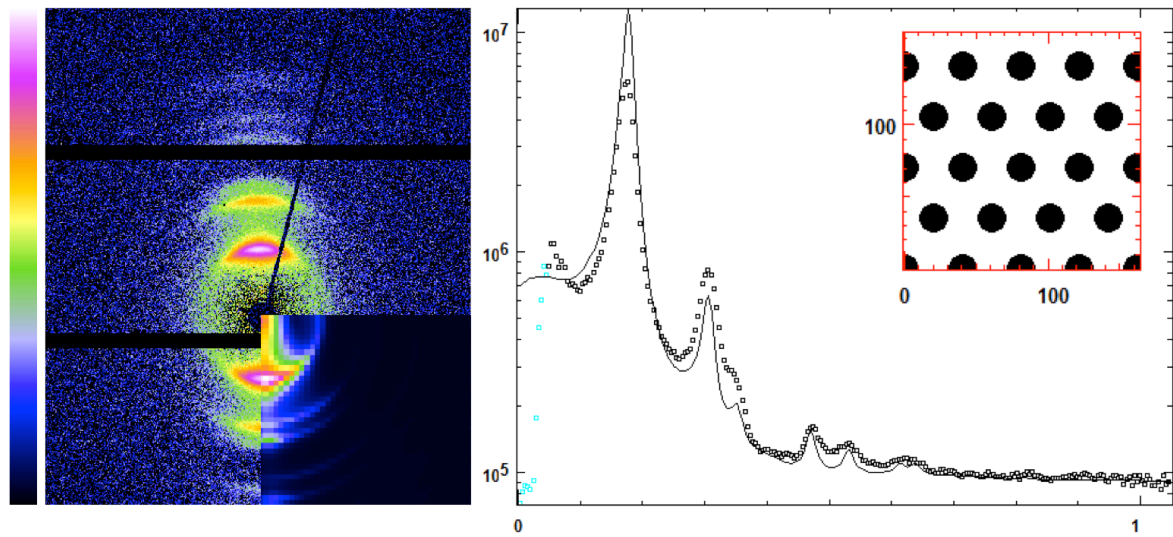


Figure 2 The obtained SAXS patterns contain various structural information of the cylindrical micelles, like i.e. particle size ($r=10$ nm), unit cell dimensions (40.9 nm) and orientational distribution (Laguerre distribution with $d_\beta=14$). The vertical crescents in this anisotropic pattern indicate parallel orientation in respect to the flow horizontal direction. After the radial averaging of this SAXS pattern, the fits and projections are calculated using the analysis software *Scatter*.^{22,23} Further, it is also possible to calculate the 2D scattering pattern, as shown in the bottom right corner, based on the corresponding 3D model of these hexagonally closest-packed cylinders.

Small-angle X-ray scattering is a complementary method that can be correlated to the results from other techniques such as micro particle image velocimetry (μ PIV), polarization microscopy and CFD-simulations which will be discussed over the course of this paper.

Generation of color-coded pixel maps from SAXS data. A fast overview over the obtained SAXS patterns of a single experiment is gained by the real-time generation of pixel maps based on the SAXS scanning locations. The SAXS pattern's structural information is then used to color-code the individual pixels based on the averaged intensity within micelle-orientation dependent regions of interest (ROI). The resulting pixel maps of different ROIs are shown in Fig.3B. The first pixel map shows the averaged intensity for all micelles orientations and gives an impression about the microchannel's shape. The ROI for the micelle orientation parallel to the flow is shown below and the color-coded pixel maps are in good agreement with the images obtained from polarization microscopy (Fig.3A). In the SAXS-based pixelmap we observe that the parallel orientation is strongest in the beginning of the tapering, where both extensional and shear forces are applied in flow direction. Parallel micelle orientation is also found close to the channel walls where the wall shear is most dominant due to the flow of the fluid. The third ROI-based pixel map represents the areas where the micelles are rotated perpendicular to the flow due to the dominance of extensional forces which are directed vertically to the main flow direction.² This perpendicular orientation can be also observed well as an orange-colored area in polarization microscopy to which the SAXS scanning position can be correlated as indicated in Fig.3A. Lastly, the plus 45° and minus 45° micelle orientations are shown below and are either the result of parallel micelle alignment to the tilted microchannel walls of the tapering or due to the transition from parallel to perpendicular orientation.

The effect of the tapering ratio on the perpendicular orientation. The velocity flow field in the microchannel and, hence, the shear and extensional forces are varied by changing the tapering ratios of the microchannel's narrow section between 10:1 and 2.5:1 with respect to the microchannel width. The flow of micelles through narrow sections under the same conditions is studied using polarization microscopy, as shown in Fig.4A. We find that the perpendicular orientation, which is indicated by the orange region, has the broadest width and is most pronounced at the largest tapering aspect ratio of 10:1. Both the color-intensity and the width of the orange stream decrease with wider microchannel taperings. The same set of experiments is also studied using microfluidic SAXS of which the resulting color-coded pixel maps are shown in Fig.4B,C. These pixel maps share the same color-scale to illustrate the relative intensity of re-orientation. Similar to the observed trends using polarization microscopy, we find that the re-orientation increases with larger tapering ratios and that less perpendicularly orientated micelles are observed with lower the tapering aspect ratios.

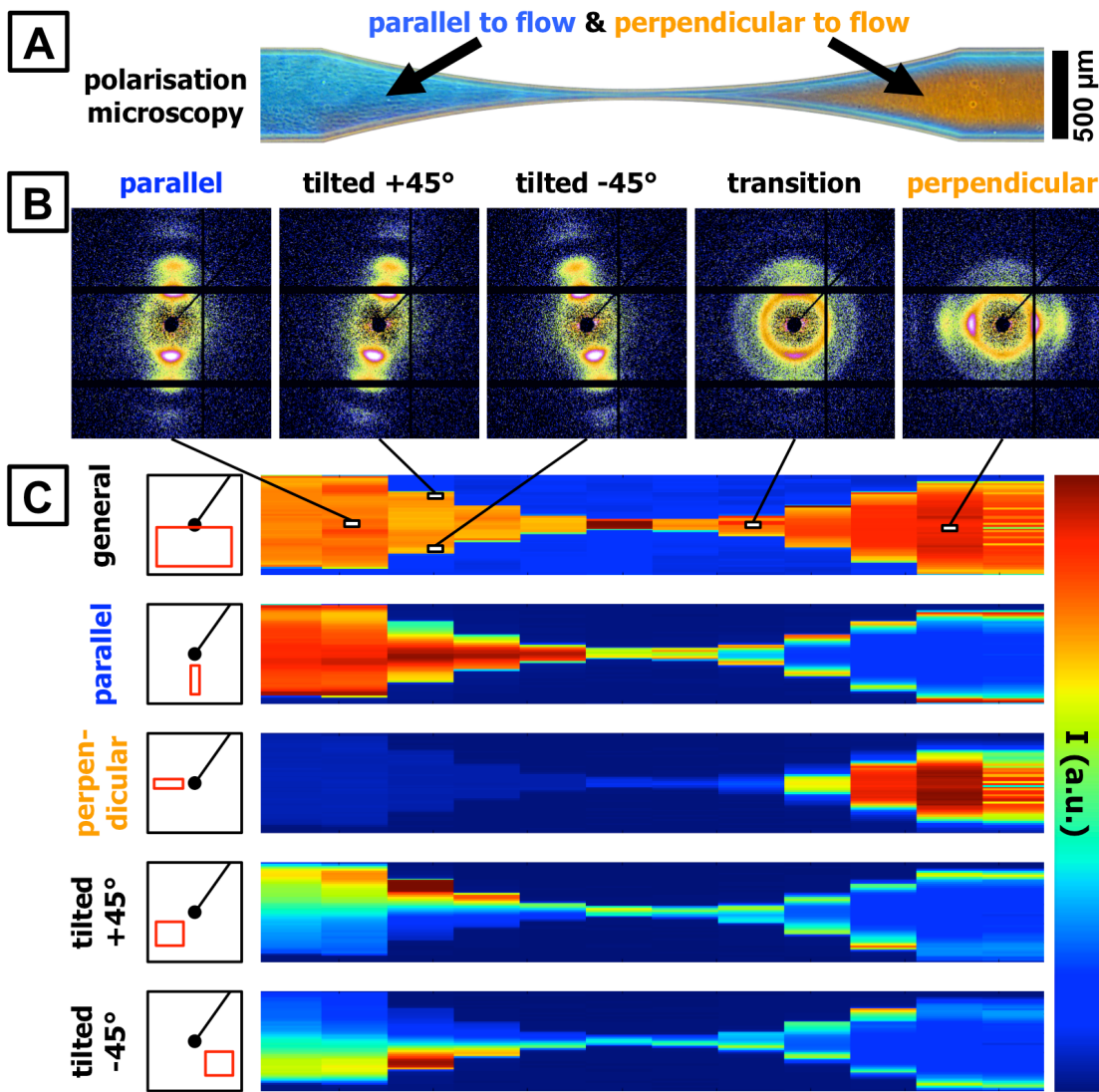


Figure 3 (A) Polarization microscopic (PM) images of the setup using crossed polarizers with a quarter wave plate give an impression about the flowing micelle's orientation: the blue color in the PM corresponds to a parallel orientation, while orange areas correspond to a perpendicular orientation of micelles in respect to the flow direction. The channel width is 500 μm with tapering narrowing down to 50 μm (10:1) over a length of 3500 μm (7:1). The micelle concentration is 30% w/w at a flow speed of 200 $\mu\text{l h}^{-1}$.

(B) This orientation is confirmed by the SAXS experiments at the P03/MiNaXS beamline which can easily be correlated with the PM because the conditions, such as flow speed, channel width, tapering ratio and length, etc. are highly reproducible in the microfluidic device. The flowing complex fluid is scanned at a given set of positions using the micro-focused X-ray beam. Each obtained pixel corresponds to a scattering pattern and therefore contains the full structural information.

(C) Color-coding these pixels based on the averaged intensity at a given region of interest (ROI) gives a detailed overview over the structural evolution. The basic types of orientational distribution in respect to the flow direction are isotropic, parallel, perpendicular, tilted plus 45° or minus 45°. The color bars of these pixel maps is adjusted individually to express the orientation regions more clearly.

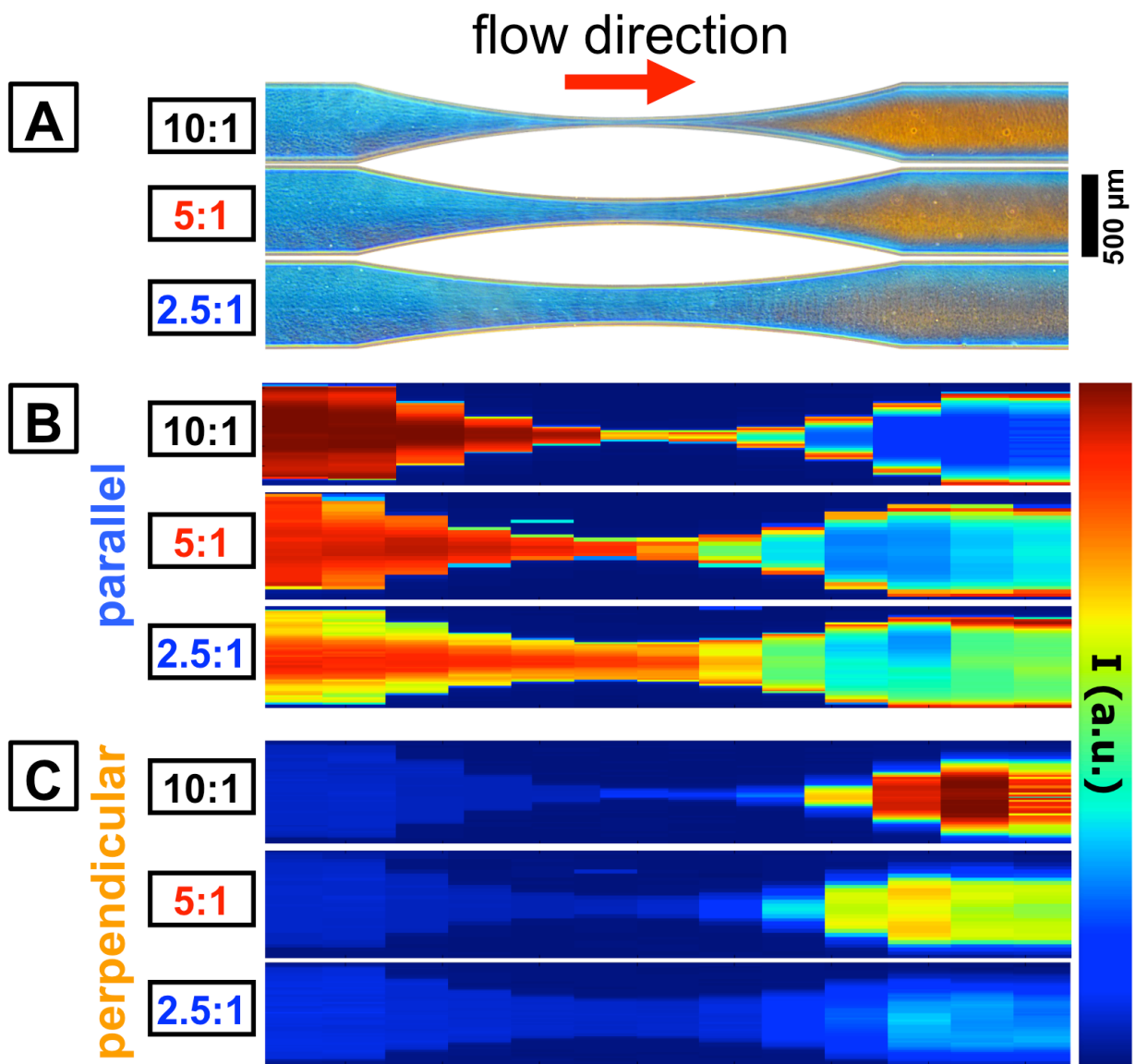


Figure 4 Comparison of the influence of the tapering ratios on the micelle orientation behavior. (A) Polarization microscopic images under the same conditions as the following SAXS pixel maps (micelle concentration 30% w/w, 200 $\mu\text{l h}^{-1}$) which show the regions of parallel (B) and perpendicular (C) orientation at different tapering ratios (10:1, 5:1, 2.5:1) with respect to the channel width of 500 μm . The color-scale is equal for all pixel maps to illustrate the relative intensity of re-orientation.

Analysis of the influence of the tapering ratio on the orientation distribution. The orientation distribution change along the microchannel has to be considered for the detailed analysis of the influence of tapering ratios on the intensity of perpendicular micelle orientation. This orientation information can be extracted from a series of SAXS patterns from the tapering ratio variation (Fig.4B,C). These vertical scans with microfocused X-ray beams, along the microchannel of each tapering aspect ratio, are compared in the Fig.5 providing a first *qualitative* analysis.

Here, the first and last rows of SAXS patterns show the parallel micelle orientation close to the walls which is indicated by the vertical position of the peaks.

The second and fourth rows show transition regions where the wormlike micelles change from parallel to perpendicular orientation and vice versa. This realignment appears as ‘fish’-shaped or crescent-like peaks in the SAXS patterns that originate from an asymmetrical orientational distribution along the azimuth. The scanning resolution of this transition is determined by the size of the X-ray microbeam which is $20 \times 30 \mu\text{m}^2$ in our experiments. Therefore, the observed ‘fish’-shape could originate from a much sharper transition region that is smeared by the overlaying X-ray beam of two scanning positions at parallel and perpendicular micelle orientation. However, the color transition in polarization microscopic images suggests a smooth orientation transition. A smaller microfocused X-ray beam could be used to resolve this region in more detail and study this transitional layer in more detail.

The central part of the microchannel scan is shown in the third row. We find that the micelle orientation distribution strongly depends on the tapering aspect ratio. In case of the 10:1 ratio, almost all micelles are aligned perpendicularly to the flow which is indicated by the peak in horizontal position. However, the horizontal peak intensity and, hence, perpendicular micelle orientation decreases with lower tapering ratios. In case of the 2.5:1 ratio, the SAXS pattern shows a more isotropic orientation characteristic with a preferred parallel orientation.

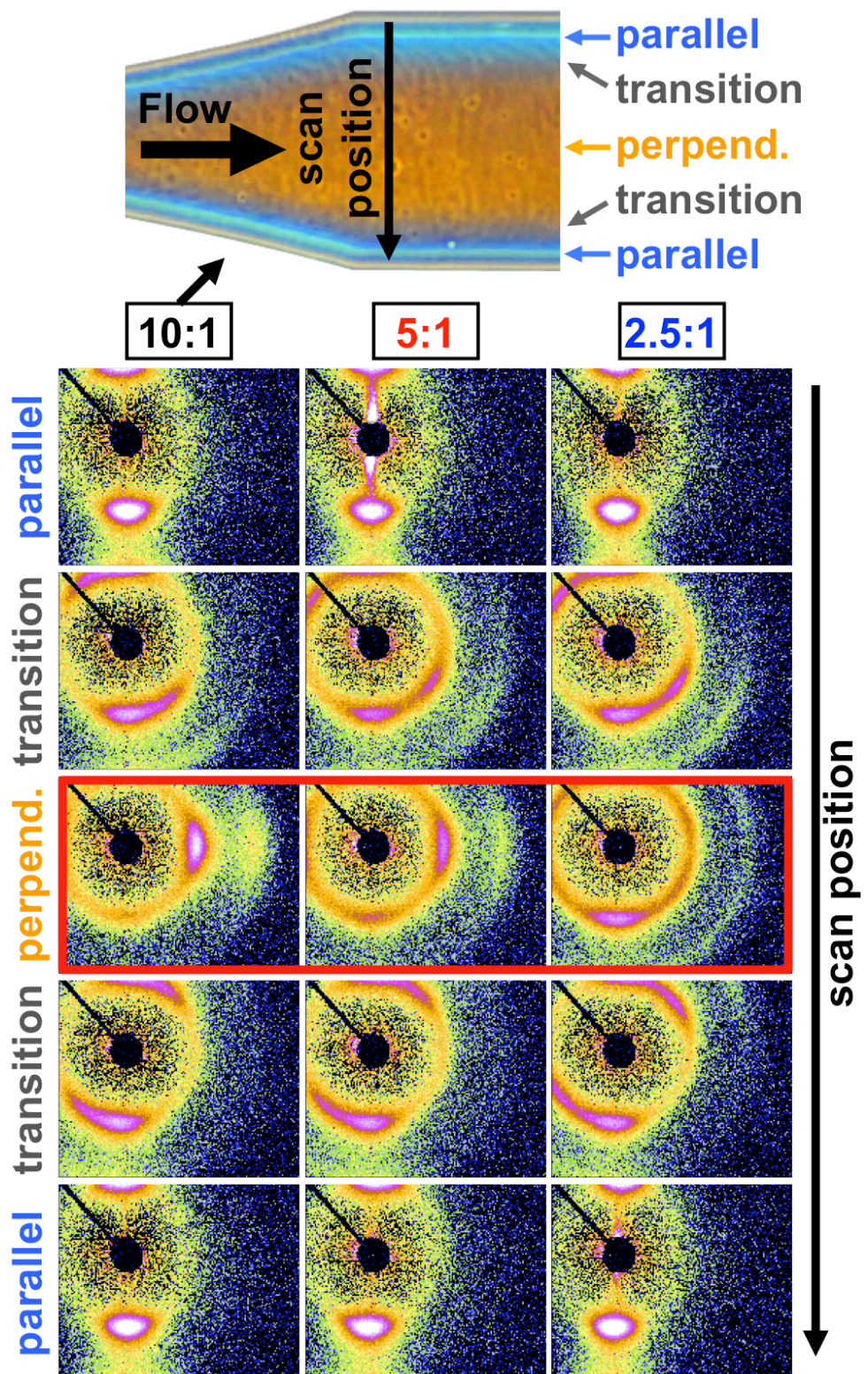


Figure 5 The detailed SAXS analysis is based on a vertical line scan across the microchannel at the tapering exit, as indicated by the long black arrow in the polarization microscopic image at the *top*. *Below*, the SAXS-patterns of womlike micelles in parallel and perpendicular orientations as well as the transitional stage are shown. Here, the ratio decreases with each column from *left* (10:1) to *right* (2.5:1). The red box marks the SAXS-patterns with are analyzed in more detail in Fig.6.

Next, this trend can be analyzed *quantitatively* by choosing a cake-like ROI of the SAXS patterns and calculating the azimuthally averaged intensity as indicated in Fig.6A. This averaging results in angle-dependent intensity curves which contain the peak intensities, - widths and -rotation angles of the parallel and perpendicular micelle orientations at the specific scan position in the microchannel. These curves at the central scan positions (see mark in Fig.6A) for all three taperings are combined in a single graph (Fig.6C) which gives an overview over the peak intensity changes. This graph reveals that the overall measured intensity stays constant and that only the orientation distribution changes with the tapering ratio. The peak of the parallel orientation at this central scan position (Fig.6C) decreases with a raising tapering ratio while the perpendicular orientation peak raises accordingly.

For a better general overview, this extraction process of angle-dependent intensity curves (see Fig.6C) is performed for the complete series of SAXS patterns. The results of the three vertical scans are then combined in individual 2D plots which are shown in Fig.6B where the color represents the extracted peak intensities. These 2D color plots now allow to differentiate between two regions of orientation intensity which are based on the parallel or perpendicular micelle orientation. Similar to the described orientation trends from above, we find that the relative peak intensities change with the tapering ratio where the most pronounced perpendicular orientation is found in the central part of the channel with a tapering ratio of 10:1. In case of the 5:1 ratio, the non-parallel orientation is weaker, but still clearly visible and has about the same intensity level as the parallel orientation. This trend continues with the 2.5:1 tapering ratio where the non-parallel orientation merely reveals itself as an isotropic orientation distribution with a preferred parallel orientation.

These micelle re-orientation shifts can also be quantified by the intensity ratio α which we define as

$$\alpha = \frac{I_{\perp}}{I_{\parallel} + I_{\perp}}$$

This ratio describes the relation between the summed peak intensities of micelles with perpendicular orientation (I_{\perp} from 61 to 117°) with the combined peak intensity sums of parallel and perpendicular micelles ($I_{\parallel} + I_{\perp}$ with I_{\parallel} from -37 to 40°). This measure allows to correlate the relative peak intensities from the SAXS experiments with the orange/blue-contrast observed in polarization microscopy. We find that a value of $\alpha = 0.1$ corresponds to the blue-colored regions with a preferred parallel micelle orientation, i.e. in proximity to the channel walls. The weakly orange-colored region at low tapering ratios (2.5:1, see Fig.4A) can be observed at $\alpha = 0.25$ which corresponds to an isotropic micelle distribution. Regions with a more pronounced orange color which can be found at higher tapering ratios (5:1 & 10:1, see Fig.4A) indicate that the orientation distribution is dominated by a perpendicular micelle alignment with α -values > 0.35 .

The observed trends can also be verified by microparticle image velocimetry (μ PIV) in the following section of this paper.

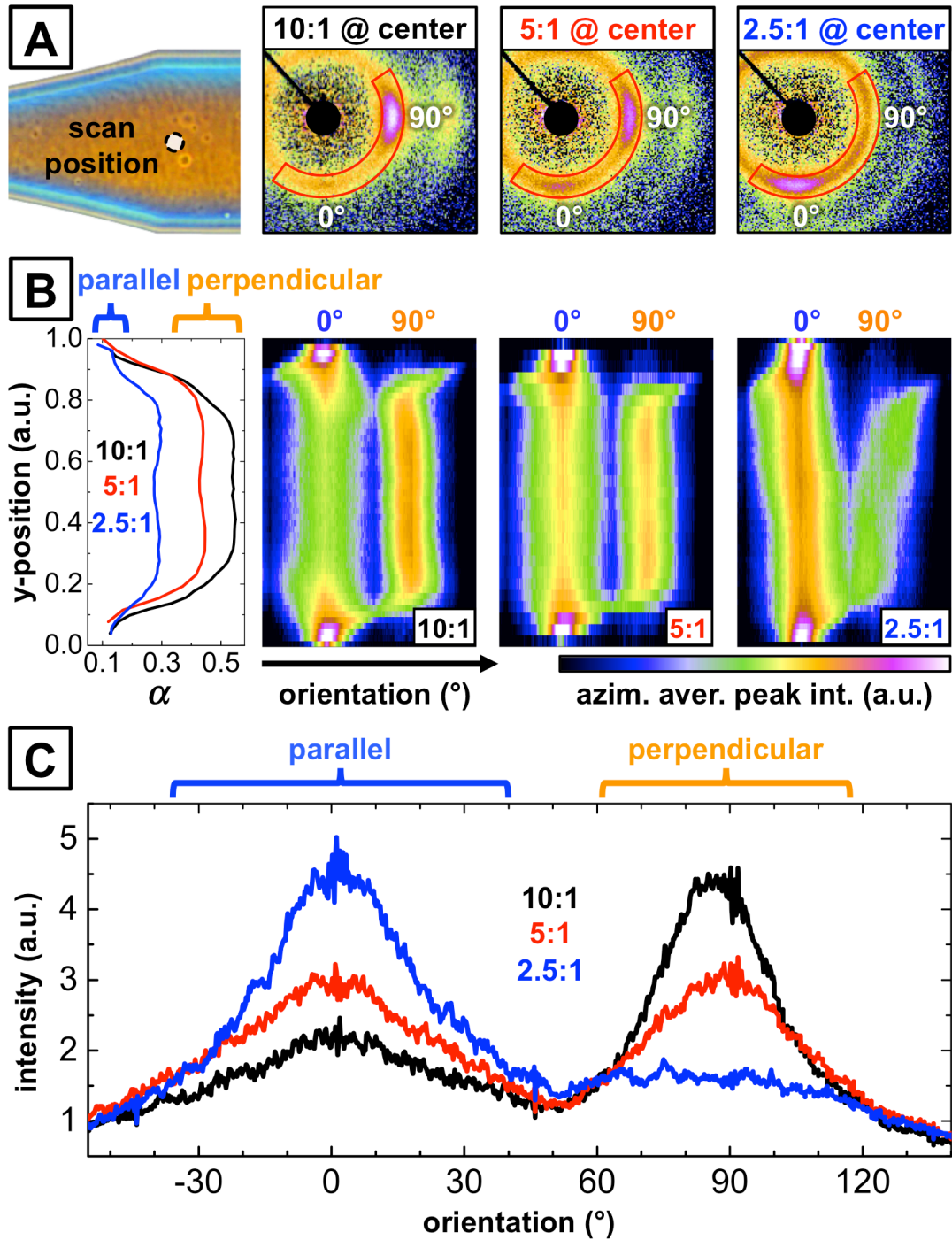


Figure 6 Extended overview over the micelle orientation distribution analysis from the SAXS pixel maps in Fig.4B,C. (A) By azimuthally averaging a cake-like slice from the SAXS image, it is possible to study and quantify the micelle's orientation distribution. (C) The resulting angle-dependent peak intensity curves reveal the influence of the microchannel's tapering ratio on the orientation distribution. (B) This effect can be studied in more detail by extracting the azimuthally averaged curves for all positions across the microchannel directly after the tapering and for different tapering ratios. The results are combined in 2D color maps of the angle-dependent peak intensity which give an overview over the micelle orientation changes across the microchannel that are quantified by the intensity ratio α .

μ PIV as a complementary analysis technique. The trends which have been described above can also be measured, supported and quantified by microparticle image velocimetry (μ PIV). This technique is complementary to the other experiments (polarization microscopy, SAXS-mapping) and involves the addition of small tracer particles to the fluid (1.65 μ m radius, PDI 1.01). The perpendicular flow orientation of the micellar solutions is maintained after the addition of small spheres, as shown in Fig.S2 in the supplemental information. Their motion results from the fluid flow and can be captured using a high speed camera at very fast frame rates (11 000 s⁻¹). The μ PIV-measurements have been performed for the same three tapering ratios as above, but at a shorter length ratio (2:1 vs. 7:1 w. r. t. the channel width) due to the camera's field of view. The captured frames are then correlated using the software JPIV which yields the velocity vector field inside the microchannel which is shown in Fig.7A/8A.²⁴

Next, the relevant velocity vector components in x- and y-direction can be extracted from these three vector fields at the widening channel sections of each tapering variation as indicated by the black arrow in Fig.7A/8A. Plotting the vector components against the position inside the microchannel yields the x- and y-velocity patterns, as shown by Fig.7B/8B. These graphs combine the velocity patterns of the three different tapering ratios to point out the relative changes of the curves.

To study the perpendicular micelle orientation in more detail, the gradients of the above velocity curves (V_x , V_y) are derived which yields the shear rate $\dot{\gamma}$ (red dots) and extensional rates $\dot{\epsilon}$ (black dots) respectively, as shown in Fig.7C/8C. These curves describe the change of velocities in x- or y-directions and clearly show that extensional forces in y-direction dominate in the central part of the microchannel. The re-orientation effect's area of influence can be described by calculating the ratio between extensional- and shear rate ($\dot{\epsilon}/\dot{\gamma}$) and mapping the results across the measured positions.² A collective overview over the 2D PIV maps at different experimental variations is given in Fig. S3 of the supplemental information.

μ PIV analysis of varying taperings. The μ PIV experiments show that the micelles in the widening section of the tapering are oriented perpendicularly to the flow due to the extensional forces in y-direction. This requirement is met in widening taperings. The higher the (widening) tapering ratio is, the stronger will the micelles be oriented perpendicularly. This is in agreement with the above results from polarization microscopy (intensity and contrast of orange color) and the SAXS-analysis (peak orientation, α -values) which both show that the perpendicular micelle orientation is strongest with high tapering ratios.

To study the wormlike micelle system, the μ PIV-measurements are performed for the generation of velocity vector maps as shown in Fig.7A. In these experiments, only the three tapering ratios are varied while the other experimental conditions are kept constant (250 μ m channel width, 2000 μ l h⁻¹, 2:1 length ratio, polymer concentration 10% w/w in pure water). The measured velocity profiles show the same trend, as described above, that the flow in y-directions (V_y) is stronger for the 10:1-tapering (black curve) compared to the 2.5:1-tapering (blue curve), as shown in Fig.7B *right*. The x-velocity profiles (V_x) in the central part of the

different microchannels vary only slightly, but they increase towards higher tapering ratios (black curve) as depicted in Fig.7B *left*. As a consequence, both extensional- and shear rates grow with higher tapering ratios which is shown in Fig.7C.

Since the micelles' orientation in the first half of the tapering is parallel to the flow, it is clear that the micelles are only re-oriented in the presence of y-elongating forces which also have to outweigh the present x-orienting shear-forces. Consequently, the tapering ratio design has great implications for controlling the perpendicular orientation of anisotropic particles because of its importance for fiber spinning and crystallinity tuning.¹²⁻¹⁶

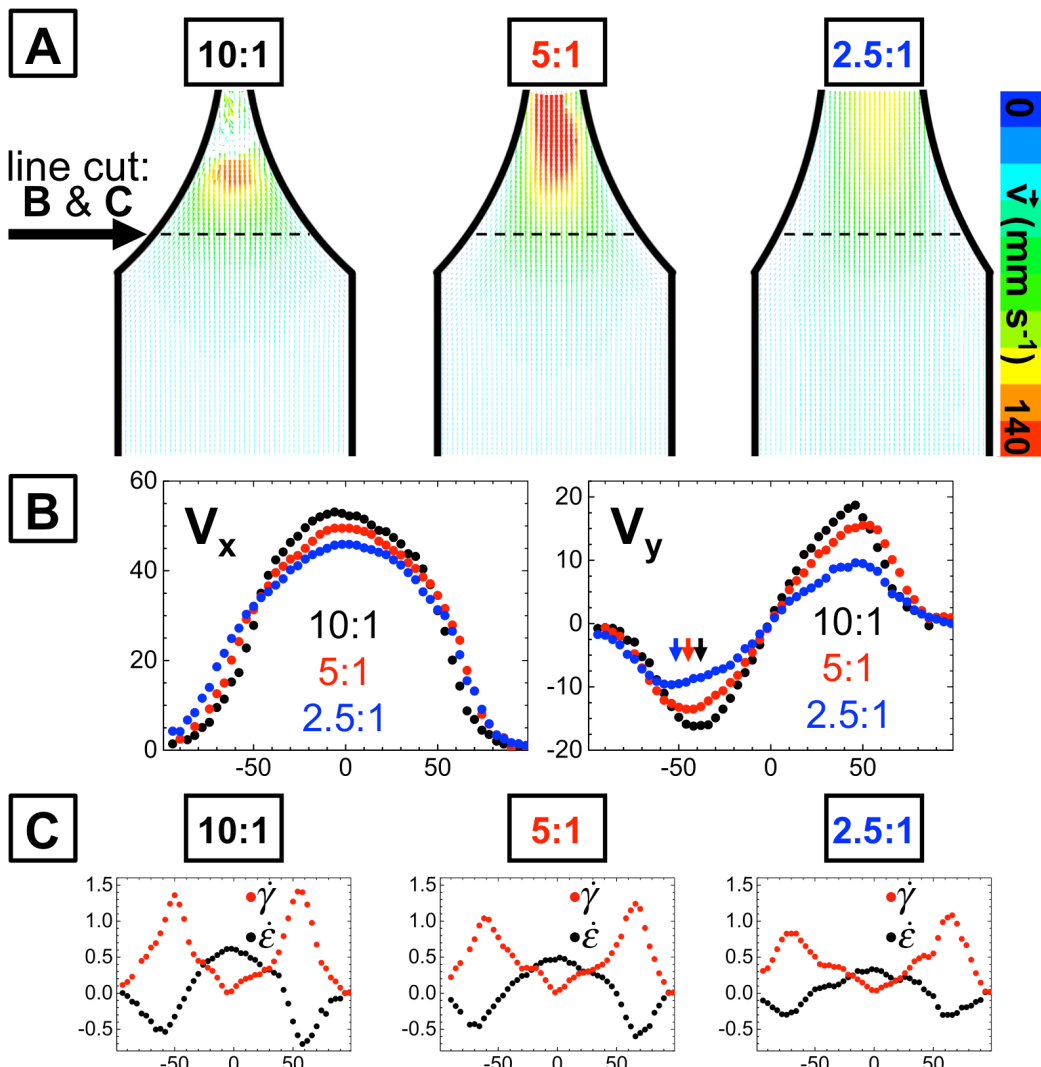


Figure 7 μPIV and experimental flow patterns for the study of the tapering ratio influence on the micelle's orientation distribution. The channels have a width of 250 µm with a 2:1 length ratio. The micelles with a concentration of 10% (w/w polymer in pure water) flow at a rate of 2000 µl h⁻¹. The tapering ratios are varied from 10:1 to 2.5:1 for these experiments. The data is obtained experimentally by microparticle image velocimetry using polystyrene spheres (1.65 µm radius, PDI 1.01) and a high speed camera at ca. 11 000 frames per second and can be used to generate (A) velocity fields, (B) velocity profiles and (C) shear- & extensional rates.

The influence of concentration on the perpendicular orientation. Additionally to the tapering variation, the flow velocity fields of different polymer concentrations were also measured to study its influence on the perpendicular micelle alignment and how the orientation effect is altered. These measurements are performed for three concentrations (25%, 10%, 0%; all w/w in pure water), while keeping the other experimental conditions constant (250 μm channel width, 2000 $\mu\text{l h}^{-1}$, 10:1 tapering-, 2:1 length ratio). The resulting velocity fields are shown in Fig.8A.

From the velocity pattern in x-direction (V_x), it becomes obvious that the particles in pure water (0%, blue curve) show a Newtonian parabolic flow profile with a maximum of ca. 68.9 mm s^{-1} . With raising concentrations (25%, black curve), the liquid's flow profile widens in the central part of the channel where it becomes relatively flat with a lower, but broader maximum velocity of ca. 33.8 mm s^{-1} . This behavior is typical for shear thinning non-Newtonian fluids as is the resulting plug-like flow.² This results in a decrease of x-orienting shear forces in the central region of the microchannel.

The velocities in y-direction (V_y) increase only slightly with increasing polymer concentrations. The V_y -curves start with a velocity of ca. 0 mm s^{-1} in the channel center which increases towards the channel walls to a value of ca. 12.5 mm s^{-1} before it slows down again. The algebraic signs indicates the different flow directions. These velocity turning points move out further towards the walls with increasing polymer concentrations, as shown in Fig.8B-right.

As shown in Fig.8C, the wide region in the center of the microchannel, where the extensional rate outweighs the shear rate, decreases noticeably with smaller polymer concentrations. This decrease leads to higher shear rates (V_x) due to the steeper parabolic velocity profile in x-direction. Fig.8C also points out that the extensional rate is larger at higher concentrations. Hence, increased shear thinning propagates the perpendicular micelle orientation due to the flow's plug-like flow nature which shields the micelles in the channel center from the wall shear and which enhances the effect of the extensional rate.

It has also been demonstrated that non-Newtonian computational fluid dynamics (CFD) simulations help to predict this effect and that this route can deliver theoretical data that are in very good agreement with experimental results obtained to μPIV .² Therefore, the present system is studied using CFD simulations as well to understand the influence on the sample's rheological properties on the perpendicular orientation. The results are described in a later section of this paper.

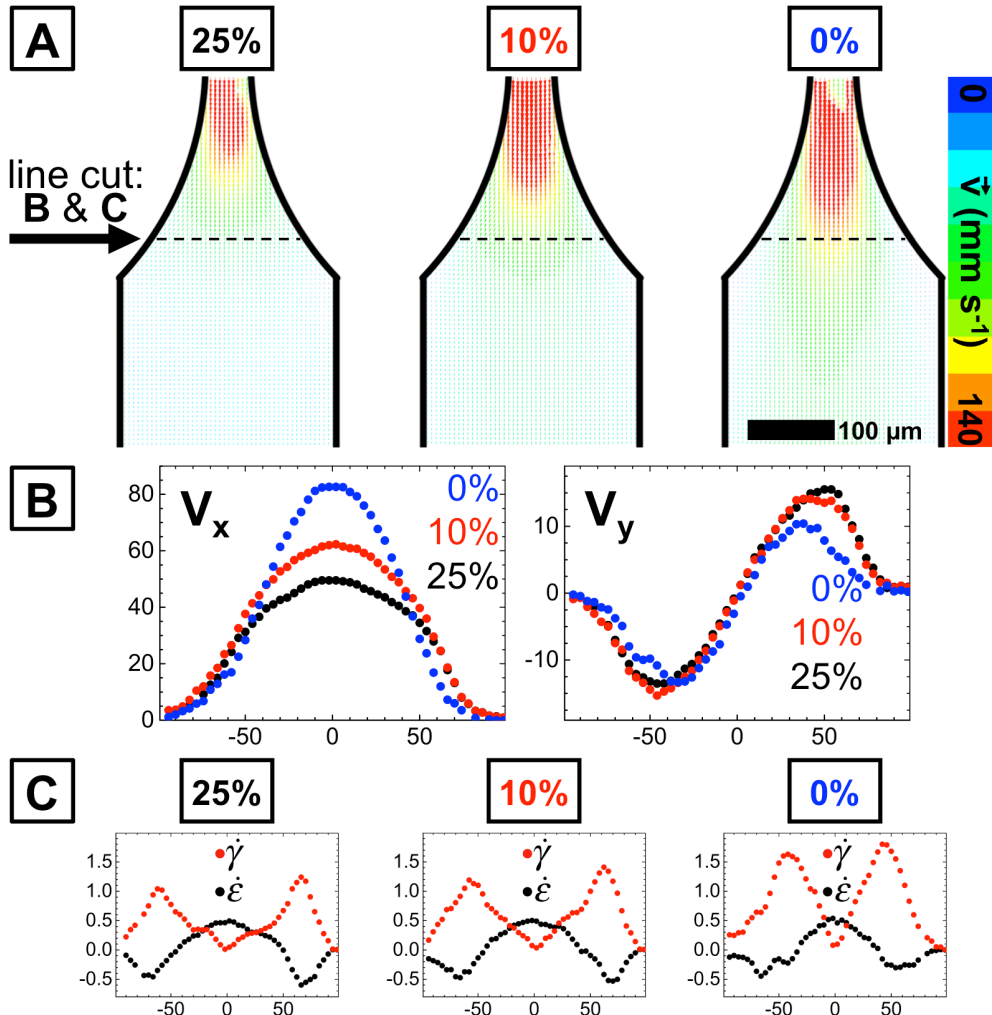


Figure 8 μPIV and experimental flow patterns for the study of the concentration influence on the micelle's orientation distribution. The channels have a width of 250 μm with a 10:1 tapering-, 2:1 length ratio. The micelles' flow speed is 2000 $\mu\text{l h}^{-1}$ at varying concentrations (25%, 10%, 0% w/w polymer in pure water). (A) The velocity fields of different polymer concentrations are measured experimentally by microparticle image velocimetry using polystyrene spheres (1.65 μm radius, PDI 1.01) and a high speed camera at ca. 11 000 frames per second. (B) Line cuts of the velocity profile in flow direction (left) and perpendicular to the flow (right) in the widening tapering at the position indicated by the black arrow in (A). (C) Line cuts of the corresponding shear rate (red) and extension rate (black) of (B) at different polymer micelle concentrations.

The interplay of different experimental parameters on the perpendicular orientation. The SAXS- and μPIV-results have shown that polarization microscopy is a valuable and precise tool for the analysis of the orientation of micelles. Therefore, the interplay of different experimental parameters and their influence on the micelle orientation are studied using polarization microscopy. This multi-parameter screening involves a range of flow rates (100 to 1000 $\mu\text{l h}^{-1}$), length- (9:1 to 5:1; w. r. t. channel width) and tapering ratios (10:1 to 2.5:1; w. r. t. channel width). The resulting width of the orange region is then measured directly after the tapering as indicated by the black arrows in Fig. 9A,B.

The first set of experiments compares the effect of the flow speed and is shown in Fig.9A. The polarization microscopic images show that the perpendicular region's width decreases with higher flow speeds. This can be explained by the stronger wall shear which lowers the viscosity of the non-Newtonian sample that changes the sample's velocity profile towards a more parabolic shape. Consequently, the region where the extensional force in y-direction dominates the micelle orientation decreases. The extensional flow in y-direction is determined by the tapering geometry and does not change with varying flow speeds.

Additionally to the flow speed data, Fig.9A *right* also contains a variation of tapering lengths which are varied from 9 to 5 times the channel width. We find that longer taperings increase the parallel-orienting effect of increased flow speeds because the area where shear from the walls can be applied to the sample is larger. This is shown by the decreasing relative widths of the orange perpendicular orientation region in Fig.9A *right*.

Next, the tapering ratios are varied which leads to results which are similar to the experimental series that have been discussed above, i.e. in Fig.4A. Varying the tapering length ratios reveals that the orange region or perpendicular micelles is decreased with longer taperings, as shown in Fig.9B *right*.

The interplay of all varied experimental parameters can be summarized in 3D multi-parameter spaces as shown in Fig.9C. The polarization microscopic images for all conditions are analyzed and the width of the orange sections of perpendicularly orientated micelles after the tapering is plotted against the different variables that define the 3D volume. The graphs show that the points of a given data series span a bended plane which lowers towards higher length ratios, faster speeds and lower tapering ratios. This is in agreement and sums up the experimental observations discussed above.

Based on each series' slope differences, this multi-parameter variation allows to rank the effects by their relative strength. The micelle concentration was not varied in this series, but as shown above and in the μ PIV-results overview (Fig. S3), higher micelle concentrations and more pronounced shear thinning of the samples strongly enhance the re-orientation effect. Therefore, the combined results yield the following hierarchy for the tendency to enhance the perpendicular orientation of anisotropic particles after narrow taperings: *tapering ratio* (y-orienting extensional rate) > *concentration* (plug-flow and non-Newtonian behavior) > *length ratio* (wall shear surface) > *flow speed* (wall shear intensity).

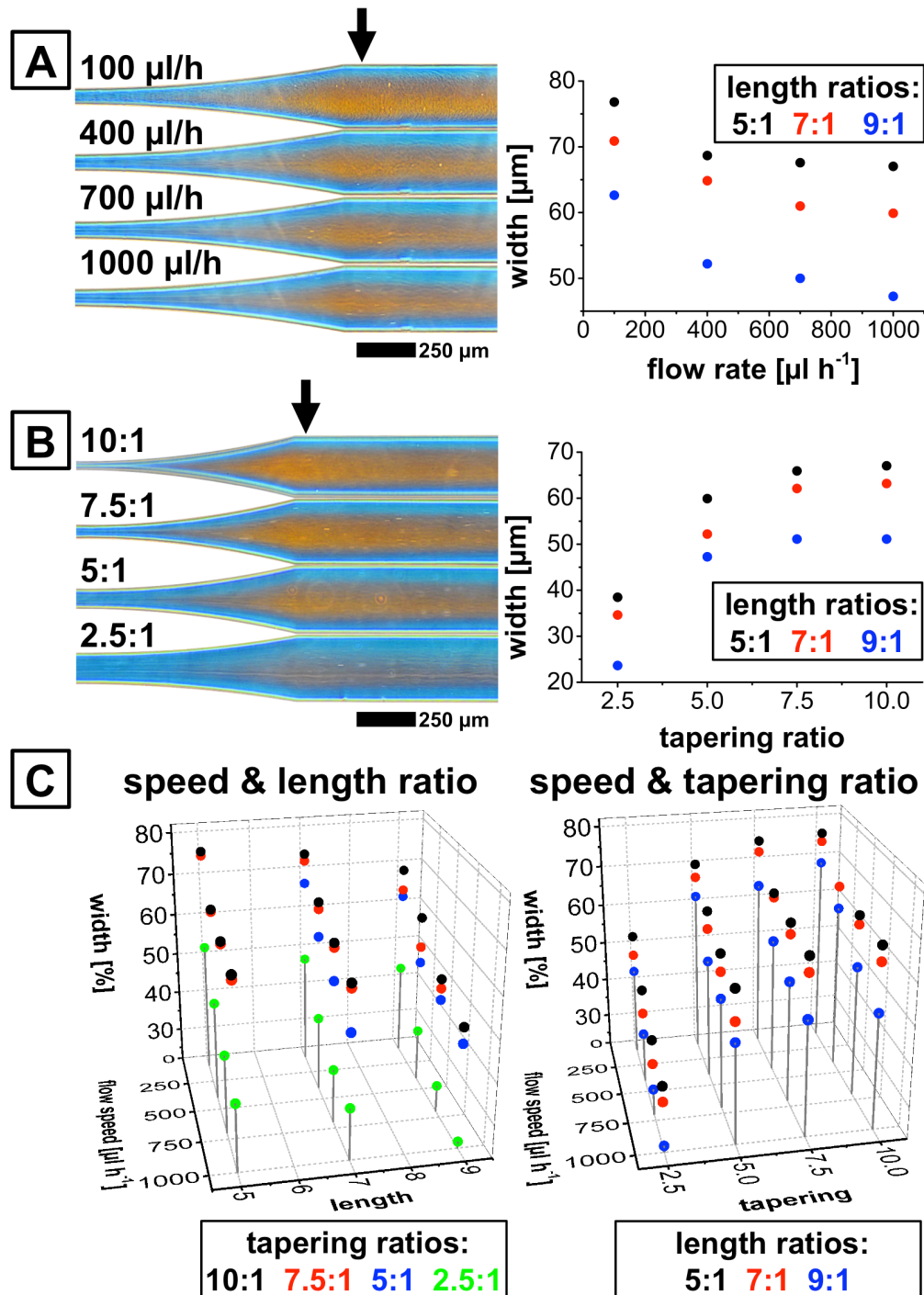


Figure 9 Parameter variations for the study of cylindrical micelle flow orientation using polarization microscopy. The orange region of perpendicular oriented micelles decreases in width with increasing flow speeds (A), lower tapering ratios (B) and increasing length of the tapering (A, B right). An overview of the combined parameter variations is given in (C). The channel width is 250 µm with a micelle concentration of 30% w/w throughout the experiments.

Influence Analysis of the rheological properties on the orientation distribution. Since the fluid dynamics of a sample depend on its rheological parameters, these parameters can be used to predict the fluid flow behavior. As demonstrated earlier for the non-Newtonian flow

of wormlike micelles, numerical CFD-simulations that are based on experimental rheometric data are in good agreement with the results from small-angle X-ray scattering, polarization microscopy and microparticle velocimetry.² Since the current system is based on the same block copolymer (PEB₃₉-PEO₁₀₂, Evonik), we assume the CFD-simulations to be also valid for predicting the general trends of the fluid's flow when the rheometric sample parameters are varied theoretically. The viscosity change of the micelle solution is described by the Cole-Cole- (or Cross-) equation which is given in the experimental section of this paper. From this formula, the zero shear viscosity η_0 as well as the internal relaxation time τ_c are varied in a series of CFD-simulations. For this, three different values for each parameter are chosen while all other parameters are kept constant, as summarized in Tab.1. An overview over the rheological curves that result from these parameter combinations are shown in Fig.10A. The different colors correspond to the varying zero shear viscosities while the symbol shapes change with varying internal relaxation times. These variations are to represent the rheological changes of a sample with different concentrations or types of anisotropic particles to study the general trends. Although similar rheological property-changes could also be achieved and studied experimentally, this CFD-simulation-based approach is easier to control and less time-consuming.

These different rheological curves for defined parameter variations are then used in the CFD-model to describe the fluid's rheometric properties.² Next, the resulting velocity flow fields from the simulation (not shown) are used to calculate the shear and extensional rates. As shown by the μ PIV-experiments and polarization microscopy, the regions of perpendicular micelle orientation can be found where the extensional rate $\dot{\epsilon}$ is comparable to the shear rate $\dot{\gamma}$.² Therefore, this ratio ($\dot{\epsilon}/\dot{\gamma}$) is used to color-code the simulated fluid flow inside the microchannel taperings. The resulting 2D color maps are arranged according to the parameter changes and shown in Fig.10B. An orange color in these 2D plots corresponds to a region where the micelle orientation is typically found to be perpendicular exceeding a value of 0.14. Accordingly, the blue area represents the regions of preferred parallel orientation with a ratio below 0.14.

The simulated results clearly show that the sample's *zero shear viscosity* η_0 has a strong influence on the width of the orange region after the tapering. The higher the initial viscosity of the sample, the more pronounced is the plug-like flow of the sample and the greater is the shielding of the central micelles against the wall-induced shear.

The *internal relaxation time* τ_c controls the capability of the micelles in the center to change their orientation while flowing through the tapering. Since this is a continuously flowing sample, the geometric shear field of the tapering can be seen as a re-orientation impulse. The shorter the internal relaxation time, the more are the anisotropic particles capable of reacting to this impulse and change their orientation according to the strongest orienting force. Further, the shorter the internal relaxation time, the less are the anisotropic particles affected

by wall shear effects because their viscosity starts to decrease at higher shear rates.

Consequently, rheological properties that are typical for non-Newtonian samples, like i.e. shear thinning and plug-like flow, strongly increases the tendency to find perpendicularly oriented micelles in microchannel after confined geometries. This observation is in agreement with the above-discussed results from small-angle X-ray scattering, polarization microscopy and microparticle image velocimetry.

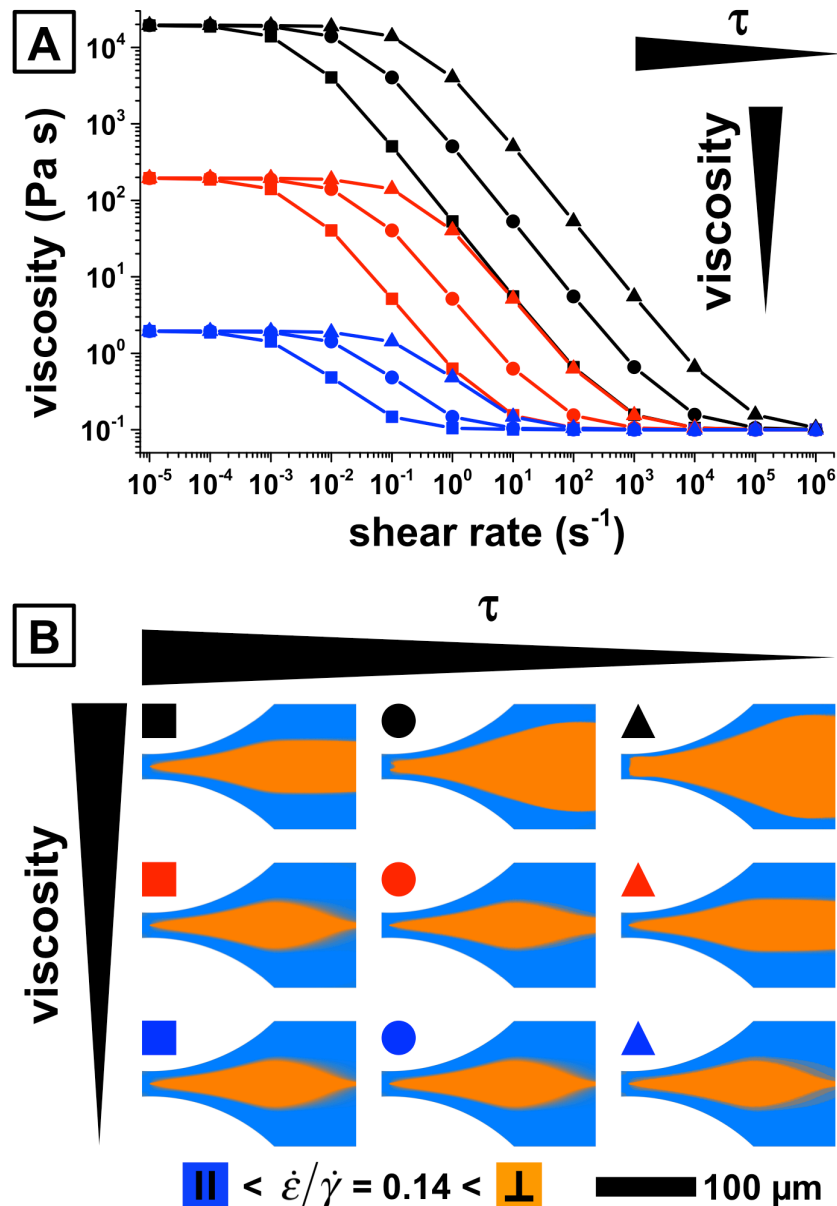


Figure 10 CFD-simulations based on theoretical variation of rheological sample parameters. (A) Curves are calculated based on the Cole-Cole-equation (see experimental section) that describe the fluid's viscosity change under the influence of shear. (B) CFD-simulation results that show color plots of the ratio ($\dot{\varepsilon}/\dot{\gamma}$) between the extensional rate $\dot{\varepsilon}$ and the shear rate $\dot{\gamma}$. The orange color represents the regions where the micelle orientation is typically found to be perpendicular (SAXS, μ PIV, polarization microscopy) because the mentioned ratio exceeds a value of 0.14. Accordingly, the blue area represents the regions of preferred parallel orientation with a ratio below 0.14.

Experimental

Preparation of Cylindrical Micelle Solution. The formation of wormlike micelles is based on the self-assembly of the amphiphile block copolymer PEB₃₉-PEO₁₀₂ (lyophilized before use, mean M_w = 7,700 g mol⁻¹, M_w/M_n = 1.06, Evonik).²⁵⁻²⁷ The polymer is dissolved in pure water (Millipore-quality with a resistivity of 18.1 MΩ cm⁻¹), homogenized using an UltraTurrax T8 (IKA Werke GmbH) and stored at room temperature for three weeks to allow the copolymer to swell. Prior to the use in microfluidic devices the solution was filtered through a polytetrafluoroethylene filter with 5 μm pore size.

Preparation of monodispere polystyrene (PS) tracer spheres for μPIV. The μPIV-experiments require to add small spherical tracer particles to the samples (4% w/w). The dispersion polymerization synthesis and characterization of these monodisperse polystyrene spheres (1.65 μm radius, PDI 1.01) is described in detail elsewhere.²⁸ To avoid clogging of the PS-spheres to the PDMS-microchannel walls, the particle hydrophilicity is increased by a treatment with polyacrylic acid (PAA, 1 g/l in 100mM NaCl) for 15 min under continuous shaking.²⁸ The excess of PAA was removed by re-suspending the particles three times with pure water (Millipore quality).

Microfluidic (SAXS) device fabrication. The microchannels are designed using AutoCAD 2013 (Autodesk) and printed on a high-resolution emulsion film mask (JD Phtoto). An example of the channel geometry is shown in Fig.1A. The subsequent fabrication of master-templates for replication and PDMS-devices (sealed with glass-slides) for polarization microscopy and the μPIV-experiments are based on standard soft lithography which is described elsewhere.^{20,21} This process involves spin coating the photo resist SU-8 50 (Microchem) onto polished silicon wafers (Si-Mat) for controlled channel heights (100 μm) and is illustrated in Fig.S41. The fabrication for the SAXS-compatible NOA81-devices includes an additional microstructuring step using a mask aligner (Süss Mikro Tec) for the generation of a two-layer microstructure as pointed out in Fig.S42. The first SU-8-layer enables to control the window thickness by adding an additional gap layer next to the microchannels for the experiments. The second layer contains the microchannels for the liquid flow (and the second layer of the gap structure). The final SU-8-master template is then replicated using standard PDMS-based soft lithography using Sylgard 184 (Dow Corning) as illustrated in Fig.S43.^{20,21}

Next, the PDMS-replica is used for microstructuring the UV-curable adhesive NOA81 (Nordland).^{17,18} This method is based on a NOA-PDMS-hybrid routine that is described elsewhere,⁹ but it is modified to allow an improved solvent compatibility.¹⁸ Instead of drilling holes through the finished device and sealing it with PDMS, glue and tapes, a different approach was used.

First, holes are punched into the replicated PDMS microchannel-template using a biopsy needle (Harris Uni-Core). Next, the tubings which only serve as a template, are inserted into these holes before the liquid NOA81 is poured over the PDMS-template. A flat PDMS-block with the intended scan-window size is laid over a liquid NOA81-drop which spreads itself. The two-layered gap structure next to the microchannels control the device material height in this step, while the liquid NOA81-drop next to the template-tubings should have a height of ca. 2-3 mm. After UV-curing, the PDMS-block and the template tubings are removed before the open microchannels are sealed with a thin NOA81-film which was prepared in a similar fashion: no template-tubing, gap structures and flat (or alternatively 3D-microchannel-structured). The sealing of the device with a second NOA81-film by UV-curing is possible because the gas-permeability at the PDMS-NOA81-interface inhibits the complete curing.⁹ This inhibition leaves a thin curable layer for the device sealing at the NOA81-surface.

The resulting NOA81-based microfluidic device is very thin in the X-ray microbeam scanning area (ca. 250 µm) with a homogenous channel height and the microfluidic device has a very low X-ray background signal. Further, the increased material thickness at the inlets, which were formed by the template-tubings, allow to attach the tubings directly to the device without using an additional tubing-interface PDMS-layer as described earlier.⁹ Therefore the full solvent compatibility of NOA81 (i.e. water, unpolar organic solvents, etc.) is maintained.¹⁸ For compatibility with higher pressures and to guarantee reliable, stable tubing interfaces (i.e. for precious synchrotron beamtimes), it is suggested to glue the tubings to the device using two-component epoxy glues (Loctite, Henkel).

Microscopic setups. The *polarization microscopic* experiments are recorded using the inverted microscope Axiovert S100 (Zeiss). The orange and blue color representation originates from using crossed polarizers and a quarter wave plate. The images are recorded using a Nikon D7000 camera.

The *microparticle image velocimetry* setup involves an IX71 inverted microscope (Olympus) with a 100 W tungsten light that was focused onto the sensor of a Phantom v9.1 (Vision Research) high speed camera (2 µs minimum exposure, maximum rate of 2 Gpx s⁻¹). The recorded video frames are analyzed using the open source software package *JPIV* which generates velocity fields by correlating the captured frames.²⁴

COMSOL simulation

The CFD-simulations are performed in COMSOL Multiphysics 4.2a using a previously described model for non-Newtonian fluid in tapered microchannels of which the theoretical background is described elsewhere.² The underlying microchannel geometry is adjusted to the existing devices (250 µm channel width, 5:1 tapering-, 2:1 length ratio, 100 µm height) at a flow rate of 2000 µl h⁻¹. The screening mainly involved a variation of the rheological properties of the sample which are described by the Cole-Cole- (or Cross-) equation:²⁹⁻³¹

$$\eta = \eta_\infty + \frac{\eta_0 - \eta_\infty}{1 + (\tau_c \dot{\gamma})^n}$$

with the zero shear viscosity η_0 , the high-shear viscosity η_∞ , the internal relaxation time τ_c and the power law exponent n characterizing the shear thinning between η_0 and η_∞ . The modeling parameters are listed in the following Tab.1.

Table 1 List of modeling parameters for the CFD-simulations including the rheological parameter variations.

Parameter	Value
Flow rate v_{flow} , $\mu\text{l h}^{-1}$	2000
Flow speed v_{speed} , m s^{-1}	0.0222
Zero shear viscosity η_0 , Pa s	19522; 195.22; 1.9522
High shear viscosity η_∞ , Pa s	0.1
Internal relaxation time τ_c , s	388.5; 38.85; 3.885
Power law exponent n	0.99
Density ρ , kg m^{-3}	998.2
Temperature T, K	293.15
Channel width W_{Ch} , μm	250
Channel height H_{Ch} , μm	100
Tapering ratio T_{Ch}	10:1
Tapering length ratio L_{Ch}	2:1

Device operation at the PETRAIII synchrotron (P03 beamline, HASYLAB/DESY). The microfluidic SAXS scanning experiments are performed at the Micro- and Nanofocus X-ray Scattering beamline (MiNaXS) in Hamburg, Germany. The fluid flow is controlled using high-precision syringe pumps (Nemesys, Cetoni GmbH). After the collection of the relevant background data from the microchannel and an extended flow equilibration time at a flow rate of $200 \mu\text{l h}^{-1}$, the SAXS-mapping scans are commenced. The microfocused X-ray beam for these scans has a wavelength of $\lambda = 0.095 \text{ nm}$ with a width of $20 \mu\text{m}$ and a height of $30 \mu\text{m}$. The SAXS patterns are recorded at a distance of 4840 mm with integration time of 0.5 s using a digital detector (Pilatus by Dectris) with a pixel size of $172 \mu\text{m}$ by $172 \mu\text{m}$ with.

Conclusions

In conclusion, we have performed a fundamental study of the re-orientation of anisotropic particles in confined geometries for a wide range of experimental conditions.

We also demonstrated in great detail how multiple analysis techniques can be used and combined in a complementary way taking advantage of the highly reproducible design control provided by microfluidics. Next to the here-demonstrated correlation of fluid dynamics to structural information, the combination of complementary methods is also applicable and extendable to other methods and more experiments, such as flow field analysis for mixing experiments, following synthetic reaction kinetics and mapping nucleation and growth processes.^{5,6,9,32-34}

Using complementary analysis tools, including small-angle X-ray scattering, microparticle image velocimetry, polarization microscopy and CFD-simulations, we could identify design rules for predicting and controlling the perpendicular re-orientation of anisotropic particles after narrow sections. A relative ranking according to the effectiveness for perpendicular alignment of anisotropic particles is derived as: *tapering ratio* (y-orienting extensional rate) > *concentration* (plug-flow and non-Newtonian behavior) > *length ratio* (wall shear surface) > *flow speed* (wall shear intensity). The regions for perpendicular orientation can be controlled with further precision by tuning the rheological properties of the sample, i. e. like the zero shear viscosity and the internal relaxation time. Consequently, the perpendicular orientation of anisotropic particles can be maximized by increasing the tapering ratio, shortening the tapering, minimizing the flow speed and increasing the sample's plug-flow by increasing its high zero shear viscosity and shortening its internal relaxation time or vice versa for maintaining and increasing parallel alignment.

In summary, the here presented study provides conditions for controlling the orientation of anisotropic particles. A strong parallel orientation is of great importance for the spinning of fibers because it typically leads to increased crystallinity in the fiber and, hence, better mechanical performance.^{12,35} However, the perpendicular orientation of particles can also be of great interest for applications that involve electrical or thermal transport perpendicular to a surface, such as in isolating materials or hybrid solar cells.³⁶⁻³⁸

References

1. D. C. Duffy, J. C. McDonald, O. J. A. Schueller, and G. M. Whitesides, *Anal. Chem.*, 1998, **70**, 4974–4984.
2. M. Trebbin, D. Steinhauser, J. Perlich, A. Buffet, S. V. Roth, W. Zimmermann, J. Thiele, and S. Förster, *PNAS*, 2013, **110**, 6706–6711.
3. A. Otten, S. Köster, B. Struth, A. Snigirev, and T. Pfohl, *J Synchrotron Rad*, 2005, **12**, 745–750.
4. R. Barrett, M. Faucon, J. Lopez, G. Cristobal, F. Destremaut, A. Dodge, P. Guillot, P. Laval, C. Masselon, and J.-B. Salmon, *Lab Chip*, 2006, **6**, 494–499.
5. T. Pfohl, A. Otten, S. Köster, R. Dootz, B. Struth, and H. M. Evans, *Biomacromolecules*, 2007, **8**, 2167–2172.
6. H. M. Evans, R. Dootz, S. Koester, B. Struth, and T. Pfohl, *Bull Pol Acad Sci-Te*, 2007, **55**, 217–227.
7. R. Dootz, H. Evans, S. Köster, and T. Pfohl, *Small*, 2007, **3**, 96–100.
8. K. N. Toft, B. Vestergaard, S. S. Nielsen, D. Snakenborg, M. G. Jeppesen, J. K. Jacobsen, L. Arleth, and J. P. Kutter, *Anal. Chem.*, 2008, **80**, 3648–3654.
9. M. E. Brennich, J.-F. Nolting, C. Dammann, B. Nöding, S. Bauch, H. Herrmann, T. Pfohl, and S. Köster, *Lab Chip*, 2011, **11**, 708.
10. S. M. Taheri, S. Fischer, M. Trebbin, S. With, J. H. Schröder, J. Perlich, S. V. Roth, and S. Förster, *Soft Matter*, 2012, **8**, 12124.
11. A. Buffet, A. Rothkirch, R. Döhrmann, V. Körstgens, M. M. Abul Kashem, J. Perlich, G. Herzog, M. Schwartzkopf, R. Gehrke, P. Müller-Buschbaum, and S. V. Roth, *J. Synchrotron Rad (2012)*, **19**, 647–655 [[doi:10.1107/S0909049512016895](https://doi.org/10.1107/S0909049512016895)], 2012, 1–7.
12. T. Vad, J. Wulffhorst, T.-T. Pan, W. Steinmann, S. Dabringhaus, M. Beckers, G. Seide, T. Gries, W. F. C. Sager, M. Heidelmann, and T. E. Weirich, *Macromolecules*, 2013, **130705124618000**.
13. H. H. Yang and S. R. Allen, *Advanced Fiber Spinning Technology*, Woodhead Publications, Abingdon, 2000.
14. J. A. Cuculo, J. F. Hotter, Q. Zhou, and Q. Structure Formation in Polymeric Fibers, Hanser Gardner Publications, 1st edn. 2004.
15. N. F. Bouxsein, L. S. Hirst, Y. Li, and C. R. Safinya, *Applied Physics ...*, 2004.
16. K. J. Humphry, P. M. Kulkarni, D. A. Weitz, J. F. Morris, and H. A. Stone, *Phys. Fluids*, 2010, **22**, 081703.
17. C. F. Carlborg, T. Haraldsson, K. Öberg, M. Malkoch, and W. van der Wijngaart, *Lab Chip*, 2010, **11**, 3136.
18. P. Wägli, A. Homsy, and N. F. de Rooij, *Sensors and Actuators B: Chemical*, 2011, **156**, 994–1001.
19. E. Sollier, C. Murray, P. Maoddi, and D. Di Carlo, *Lab Chip*, 2011, **11**, 3752.
20. G. M. Whitesides and Y. Xia, *Angew. Chem. Int. Ed.*, 1998, **37**, 550–575.
21. Y. Xia and G. M. Whitesides, *Annual review of materials science*, 1998, **28**, 153–184.
22. S. Förster, L. Apostol, and W. Bras, *J Appl Cryst*, 2010, **43**, 639–646.

23. S. Förster, S. Fischer, K. Zielske, C. Schellbach, M. Sztucki, P. Lindner, and J. Perlich, *Advances in Colloid and Interface Science*, 2011, **163**, 53–83.
24. *JPIV v1.0: Open source software package for particle image velocimetry. Available at www.jpv.vennemann-online.de. Accessed July 1, 2015.*
25. S. Förster and T. Plantenberg, *Angew. Chem. Int. Ed.*, 2002, **41**.
26. M. Antonietti and S. Förster, *Advanced Materials*, 2003, **15**, 1323–1333.
27. S. Förster, M. Konrad, and P. Lindner, *Phys. Rev. Lett.*, 2005, **94**.
28. C. Hanske, J. Erath, C. Kühr, M. Trebbin, C. Schneider, A. Wittemann, and A. Fery, *Zeitschrift für Physikalische Chemie*, 2012, **226**, 569–584.
29. K. S. Cole and R. H. Cole, *J. Chem. Phys.*, 1941, **9**, 341.
30. K. S. Cole, *J. Chem. Phys.*, 1942, **10**, 98.
31. M. M. Cross, *J Coll Sci Imp U Tok*, 1965, **20**, 417–437.
32. L. Pollack, M. Tate, N. Darnton, J. Knight, S. Gruner, W. Eaton, and R. Austin, *PNAS*, 1999, **96**, 10115–10117.
33. L. Pollack, M. W. Tate, A. C. Finnefrock, C. Kalidas, S. Trotter, N. C. Darnton, L. Lurio, R. H. Austin, C. A. Batt, S. M. Gruner, and S. Mochrie, *Phys. Rev. Lett.*, 2001, **86**, 4962–4965.
34. R. Russell, I. S. Millettt, M. W. Tate, L. W. Kwok, B. Nakatani, S. M. Gruner, S. Mochrie, V. Pande, S. Doniach, D. Herschlag, and L. Pollack, *Proceedings of the National Academy of Sciences*, 2002, **99**, 4266–4271.
35. M. E. Kinahan, E. Filippidi, S. Köster, X. Hu, H. M. Evans, T. Pfohl, D. L. Kaplan, and J. Wong, *Biomacromolecules*, 2011, **12**, 1504–1511.
36. G. Kaune, M. A. Ruderer, E. Metwalli, W. Wang, S. Couet, K. Schlage, R. Röhlsberger, S. V. Roth, and P. Müller-Buschbaum, *ACS Appl. Mater. Interfaces*, 2009, **1**, 353–360.
37. M. Rawolle, M. A. Niedermeier, G. Kaune, J. Perlich, P. Lellig, M. Memesa, Y.-J. Cheng, J. S. Gutmann, and P. Müller-Buschbaum, *Chem. Soc. Rev.*, 2012, **41**, 5131.
38. M. A. Ruderer, S. Guo, R. Meier, H.-Y. Chiang, V. Körstgens, J. Wiedersich, J. Perlich, S. V. Roth, and P. Müller-Buschbaum, *Adv. Funct. Mater.*, 2011, **21**, 3382–3391.

Supplemental Information

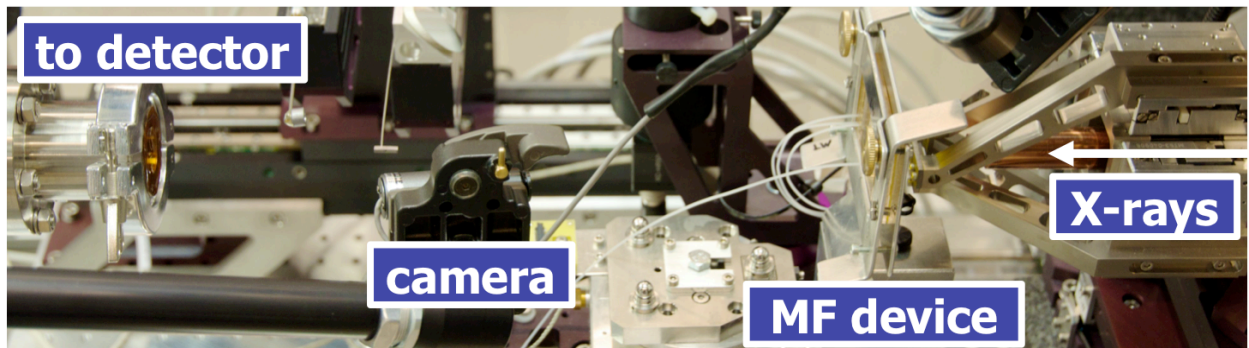


Figure S1 Experimental setup for capturing structural information of complex fluids *in situ* at the microfocus beamline P03/MiNaXS at the highly brilliant synchrotron source PETRA III (HASYLAB, DESY). ¹¹ The typical experimental setup consist of three fundamental elements: microfocused X-ray beam, X-ray compatible microfluidic device and X-ray detector. This combination of microfluidics and X-ray microbeams is a powerful experimental technique which offers various advantages compared to non-continuous SAXS experiments.

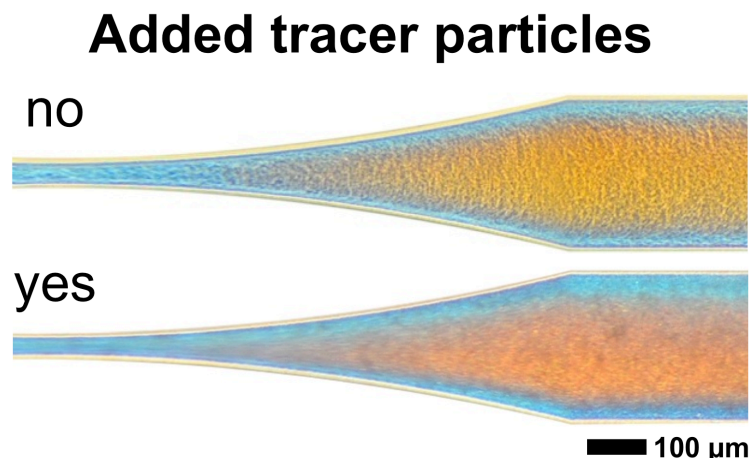


Figure S2 Polarization microscopic image for the illustration that the perpendicular micelle orientation effect is maintained after the addition of small polystyrene tracer spheres (1.65 μm radius, PDI 1.01).

Combined μ PIV-analysis. To get a better overview over the re-orientation effect and extend the above PIV analysis, the measured μ PIV-data is used to calculate the ratio between the extensional- and the shear-rate ($\dot{\epsilon}/\dot{\gamma}$). The corresponding 2D color maps are generated from these calculated ratios for all positions, as shown in Fig.S3. In these graphs, the red areas indicate the areas where the micelles are oriented parallel to the flow due to dominating shear forces in flow direction. The blue color mark the regions where perpendicular-oriented micelles are observed because the extensional forces perpendicular to the flow exceed the forces of the parallel shear.

Since the 2D graphs are based on the ratio of extensional and shear rates, little noise is strongly amplified due to its very flat velocity profile at lower flow rates (division by ‘close to’ zero). Therefore these regions appear as speckled patterns (i.e. Fig.S3C *left*) where homogenous regions of perpendicular micelle orientation are observed in polarization microscopy.

The *tapering ratio* variation is analyzed and similar to the results from SAXS, polarization microscopy and CFD-simulations, we find in the μ PIV-experiments that the regions for perpendicular orientation in all taperings and the perpendicular orientation are most pronounced at higher tapering ratios (Fig.S3A). Here, the strength of extensional forces perpendicular to the flow strongly dominate micelle orientation compared to parallel-directed shear forces.

The *concentration* variation reveals that perpendicular orientation of anisotropic particles can also be expected of Newtonian fluids, but only in the channel’s center region where the x-velocity profile has its turning point with low shear rates close to zero. In case of the non-Newtonian fluids, the flow profile becomes relatively flat at high concentrations. This leads to a plug-like flow profile which shields the parallel-orienting wall shear and the perpendicular micelle orientation is maintained.

The varying *flow speeds* supports the characteristic, that the perpendicular micelle orientation decreases with higher flow speeds, which is demonstrated above in Fig.9.

In summary, the highest perpendicular micelle orientation is observed after taperings with high aspect ratios, at high micelle concentrations and low flow speeds (Fig.S3).

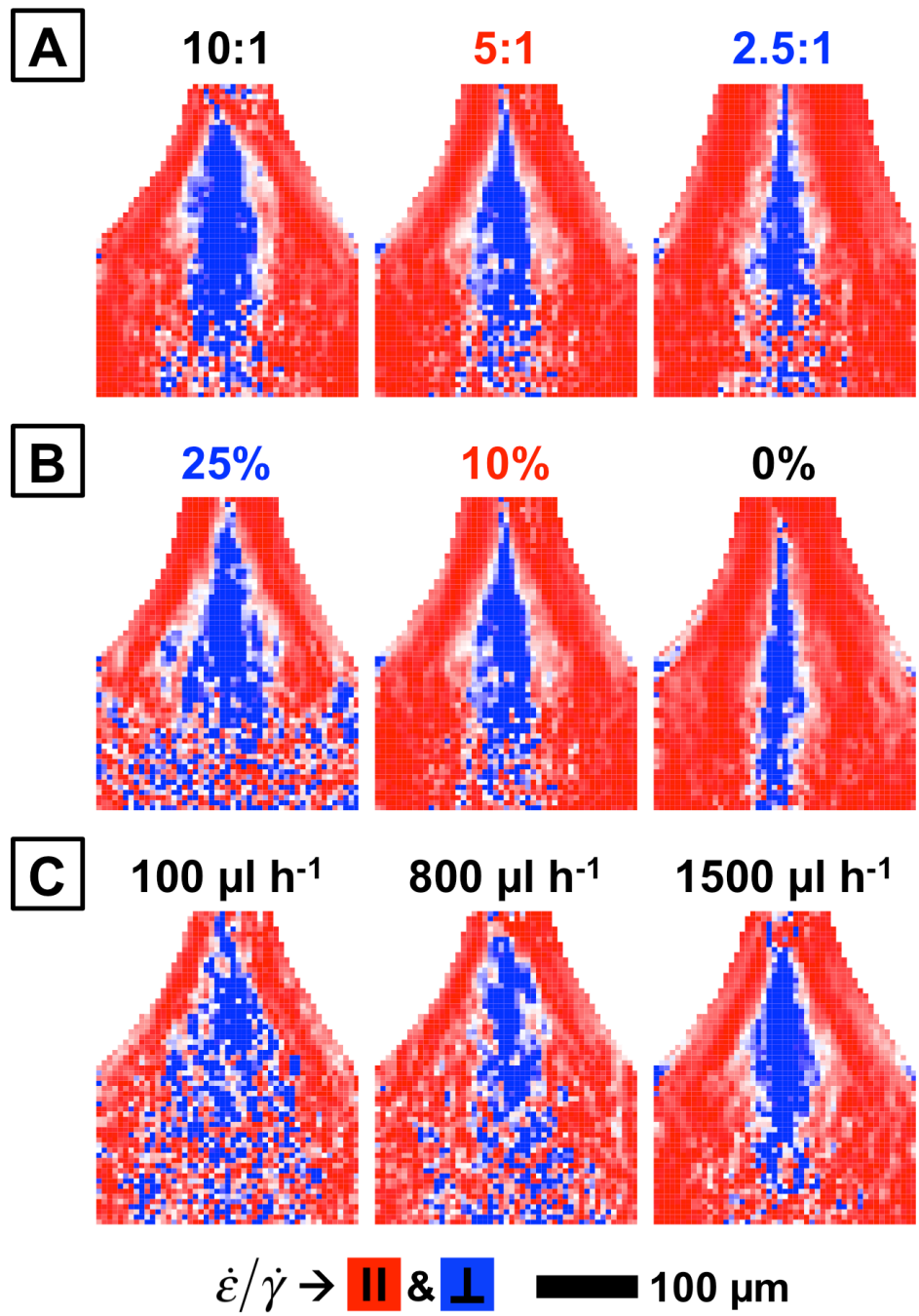


Figure S3 Overview over the ratio between extensional- and shear rate ($\dot{\varepsilon}/\dot{\gamma}$) which is plotted in 2D PIV maps across the microchannel at different experimental variations: (A) tapering ratios from 10:1 to 2.5:1 (2000 $\mu\text{l h}^{-1}$, polymer concentration 10% w/w in pure water), (B) polymer concentrations from 25% to 0% (all w/w in pure water, 5:1 tapering ratio, 2000 $\mu\text{l h}^{-1}$) and (C) speeds from 100 $\mu\text{l h}^{-1}$ to 1500 $\mu\text{l h}^{-1}$ (10:1 tapering-, polymer concentration 10% w/w in pure water). All experiments were performed in 250 μm -wide microchannel with a 2:1 length ratio. The red color represents the regions where the shear rate $\dot{\gamma}$ dominates the flow which leads a stronger parallel micelle orientation. The blue color marks the regions where the stronger extensional rate $\dot{\varepsilon}$ leads to perpendicularly oriented micelles. The speckles in the straight sections of the microchannel are the result of data noise due to the relatively flat velocity profiles of the non-Newtonian fluids.

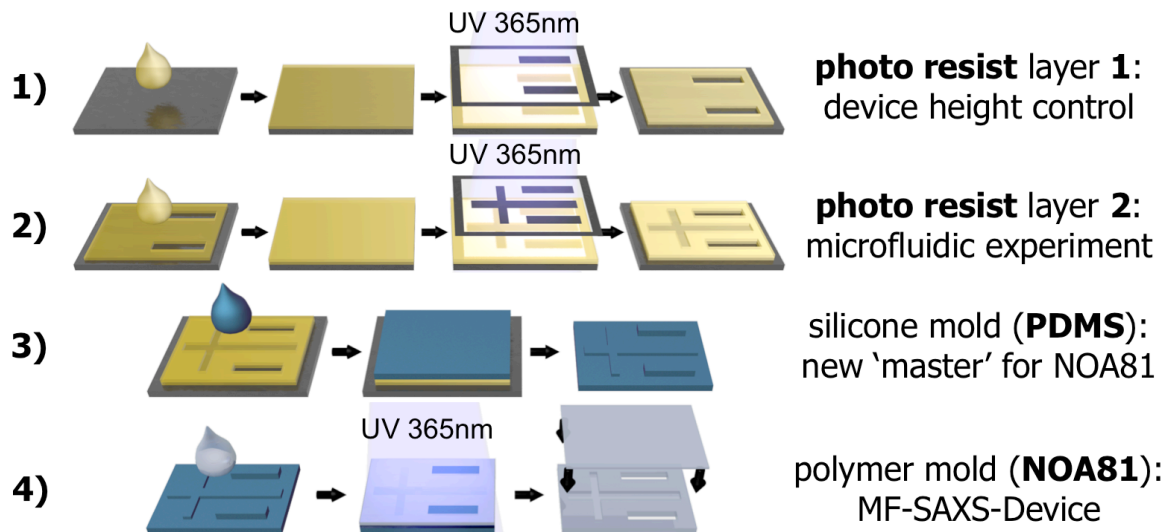


Figure S4 Illustration of the device fabrication of X-ray compatible microfluidic devices. (1,2) A polished silicon wafer is spin coated with a photo resist and exposed with UV light in a multi-layer-lithographic process. (3) The resulting microstructured master is replicated using PDMS.^{20,21} (4) The PDMS-master is then used as a replication template for NOA81.⁹

7.3 Microfluidic Liquid Jet System with compatibility for atmospheric and vacuum conditions

Martin Trebbin,¹ Kilian Krüger,¹ Daniel DePonte,^{2,3} Stephan V. Roth,⁴ Henry N. Chapman,³ and Stephan Förster^{1*}

¹ University of Bayreuth, Physical Chemistry I

² SLAC, Stanford, California, USA.

³ CFEL, DESY, Hamburg, Germany.

⁴ HASYLAB, DESY, Hamburg, Germany.

We present microfluidic chip based devices that produce liquid jets with micrometer diameters while operating at very low flow rates. The chip production is based on established soft-lithographical techniques employing a three-layer design protocol. This allows the exact, controlled and reproducible design of critical parts such as nozzles and the production of nozzle arrays. The microfluidic chips reproducibly generate liquid jets exiting at perfect right angles with diameters between 20 μm and 2 μm ; under special circumstances even down to 0.9 μm . Jetting diameter, jet length, the domain of the jetting/dripping instability can be predicted and controlled based on the theory for liquid jets in the plate-orifice configuration described by Gañán-Calvo *et al.* Additionally, conditions under which the device produces highly reproducible monodisperse droplets at exact and predictable rates can be achieved. The devices operate under atmospheric and under vacuum conditions making them highly relevant for a wide range of applications, for example at free-electron lasers. Further, the straightforward integration of additional features such as a jet-in-jet is demonstrated. This device design has the potential to integrate more features based on established microfluidic components and become a standard device for small liquid jet production.

Introduction

The generation of liquid jets with diameters in the micron- or sub-micron range are of high relevance in many technologies such as microfiber spinning,¹⁻⁷ inkjet printing,⁸⁻¹⁰ the microanalytical dosing of liquids,^{11,12} mostly applied for pharmaceutical formulations^{13,14} and in microbioanalytics.^{15,16} A very challenging example of the latter is its use at free electron lasers (FEL) to provide sub-micron diameter liquid jets for femtosecond X-ray nanocrystallography.^{17,18} The enormous intensity of the X-ray pulses at FELs demands a continuous stream of fresh sample, in some cases also at high vacuum conditions, which can be realized by the generation of very small liquid jets that consume only very small amounts of sample over time.

Thin liquid jets can be generated based on the principles of hydrodynamic focusing using gas sheath developed by Gañán-Calvo *et al.*¹⁹⁻²² Microjets can also be realized by other techniques such as high-pressure liquid flows or electric fields (electro-spinning).^{1,3,5}

The success of pressurized gas systems is based on the gas dynamic virtual nozzle (GDVN)-principle where the liquid enters a volume which is completely filled with pressurized gas that is moving towards the nozzle's exit. This gas flow controls the liquid's shape and flow, forming a continuous liquid jet that is smaller than the liquid inlet geometry and that exits the nozzle without wall contact. Hence, nozzle clogging is essentially eliminated as an experimental concern and sub-10 µm jets and droplets will only be feasible using the GDVN-principle.^{5,23,24} Further, the underlying physics of the GDVN-principle is well understood which helps to create devices that allow resilient jetting of a wide range of liquid samples with only very little consumption of sample over time.^{14,25-31} As an example, recent publications show that sub-micrometer liquid jets at flow rates around 75 µl h⁻¹ are possible using this principle.^{32,33} This high efficiency of sample consumption for the generation of continuous liquid jets is a key element for microanalytical applications.^{17,34-37}

Current realizations of pressurized gas devices for the generation of liquid jets use either a plate-orifice configuration or co-axial glass capillaries^{5,23} of which the latter are particularly used for free electron lasers.^{17,19,23,24,29,35-48} A recent publication also describes a hybrid GDVN-design that incorporates glass-capillaries within a microfluidic channel structure, but the liquid jets are only generated within the closed channel geometry.²⁴

The production of such glass capillaries requires complex production steps such as flame polishing, careful alignment of the inner and outer glass capillaries, and final grinding of the tip.^{23,24,29,32,44,49,50} The jetting capability can only be assessed after fabrication, thus limiting the production efficiency. Although FEM-simulations have been performed to predict jetting performance in glass capillary nozzles,³² variations in nozzle dimensions during manufacturing can lead to deviations from the targeted design. This complex fabrication process and complicated geometry control currently limits their availability. Alternatives

which satisfy the raising demand for such liquid jet delivery systems are greatly required. Further, there is a great need to implement additional features such as micromixers or nozzle arrays for advanced multi-functional automated sample delivery.

Microfluidics has become a powerful technology for the handling and manipulation of very small fluid volumes. Devices are easy to fabricate and can contain components for mixing,⁵¹⁻⁵⁴ sorting,⁵⁵⁻⁵⁹ monitoring,^{60,61} injecting,⁶²⁻⁶⁶ and many other applications.⁶⁷⁻⁷² Especially the development of microfluidic devices as an experimental sample environment for (microfocus) X-ray experiments have made enormous progress in the recent years.⁷³⁻⁸⁸ These devices are designed for X-ray transmission measurements in closed microchannels. With the advent of high-intensity sub-micron X-ray beams many devices are not useful because of beam degradation and high X-ray background of the chip materials in the beam. Here micro liquid jets, produced by established microfluidic technology would be highly desirable.

There have been only few examples of microfluidic devices that were used for the generation of free liquid jets.^{89,90} These devices have been optimized to perform fast mixing experiments at 3rd generation synchrotron sources based on hydrodynamic focusing at very high flow rates. As a consequence, the devices will operate in the jetting regime, but require samples that are available in sufficient amounts. Another approach to deliver samples in mid-air could be the use of sprays using microfluidic spray dryers that are designed for drug formulation.⁸⁹⁻⁹¹

In this paper we present the development, fabrication and testing of easy-to-build microfluidic micron-size liquid jet devices which run essentially clogging-free due to their GDVN-based design.²³ Further, these devices are capable to operate under atmospheric and vacuum conditions making them compatible with evacuated sample environments. For the device production we developed a three-layer soft-lithography protocol that allows the efficient and reproducible fabrication of microfluidic liquid jet devices that incorporate arrays of multiple jet-nozzles on each single chip. The capability to predict jetting characteristics is demonstrated by the comparison of experimental data using a high speed camera with theoretical models and is underlined by additional 3D finite-element-based CFD-simulations of the given nozzle design. Further, we show the potential of sub-micrometer jetting under vacuum conditions and demonstrate, with the example of a jet-in-jet system, the possibility to integrate more complicated design structures into the microfluidic device without the need of additional production steps.

Device production

Microfluidic soft lithography. The microfluidic liquid jet devices are fabricated using established soft lithography techniques.⁹²⁻⁹⁶ This process can be seen as a two-part sequence.

The first part is about creating a microstructured master which will then be used as a molding template in the second part of the device fabrication routine. This master can be created relatively fast which enables rapid prototyping due to the use of established SU-8-

based photolithographic procedures. Further, this master can be re-used multiple times in the subsequent fabrication process.

The second part of the fabrication process can be performed easily and a large number of nozzle geometries can be replicated with each single mold. The molding and device sealing steps only require minimal equipment, which should help to migrate the microfluidic liquid jet technology to a wide range of users. An overview of this process is illustrated in Fig. 1 while further details are outlined in the next paragraph and the experimental section.

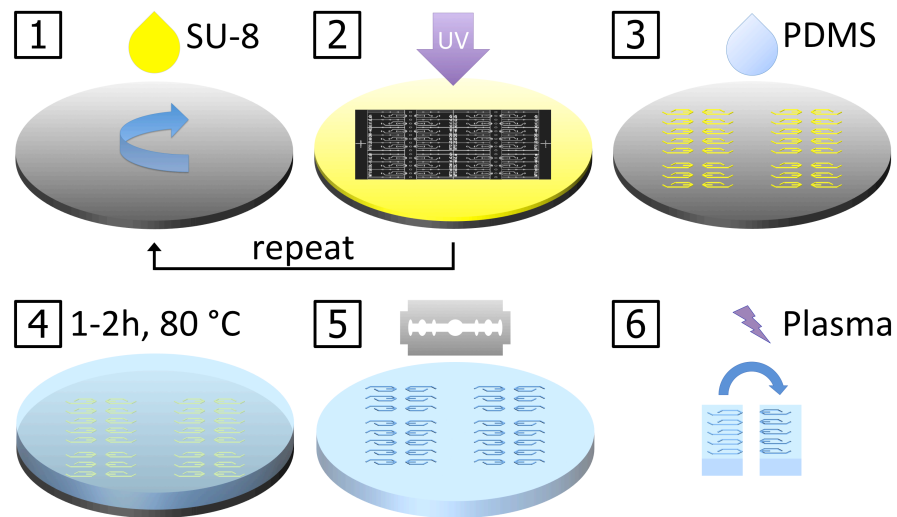


Fig. 1 Soft lithographic fabrication sequence for microfluidic liquid jet devices. The photolithographic master fabrication involves repeating steps to build up a multilayered microstructure: spin-coating (1) and UV-exposure (2). After development, the uncured photoresist is removed and the resulting microchannel template is replicated using polydimethylsiloxane (PDMS; 3,4). The replica is peeled off the master device and inlet ports for fluids are added. The polymer is cut using a razor blade (5) and the device is sealed using air plasma treatment (6).

Microfluidic liquid jet device fabrication. The integration of the GDVN-principle into the microfluidic chips is realized by fabricating 3D-microchannels that are replicated from multilayered SU-8-microstructures on a polished silicon wafer. The underlying photolithographic sequence for the creation of these multilayered templates involves repeating cycles of spin coating the photo resist, photo mask alignment and UV exposure. In this process, the layer combinations A+B+C or B+C are exposed onto the photoresist to create the desired nozzle geometries, as illustrated in Fig. 2.

Next, the master structure is replicated with polydimethylsiloxane (PDMS) which, in a single molding step, yields the upper and lower halves of the three-dimensional microchannels. Scanning electron micrographs of these PDMS-nozzle geometries are shown in Fig. 2 while their exact dimensions are summarized in Tab. 1.

Prior to the alignment and sealing of these PDMS-halves, the microfluidic liquid jet device fabrication requires to cut off excess PDMS next to the nozzle tips with a razor blade. This

cutting position is indicated by a red dotted line in Fig. 2. It is important to note that the jet nozzles are solely shaped by the lithographically created microstructures and will not be touched by the blade. This is ensured by the integration of the third C-layer which acts as a spacer- or sacrificial layer at the nozzle tip. It protects the function and integrity of the nozzle, ensures easier cutting and also acts as an optical guide for the eye. Since X-ray beams will hit the liquid jet in close proximity to the microfluidic device, the range of observable scattering angles (at high q) depends on the microfluidic design itself and the razor blade cutting angle. Consequently, the observable q -range can be easily extended by tilting the razor blade accordingly.

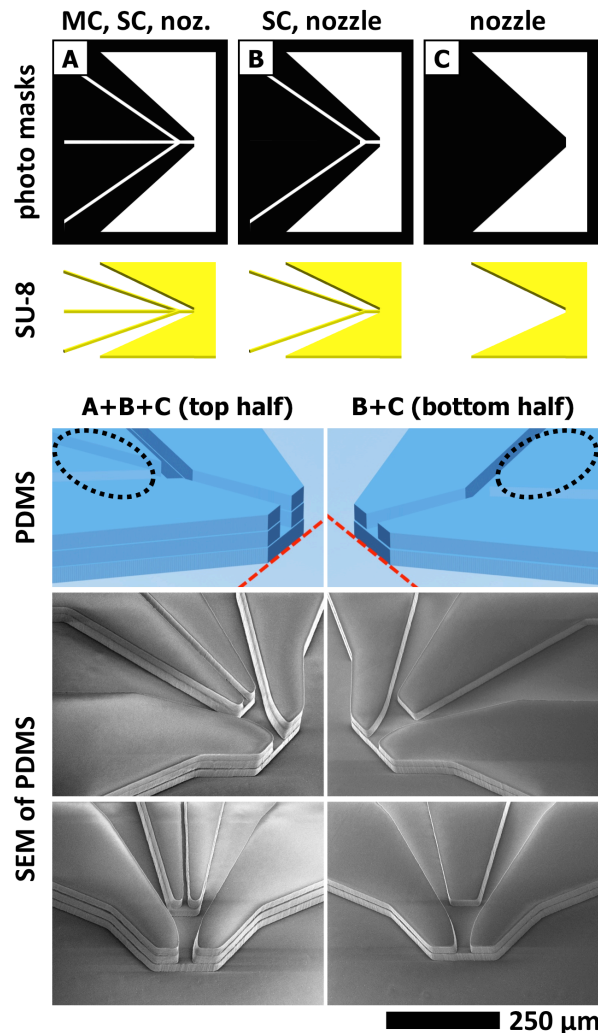


Fig. 2 Illustration of the multilayer principle for the creation of 3D microfluidic liquid jet nozzle arrays (aperture-less nozzle version). (A-C) Representation of the individual emulsion film masks (top) and their resulting structured SU-8 layers (middle). These are combined differently to create multilayered SU-8 structures which are replicated using PDMS (bottom). Illustrations and scanning electron microscopic images show the upper (bottom left) and lower (bottom right) PDMS halves of a 3D nozzle prior to the subsequent device bonding steps. The B-layer can include a blocking element at the nozzle tip (nozzle version with aperture) to reduce the outlet cross section for smaller jets and lower gas flows (see Supplemental Information).

The last step involves the exact alignment and plasma-activated sealing of this pair to PDMS-microchannel halves. The precise alignment is achieved by additional multilayered orientation structures next to the main nozzle geometries. These guiding pairs of 3D-microstructures have already been included in the above photolithographic steps and, now, facilitate the necessary alignment almost automatically by snapping into each other. This results in well-centered microchannels and liquid jets that exit the microfluidic nozzle in a straight line at perfect right angles. A photograph of the final PDMS-device including the attached tubing, as well as a microscopic image of the nozzle during operation, are shown in Fig. 3.

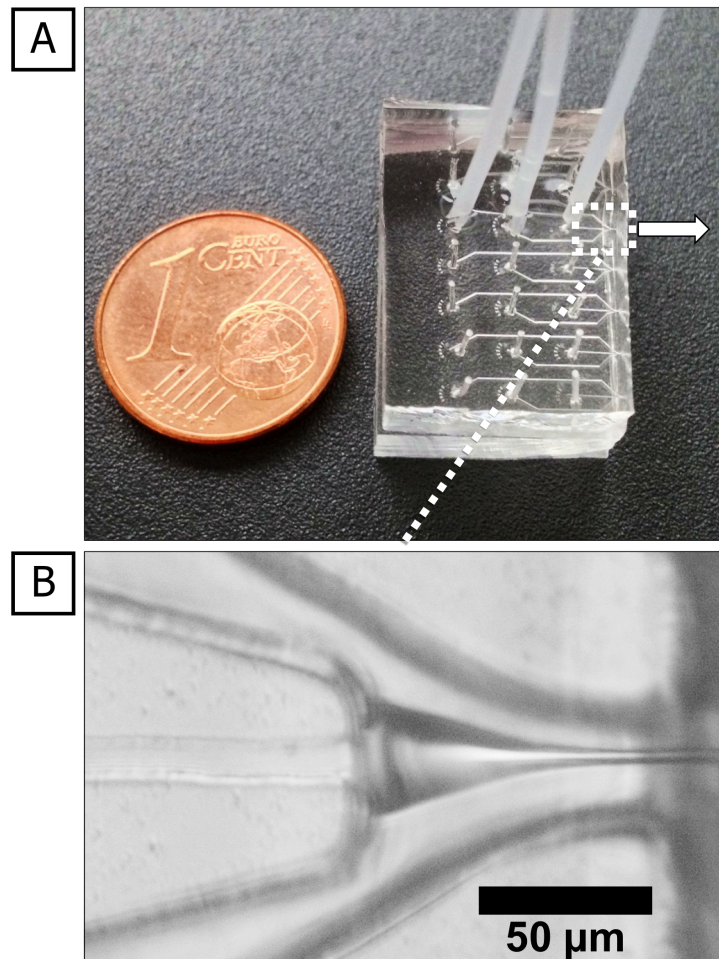


Fig. 3 (A) Photograph of the final microfluidic device with an array of liquid jet nozzles that can be operated individually or in parallel. (B) Light microscopic image of one microfluidic nozzle during operation. The liquid in the central channel is focused with pressured air which enables stable liquid jets with small diameters at low sample flow rates while it runs essentially clogging-free due to this air sheath. The microfluidic liquid jet devices operate well under atmospheric pressures and under vacuum conditions.

Nozzle design. The benefit of using soft-lithography-based microfluidics for the generation of liquid jets lies in the high reproducibility of microstructures and the precise control over very small features in the μm -range. As a result, the liquid inlet is perfectly centered and the jet exits the nozzle's outlet in a straight line. The microfluidic liquid jet devices are designed

using the software AutoCAD that allows controlling the design parameters of the nozzle geometry that directly determine the conditions for liquid jetting. This microfluidic nozzle design and the design parameters definitions are presented in Fig. 4 and the following Tab. 1.

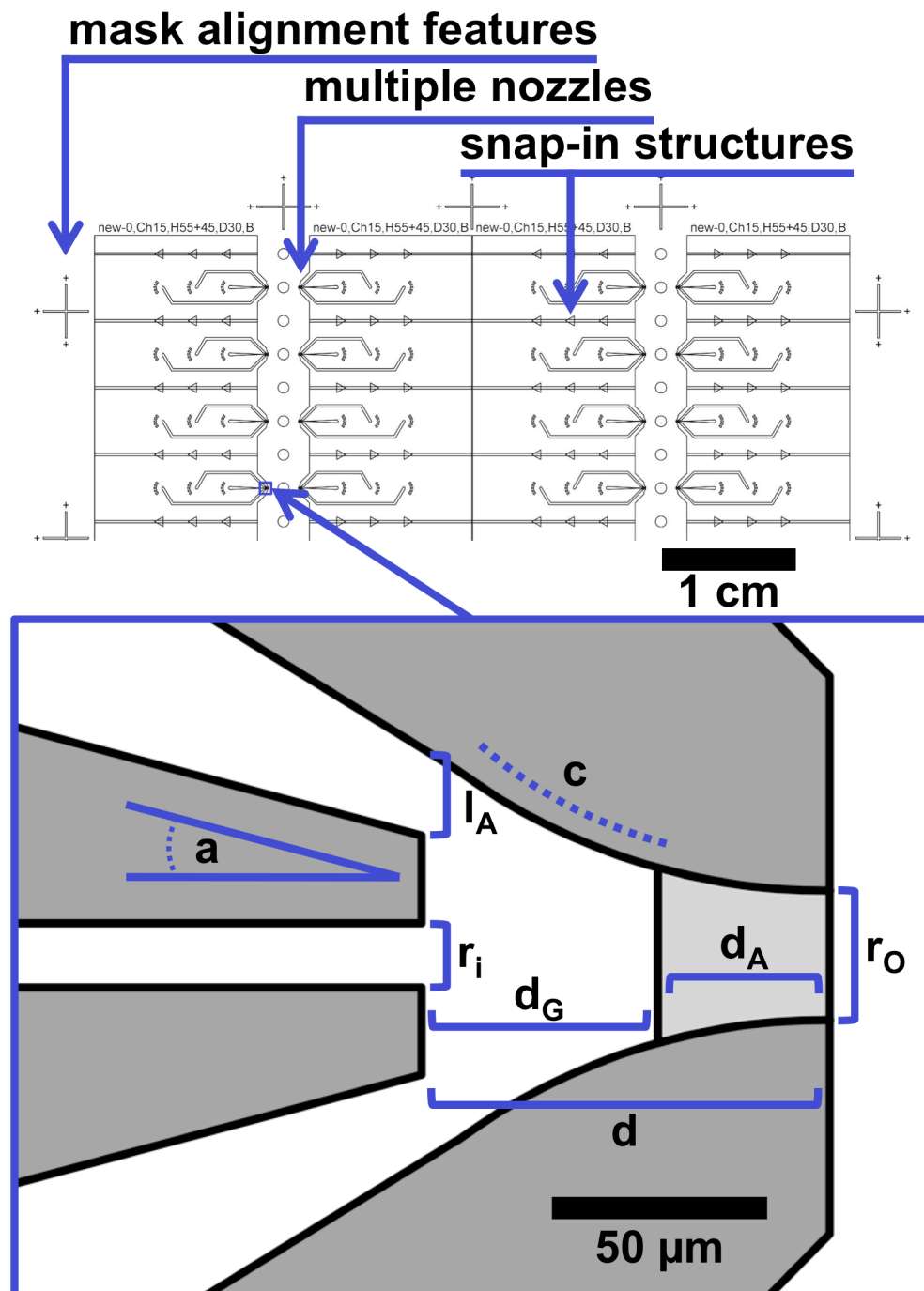


Fig. 4 Nozzle design parameters. (Top) Excerpt of a CAD drawing which contains features for aligning the mask during the photolithographic process and snap-in structures for the later replica alignment during the device fabrication. (Bottom) An illustration of the controllable design parameters is depicted below. These features can be adjusted with high precision and reproducibility to fine-tune the jetting behavior of the desired liquid.

Tab. 1 List of microchannel design parameters and their definitions along with relevant parameter combinations and ratios.

Design Parameter	Definition
r_o	width at the outlet (30 μm)
r_i	width of the main channel (15 μm)
d	distance from main channel inlet to nozzle outlet (95 μm)
d_G	distance of the gap between main channel inlet (55 μm)
d_A	distance of the aperture (40 μm)
l_A	length of the air inlet (20.4 μm)
a	angle of the air stream (15 °)
c	curvature of the tapering (144.3 μm arc radius)
not shown in the illustration:	
h_n	height of layer n (30 μm)
extra aperture	presence of an aperture at top and bottom layer of the nozzle outlet
Relevant design parameter ratios	
$r_o : d$	$d_G : d_A$
$r_i : r_o$	$l_A : r_i : l_A$
$(r_i + 2 * l_A) : r_o$	$(r_i + 2 * l_A) : d$
$a : d$	$c : d$

Nozzle arrays. The master structures can contain multiple dense nozzle arrays on a single device which are replicated simultaneously with each molding step. The resulting nozzles can be operated individually or in parallel. Next to the possibility of massive parallelization of nozzles, the integration of dense nozzle arrays on a microfluidic chip also allows to maintain a very small device footprint. The current microfluidic designs contain adjacent liquid jet nozzles every 3.3 mm which could also be reduced easily.

Disposable chips. The effectiveness and ease of the production process allows even to fabricate disposable microfluidic liquid jet devices in large numbers. The use of such disposable liquid jet devices can be of great advantage when hazardous or toxic samples like virii, bacteria, bio-active compounds or nanoparticles need to be handled.

Results and Discussion

Design control and performance. The microfluidic chips reliably produce stable liquid jets, using water in our case, with typical diameters in the lower μm -range that can be controlled precisely. The 3D design gives the option to incorporate additional obstacles at the top and bottom of the 3-layered microchannel's exit, reducing the cross section of the aperture to a fraction, depending on the individual layer heights. Further, this aperture integration also reduces the gas flow (see Supplemental Information) and the generated jets are generally smaller in diameter, exit at higher velocities, and the stable jetting requires lower minimal liquid flow rates than their aperture-less analogues. We studied the microfluidic liquid jetting behavior in this enhanced version of the nozzle at atmospheric ambient pressure and the results are shown in Fig. 5.

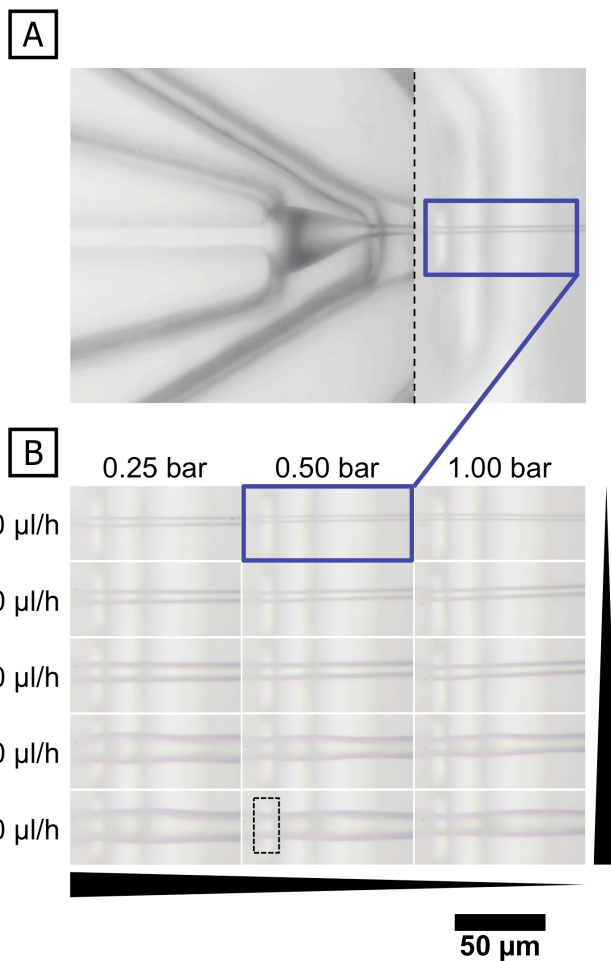


Fig. 5 Jet diameter control visualized by microscopic images of the microfluidic liquid jet nozzle during operation. (A) The water enters the nozzle and is shaped by the pressured air flow and the geometric device design. This results in a constant and stable liquid jet. The top image is merged from two frames at different focus positions due to the optical distortion of PDMS and is indicated by a dotted line. (B) The change of jet diameters at varying conditions is shown below and was measured directly at the nozzle outlet. The black dotted rectangle marks the region of the jet diameter measurements while the stretched black triangles indicate the trends of increasing or decreasing liquid jet diameters.

Jet diameter control. The jet at the outlet of the liquid jet nozzle is imaged to analyze the relation between its diameter and the applied experimental parameters. We observe the trend that lower liquid flow rates and increased gas pressures both lead to smaller jet diameters as shown in Fig. 5. In this image series at atmospheric ambient pressure, the flow rates were varied between $600 \mu\text{l h}^{-1}$ and $9000 \mu\text{l h}^{-1}$ at compressed air pressures between 0.25 bar and 1.00 bar which results in jet diameters between $3.5 \mu\text{m}$ and $19 \mu\text{m}$. Assuming that the well-studied plate-orifice configuration and this microfluidic liquid jet system share the same underlying physics, we apply the model described by Gañán-Calvo *et al.* which describes the liquid jet diameter d_j :^{19,26,97-99}

$$d_j \approx \left(\frac{8\rho_l}{\pi^2 \Delta p_g} \right)^{1/4} Q^{1/2} \quad (1)$$

with the density of the liquid ρ_l , the pressure difference Δp_g and the flow rate Q . For best reproducibility, the jet diameter is measured manually using ImageJ at multiple positions directly next to the nozzle exit (see indication in Fig. 5). We find that this theoretical model and the experimental results are in very good agreement for almost all flow rates, as shown in Fig. 6A. The measured diameters only start to deviate from the predicted values at high flow rates ($\geq 6000 \mu\text{l h}^{-1}$) which might originate from the curved surface instabilities that modulate the liquid jet diameter downstream, as shown in Fig. 5.

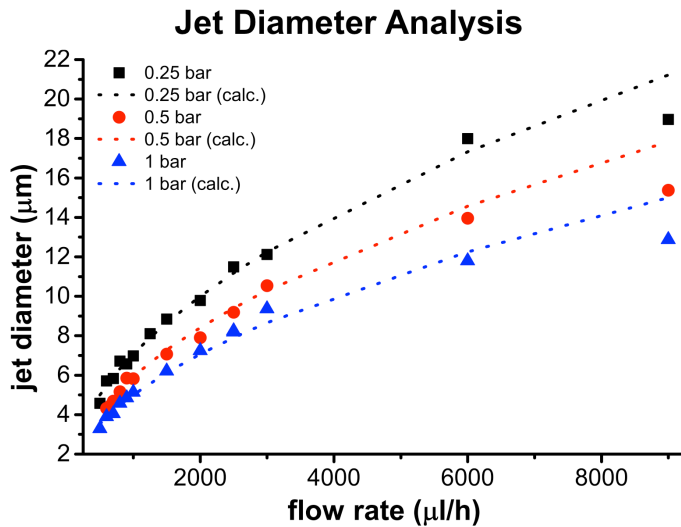


Fig. 6 Comparison of experimental data with theoretical predictions regarding jet diameter and breakup transition analysis. The jet diameter at different flow rates and applied pressures with a controllable jet diameter between $3.5 \mu\text{m}$ and $19 \mu\text{m}$.

Controlled droplet breakup. The liquid jets exit the microfluidic devices at velocities in the range of tens of m/s and the droplet breakup consequently appear as a thin blurred line to the eye. Therefore we studied the jetting behavior and droplet breakup of a water jet using a high speed camera at $2 \mu\text{s}$ exposure times and frames rates of ca. 15,000 fps, using the aperture-less nozzle design for lower droplet velocities to ensure sharper images. The required high speed video setup is described in more detail in the experimental section while the resulting images

are shown in Fig. 7. The droplet breakup is studied at a constant air pressure of 0.25 bar while the liquid flow rate was varied to study its influence on the breakup characteristics.

The high speed camera frames reveal that an increasing flow rate leads to larger droplets with an increase from 8.7 μm at 500 $\mu\text{l h}^{-1}$ to 29.8 μm at 9000 $\mu\text{l h}^{-1}$. Further, the length of the continuous jet, before it breaks up into droplets, increases from 137 μm to 867 μm over the same flow rate interval. This has important implications for the integration of microfluidic liquid jet devices at X-ray sources because the length of the uninterrupted liquid stream dictates the proximity of the X-ray beam to the nozzle at a given flow rate.

Further, this high speed video setup allows the experimental classification of the droplet breakup type. The breakup of a liquid jet leads to the formation of drops due to the growth downstream of axisymmetric capillary waves (the Rayleigh instability¹⁰⁰) that are commensurate with the jet diameter. The different possible droplet breakup types that can be identified are described in more detail elsewhere and will be covered only briefly.^{28,75,101,102} (I) The jetting state shown in Fig. 7B corresponds to the first type, which is globally and locally stable (GS/LS). Here, the liquid meniscus is stable inside the nozzle and the liquid exits the orifice as a continuous column because the growing axisymmetric perturbations are swept away downstream (convectively unstable¹⁰³ (II) Unstable states, such as spraying, where the tapering liquid meniscus is unstable, can be observed at increasing pressures for a given liquid flow rate and they correspond to the global and local instability (GI/LI). (III) The third parameter domain corresponds to a globally stable, but locally unstable jetting regime (GS/LI). Here, the liquid meniscus is stable inside the nozzle geometry, as shown in Fig. 7C, but the jet breaks up into a continuous droplet stream because the growing perturbations travel upstream and pinch off the interface close to the orifice (absolutely unstable¹⁰⁵). This GS/LS- to GS/LI-transition lies in the range of the Leib-Goldstein limit that predicts the convection/absolute instability transition.^{101,102,104} The GS/LI-state can be reached by starting with stable jetting (GS/LS, case I) and then lowering the pressure (>0.1 bar) at a given liquid flow rate (3000 $\mu\text{l h}^{-1}$). Under these conditions a homogenous stream of equidistant drops (135 μm) with a diameter of 50.5 μm can be observed at a constant rate (ca. 12.36 kHz). If the pressure, at this given flow rate, is decreased even further towards 0 bar, the jetting collapses (GI/LI, case II).

These findings and the predictable jet diameters are particularly interesting because they suggest that the knowledge and theories about the well-studied plate-orifice- and GDVN-designs can be applied to the microfluidic liquid jet devices as well. This would help tremendously with the theoretical prediction of jetting behavior as well as the development of future optimized devices. Further, this principle could potentially be used to generate small droplets at a constant and controllable rate if the flow rates and other relevant experimental parameters are adjusted accordingly. This possibility could be interesting for applications that require synchronization of homogenous droplet streams to a certain frequency.

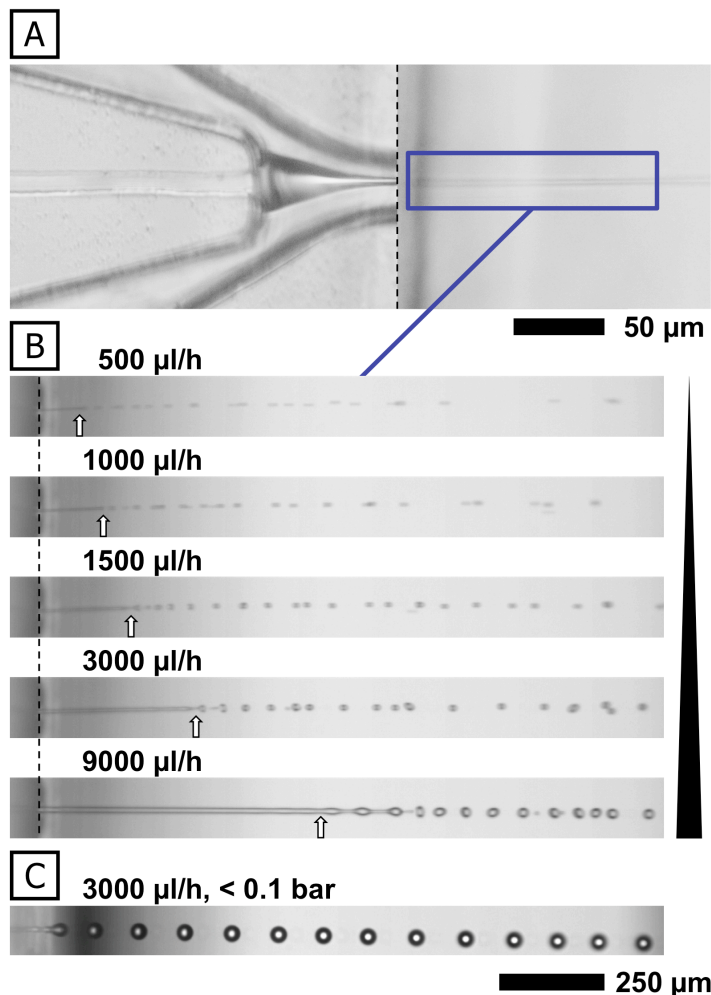


Fig. 7 Controlled droplet break-up. (A) Light microscopic image of a microfluidic liquid jet device that focuses a water jet with pressured air (GS/LS). (B) High speed camera frames (2 μ s exposure, ca. 15,000 fps) of the jetting lengths, with the black dotted line marking the zero position, and droplet breakup (global and local stability) at flow rates between $500 \text{ } \mu\text{l h}^{-1}$ and $9000 \text{ } \mu\text{l h}^{-1}$ at a pressure of 0.25 bar (global instability transition) and (C) Rayleigh breakup (global stability, local instability) in the same device at lower pressures (< 0.1 bar) and a flow rate of $3000 \text{ } \mu\text{l h}^{-1}$. The highly constant droplet-frequency and -size can be adjusted by changing the experimental parameters, such as pressure or flow rate.

CFD-based jet optimization. It is possible to analyze further design details on the jetting behavior using established computational fluid dynamic (CFD)-simulations that allow the microchannel design to be adjusted accordingly in AutoCAD. This combination of precise fabrication control and CFD-simulations is known as computer-aided rapid prototyping.^{80,93,105} As an example, the jetting behavior of a water jet in air is simulated with the CFD-software package COMSOL using a time-resolved Newtonian two-phase model. First, the microfluidic nozzle geometry is imported from the CAD- into the CFD-software and the boundary conditions, such as inlets, outlets, etc., are set as described in further detail in the Supplemental Information. We choose a time-resolved model because the initial fluid interface is a flat plane, between the inlet channel and the gas flow volume, which then

evolves to the stable liquid jet that is shown in blue in Fig. 8. Due to the complexity of this 3D model, symmetry of the microfluidic liquid jet nozzle was taken into account which enables to consider the geometry's full 3D shape while only modeling its top right quarter. This reduced the amount of necessary finite elements and allowed us to increase the modeling quality of the liquid jet. These detailed finite element meshes are shown in Fig. S1 of the Supplemental Information.

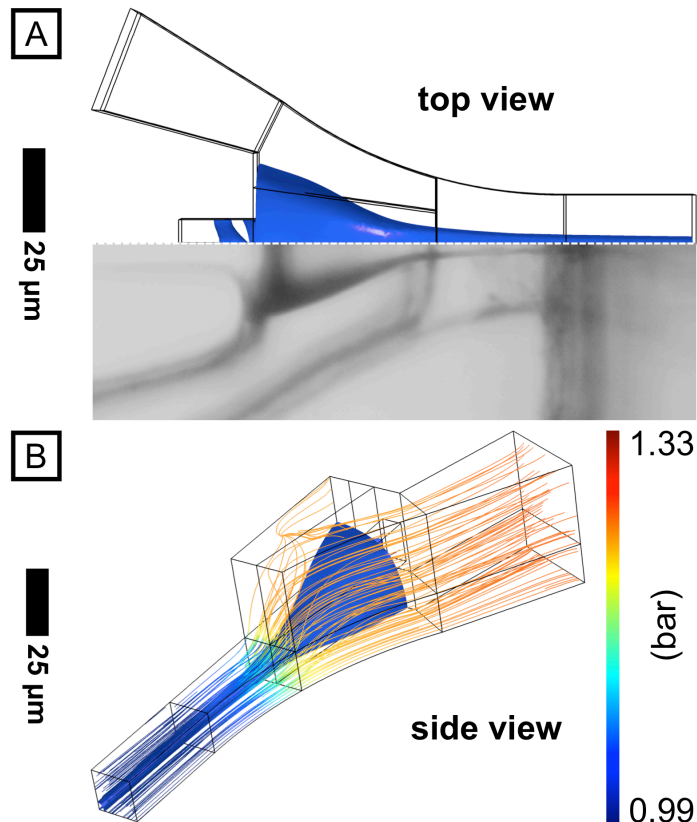


Fig. 8 3D CFD-simulation results compared to the experimental data under the same conditions: water jet in air at a flow rate of $600 \mu\text{l h}^{-1}$ with a pressure difference of 0.25 bar. (A) Top view on the 3D simulation the corresponding light microscopic image shows the good agreement between the theoretical and experimental jet shape. (B) Side view on the 3D shape of the liquid jet where the blue shape represents the interface between the two simulated fluid phases of water and air. The streamlines are color-coded to show the pressure gradient in the focusing area.

This CFD-simulation of a liquid jet is an example for future similar models that can be used to optimize the system, gain important insights into the 3D liquid jet shape and understand its dynamics under different conditions because the CFD-model considers the exact geometry of the microfluidic nozzle which can be fabricated reproducibly using soft lithography.

The CFD-simulations clearly show that the resulting liquid jet is shaped by the interplay of microchannel geometry and the compressed air at high velocities. We performed the simulation of the water liquid jet for the same parameters as the experiment: with a water flow rate of $600 \mu\text{l h}^{-1}$ and air at a pressure difference of 0.25 bar. As a verification of the CFD-model, the simulation results are compared to the experimental high speed video data

under these exactly same conditions and we find that the results are in very good agreement, as shown in Fig. 8A. Further, the color-coded flow lines in this figure indicate the pressure drop which results from the volume expansion when the air from the side channels enters the bigger volume where the fluid focusing occurs. The compressed air expectably shapes the liquid jet not only from the sides, but also from top and bottom according to the GDVN-principle which prevents any contact of the liquid to the nozzle wall and yields a very small liquid jet diameter at the nozzle outlet.

Vacuum operation. The microfluidic liquid jet devices operate well under atmospheric ambient pressures or under vacuum conditions. The low gas flow rates are measured experimentally and should allow a vacuum in the range of 10^{-6} bar, as described in further detail in the Supplemental Information. To demonstrate the stable jetting behavior under vacuum conditions, we performed tests in a scanning electron microscope (SEM, EVO LS, Carl Zeiss AG) using a microfluidic liquid jet device and water as a liquid sample. The SEM is operated at a chamber pressure of < 10 mbar and the liquid- and air-flows are pumped by applying adjustable pressures. The flow rates are monitored in situ using a micro-volume flow meter (Sensirion AG). The observed jet diameters typically were in a range of $2 \mu\text{m}$ to $4 \mu\text{m}$ at flow rates between $150 \mu\text{L h}^{-1}$ and $1000 \mu\text{l h}^{-1}$ and pressures up to 3 bar.

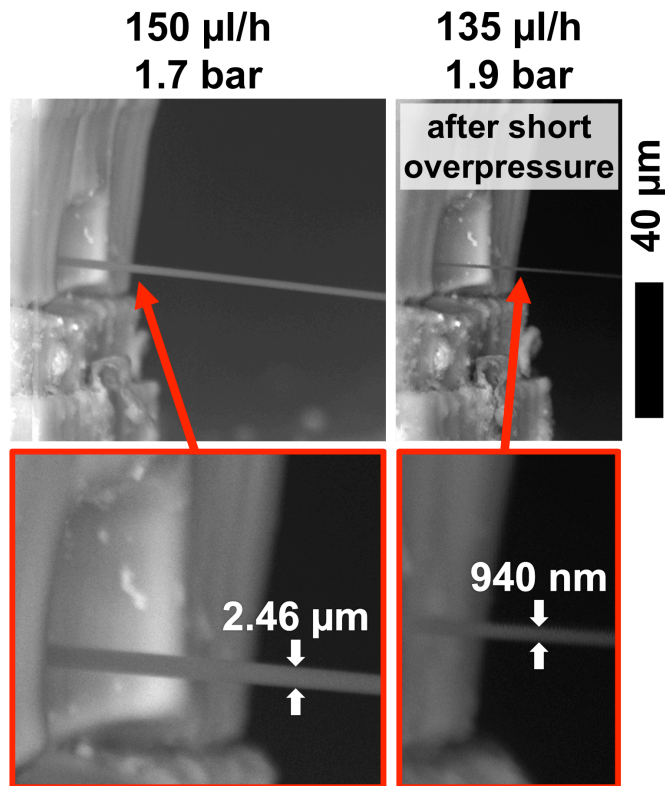


Fig. 9 Liquid jetting under vacuum conditions. Scanning electron microscopic (SEM) image of microfluidic liquid jet device during operation under vacuum conditions. The liquid jet (pure water) exits the nozzle as a straight continuous sample stream while its GDVN-based design enables essentially clogging-free stable jetting with small diameters at low sample flow rates. By regulating pressure and sample flow rates, the jet diameter can be adjusted.

An example SEM image of a liquid jet in a microfluidic device in operation is depicted in Fig. 9. The device runs at the low flow rate of $150 \mu\text{L h}^{-1}$ at an air pressure of 1.7 bar yielding a stable liquid jet with a diameter of $2.46 \mu\text{m}$. After a short, unintentional high overpressure burst, we observed a stable microfluidic liquid jet with a sub-micron diameter (940 nm) at an even lower flow rate of $135 \mu\text{l h}^{-1}$ at an applied pressure of 1.9 bar. This observation indicates the optimization potential of this microfluidic liquid jet system. We suspect that the d/r_0 -ratio (see Fig. 4) changed in this event because this ratio is known to have a sensitive effect on the lowest minimal flow rate.²⁷

These vacuum conditions in the SEM sample chamber mimic the conditions that are typically found in the sample chambers at free electron lasers. Combined with the low liquid flow rates, this compatibility makes the microfluidic liquid jet device a suitable alternative to current sample environments.

Sample consumption and -compatibility. Due to the air-focusing design, the here presented microfluidic liquid jet devices can be operated at very low sample consumption rates which is highly important for solutions of scarce valuable samples such as proteins. The current minimum flow rates for stable jetting are typically in the range of the commonly used glass capillaries (135 to $500 \mu\text{l h}^{-1}$).^{17,32,106} Ongoing studies indicate that these minimal flow rates for stable jetting can be further decreased by adjusting the design parameters, like channel-shapes, -heights, -dimensions and aspect ratios, according to the sample's individual fluid properties.

The GDVN-based design typically results in the very reliable and continuous generation of liquid jets which are resilient to a wide range of experimental conditions; both for microfluidic devices and glass capillaries. However, there are extreme examples of samples where the GDVN-design is stretched to its limits. This is the case for highly viscous samples or solutions that contain high concentrations of salts because solution components tend to plate out at the periphery of this wetted region and eventually grow back to occlude the capillary exit or alter the gas flow. In case of glass capillaries, this problem can be overcome by forming micrometer-sharp edges on the front of the liquid capillary.²⁴ While the side edges of the microfluidic liquid inlet channel can be fabricated with a similar sharpness, to reduce the wetted area, the edge at the top and bottom remain rather flat. However, this wetted region can be minimized even further by using established surface treatments, such as Aquapel™- or parylene-coating, which have been successfully used against device fouling.¹⁰⁷⁻¹⁰⁹

To demonstrate the wide sample compatibility of *untreated* microfluidic liquid jet devices, the chips are tested with different solutions that are examples for commonly used protein crystallization buffers and which contain high concentrations of poly(ethylene glycol) and salts. The microfluidic liquid jet devices operate error free and without any indication of clogging for a period of 60 min after which the experiment is *intentionally* stopped (see Supplemental Information).

Solvent compatibility. PDMS is compatible with aqueous and polar solvents, and thus suitable for most biological or protein samples.^{106,110,111} For use with nonpolar solvents, coating procedures based on established PDMS surface chemistry, e.g. borosilicate glass or fluorinated repellent coatings, have been demonstrated^{89,92,94,96,106}. Further, the described device fabrication procedures can be transferred to other elastomer materials and other microfluidic production techniques such as (hot) soft embossing, including materials such as Teflon®⁹⁷⁻⁹⁹ Kapton®,⁷⁵ THV®,¹⁰⁴ COC/TOPAS®,⁸⁰ PS,¹⁰⁶ PE,¹⁰⁶ PMMA,^{89,106} NOA81,^{112,113} glass¹¹⁴ and silicon.¹¹⁴ Combined with the here-described integrated snap-in structure for device alignment, this enables the use of a broad range of solvents in microfluidic liquid jet devices. Production techniques such as (hot) soft embossing or micro injection molding also open the path to industrial large scale productions with the possibility to mass-produce disposable devices.

Integration of additional features. The soft lithography-based liquid jet device production allows the integration of additional features or microfluidic building blocks without any additional processing steps. Available microfluidic building blocks include design concepts for simple functions like i.e. mixing, sorting, measuring, injecting, switching or droplet- and microparticle-generation, which can be stacked to build up complex chip-labs. A prominent example of stacked, simple elements that perform complex tasks is the concept of microfluidic large scale integration by Quake *et al.* which includes pumps,¹¹⁵ valves¹¹⁶ and multiplexers.⁷¹ This building block concept enables the sample handling and fluid manipulation within the microfluidic liquid jet device and opens up many new opportunities for liquid jets.

Jet-in-jet. As an example for the integration of microfluidic tools into the liquid jet device, we demonstrate the fabrication of a jet-in-jet geometry that focuses two liquids hydrodynamically into a gas-focused jet of the combined liquids. Hydrodynamic flow focusing and its combination with a coaxial gas flow using capillaries has been described before,^{22,51} but each additional liquid stream inside a liquid stream requires additional working steps due to the capillary-based design. In this soft lithography-based example however, mixing geometries are handled as individual microfluidic building blocks of which one or many can be simply added to the existing GDVN-nozzle design with high precision and reproducibility; without the need of any additional fabrication steps. This simple combination enables *in situ* mixing experiments within the liquid jet, like i.e. the study of nanoparticle growth,^{89,90} the time-triggered dosing of liquids into a stable liquid jet or ultra-fast pump-probe laser experiments.^{2,4,6,7,33}

We demonstrate a microfluidic jet-in-jet device mixing two dyes, fluoresceine and rhodamine B, by hydrodynamic flow focusing which are then focused as a liquid jet using the GDVN-principle. The pressurized air is adjusted to 1 bar and the liquid flow rate is 500 µl h⁻¹ for each liquid channel which results in a flow rate ratio between side and main channels (SC:MC:SC) of 1:1:1. The jetting behavior is imaged using a light microscope (rhodamine B in water) and confocal laser scanning microscopy (fluoresceine in rhodamine B) as shown in Fig. 10.

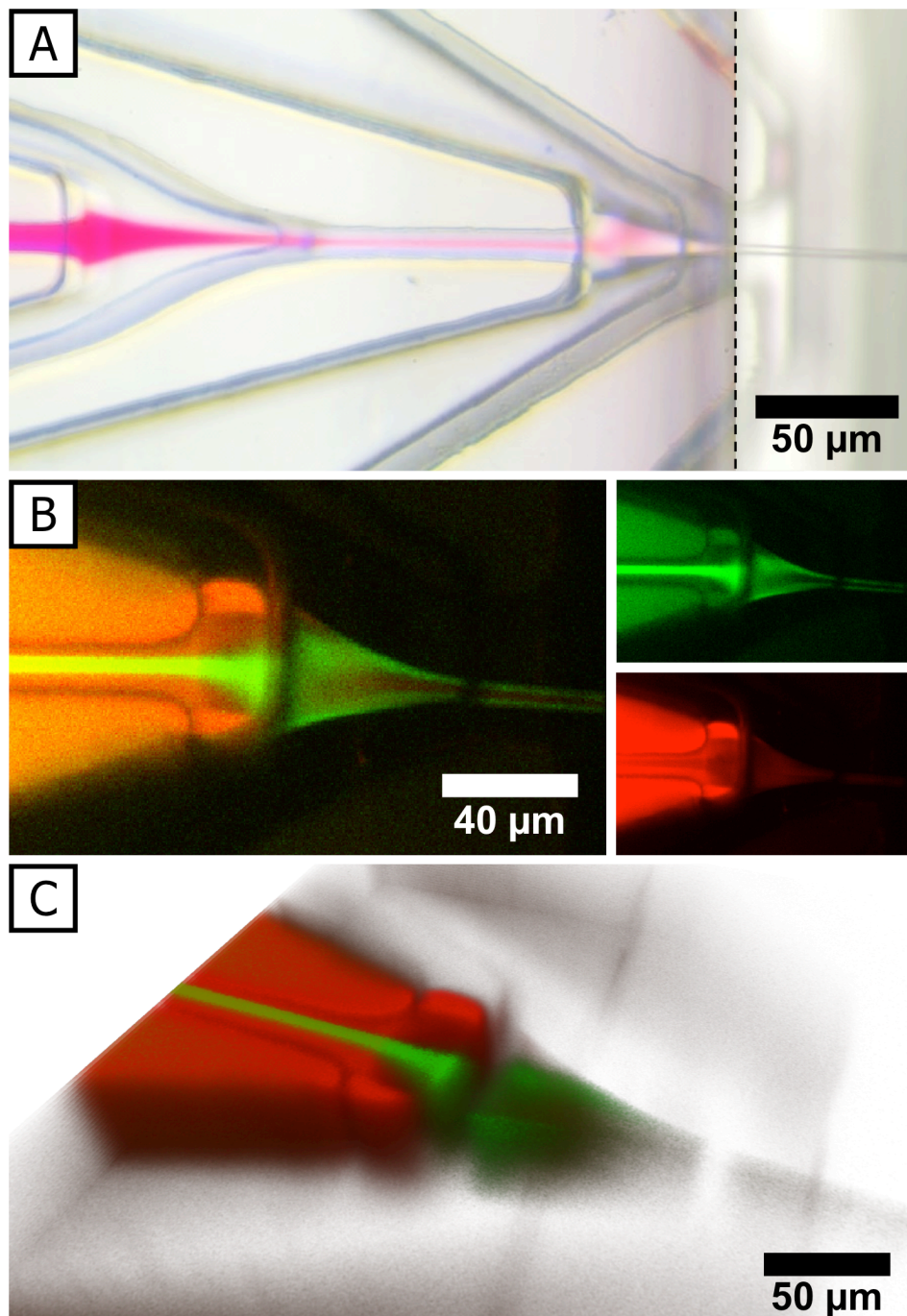


Fig. 10 Jet in Jet. Microscopic images of a microfluidic liquid jet in jet device during operation at 1 bar and a (medium) flow rate of $500 \mu\text{l h}^{-1}$ for each liquid channel. The flow rate ratio between side and main channels (SC:MC:SC) is therefore 1:1:1. (A) The light microscopic image shows a solution of rhodamine B dye which is focused in pure water before it exits the device as a liquid jet. (B left) Fluorescence image of the liquid jet's cut plane taken with a confocal laser scanning microscope at its center. This is the same device as (A), but it is operated with different dyes which are recorded on individual color channels: fluoresceine (B top right, green channel) and rhodamine B (B bottom right, red channel). An inversion of dyes is observed. (C) A complete stack of confocal cut plane images at different focus positions of this liquid jet has been recorded. The resulting 3D-reconstruction is presented from an angled top-down view angle.

The green and red fluorescence of these dyes at the center of the liquid jet is recorded on individual color channels of the confocal microscope as shown in Fig. 10B. Additionally, we record a complete stack of confocal cut plane images at different focus positions of this liquid jet enabling a 3D-reconstruction of the liquid jet. The lower half of this resulting 3D-reconstruction is presented from an angled top-down view angle in Fig. 10C. We observe that the liquid jet is not only focused from the sides but also from top and bottom. This observation and the liquid jet's 3D shape are in good agreement with the CFD simulation results that have been discussed above.

Experimental

Photolithographic Master Fabrication. This part of the fabrication process is performed in a clean room and starts by spin-coating (Cee 200X, Brewer Science Inc.) a 3" silicon wafer with a negative photoresist (SU-8 50, Microchem Co.). This step is illustrated in Fig. 1.1. The microchannel structures are imparted to the photoresist using a mask aligner (MJB4, Süss MicroTec AG) as shown in Fig. 1.2. The previous steps are repeated to build up two additional layers onto the silicon wafer, as shown in Fig. 2. The uncured photoresist is removed in the subsequent development process which yields a multi-layered master. All relevant process parameters are optimized to obtain microstructured layers with a very uniform height of 30 μm per coating-exposure-iteration. The geometric design parameters of the microchannel are summarized in Tab. 1.

Microfluidic Device Fabrication. The second part of the fabrication process continues under dust-free conditions by replicating this microstructured master using polydimethylsiloxane (PDMS, Sylgard 184 kit, Dow Corning Co.) and curing it for ca. 2 h at 80 °C. These steps are depicted in Fig. 1.3&4. The PDMS replica is removed from the master and inlet ports are punched into the polymer using a biopsy punch needle (Harris Uni-Core™ 0.75 mm). The polymer is cut into smaller pieces for better handling and the excess PDMS next to the outlet nozzles is cut off using a razor blade, as shown in Fig. 1.5. This step is performed under a microscope to ensure high quality. The microchannel design allows preparing several nozzles simultaneously since the replicated structures incorporate an additional PDMS-layer that protects the nozzle's integrity and function during the cutting process (see discussion of Fig. 2). Additionally, cutting in a steeper angle (or adjusting the CAD drawing) will extend the range of coverable X-ray scattering angles. The final array of microfluidic 3D-focused liquid jet nozzles is created by bonding the two halves of PDMS. This is achieved by activating the surface using air plasma (MiniFlecto-PC-MFC, GaLa Instrumente GmbH), adding a little drop of pure water (0.2 μm -filtered Millipore), aligning the structures and drying at 30 °C for ca. 1 h. The use of a microscope will help during the alignment step, but typically the integrated orientation structures of the multi-layer design will snap in and align the microstructures automatically and with high precision.

Microfluidic liquid jet device operation. The microfluidic liquid jet devices operate stably under different conditions. The devices are tested over periods of several hours to demonstrate the long term stability of the system. Syringe pumps (Nemesys, Cetoni GmbH) are connected to the device using PE tubings (Science Commodities Inc.). All tested liquids, such as pure water (Milli-Q, Millipore), are filtered through a 0.2 µm- or 5 µm-PTFE filter prior to use. The experimental conditions include flow rates between 150 µL h⁻¹ and 9000 µL h⁻¹ at constant pressures between < 0.1 bar and 5 bar. During the startup sequence, the air flow is started first and then adjusted to the desired value. Next, the syringe pumps are started and regulated down to the targeted flow rate for stable jetting. The imaging setup involves an Olympus IX71 inverse microscope and a highly intense, focused light source that allows exposures down to 2 µs. The fast processes, as the droplet breakup or the startup evolution, are recorded using a high speed camera (Phantom v9.1, Vision Research) allowing to capture frames at a rate of 150,000 s⁻¹. The stable jetting behavior is also studied and captured using a DSLR camera (D7000, Nikon) which delivers high resolution images for further analysis.

Conclusions

In conclusion we demonstrate the production of microfluidic chip based devices that produce liquid jets with micrometer diameters while operating at very low flow rates. The chip production is based on established soft-lithographical techniques employing a three-layer design protocol. This allows the exact, controlled and reproducible design of critical parts such as nozzles and the production of nozzle arrays. The microfluidic chips reproducibly generate liquid jets exiting at perfect right angles with diameters between 20 µm and 2 µm; under special circumstances even down to 0.9 µm. Jetting diameter, jet length, the domain of the jetting/dripping instability can be predicted and controlled based on the theory for liquid jets in the plate-orifice configuration described by Gañán-Calvo *et al.* Additionally, conditions under which the device produces highly reproducible monodisperse droplets at exact and predictable rates can be achieved. The devices operate under atmospheric and under vacuum conditions making them highly relevant for a wide range of applications, for example at free-electron lasers. Further, the straightforward integration of additional features such as a jet-in-jet is demonstrated. This device design has the potential to integrate more features based on established microfluidic components and become a standard device for small liquid jet production.

Acknowledgements

We thank the European Research Council for financial support within the ERC Advanced Grant project STREAM (#291211) and the Federal Ministry of Research (BMBF, #05K13WC5). Very helpful discussions with Joachim Schulz (XFEL, Hamburg, Germany), Kenneth Beyerlein and Dominik Oberthür (both CFEL/DESY, Hamburg, Germany) are gratefully acknowledged.

References

1. A. M. Gañán-Calvo, *Journal of Aerosol Science*, 1999.
2. Y. M. Shin, M. M. Hohman, M. P. Brenner, and G. C. Rutledge, *Appl. Phys. Lett.*, 2001, **78**, 1149.
3. A. M. Gañán-Calvo, *Phys. Rev. Lett.*, 1997, **79**, 217–220.
4. A. Greiner and J. H. Wendorff, *Angewandte Chemie International ...*, 2007.
5. A. M. Gañán-Calvo and A. Barrero, *Journal of Aerosol Science*, 1999, 1–9.
6. J. E. Díaz, A. Fernández-Nieves, A. Barrero, M. Marquez, and I. G. Loscertales, *J. Phys.: Conf. Ser.*, 2008, **127**, 012008.
7. A. Greiner and J. H. Wendorff, Springer Berlin Heidelberg, Berlin, Heidelberg, 2008, pp. 107–171.
8. B.-J. de Gans and U. S. Schubert, *Macromol. Rapid Commun.*, 2003, **24**, 659–666.
9. S. Hauschild, U. Lipprandt, A. Rumplecker, U. Borchert, A. Rank, R. Schubert, and S. Förster, *Small*, 2005, **1**, 1177–1180.
10. G. D. Martin, S. D. Hoath, and I. M. Hutchings, *J. Phys.: Conf. Ser.*, 2008, **105**, 012001.
11. C. M. Whitehouse, R. N. Dreyer, M. Yamashita, and J. B. Fenn, *Anal. Chem.*, 1985, **57**, 675–679.
12. K. Tang and A. Gomez, *Journal of Colloid and Interface Science*, 1995, **175**, 326–332.
13. S. Agarwal, A. Greiner, and J. H. Wendorff, *Adv. Funct. Mater.*, 2009, **19**, 2863–2879.
14. A. M. Gañán-Calvo and J. M. Montanero, *Phys Rev E Stat Nonlin Soft Matter Phys*, 2009, **79**, 066305.
15. N. Mongkoldhumrongkul, S. Best, E. Aarons, and S. N. Jayasinghe, *J Tissue Eng Regen Med*, 2009, **3**, 562–566.
16. S. N. Jayasinghe, *Analyst*, 2011, **136**, 878–890.
17. H. N. Chapman, P. Fromme, A. Barty, T. A. White, R. A. Kirian, A. Aquila, M. S. Hunter, J. Schulz, D. P. DePonte, U. Weierstall, R. B. Doak, F. R. N. C. Maia, A. V. Martin, I. Schlichting, L. Lomb, N. Coppola, R. L. Shoeman, S. W. Epp, R. Hartmann, D. Rolles, A. Rudenko, L. Foucar, N. Kimmel, G. Weidenspointner, P. Holl, M. Liang, M. Barthelmess, C. Caleman, S. Boutet, M. J. Bogan, J. Krzywinski, C. Bostedt, S. Bajt, L. Gumprecht, B. Rudek, B. Erk, C. Schmidt, A. Hömke, C. Reich, D. Pietschner, L. Strüder, G. Hauser, H. Gorke, J. Ullrich, S. Herrmann, G. Schaller, F. Schopper, H. Soltau, K.-U. Künnel, M. Messerschmidt, J. D. Bozek, S. P. Hau-Riege, M. Frank, C. Y. Hampton, R. G. Sierra, D. Starodub, G. J. Williams, J. Hajdu, N. Timneanu, M. M. Seibert, J. Andreasson, A. Rocker, O. Jönsson, M. Svenda, S. Stern, K. Nass, R. Andritschke, C.-D. Schröter, F. Krasniqi, M. Bott, K. E. Schmidt, X. Wang, I. Grotjohann, J. M. Holton, T. R. M. Barends, R. Neutze, S. Marchesini, R. Fromme, S. Schorb, D. Rupp, M. Adolph, T. Gorkhover, I. Andersson, H. Hirsemann, G. Potdevin, H. Graafsma, B. Nilsson, and J. C. H. Spence, *Nature*, 2011, **470**, 73–77.
18. J. Ullrich, A. Rudenko, and R. Moshammer, *Annu Rev Phys Chem*, 2012, **63**, 635–660.
19. A. M. Gañán-Calvo, *Phys. Rev. Lett.*, 1998, **80**, 285–288.

20. A. M. Gañán-Calvo, J. C. Lasheras, J. Davila, and A. Barrero, *Journal of Aerosol Science*, 1994, **25**, 1121–1142.
21. A. M. Gañán-Calvo, *J. Fluid Mech.*, 1997, **335**, 165–188.
22. L. Martín-Banderas, M. Flores-Mosquera, P. Riesco-Chueca, A. Rodríguez-Gil, A. Cebolla, S. Chávez, and A. M. Gañán-Calvo, *Small*, 2005, **1**, 688–692.
23. D. P. DePonte, U. Weierstall, K. Schmidt, J. Warner, D. Starodub, J. C. H. Spence, and R. B. Doak, *J. Phys. D: Appl. Phys.*, 2008, **41**, 195505.
24. R. B. Doak, D. P. DePonte, G. Nelson, F. Camacho-Alanis, A. Ros, J. C. H. Spence, and U. Weierstall, AIP, 2012, vol. 1501, pp. 1314–1323.
25. J. M. Gordillo, M. PÉREZ-SABORID, and A. M. Gañán-Calvo, *J. Fluid Mech.*, 2001, **448**.
26. A. M. Gañán-Calvo, *J. Fluid Mech.*, 2006, **553**, 75–84.
27. M. A. Herrada, A. M. Gañán-Calvo, A. Ojeda-Monge, B. Bluth, and P. Riesco-Chueca, *Phys. Rev. E*, 2008, **78**, 036323.
28. E. J. Vega, J. M. Montanero, M. A. Herrada, and A. M. Gañán-Calvo, *Phys. Fluids*, 2010, **22**, 064105.
29. J. M. Montanero, A. M. Gañán-Calvo, A. J. Acero, and E. J. Vega, *J. Micromech. Microeng.*, 2010, **20**, 075035.
30. J. M. Montanero, N. Rebollo-Muñoz, M. A. Herrada, and A. M. Gañán-Calvo, *Phys. Rev E Stat Nonlin Soft Matter Phys.*, 2011, **83**, 036309.
31. A. J. Acero, C. Ferrera, J. M. Montanero, and A. M. Gañán-Calvo, *J. Micromech. Microeng.*, 2012, **22**, 065011.
32. A. M. Gañán-Calvo, D. P. DePonte, M. A. Herrada, J. C. H. Spence, U. Weierstall, and R. B. Doak, *Small*, 2010, **6**, 822–824.
33. A. Aquila, M. S. Hunter, R. B. Doak, R. A. Kirian, P. Fromme, T. A. White, J. Andreasson, D. Arnlund, S. Bajt, T. R. M. Barends, M. Barthelmess, M. J. Bogan, C. Bostedt, H. Bottin, J. D. Bozek, C. Caleman, N. Coppola, J. Davidsson, D. P. DePonte, V. Elser, S. W. Epp, B. Erk, H. Fleckenstein, L. Foucar, M. Frank, R. Fromme, H. Graafsma, I. Grotjohann, L. Gumprecht, J. Hajdu, C. Y. Hampton, A. Hartmann, R. Hartmann, S. Hau-Riege, G. Hauser, H. Hirsemann, P. Holl, J. M. Holton, A. Hömke, L. Johansson, N. Kimmel, S. Kassemeyer, F. Krasniqi, K.-U. Kühnle, M. Liang, L. Lomb, E. Malmerberg, S. Marchesini, A. V. Martin, F. R. N. C. Maia, M. Messerschmidt, K. Nass, C. Reich, R. Neutze, D. Rolles, B. Rudek, A. Rudenko, I. Schlichting, C. Schmidt, K. E. Schmidt, J. Schulz, M. M. Seibert, R. L. Shoeman, R. Sierra, H. Soltau, D. Starodub, F. Stellato, S. Stern, L. Strüder, N. Timneanu, J. Ullrich, X. Wang, G. J. Williams, G. Weidenspointner, U. Weierstall, C. Wunderer, A. Barty, J. C. H. Spence, and H. N. Chapman, *Optics Express*, 2012, **20**, 2706–2716.
34. R. Neutze, R. Wouts, D. van der Spoel, E. Weckert, and J. Hajdu, *nature*, 2000, **406**, 752–757.
35. S. Boutet, L. Lomb, G. J. Williams, T. R. M. Barends, A. Aquila, R. B. Doak, U. Weierstall, D. P. DePonte, J. Steinbrener, R. L. Shoeman, M. Messerschmidt, A.

- Barty, T. A. White, S. Kassemeyer, R. A. Kirian, M. M. Seibert, P. A. Montanez, C. Kenney, R. Herbst, P. Hart, J. Pines, G. Haller, S. M. Gruner, H. T. Philipp, M. W. Tate, M. Hromalik, L. J. Koerner, N. van Bakel, J. Morse, W. Ghonsalves, D. Arnlund, M. J. Bogan, C. Caleman, R. Fromme, C. Y. Hampton, M. S. Hunter, L. C. Johansson, G. Katona, C. Kupitz, M. Liang, A. V. Martin, K. Nass, L. Redecke, F. Stellato, N. Timneanu, D. Wang, N. A. Zatsepin, D. Schafer, J. Defever, R. Neutze, P. Fromme, J. C. H. Spence, H. N. Chapman, and I. Schlichting, *Science*, 2012, **337**, 362–364.
36. J. Kern, R. Alonso-Mori, J. Hellmich, R. Tran, J. Hattne, H. Laksmono, C. Glockner, N. Echols, R. G. Sierra, J. Sellberg, B. Lassalle-Kaiser, R. J. Gildea, P. Glatzel, R. W. Grosse-Kunstleve, M. J. Latimer, T. A. McQueen, D. DiFiore, A. R. Fry, M. Messerschmidt, A. Miahnahri, D. W. Schafer, M. M. Seibert, D. Sokaras, T. C. Weng, P. H. Zwart, W. E. White, P. D. Adams, M. J. Bogan, S. Boutet, G. J. Williams, J. Messinger, N. K. Sauter, A. Zouni, U. Bergmann, J. Yano, and V. K. Yachandra, *PNAS*, 2012, **109**, 9721–9726.
37. A. Barty, J. Küpper, and H. N. Chapman, *Annu Rev Phys Chem*, 2013, **64**, 415–435.
38. D. A. Shapiro, H. N. Chapman, D. DePonte, R. B. Doak, P. Fromme, G. Hembree, M. Hunter, S. Marchesini, K. Schmidt, J. Spence, D. Starodub, and U. Weierstall, *J. Synchrotron Rad (2008)*, **15**, 593–599 [[doi:10.1107/S0909049508024151](https://doi.org/10.1107/S0909049508024151)], 2008, 1–7.
39. D. P. DePonte, R. B. Doak, M. Hunter, Z. Liu, U. Weierstall, and J. C. H. Spence, *Micron*, 2009, **40**, 507–509.
40. M. Priebe, S. Kalbfleisch, M. Tolkihn, S. Köster, B. Abel, R. J. Davies, and T. Salditt, *New J. Phys.*, 2010, **12**, 043056.
41. L. Lomb, T. Barends, S. Kassemeyer, A. Aquila, S. Epp, B. Erk, L. Foucar, R. Hartmann, B. Rudek, D. Rolles, A. Rudenko, R. Shoeman, J. Andreasson, S. Bajt, M. Barthelmess, A. Barty, M. Bogan, C. Bostedt, J. Bozek, C. Caleman, R. Coffee, N. Coppola, D. DePonte, R. B. Doak, T. Ekeberg, H. Fleckenstein, P. Fromme, M. Gebhardt, H. Graafsma, L. Gumprecht, C. Hampton, A. Hartmann, G. Hauser, H. Hirsemann, P. Holl, J. Holton, M. Hunter, W. Kabsch, N. Kimmel, R. Kirian, M. Liang, F. R. N. Maia, A. Meinhart, S. Marchesini, A. Martin, K. Nass, C. Reich, J. Schulz, M. M. Seibert, R. Sierra, H. Soltau, J. C. Spence, J. Steinbrener, F. Stellato, S. Stern, N. Timneanu, X. Wang, G. Weidenspointner, U. Weierstall, T. White, C. Wunderer, H. Chapman, J. Ullrich, L. Strüder, and I. Schlichting, *Phys. Rev. B*, 2011, **84**, 214111.
42. A. Barty, C. Caleman, A. Aquila, N. Timneanu, L. Lomb, T. A. White, J. Andreasson, D. Arnlund, S. Bajt, T. R. M. Barends, M. Barthelmess, M. J. Bogan, C. Bostedt, J. D. Bozek, R. Coffee, N. Coppola, J. Davidsson, D. P. DePonte, R. B. Doak, T. Ekeberg, V. Elser, S. W. Epp, B. Erk, H. Fleckenstein, L. Foucar, P. Fromme, H. Graafsma, L. Gumprecht, J. Hajdu, C. Y. Hampton, R. Hartmann, A. Hartmann, G. Hauser, H. Hirsemann, P. Holl, M. S. Hunter, L. Johansson, S. Kassemeyer, N. Kimmel, R. A. Kirian, M. Liang, F. R. N. C. Maia, E. Malmerberg, S. Marchesini, A. V. Martin, K. Nass, R. Neutze, C. Reich, D. Rolles, B. Rudek, A. Rudenko, H. Scott, I. Schlichting,

- J. Schulz, M. M. Seibert, R. L. Shoeman, R. G. Sierra, H. Soltau, J. C. H. Spence, F. Stellato, S. Stern, L. Strüder, J. Ullrich, X. Wang, G. Weidenspointner, U. Weierstall, C. B. Wunderer, and H. N. Chapman, *Nature Photon*, 2011, **6**, 35–40.
43. M. S. Hunter, D. P. DePonte, D. A. Shapiro, R. A. Kirian, X. Wang, D. Starodub, S. Marchesini, U. Weierstall, R. B. Doak, J. C. H. Spence, and P. Fromme, *Biophys. J.*, 2011, **100**, 198–206.
44. U. Weierstall, J. C. H. Spence, and R. B. Doak, *Rev. Sci. Instrum.*, 2012, **83**, 035108.
45. J. Kern, R. Alonso-Mori, R. Tran, J. Hattne, R. J. Gildea, N. Echols, C. Glockner, J. Hellmich, H. Laksmono, R. G. Sierra, B. Lassalle-Kaiser, S. Koroidov, A. Lampe, G. Han, S. Gul, D. DiFiore, D. Milathianaki, A. R. Fry, A. Miahnahri, D. W. Schafer, M. Messerschmidt, M. M. Seibert, J. E. Koglin, D. Sokaras, T. C. Weng, J. Sellberg, M. J. Latimer, R. W. Grosse-Kunstleve, P. H. Zwart, W. E. White, P. Glatzel, P. D. Adams, M. J. Bogan, G. J. Williams, S. Boutet, J. Messinger, A. Zouni, N. K. Sauter, V. K. Yachandra, U. Bergmann, and J. Yano, *Science*, 2013, **340**, 491–495.
46. L. Redecke, K. Nass, D. P. DePonte, T. A. White, D. Rehders, A. Barty, F. Stellato, M. Liang, T. R. M. Barends, S. Boutet, G. J. Williams, M. Messerschmidt, M. M. Seibert, A. Aquila, D. Arnlund, S. Bajt, T. Barth, M. J. Bogan, C. Caleman, T.-C. Chao, R. B. Doak, H. Fleckenstein, M. Frank, R. Fromme, L. Galli, I. Grotjohann, M. S. Hunter, L. C. Johansson, S. Kassemeyer, G. Katona, R. A. Kirian, R. Koopmann, C. Kupitz, L. Lomb, A. V. Martin, S. Mogk, R. Neutze, R. L. Shoeman, J. Steinbrenner, N. Timneanu, D. Wang, U. Weierstall, N. A. Zatsepin, J. C. H. Spence, P. Fromme, I. Schlichting, M. Duszenko, C. Betzel, and H. N. Chapman, 2013.
47. T. Oroguchi and M. Nakasako, *Phys. Rev. E*, 2013, **87**, 022712.
48. T. R. M. Barends, L. Foucar, R. L. Shoeman, S. Bari, S. W. Epp, R. Hartmann, G. Hauser, M. Huth, C. Kieser, L. Lomb, K. Motomura, K. Nagaya, C. Schmidt, R. Strecker, D. Anielski, R. Boll, B. Erk, H. Fukuzawa, E. Hartmann, T. Hatsui, P. Holl, Y. Inubushi, T. Ishikawa, S. Kassemeyer, C. Kaiser, F. Koeck, N. Kunishima, M. Kurka, D. Rolles, B. Rudek, A. Rudenko, T. Sato, C. D. Schroeter, H. Soltau, L. Strueder, T. Tanaka, T. Togashi, K. Tono, J. Ullrich, S. Yase, S. Wada, M. Yao, M. Yabashi, K. Ueda, and I. Schlichting, *Acta Cryst (2013)*. *D69* [[doi:10.1107/S0907444913002448](https://doi.org/10.1107/S0907444913002448)], 2013, 1–5.
49. U. Weierstall, R. B. Doak, J. C. H. Spence, D. Starodub, D. Shapiro, P. Kennedy, J. Warner, G. G. Hembree, P. Fromme, and H. N. Chapman, *Exp Fluids*, 2008, **44**, 675–689.
50. U. Weierstall, R. B. Doak, and J. C. H. Spence, *arXiv*, 2011, physics.ins-det.
51. J. B. Knight, A. Vishwanath, J. P. Brody, and R. H. Austin, *Phys. Rev. Lett.*, 1998, **80**, 3863–3866.
52. A. Jahn, W. N. Vreeland, M. Gaitan, and L. E. Locascio, *J. Am. Chem. Soc.*, 2004, **126**, 2674–2675.
53. C. Neils, Z. Tyree, B. Finlayson, and A. Folch, *Lab Chip*, 2004, **4**, 342–350.
54. D. S. Kim, S. H. Lee, T. H. Kwon, and C. H. Ahn, *Lab Chip*, 2005, **5**, 739.
55. N. Pamme, *Lab Chip*, 2007, **7**, 1644.

56. T. Franke, A. R. Abate, D. A. Weitz, and A. Wixforth, *Lab Chip*, 2009, **9**, 2625.
57. J.-C. Baret, O. J. Miller, V. Taly, M. Ryckelynck, A. El-Harrak, L. Frenz, C. Rick, M. L. Samuels, J. B. Hutchison, J. J. Agresti, D. R. Link, D. A. Weitz, and A. D. Griffiths, *Lab Chip*, 2009, **9**, 1850.
58. A. R. Abate, J. J. Agresti, and D. A. Weitz, *Appl. Phys. Lett.*, 2010, **96**, 203509.
59. D. R. Gossett, W. M. Weaver, A. J. Mach, S. C. Hur, H. T. K. Tse, W. Lee, H. Amini, and D. Di Carlo, *Anal Bioanal Chem*, 2010, **397**, 3249–3267.
60. S.-H. Chao, M. R. Holl, J. H. Koschwanez, R. H. Carlson, L.-S. Jang, and D. R. Meldrum, *Microfluid Nanofluid*, 2005, **1**, 155–160.
61. H. Zhang, C. H. Chon, X. Pan, and D. Li, *Microfluid Nanofluid*, 2009, **7**, 739–749.
62. H. Song, J. Tice, and R. Ismagilov, *Angewandte Chemie (International ed. in English)*, 2003, **42**, 768.
63. M. Seo, Z. Nie, S. Xu, M. Mok, P. C. Lewis, R. Graham, and E. Kumacheva, *Langmuir*, 2005, **21**, 11614–11622.
64. W. Li, E. W. K. Young, M. Seo, Z. Nie, P. Garstecki, C. A. Simmons, and E. Kumacheva, *Soft Matter*, 2008, **4**, 258.
65. H. C. Shum, A. R. Abate, D. Lee, A. R. Studart, B. Wang, C.-H. Chen, J. Thiele, R. K. Shah, A. Krummel, and D. A. Weitz, *Macromol. Rapid Commun.*, 2009, NA–NA.
66. J. Thiele, A. R. Abate, H. C. Shum, S. Bachtler, S. Förster, and D. A. Weitz, *Small*, 2010, **6**, 1723–1727.
67. W. Li, J. Greener, D. Voicu, and E. Kumacheva, *Lab Chip*, 2009, **9**, 2715.
68. T. Thorsen, S. J. Maerkl, and S. R. Quake, *Science*, 2002, **298**, 580–584.
69. J. W. Hong and S. R. Quake, *Nature biotechnology*, 2003, **21**, 1179–1183.
70. J. W. Hong, V. Studer, G. Hang, W. F. Anderson, and S. R. Quake, *Nature biotechnology*, 2004, **22**, 435–439.
71. J. Melin and S. R. Quake, *Annual review of biophysics and biomolecular structure*, 2007, **36**, 213–231.
72. A. J. deMello, *Nature*, 2006, **442**, 394–402.
73. C. L. Hansen, E. Skordalakes, J. M. Berger, and S. R. Quake, *Proceedings of the National Academy of Sciences*, 2002, **99**, 16531.
74. A. Otten, S. Köster, B. Struth, A. Snigirev, and T. Pfohl, *J Synchrotron Rad*, 2005, **12**, 745–750.
75. R. Barrett, M. Faucon, J. Lopez, G. Cristobal, F. Destremaut, A. Dodge, P. Guillot, P. Laval, C. Masselon, and J.-B. Salmon, *Lab Chip*, 2006, **6**, 494–499.
76. H. M. Evans, R. Dootz, S. Koester, B. Struth, and T. Pfohl, *Bull Pol Acad Sci-Te*, 2007, **55**, 217–227.
77. R. Dootz, H. Evans, S. Köster, and T. Pfohl, *Small*, 2007, **3**, 96–100.
78. T. Pfohl, A. Otten, S. Köster, R. Dootz, B. Struth, and H. M. Evans, *Biomacromolecules*, 2007, **8**, 2167–2172.
79. J. F. Moulin, S. V. Roth, and P. Müller-Buschbaum, *Rev. Sci. Instrum.*, 2008, **79**, 015109.

80. K. N. Toft, B. Vestergaard, S. S. Nielsen, D. Snakenborg, M. G. Jeppesen, J. K. Jacobsen, L. Arleth, and J. P. Kutter, *Anal. Chem.*, 2008, **80**, 3648–3654.
81. E. Metwalli, J. F. Moulin, J. Perlich, W. Wang, A. Diethert, S. V. Roth, and P. Müller-Buschbaum, *Langmuir*, 2009, **25**, 11815–11821.
82. T. Narayanan, *Curr Opin Colloid in*, 2009.
83. H. P. Martin, N. J. Brooks, J. M. Seddon, N. J. Terrill, P. F. Luckham, A. J. Kowalski, and J. T. Cabral, *J. Phys.: Conf. Ser.*, 2010, **247**, 012050.
84. S. Köster and T. Pfohl, *Mod. Phys. Lett. B*, 2012, **26**, 1230018.
85. S. M. Taheri, S. Fischer, M. Trebbin, S. With, J. H. Schröder, J. Perlich, S. V. Roth, and S. Förster, *Soft Matter*, 2012, **8**, 12124.
86. A. Buffet, A. Rothkirch, R. Döhrmann, V. Körstgens, M. M. Abul Kashem, J. Perlich, G. Herzog, M. Schwartzkopf, R. Gehrke, P. Müller-Buschbaum, and S. V. Roth, *J. Synchrotron Rad (2012)*, **19**, 647–655 [[doi:10.1107/S0909049512016895](https://doi.org/10.1107/S0909049512016895)], 2012, 1–7.
87. L. Daubersies, J. Leng, and J.-B. Salmon, *Lab Chip*, 2013, **13**, 910.
88. M. Trebbin, D. Steinhauser, J. Perlich, A. Buffet, S. V. Roth, W. Zimmermann, J. Thiele, and S. Förster, *PNAS*, 2013, **110**, 6706–6711.
89. B. Marmiroli, G. Grenci, F. Cacho-Nerin, B. Sartori, E. Ferrari, P. Laggner, L. Businaro, and H. Amenitsch, *Lab Chip*, 2009, **9**, 2063.
90. B. Marmiroli, G. Grenci, F. Cacho-Nerin, B. Sartori, P. Laggner, L. Businaro, and H. Amenitsch, *Nuclear Inst. and Methods in Physics Research, B*, 2010, **268**, 329–333.
91. J. Thiele, M. Windbergs, A. R. Abate, M. Trebbin, H. C. Shum, S. Förster, and D. A. Weitz, *Lab Chip*, 2011, **11**, 2362.
92. A. R. Abate, S. Seiffert, A. S. Utada, A. Shum, R. Shah, J. Thiele, W. J. Duncanson, A. Abbaspourad, M. H. Lee, and I. Akartuna, 2007.
93. G. M. Whitesides and Y. Xia, *Angew. Chem. Int. Ed.*, 1998, **37**, 550–575.
94. J.-B. Orhan, V. K. Parashar, J. Flueckiger, and M. A. M. Gijs, *Langmuir*, 2008, **24**, 9154–9161.
95. Y. Xia and G. M. Whitesides, *Annual review of materials science*, 1998, **28**, 153–184.
96. A. R. Abate, D. Lee, T. Do, C. Holtze, and D. A. Weitz, *Lab Chip*, 2008, **8**, 516.
97. P. A. Willis, B. D. Hunt, V. E. White, M. C. Lee, M. Ikeda, S. Bae, M. J. Pelletier, and F. J. Grunthaner, *Lab Chip*, 2007, **7**, 1469–1474.
98. J. P. Rolland, R. M. Van Dam, D. A. Schorzman, S. R. Quake, and J. M. Desimone, *J. Am. Chem. Soc.*, 2004, **126**, 2322–2323.
99. K. Ren, W. Dai, J. Zhou, J. Su, and H. Wu, *Proceedings of the National Academy of Sciences*, 2011, **108**, 8162.
100. L. Rayleigh, *Proceedings of the London Mathematical Society*, 1879, **1**, 57–72.
101. S. J. Leib and M. E. Goldstein, *Phys. Fluids*, 1986, **29**, 952–954.
102. S. J. Leib and M. E. Goldstein, *J. Fluid Mech.*, 1986, **168**, 479–500.
103. P. Huerre and P. A. Monkewitz, *Annu. Rev. Fluid Mech.*, 1990, **22**, 473–537.
104. S. Begolo, G. Colas, J.-L. Viovy, and L. Malaquin, *Lab Chip*, 2011, **11**, 508.
105. D. C. Duffy, J. C. McDonald, O. J. A. Schueller, and G. M. Whitesides, *Anal. Chem.*, 1998, **70**, 4974–4984.

106. H. Becker and C. Gartner, *Electrophoresis*, 2000, **21**, 12–26.
107. A. R. Abate, D. Lee, C. Holtze, A. Krummel, T. Do, and D. A. Weitz, *Functionalized glass coating for PDMS microfluidic devices*, Caister Academic Press, 2009.
108. K. A. Heyries and C. L. Hansen, *Lab Chip*, 2011, **11**, 4122.
109. H. Sasaki, H. Onoe, T. Osaki, R. Kawano, and S. Takeuchi, *Sensors and Actuators B: Chemical*, 2010, **150**, 478–482.
110. J. N. Lee, C. Park, and G. M. Whitesides, *Anal. Chem.*, 2003, **75**, 6544–6554.
111. E. Sollier, C. Murray, P. Maoddi, and D. Di Carlo, *Lab Chip*, 2011, **11**, 3752.
112. P. Wagli, A. Homsy, and N. F. de Rooij, *Sensors and Actuators B: Chemical*, 2011, **156**, 994–1001.
113. C. F. Carlborg, T. Haraldsson, K. Oberg, M. Malkoch, and W. van der Wijngaart, *Lab Chip*, 2010, **11**, 3136.
114. N. Naik, C. Courcimault, H. Hunter, J. Berg, J. Lee, K. Naeli, T. Wright, M. Allen, O. Brand, A. Glezer, and W. King, *Sensors and Actuators A: Physical*, 2007, **134**, 119–127.
115. H. P. Chou, M. A. Unger, and S. R. Quake, *Biomedical Microdevices*, 2001, **3**, 323–330.
116. M. A. Unger, H. P. Chou, T. Thorsen, A. Scherer, and S. R. Quake, *Science*, 2000, **288**, 113–116.

Supplemental Information

Computational Fluid Dynamics Simulations (CFD)

The liquid jet formation in a microfluidic liquid jet device is simulated using COMSOL Multiphysics v4.2a. The tasks for CFD-simulations involve the creation of the 3D-geometry, the setup of the fluid model, mesh generation and the analysis of the results, as illustrated in Fig. S1.

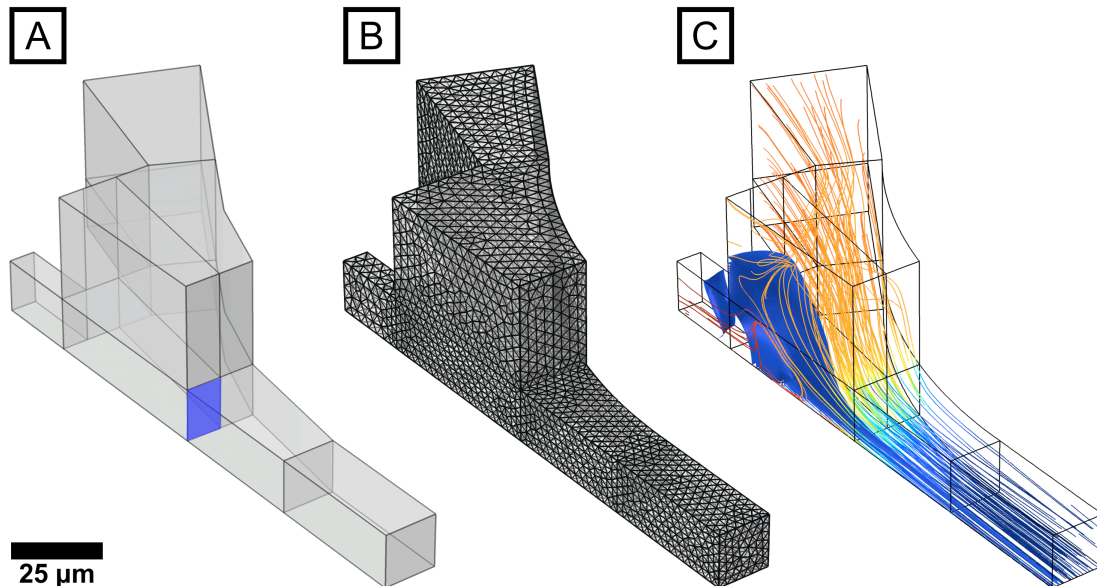


Fig. S1 Towards the simulation of the fluid flow inside the microfluidic liquid jet device: (A) Import of the 3D device geometry drawn in AutoCAD 2013 (the blue square marks the initial liquid-gas interface) (B) mesh generation and (C) solution of the model. The scale bar denotes 100 μm .

First, the CAD-designed geometry of the microfluidic liquid jet device is imported into COMSOL. This file contains exactly the same geometric design which was used for the photo mask of the soft lithographic fabrication process. Thereafter, the boundary conditions are assigned to the microchannel walls, to the inlets and the outlet of the device assuming time-dependent conditions and finite elements are generated based on this geometry. To describe the interplay of air and water, we chose a two-phase model which is based on the level-set method.^{S1,S2} Using this model, we performed the simulation for the Newtonian fluid water and the underlying fluid dynamics are described by the incompressible Navier-Stokes equations:

$$\rho \frac{\partial \mathbf{u}}{\partial t} + \rho (\mathbf{u} \cdot \nabla) \mathbf{u} = \nabla \cdot \left[-p \mathbf{I} + \mu (\nabla \mathbf{u} + \nabla \mathbf{u}^T) \right] + \mathbf{F}_g + \mathbf{F}_{st} + \mathbf{F}_{ext} + \mathbf{F}$$

$$\nabla \cdot \mathbf{u} = 0$$

with the density of the fluid ρ , the pressure p , the identity matrix \mathbf{I} , the dynamic viscosity of the fluid μ , the velocity field \mathbf{u} and the different forces \mathbf{F} (gravity (g), surface tension (st), external free energy (ext), volume (no index)).

The movement of the fluid-fluid interface of the two-phase flow within the velocity field are described by the mentioned level set method which is based on the following formulas.

$$\frac{\partial \phi}{\partial t} + \mathbf{u} \cdot \nabla = \gamma \nabla \cdot \left(\varepsilon \nabla \phi - \phi(1-\phi) \frac{\nabla \phi}{|\nabla \phi|} \right)$$

$$\rho = \rho_1 + (\rho_2 - \rho_1)\phi$$

$$\mu = \mu_1 + (\mu_2 - \mu_1)\phi$$

The parameter ε determines the thickness of the region where ϕ goes smoothly from zero to one and is typically of the same order as the size of the elements of the mesh. ε is constant within each domain and equals the largest value of the mesh size h within the domain. The parameter γ determines the amount of reinitialization or stabilization of the level set function. The constant densities of fluid 1 and 2 are described by ρ_1 and ρ_2 and their dynamic viscosities by μ_1 and μ_2 , respectively. Here, fluid 1 corresponds to the domain where $\phi < 0.5$, and fluid 2 corresponds to the domain where $\phi > 0.5$.

The 3D model is solved for 77223 finite elements and 402905 degrees of freedom. The average element quality of the mesh is 0.7659 on a scale from 0 to 1, where 1 is the highest quality. All relevant constants that are used in the simulations are summarized in Tab. S1.

Tab. S1 Material properties used in the simulation model.

Parameter	Value
flow speed v ($\mu\text{L h}^{-1}$)	600
flow speed v (m s^{-1})	0.37037
main channel height h_{MC} (μm)	30
main channel width w_{MC} (μm)	15
temperature T (K)	293.15
pressure difference Δp_g (bar)	0.25
surface tension water/air σ (N m^{-1}) ^{S3}	0.0782
viscosity η ($\text{kg} \cdot \text{m}^{-1} \text{s}^{-1}$) ^{S4}	
time frame t (μs)	0 to 750

Gas flow rate analysis

The gas flow rate is analyzed to quantify the vacuum compatibility of the microfluidic liquid jet devices. This task is performed by putting the microfluidic device slightly under water and measuring the time until 25 mL of gas are collected in a reservoir. The results are shown in Fig. S2 and Tab. S2. The measured gas flow rates should allow a vacuum of 10^{-6} bar at a (high, but reasonable) vacuum pumping speed of 1000 l s^{-1} .

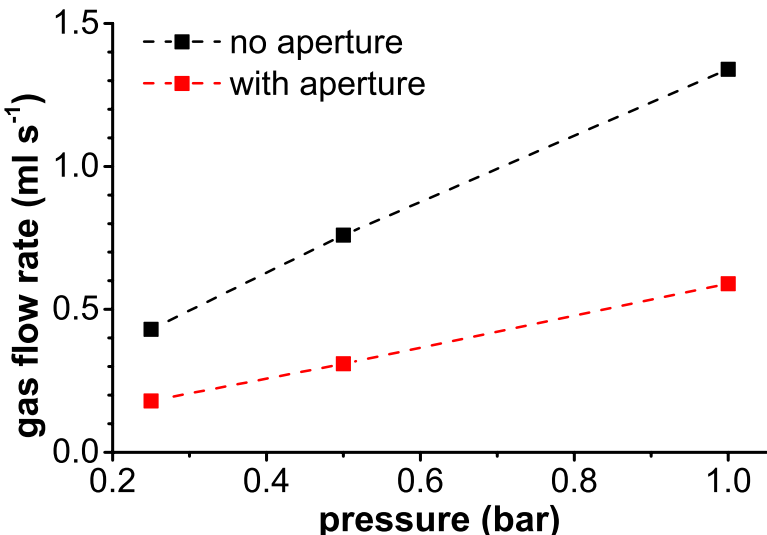


Fig. S2 Change of the gas flow rates depending on the applied pressures and on the nozzle geometry. The outlet cross section with an aperture is $30\cdot30\text{ }\mu\text{m}^2$ while the nozzle-less version has a cross section of $30\cdot90\text{ }\mu\text{m}^2$.

Tab. S2 Gas flow rates under different conditions.

p (bar)	no aperture ($30\cdot90\text{ }\mu\text{m}^2$)	with aperture ($30\cdot30\text{ }\mu\text{m}^2$)
	flow rate (ml s ⁻¹)	flow rate (ml s ⁻¹)
0.25	0.43	0.18
0.5	0.76	0.31
1	1.34	0.59

Jetting of protein crystallization buffers

To demonstrate the microfluidic liquid jet devices' compatibility with other liquids than pure water, the devices are operated with different solutions that are examples for commonly used protein crystallization buffers. These aqueous solutions contain high concentrations of poly(ethylene glycol) (PEG, $M_n = 400 \& 3350\text{ g mol}^{-1}$), ammonium sulfate ($(\text{NH}_4)_2\text{SO}_4$), 2-methyl-2,4-pentanediol (MPD) (all obtained from Sigma Aldrich) and/or TacsimateTM pH 4.0. The latter is a readily-available crystallization reagent by Hampton Research and contains 1.8305 M malonic acid, 0.25 M ammonium citrate tribasic, 0.12 M succinic acid, 0.3 M DL-malic acid, 0.4 M sodium acetate trihydrate, 0.5 M sodium formate and 0.16 M ammonium tartrate dibasic.^{S5,S6}

The liquid flow rate is set to $1000\text{ }\mu\text{l h}^{-1}$ at an applied pressure of 0.5 bar and images are captured every 20 s until the experiment was *intentionally* stopped after 60 min. The microfluidic liquid jet devices operate error free and without any indication of clogging as shown in Fig. S3.

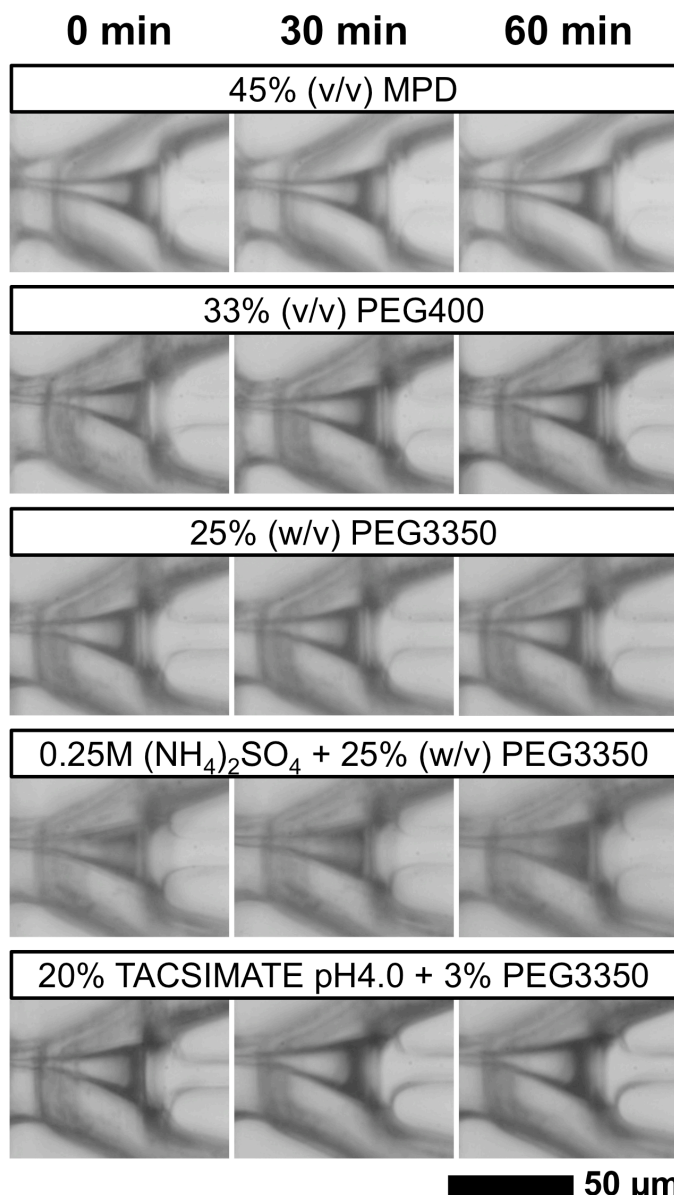


Fig. S3 Microscopic images of the microfluidic liquid jet device during operation with different solutions over extended times. These solutions are examples of commonly used protein crystallization buffers containing high concentrations of PEG and/or salts. The liquid flow rate is set to 1000 $\mu\text{l h}^{-1}$ at an applied pressure of 0.5 bar.

- S1. CFD Module User's Guide for COMSOL v4.2a, COMSOL AB, 2011, 211-215.
- S2. E. Olsson and G. Kreiss, *J. Comput. Phys.* 2005, **210**, 225–246.
- S3. N. R. Pallas and Y. Harrison, *Colloids Surf.*, 1990, **43**, 169–194.
- S4. R. Weast, M. Astle, *Handbook of Chemistry and Physics*, 60th edition, CRC Press, Boca Raton, 1979, F-11, F-49.
- S5. Hampton Research - Production Information: What is TacsimateTM?
http://hamptonresearch.com/documents/product/hr000175_what_is_tacsimate_new.pdf, (accessed Jan 2014).
- S6. A. McPherson and B. Cudney, *J. Struct. Biol.*, 2006, **156**, 387–406.

7.4 Lyotropic phase behavior of polymer-coated iron oxide nanoparticles

Lyotropic phase behavior of polymer-coated iron oxide nanoparticles[†]

Sara Mehdizadeh Taheri,^{*a} Steffen Fischer,^a Martin Trebbin,^a Sebastian With,^a Jan H. Schröder,^a Jan Perlich,^b Stephan V. Roth^b and Stephan Förster^a

Received 1st August 2012, Accepted 18th September 2012

DOI: 10.1039/c2sm26777b

We show that monodisperse iron oxide nanoparticles in the size range of 6–17 nm, coated with brush-like layers of polystyrene or polyisoprene of different molecular weights, form well-defined lyotropic liquid crystalline phases. The lyotropic phase behaviour was investigated by synchrotron small-angle X-ray scattering. With increasing concentration, the polymer-coated nanoparticles show a disorder-order transition into well ordered bcc- or fcc-phases, depending on nanoparticle size and polymer molecular weights. The lyotropic phases can be shear oriented to obtain macroscopic highly ordered single crystalline nanoparticle superlattices exhibiting more than 100 Bragg-peaks. Within the ordered phases, the distance between adjacent nanoparticles can be varied systematically *via* concentration and attached polymer molecular weights in a range of 10–40 nm. We further demonstrate the versatility of lithographically patterned microstructured sample holders in combination with microfocus X-ray beams, which allow the investigation of very small sample volumes.

Introduction

The spontaneous assembly to form ordered crystalline phases is a well-known property of colloidal particles. Common examples comprise dispersion colloids such as polymer latices, silica particles or microgels, as well as association colloids such as surfactant and polymer micelles. Of particular current interest are colloidal particles that form ordered phases in solution, *i.e.* in the lyotropic state, because established wet-chemical processes such as sol–gel-chemistry or polymerization reactions can be used to transform them into solid ordered materials that would otherwise be very difficult or impossible to prepare. The most prominent example is their use as templates to generate photonic crystals.

For many applications, it would be desirable to similarly assemble nanoparticles into lyotropic colloidal crystals. The formation of ordered crystalline assemblies of nanoparticles was quickly reported after synthetic methods to generate nanoparticles with sufficiently narrow size distributions had been established.¹ Since then, there have been many reports of superlattice formation for different nanoparticles and also binary nanoparticle mixtures,² mostly in the form of monolayers or micron-size crystals.³ These assemblies are mostly produced *via*

drop casting on solid supports, or by controlled crystallization from dilute solutions.⁴

In most cases of ordered nanoparticle assembly, a control over the interparticle distance was neither possible nor intended. For conventional nanoparticle assemblies, some control of the interparticle distance is possible *via* the choice of the stabilizing surfactants that can differ in the length of their alkyl chains.⁵ A breakthrough has been the use of DNA-ligands by Alivisatos and Mirkin *et al.*,^{6–8} who for gold nanoparticles tailored the superlattice type and nanoparticle distance *via* hybridization of DNA-chains. If the DNA-chains were not hybridizing, lyotropic phases of cubic symmetry were formed. The lyotropic phase behaviour could be followed by microfocus synchrotron X-ray scattering of a small droplet of a DNA-coated gold nanoparticle aqueous solution upon drying.^{9,10}

Since the DNA@Au system builds upon the unique and stable Au–S–DNA end group attachment and has its limitations in the amount of material that can be produced, it would be highly desirable to have more versatile and upscalable polymer@-nanoparticle systems. We have recently developed a method to attach polymer chains with their chain end to nanoparticles *via* a ligand exchange procedure.^{11,12} It builds upon the advantages of state-of-the-art methods for nanoparticle synthesis such as the hot-injection technique¹³ to produce nanoparticles that are stabilized by short chain alkyl ligands having coordinatively binding groups such as phosphines, carboxylic acids, or amines. In the ligand exchange procedure these ligands are replaced by polymer chains having the same end groups to obtain nanoparticles coated with polymer chains, which are bound to the nanoparticle surface with their chain ends to form a spherical polymer brush. By varying the surface density and length of the

^aUniversität Bayreuth, Universitätsstrasse 30, Bayreuth, Germany. E-mail: sara.mehdizadeh.taheri@uni-bayreuth.de; stephan.foerster@uni-bayreuth.de; Fax: +49 921-55-2780; Tel: +49 921-55-3924

^bHASYLAB at DESY, Notkestrasse 85, Hamburg, Germany. E-mail: stephan.roth@desy.de; jan.perlich@desy.de; Fax: +49 40 8994 2934; Tel: +49 40 8998 2934

[†] Electronic supplementary information (ESI) available: TEM, TGA, SAXS results. See DOI: 10.1039/c2sm26777b

Published on 15 October 2012. Downloaded by UNIVERSITAT BAYREUTH on 12/02/2014 10:23:28.

polymer chains, nanoparticles with polymer layers of adjustable density and thickness can be prepared. This procedure is very versatile and can be used to coat different types of nanoparticles (Fe_2O_3 , CdSe, PbS, ZnO, Au, Ag) with various types of polymers (polystyrene, polyisoprene, polyethylene oxide, polyethylene).¹² We could show that for high surface densities, the nanoparticles are very well stabilized in solution.¹⁴

These polymer-coated nanoparticles have a well-defined core–shell structure, the core being the nanoparticle and the shell being the solvent-swollen polymer brush. This very much resembles the core–shell structure of block copolymer micelles, which have a core of insoluble polymer blocks, and a solvent-swollen shell of the soluble block. Block copolymer micelles are known to assemble into highly ordered lyotropic phases.^{15,16} Therefore we expected that polymer-coated nanoparticles would assemble similarly into lyotropic phases. This would open a route to well-defined nanoparticle superlattices without relying on DNA-hybridization, but rather employing conventional polymers on a larger scale, and a large range of nanoparticle types, which has not been attempted so far.

In the present study, we investigated narrow disperse maghemite nanoparticles in the size range of 6–17 nm, which were coated with polystyrene or polyisoprene of different molecular weights. We investigated their self-assembly behaviour in toluene, a good solvent for the polymers. Using small-angle X-ray scattering, we show for the first time that polymer stabilized nanoparticles can form highly ordered lyotropic phases. As for polymer micelles, fcc and bcc-lattices are formed, depending on the concentration and nanoparticle-to-layer size ratio and thus the softness of the interaction potential. By shear orientation in a shear-cell, macroscopic, highly ordered single crystals can be obtained. Additionally, shear orientation is possible for very small sample amounts (μL) by shear-alignment on lithographically patterned microfluidic grids.

Experimental part

Nanoparticle synthesis

Iron-oxide nanoparticles were synthesized *via* thermal decomposition of an iron oleate complex, according to the procedure of Park *et al.*¹³ Typically, 10–30 g of oleate were reacted to obtain 2–8 g of monodisperse maghemite nanoparticles. The nanoparticles were characterized by transmission electron microscopy (see ESI†).

Polymer ligands

Polystyrene and polyisoprene were synthesized by living anionic polymerization initiated by sec-butyl lithium in THF at -70°C . After completion of the polymerization, the living end groups reacted either with acetic acid to obtain unfunctionalized polymer, with CO_2 to obtain polymer with a COOH-end group, or with ethylene oxide to obtain an –OH-end group. The OH-group was activated with carbonyl diimidazol (CDI) and reacted with diethylenetriamin (DETA) or pentaethylhexamin (PEHA) to obtain amino-end functionalized polymers.^{11,14} Polystyrenes and polyisoprenes with COOH- and $-\text{C}_{10}\text{H}_{28}\text{N}_6$ -end groups were used as stabilizing ligands. The polymers were characterized by GPC, MALDI-TOF-MS, and $^1\text{H-NMR}$.

Attachment of polymer chains

After their synthesis, the nanoparticles are covered with a stabilizing layer of oleic acid. The oleic acid is exchanged by a layer of end functionalized polymers *via* ligand exchange. In the case of iron-oxide nanoparticles, we used PS-COOH and PS-PEHA, PI-COOH, and PI-DETA. For the ligand exchange, a solution containing an excess of PS/PI-ligands (70 mg) in THF (1 mL) is added to a solution (200 μL) of nanoparticles (20 wt%) in toluene. Free oleic acid is removed by quantitative precipitation in ethanol. The solid containing nanoparticles, excess polymer and traces of low-molecular weight ligand is then redissolved in THF and again quantitatively precipitated in ethanol. After redissolution of the solid in THF, ethanol is added dropwise to selectively precipitate the nanoparticles from the supernatant containing the free polymer. The selective precipitation for the PS-nanocomposites is repeated in heptane. The amount of attached polymer was determined by thermal gravimetric analysis (TGA) (see ESI†).

Preparation of lyotropic solutions

For the preparation of the lyotropic nanoparticle solutions, the polymer coated nanoparticles were dissolved in the calculated amount of toluene to obtain a concentration series of 10–90% w/w. From each concentration, 15 μL were transformed into a capillary tube (diameter of 1 mm), which were melted off to avoid solvent evaporation.

For shear orientation of very small volumes of lyotropic phases, lithographically patterned microfluidic channel grids were used (Fig. 5). These grids consist of parallel aligned micron-sized channels with variable width and depth. They were produced by standard soft lithographic techniques from a PDMS master, which was used as a mold for NOA81 (Norland Optical Adhesive). NOA 81 is a UV-curable adhesive and more solvent-resisting than PDMS,^{17–19} especially to toluene. For the measurements, an amount of 2–5 μL of the sample was spread on the microstructured grid. The grid was taped with Kapton to prevent solvent evaporation.

Synchrotron experiments

The measurements were performed at the beamlines BW4 and P03 at HASYLAB/DESY. At BW4, the samples were measured at a wavelength of 0.138 nm and a sample-detector distance of 108 cm. The diameter of the beam was 60 μm . The scattering patterns were detected with a MAR CCD-camera. At P03, the samples were measured at a wavelength of 0.09 nm and a sample-detector-distance of 200 cm. The diameter of the beam was 10 μm . The scattering patterns were recorded with a Pilatus 300k and Pilatus 1M detector.

Scattering curves of ordered particle systems

In the following, we describe the calculation of scattering curves for isotropic systems and scattering patterns of anisotropic shear-oriented systems of nanoparticles with solvent-swollen polymer shells dispersed in a solvent. For two-phase systems consisting of particles (phase “1”) with scattering length b_1 and volume fraction ϕ_1 in a solvent (phase “2”) of scattering length b_2

and a volume fraction $\phi_2 = 1 - \phi_1$, separated by sharp interfaces, the scattered intensity per unit volume is given by^{20,21}

$$I(\mathbf{q}) = (b_1 - b_2)^2 \rho_N P(q, R) [1 + \beta(q, R) (Z(\mathbf{q}, \mathbf{g}) - 1) G(q, g)] \quad (1)$$

where

$$P(q, R) = \langle F^2(q, R) \rangle_R \quad (2)$$

is the particle form factor, $F(q)$ the scattering amplitude or Fourier transform of the particle form, $\rho_N = N/V$ is the number density of the particles, $Z(\mathbf{q})$ is the lattice factor describing the spatial distribution of the particles, \mathbf{q} is the scattering vector, and $G(q)$ is the Debye–Waller factor. $\langle \dots \rangle_R$ denotes the average over the distributions of radii R . The ratio $\beta(q)$ is given by

$$\beta(q, R) = \frac{\langle F(q, R) \rangle_R^2}{\langle F^2(q, R) \rangle_R} \quad (3)$$

The effect of the ratio $\beta(q, R)$ on the scattered intensity is similar to the Debye–Waller factor, resulting in a decay of the Bragg-intensities with increasing scattering vector \mathbf{q} . Eqn (1) considers the effect of the particles – *via* their first and second moment of the particle size distribution – and of the lattice – *via* the first and second moment of the distribution of lattice points – on the scattered intensity $I(\mathbf{q})$.

The scattering amplitude for spheres of radius R is given by

$$F(q, R) = \frac{3}{(qR)^3} (\sin(qR) - qR \cos(qR)) \quad (4)$$

For the calculation of the average over the size distribution the Schulz-Zimm distribution is used, which yields for the z -average of a function $f(q, R)$

$$\langle f(q, R) \rangle_R = \int_0^\infty f(q, R) R^m h(R) dR \quad (5)$$

with

$$h(R) = \frac{(z+1)^{z+m+1} R^z}{R^{z+m+1} \Gamma(z+m+1)} \exp\left[-(z+1)\frac{R}{\bar{R}}\right] \quad (6)$$

and $m = 6$ is the weighting factor for the radius R , the average radius \bar{R} , and the relative standard deviation $\sigma_R = (z+1)^{-1/2}$. The distribution is normalized such that $\int_0^\infty R^m h(R) dR = 1$. The use of a Schulz-Zimm distribution has the advantage of yielding analytical expressions for $\langle P(q) \rangle$, $\langle F(q) \rangle$, and $\beta(q)$.²⁰

Using the Miller indices (hkl) for a given crystal lattice plane, the lattice factor for an ideal undistorted lattice can be written as

$$Z(\mathbf{q}, \mathbf{g}) = \frac{(2\pi)^3}{nv} \sum_{\substack{h, k, l = -\infty \\ (hkl) \neq (000)}}^{\infty} f_{hkl}^2 L_{hkl}(\mathbf{q}, \mathbf{g}_{hkl}) \quad (7)$$

where n is the number of particles per unit cell, f_{hkl} is the structure factor of the unit cell, v is the volume of the unit cell, and $L_{hkl}(\mathbf{q}, \mathbf{g}_{hkl})$ is a normalized peak shape function that depends on the reciprocal lattice vectors $\mathbf{g}_{hkl} = ha^* + kb^* + lc^*$ for the corresponding twins are given in Table 1.

$(2\pi)^{-3} V \int I(q) dq = Q = \phi_1(1 - \phi_1)$. The Debye–Waller factor $G(q)$ is given by

$$G(q) = \exp[-\sigma_a^2 \bar{a}^2 q^2] \quad (8)$$

where \bar{a} is the next nearest neighbour distance between adjacent particles, which for an FCC-lattice is $\bar{a} = \frac{\sqrt{2}}{2} a$ and for a BCC-lattice is given by $\bar{a} = \frac{\sqrt{3}}{2} a$. The peak shape function $L(\mathbf{q}, \mathbf{g}_{hkl})$ depends on the scattering vector $\mathbf{q} = (q_x, q_y, q_z)$ and the reciprocal lattice vector $\mathbf{g}_{hkl} = (g_{x,hkl}, g_{y,hkl}, g_{z,hkl})$ and can be factorized into a radial part depending on the modulus of the scattering vector, $L_q(q, g_{hkl})$, and an azimuthal part depending on the deviation angle ψ with respect to the scattering vector, $L_\psi(q, g_{hkl}, \psi_{hkl})$ as

$$L(\mathbf{q}, \mathbf{g}_{hkl}) = L_q(q, g_{hkl}) L_\psi(q, g_{hkl}, \psi_{hkl}) \quad (9)$$

This peak shape function is normalized such that

$$\int_0^\infty \int_0^\pi \int_0^{2\pi} L_q(q, g_{hkl}) L_\psi(q, g_{hkl}, \psi_{hkl}) q^2 \sin \psi d\theta d\psi dq = 1 \quad (10)$$

with the polar angles ψ , θ . For the radial peak shape function, we use a normalized Gaussian

$$L_q(q, g_{hkl}) = \frac{2}{\pi \delta_q} \exp\left[-\frac{4(\mathbf{q} - \mathbf{g}_{hkl})^2}{\pi \delta_q^2}\right] \quad (11)$$

where δ_q is the radial peak width, which can be related to an average domain size

$$D_l = \frac{4}{\delta_q}. \quad (12)$$

For the azimuthal peak shape, we also use a Gaussian given by

$$\tilde{L}_\psi(q, g_{hkl}, \psi_{hkl}) = \frac{1}{2\pi g_{hkl}^2 K(a_{hkl})} \exp\left[-\frac{4\psi_{hkl}^2 q^2}{\pi \delta_\psi^2}\right] \quad (13)$$

where $a_{hkl} = \frac{4g_{hkl}^2}{\pi \delta_\psi^2}$ and $K(a_{hkl})$ is a normalization function derived in ref. 21. In the isotropic limit $\lim_{a \rightarrow 0} L_\psi(q, \psi) = \frac{1}{4\pi q^2}$. The azimuthal peak width δ_ψ can be related to an azimuthal peak width or an angular spread $\Delta\theta$ via

$$D_\psi = \frac{4}{\delta_\psi} = \frac{2a}{\tan \Delta\theta} \quad (14)$$

In the following, we will consider bcc- and fcc-lattices, for which the structure factors are given by

$$f_{hkl} = \begin{cases} 1 + \cos[\pi(h+k+l)] & \text{for bcc} \\ 1 + \cos[\pi(h+k)] + \cos[\pi(h+l)] + \cos[\pi(k+l)] & \text{for fcc} \end{cases} \quad (15)$$

Fcc and bcc lattices occur in twinned configurations. The reciprocal lattice vectors $\mathbf{g}_{hkl} = ha^* + kb^* + lc^*$ for the corresponding twins are given in Table 1.

We have found that eqn (1) describes scattering curves and scattering patterns remarkably well for a large variety of mesoscopically ordered materials.²¹ The use of closed analytical

Table 1 Reciprocal lattice vectors a^*, b^*, c^* for FCC and BCC twins. e_x , e_y , and e_z are the unit vectors of the Cartesian coordinate system

	a^*	b^*	c^*
FCC twin A	$\frac{2\pi}{a} e_x$	$\frac{2\pi}{a} e_y$	$\frac{2\pi}{a} e_z$
FCC twin B	$\frac{2\pi}{3a} (2e_x - e_y + 2e_z)$	$\frac{2\pi}{3a} (2e_x + 2e_y - e_z)$	$\frac{2\pi}{3a} (-e_x + 2e_y + 2e_z)$
BCC twin A	$\frac{2\pi}{a} e_x$	$\frac{2\pi}{a} e_y$	$\frac{2\pi}{a} e_z$
BCC twin B	$\frac{2\pi}{3a} (2e_x + e_y - 2e_z)$	$\frac{2\pi}{3a} (e_x + 2e_y + 2e_z)$	$\frac{2\pi}{3a} (2e_x - 2e_y + e_z)$

functions facilitates computing and allows efficient implementation into fitting routines. It allows to quickly extract the unit cell size a , the mean deviation from the lattice points σ_a , the nanoparticle radius R , its relative standard deviation σ_R (polydispersity), and the mean size of the crystalline domains D from measured scattering curves and scattering patterns. Eqn (1) also reproduces correctly secondary Bragg-peaks that appear as a consequence of the finite peak width as outlined in ref. 21. An executable version of the software (Scatter)²² can be obtained from the author.

Results and discussion

Isotropic concentration series

Fig. 1 shows measured synchrotron-SAXS curves of a concentration series of Fe_2O_3 (6 nm)@PS-COOH(8k) nanoparticles in toluene. At the lowest concentrations we observe a broad maximum at $q \sim 0.3 \text{ nm}^{-1}$ indicating weak positional correlations between the nanoparticles. The minimum at $q = 1.4 \text{ nm}^{-1}$ corresponds to the sphere form factor minimum, from which the radius of the nanoparticles can be estimated to be 6.1 nm, in good agreement with the TEM measurements. With increasing

concentration, the maximum becomes more pronounced and shifts to larger q -values. Between a concentration of 60 and 70 wt%, we observe a disorder–order transition, indicated by the sharp Lorentzian-type shape of the first-order peak and the appearance of higher order reflections.

The peak positions can be indexed on a bcc-lattice (space group $Im\bar{3}m$). Also in the dry state we observe the formation of a bcc-lattice. The lattice order is well comparable to micellar lyotropic phases in water. The form factor minimum does not vanish or shift, indicating that the polymer-stabilized nanoparticles show no aggregation, even for the highest concentrations and in bulk.

The measured scattering curves can be quantitatively described by eqn (1) to obtain more detailed structural information. From the analysis we directly obtain the unit cell dimension, the mean displacement of the nanoparticles from the lattice points, the nanoparticle radius with the relative standard deviation (particle polydispersity), as well as the mean size of the crystalline domains. All values are summarized in Table S2 in the ESI.† The observed values are all typical for lyotropic phases. The unit cell sizes decrease with increasing concentration from 28–15 nm, the mean deviation from the lattice points is 2.1 nm (12% relative to the unit cell size) and the domain sizes increase with increasing concentration from 30–97 nm. The radius of the nanoparticles is 6.1 nm with a polydispersity of 9.5%.

Fig. 2 shows measured synchrotron-SAXS curves of a concentration series of Fe_2O_3 (17 nm)@PS-N₆(28k) nanoparticles in toluene. Since the nanoparticles are larger, we observe more form factor oscillation in the measured q -range, with the first minimum at $q \sim 0.55 \text{ nm}^{-1}$. Also for this case we did not observe shifts or damping of the form factor oscillations which would indicate nanoparticle aggregation, even at the highest concentrations and in the solid state. Since the attached polymer chains are larger, we observe the disorder–order transition at lower concentrations, *i.e.* between 30 and 40 wt%. Then with increasing concentration the nanoparticles first form an

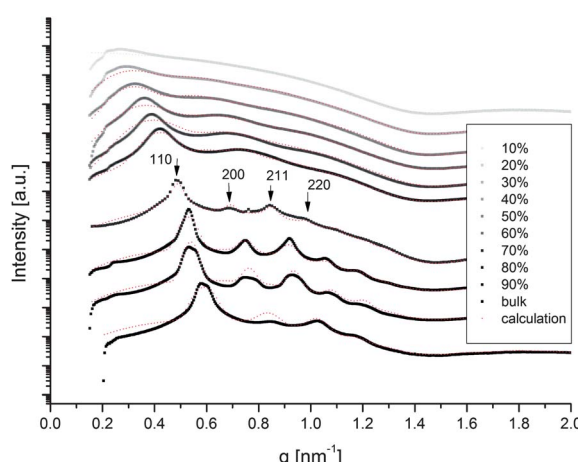


Fig. 1 Synchrotron SAXS-curves measured at BW4/DESY for Fe_2O_3 (6 nm)@PS-COOH(8k) at different concentrations in toluene. At a concentration between 60 and 70%, we observe a disorder–order transition into a bcc-phase. The dotted lines indicate fits to the measured scattering curves using eqn (1).

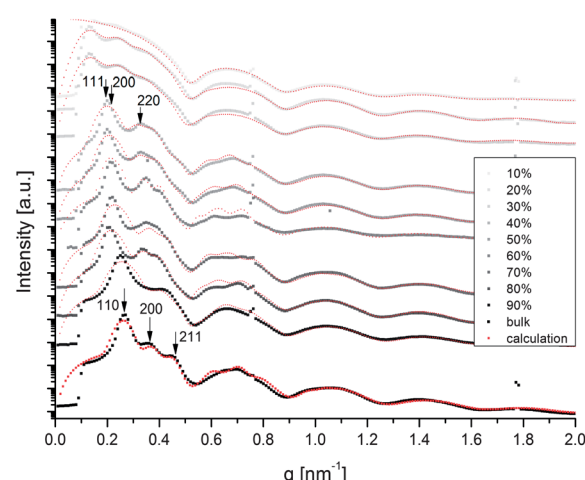


Fig. 2 Synchrotron SAXS-curves measured at BW4/DESY for Fe_2O_3 (17 nm)@PS-N₆(28k) at different concentrations in toluene. At a concentration between 30 and 40% we observe a disorder–order transition into an fcc-phase, and at 70% into a bcc-phase. The dotted lines indicate fits to the measured scattering curves using eqn (1).

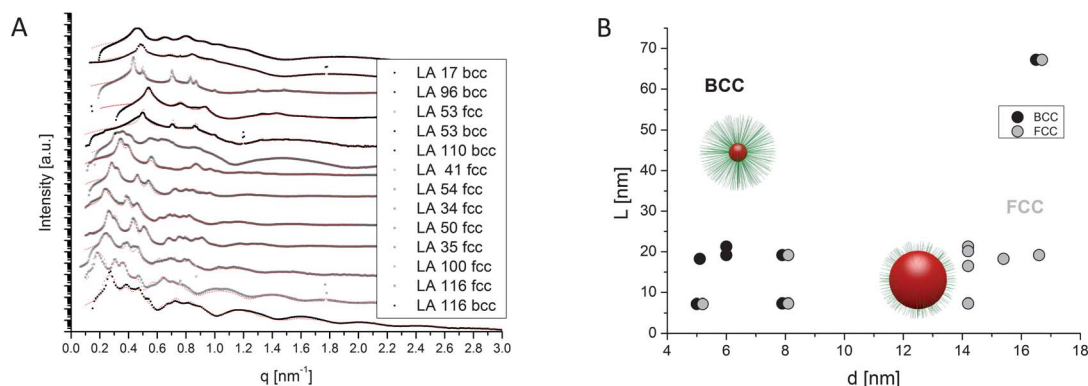


Fig. 3 (A) Synchrotron SAXS-curves measured at BW4/DESY for different nanoparticle/polymer-systems in toluene in the ordered lyotropic state. The sample codes are related to the nanoparticle diameters and polymer molecular weights in Table 2. (B) Stability regions of bcc- and fcc-phases as a function of nanoparticle diameter and polymer contour length.

fcc-structure (*Fm3m*) and at 70 wt% they show a phase transition to a bcc structure (*Im3m*). For the bulk sample the bcc unit cell size is 33 nm. Also this set of scattering curves could be fit quantitatively to eqn (1) to obtain structural details of the lyotropic phases. The unit cell sizes decrease with increasing concentration from 54–45 nm for fcc, and then from 40–35 nm for the bcc-lattices. The mean deviation from the lattice points is 2.6 nm (12% relative to the unit cell size) and the domain sizes are in the range of 300–400 nm. The radius of the nanoparticles is 17.1 nm with a polydispersity of 7.5%.

Using synchrotron-SAXS we have investigated many more nanoparticle/polymer lyotropic phases at different concentrations with different nanoparticle sizes (5–17 nm) and attached polymer molecular weights (2000–28 000 g mol⁻¹). The measured scattering curves are shown in Fig. 3A. Results of the fits to the scattering curves are all summarized in Table S3 in the ESI.† With increasing concentration up to the bulk nanoparticle/polymer nanocomposite we observe two typical lyotropic phase sequences DIS → FCC → BCC or DIS → BCC, depending on the nanoparticle size and attached polymer chain molecular weight.

From our investigations, we can give a schematic overview for the stability ranges for bcc- and fcc-structures, which appears to depend on the ratio of nanoparticle radius to attached polymer molecular weight. To compare the effect of different molecular weights of polystyrene and polyisoprene, we related the molecular weights to the contour lengths of the polymer chains, assuming a contour length of 0.25 nm for the monomers. The values are given in Table 2. In Fig. 3B, we have plotted a diagram displaying the observed lyotropic phase structure as a function of nanoparticle size and polymer contour length. We observe that systems consisting of small

nanoparticles (5–8 nm) with long polymer chains (18–22 nm) prefer bcc-packing, whereas larger nanoparticles (14–17 nm) with attached polymer chains in the contour length range of 7–21 nm prefer fcc-packing. For the largest nanoparticle (17 nm) with the longest polymer chains (67 nm), we observe a fcc/bcc-coexistence. In the schematic representation in Fig. 3B we observe bcc phases in the upper left and fcc in the lower right, with a coexistence region in between. The scheme in Fig. 3B is not meant as a phase diagram, but merely to display the observed trend. For large polymer chains attached to small nanoparticles, where mainly bcc-structures are observed, we have a strongly curved spherical polymer brush structure with low segment densities at the layer periphery. These would mediate very soft interactions. For shorter polymer chains attached to larger nanoparticles, we have less curved spherical polymer brush structures with dense layers and higher segment density at the periphery, which is expected to mediate harder interactions. The observation of bcc-structures for soft interacting colloids and fcc-structures for colloids with harder interactions is similarly observed for block copolymer micelles as shown by Gast.²³ In the solid state, bcc is always stable, analogous to block copolymer melts.

Shear-oriented lyotropic phases

As for block copolymer melts or block copolymer lyotropic phases, we found it to be possible to shear-orient lyotropic nanoparticle phases to obtain for the first time macroscopically oriented single crystalline nanoparticle superlattices. Shear-orientation was performed in a plate–plate shear cell (Linkam) with a gap size of 100 µm. We found that oscillatory shear at frequencies of 1–10 s⁻¹ and shear amplitudes of 5–10 for 10 s

Table 2 Sample codes, polymer types (PS = polystyrene, PI = polyisoprene), lattice type of the lyotropic phase, polymer molecular weight, contour length, and nanoparticle diameters for the nanocomposites measured in Fig. 3A

Sample	LA 17 (PI)	LA 96 (PS)	LA 53 (PI)	LA 110 (PS)	LA 41 (PS)	LA 54 (PI)	LA 34 (PI)	LA 50 (PI)	LA 35 (PS)	LA 100 (PS)	LA 116 (PS)
Lattice	Bcc	Bcc	Fcc/Bcc	Bcc	Fcc	Fcc	Fcc	Fcc	Fcc	Fcc	Fcc/Bcc
Polymer [g mol ⁻¹]	5800	8000	2000	8000	8000	2000	4500	5800	8400	8000	28 000
Contour length [nm]	21.3	19.2	7.3	19.2	19.2	7.3	16.5	21.3	20.1	19.2	67.2
Nanoparticle diameter [nm]	6	6	8	8	8	14.2	14.2	14.2	14.2	16.6	16.6

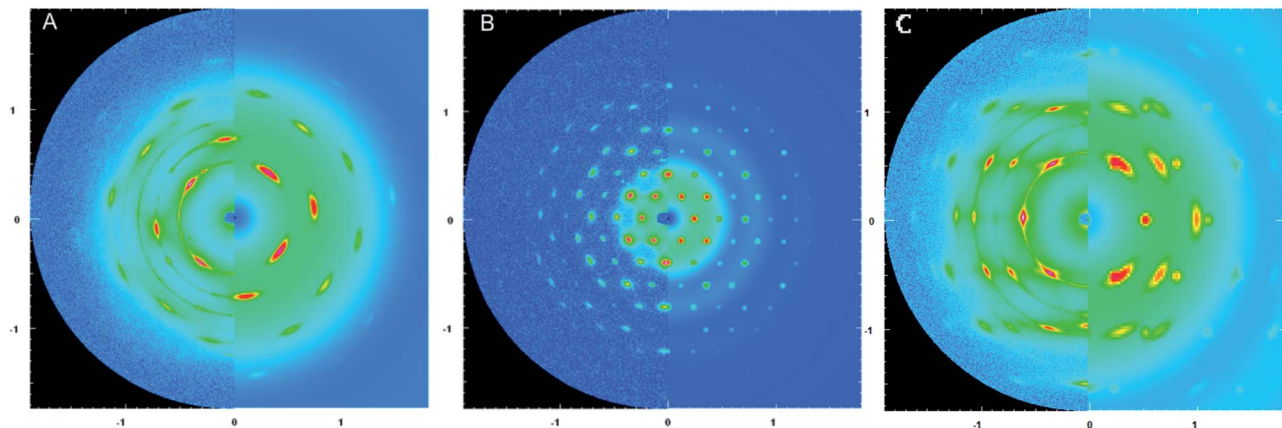


Fig. 4 Scattering patterns of shear-oriented lyotropic phases of Fe_2O_3 (5.1 nm)@PS-DETA(7.6k) forming a bcc-structure (A), Fe_2O_3 (15.4 nm)@PS-DETA(7.6k) forming a fcc-structure (B), and Fe_2O_3 (5.1 nm)@PS-DETA(3k) (C) showing a coexistence of bcc and fcc structures measured at BW4/DESY. Measurements are shown on the left halves, and calculations using eqn (1) are shown on the right halves of the patterns.

were suitable conditions for shear-alignment. The measured scattering patterns for different nanoparticle/polymer lyotropic phases are shown in Fig. 4. We observe a large number (>100 in Fig. 4B) of Bragg-reflections, indicating a high degree of lyotropic crystalline order. Indexing of these reflections is only possible by taking into account secondary Bragg-peaks which are observable as a consequence of the large peak widths typical for lyotropic crystals as outlined in ref. 24.

For Fe_2O_3 (5.1 nm)@PS-DETA(7.6k) (Fig. 4A), which was shear-oriented at 4 Hz and a shear amplitude of 9, we observe a bcc-structure oriented such that the $[1\bar{1}0]$ -direction is parallel to the X-ray beam and the $[\bar{1}\bar{1}2]$ -direction is oriented in the shear direction. This shear-alignment structure is typical for colloidal lyotropic crystals. The alignment orients the line of highest particle density $[\bar{1}\bar{1}2]$ parallel to the flow-direction and the plane of highest particle density $(1\bar{1}0)$ normal to the gradient direction, which is parallel to the X-ray beam. Bcc occurs in a twinned configuration. The twins both align with their $[\bar{1}\bar{1}2]$ -direction in the shear direction, with the $(\bar{1}\bar{1}2)$ -plane being the mirror plane that relates each of the twins.²⁴ The scattering pattern can be quantitatively analyzed by eqn (1). The calculated scattering pattern is merged into the measured scattering pattern to show remarkably good agreement. The structural parameters derived from the calculation such as unit cell dimension, mean deviation from the lattice points, domain size, particle size and its mean square deviation are given in Table 3. The nearest neighbour distance between adjacent nanoparticles is 15 nm, which is considerably larger compared to the 8.8 nm observed for the bulk phase. We observe that both twin structures occur with equal probability.

For Fe_2O_3 (15.4 nm)@PS-DETA(7.6k) (Fig. 4B), which was shear-oriented at 8 Hz and an amplitude of 9, we observe a fcc-structure. It orients such that the line of highest particle density $[\bar{1}10]$ is parallel to the flow direction and the plane of highest particle density $[111]$ orients normal to the gradient direction, parallel to the X-ray beam. Also in this case, eqn (1) very well describes the scattering pattern. The calculated scattering pattern is merged into the measured scattering pattern to show excellent agreement. It is worth mentioning that nearly 2/3 of the more than 100 observed peaks are secondary Bragg reflections due to finite peak widths, which would usually be considered crystallographically forbidden. Also for this calculation, the structural parameters are given in Table 3. The nearest neighbour distance is 31 nm which can be compared to the bulk value of 21 nm.

A complex and very interesting scattering pattern is shown in Fig. 4C. This scattering pattern was measured for Fe_2O_3 (5.1 nm)

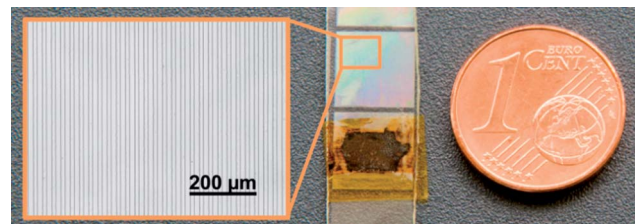


Fig. 5 Micro structured NOA 81 array with $1\text{ cm} \times 1\text{ cm}$ patches consisting of $14\text{ }\mu\text{m}$ channel grids, used to spread and shear-orient very small sample amounts ($2\text{--}5\text{ }\mu\text{L}$) of lyotropic phases. The lower patch has been filled with a nanoparticle lyotropic gel and sealed with Kapton tape to avoid solvent evaporation during X-ray measurements.

Table 3 Calculated structural information for measured 2D-SAXS pattern

Sample	Lattice	q_x	q_y	q_z	Unit cell [nm]	Mean displacement [nm]	Radial domain size [nm]	Azimuthal domain size [nm]
Fe_2O_3 (5.1 nm)@PS-DETA(7.6k)	BCC	$1\bar{1}1$	$\bar{1}1\bar{2}$	110	17.0	2.0	180	50
Fe_2O_3 (15.4 nm)@PS-DETA(7.6k)	FCC	$\bar{1}\bar{1}2$	$1\bar{1}0$	111	44.0	2.8	200	50
Fe_2O_3 (5.1 nm)@PS-DETA(3k)	BCC	$1\bar{1}1$	$\bar{1}\bar{1}2$	110	14.0	1.0	100	10
	FCC	$1\bar{1}2$	$1\bar{1}0$	111	17.0	1.0	100	35

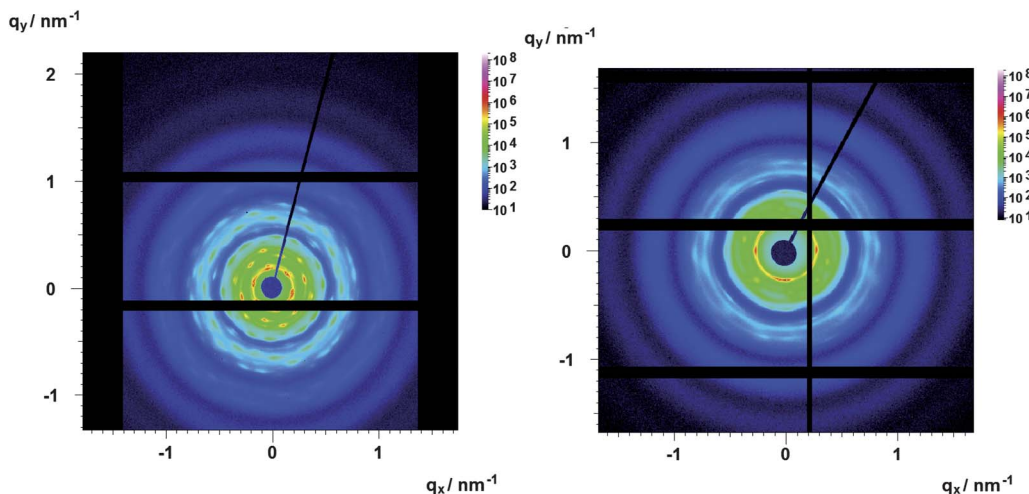


Fig. 6 SAXS-patterns measured with a microfocused X-ray beam at P03/DESY for Fe_2O_3 (16.6 nm)@PS-DETA(28k) at a concentration of 50%wt (fcc) (A) and 70%wt (bcc) (B). The samples were oriented in a specially designed microchannel sample holder where sample amounts of only 2–5 μL are needed.

@PS-DETA(3k). The sample could only be oriented by applying continuous shear at a shear rate of 750 s^{-1} . The pattern has similarities to the patterns observed for the bcc and fcc-structures and corresponds to a coexistence of both phases. Assuming both structures to be aligned as in Fig. 4A and B, then all peaks can be appropriately indexed and even a quantitative calculation is possible that is merged into the experimentally determined scattering pattern. It gives very good agreement and yields a relative composition fcc–bcc of 0.7 : 0.3.

An interesting point is that in coexistence there should be an epitaxial relation with respect to both the unit cell dimensions and orientations. The phase transition is believed to proceed *via* slight rearrangements of the particles within the unit cells *via* a tetragonal transition state (Bain transition) similar to the Martensitic transition in steel. If this is the case, then the 111-reflection for fcc and the 110-reflection for bcc should appear at the same position. Assuming the volume fraction ϕ is constant upon this transition, then the unit cell dimensions should be related as $a_{\text{fcc}} = 2^{1/3} a_{\text{bcc}} \approx 1.26 a_{\text{bcc}}$, which is experimentally well fulfilled as $a_{\text{fcc}}/a_{\text{bcc}} = 17/14 = 1.22$ (see Table 3).

Also the phase structures for the shear-oriented nanoparticle lyotropic phases are included in the Scheme in Fig. 3B and fit well into the trend that small nanoparticles (5.1 nm) with large polymer chains (7.6 k) form bcc structures (Fig. 4A), larger nanoparticles (15.4 nm) form fcc structure with the same polymer (7.6 k) (Fig. 4B), and small nanoparticles (5.1 nm) with shorter polymer chains (3 k) show a tendency toward fcc structures, leading to the observed bcc/fcc-coexistence (Fig. 4C).

Shear-orientation in micro structured grids

For shear orientation in conventional shear cells (Couette, Searle, plate–plate), at least 1–5 mL of the sample is usually required, which is often more than can be produced when dealing with valuable materials such as nanoparticles, proteins or DNA. This motivated us to prepare micro sample holders which allowed shear orientation of very small amounts of gel-like samples. In an analogous fashion to the production of

microchannels for microfluidic chips, we used soft lithography to prepare sample holders with linear arrays of $1 \text{ cm} \times 1 \text{ cm}$ patches, each consisting of 10–100 parallel aligned microchannels with diameters between 10 and 100 μm and a depth of 300 μm .

Fig. 5 shows an example of a linear array of patches consisting of 14 μm width channels. The sample holder is produced in NOA 81 (Norland Optical Adhesive), which can be produced by conventional soft lithography, is resistant against a large variety of solvents, including water and toluene, and is X-ray transparent, mechanically stable and amorphous with very little X-ray background. By spreading a gel-like sample into a microchannel patch, the shear force orients the liquid crystalline structure. For the microstructured channel device shown in Fig. 5, only 2–5 μL of the sample is needed. The microchannel patch can be sealed with conventional Kapton tape to avoid solvent evaporation. Fig. 6 shows the scattering patterns measured for the sample Fe_2O_3 (16.6 nm)@PS-DETA(28k). We observe the typical 111-orientation of the shear-oriented fcc-phase at lower concentrations (Fig. 6A) and the transition into the bcc-phase at higher concentrations (Fig. 6B).

Conclusions

We show that polymer-coated nanoparticles can form liquid crystalline lyotropic phases with high order very similar to micellar lyotropic liquid crystals of surfactants and polymers. We observe the formation of bcc and fcc phases with a trend that small nanoparticle/large polymer systems form bcc-structures, and large nanoparticle/small polymer systems form fcc-structures. This appears to be a consequence of the softness of the polymer layers and the segment density at the periphery of the layer and is very similar to observations of block copolymer micelles in solution and bulk. Within the ordered phases, the distance between adjacent nanoparticles can be varied systematically *via* concentration and attached polymer molecular weights in a range of 10–40 nm. It is possible to shear-orient the nanoparticle lyotropic phases to obtain for the first time

macroscopically oriented highly ordered nanoparticle superlattice single crystals. In addition, we present microstructured sample holders that allow shear orientation and investigations of very small sample amounts (μL) of lyotropic phases.

Notes and references

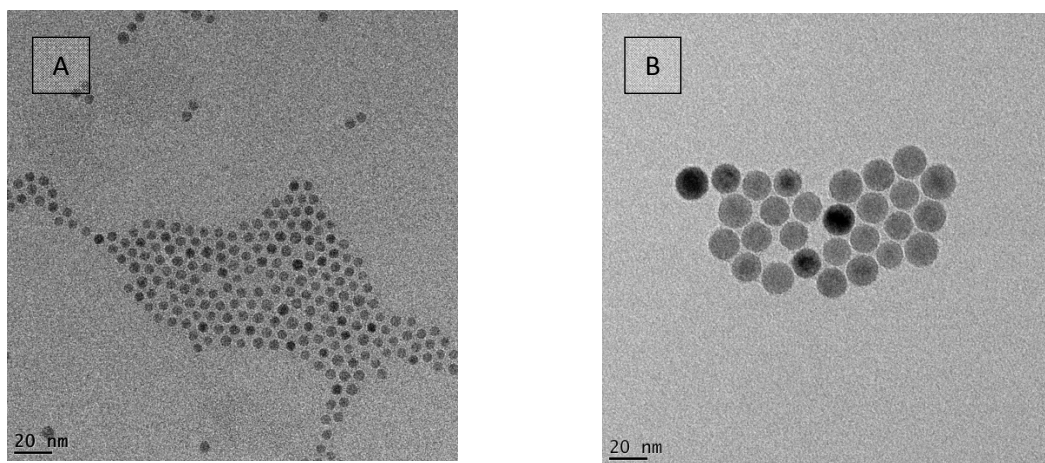
- 1 C. B. Murray, C. R. Kagan and M. G. Bawendi, *Science*, 2008, **270**, 1335.
- 2 D. V. Talapin, J.-S. Lee, M. V. Kovalenko and E. V. Shevchenko, *Chem. Rev.*, 2010, **110**, 389.
- 3 S. M. Taheri, S. Fischer and S. Förster, *Polymer*, 2011, **3**, 662.
- 4 E. V. Shevchenko, D. V. Talapin, A. Kornowski, F. Wiekhorst, J. Kötzler, M. Haase, A. L. Rogach and H. Weller, *Adv. Mater.*, 2002, **14**, 287.
- 5 J. E. Martin, J. P. Wilcoxon, J. Odinek and P. Provencio, *J. Phys. Chem. B*, 2000, **104**, 9475.
- 6 A. P. Alivisatos, K. P. Johnsson, X. Peng, T. E. Wilson, C. J. Loweth, M. P. Bruchez, Jr and P. G. Schultz, *Nature*, 1996, **382**, 609.
- 7 C. A. Mirkin, R. L. Letsinger, R. C. Mucic and J. J. Storhoff, *Nature*, 1996, **382**, 607.
- 8 R. J. Macfarlane, M. R. Jones, A. J. Senesi, K. L. Young, B. Lee, J. Wu and C. A. Mirkin, *Angew. Chem., Int. Ed.*, 2010, **49**, 4589.
- 9 W. Cheng, M. J. Campolongo, J. J. Cha, S. J. Tan, C. C. Umbach, D. A. Muller and D. Luo, *Nat. Mater.*, 2009, **8**, 519.
- 10 W. Cheng, M. R. Hartman, D.-M. Smilgies, R. Long, M. J. Campolongo, R. Li, K. Sekar, C.-Y. Hui and D. Luo, *Angew. Chem., Int. Ed.*, 2010, **49**, 380.
- 11 M. A. Nikolic, V. Alexandrovic, M. Krack, A. Kornowski, S. Förster and H. Weller, *Angew. Chem., Int. Ed.*, 2006, **45**, 6577.
- 12 S. Fischer, A. Salcher, A. Kornowski, H. Weller and S. Förster, *Angew. Chem., Int. Ed.*, 2011, **123**, 7957.
- 13 J. Park, K. An, Y. Hwang, J.-G. Park, H.-J. Noh, J.-Y. Kim, J.-H. Park, N.-M. Hwang and T. Hyeon, *Nat. Mater.*, 2004, **3**, 891.
- 14 M. S. Nikolic, A. Kornowski, A. Rank, R. Schubert, A. Frömsdorf, H. Weller and S. Förster, *Angew. Chem., Int. Ed.*, 2009, **48**, 2619.
- 15 H.-P. Hentze, E. Krämer, B. Berton, D. Förster and M. Antonietti, *Macromolecules*, 2000, **35**, 3523.
- 16 S. Förster and T. Plantenberg, *Angew. Chem., Int. Ed.*, 2002, **41**, 688.
- 17 D. Bartolo, G. Degré, P. Nghe and V. Studer, *Lab Chip*, 2008, **8**, 274.
- 18 L.-H. Hung, R. Lin and A. P. Lee, *Lab Chip*, 2008, **8**, 983.
- 19 Ph. Wägli, B. Y. Guélat, A. Homsy and N. F. Rooij, *14th International Conference on Miniaturized Systems for Chemistry and Life Sciences*, 2010, p. 1937.
- 20 S. Förster, A. Timmann, M. Konrad, C. Schellbach, A. Meyer, S. S. Funari, P. Mulvaney and R. Knott, *J. Phys. Chem. B*, 2005, **109**, 1347.
- 21 S. Förster, S. Fischer, K. Zielske, C. Schellbach, M. Sztucki, P. Lindner and J. Perlich, *Adv. Colloid Interface Sci.*, 2011, **163**, 53.
- 22 S. Förster, L. Apostol and W. Bras, *J. Appl. Crystallogr.*, 2010, **43**, 639.
- 23 G. A. McConnell, A. P. Gast, J. S. Huang and S. D. Smith, *Phys. Rev. Lett.*, 1993, **71**, 2102.
- 24 S. Förster, A. Timmann, C. Schellbach, A. Frömsdorf, A. Kornowski, H. Weller, S. V. Roth and P. Lindner, *Nat. Mater.*, 2007, **6**, 888.

Lyotropic phase behavior of polymer-coated iron oxide nanoparticles

Sara Mehdizadeh Taheri^{a,*}, Steffen Fischer^a, Martin Trebbin^a, Sebastian With^a, Jan H. Schröder^a, Jan Perlich^b, Stephan V. Roth^b and Stephan Förster^a

5 TEM Characterization

Figure S1 shows TEM images of two of the ironoxide nanoparticles used in the present study. These nanoparticles were used for the nanocomposites LA 96 (A, 6 nm) and LA 116 (B, 16.6 nm).

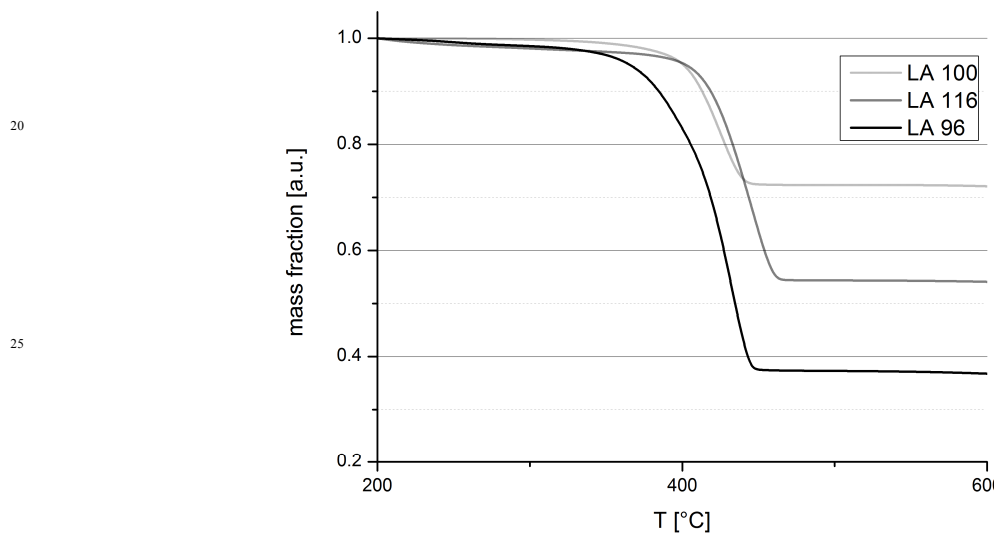


10

Fig S1. Representative TEM Image of 6 and 17 nm ironoxide nanoparticles coated with oleic acid.

TGA Characterization

In Figure S2 TGA measurements of representative nanoparticle/polymer systems with different nanoparticle sizes and polymer molecular weights are shown. The smallest mass fraction of polymer is observed for the sample LA 96 consisting of very small nanoparticles and relatively long polymer chains (6nm@8k PS). This sample forms bcc lyotropic phases. Large nanoparticles coated with the same polymer have larger weight fractions of nanoparticles (LA 100; 16.6 nm@8k PS) and form fcc lyotropic phases. LA 116 (16.6 nm@28k PS) is in between these two extreme cases. For this system we observe both, fcc and bcc structures.



20

Fig S2. Representative TGA measurements of LA 100 (8nm@8kPS), LA 116 (17nm@28kPS) and LA 96 (6nm@8kPS)

Table S1 Calculated grafting densities of representative nanoparticle/polymer systems

Sample	Grafting density [polymerchain/nm ²]
LA 100 (8nm@8kPS)	0.42
LA 116 (17nm@28kPS)	0.25
LA 96 (6nm@8kPS)	0.63

One can calculate the grafting density N/A (in 1/nm²) from the weight fraction of polymer f_p (obtained from the TGA measurements), the radius of the nanoparticles R, the density ρ of the nanoparticles, assumed to be equal to the bulk values (5.2 g/cm³), Avogadro's number N_A , and the molecular weight of the polymer M_p as

$$\frac{N}{A} = \frac{f_p * R * \rho * N_A}{3 * M_p}$$

Where the factor $\frac{R}{3}$ arrives from the volume to surface ratio of the nanoparticles. The values of the grafting densities are summarized in Table S1.

Results for calculated SAXS-measurements

The scattering curves in Figure 1, 2 and the 2D-SAXS patterns in Figure 4 were fitted to Eq. (1) using the software Scatter. The obtained structural parameters such as lattice type, unit cell, mean radius of the nanoparticles, nearest neighbour distance *n.n.d.*, and sizes of the domains are listed in Table S2 and S3.

Table S2 Structural parameters obtained by fitting Eq. (1) to the measured scattering curves of LA 96

Concentration of LA 96 [% w/w]	lattice	radius [nm]	standard-deviation of the radius	unit cell [nm]	radial domain [nm]	n.n.d. [nm]
10	none	3.2	0.09	-	-	-
20	dis	3.2	0.09	27.8	30	24.0
30	dis	3.2	0.1	27.1	40	23.5
40	dis	3.2	0.09	23.6	32.5	20.5
50	dis	3.2	0.1	21.8	32.6	18.9
60	dis	3.2	0.1	20.7	48.4	17.9
70	bcc	3.2	0.09	18.0	80	15.7
80	bcc	3.2	0.1	16.7	97.4	14.5
90	bcc	3.2	0.1	16.4	117	14.2
bulk	bcc	3.2	0.9	14.9	72.9	12.9

Table S3 Structural parameters obtained by fitting Eq. (1) to the measured scattering curves of LA 116

Concentration of LA 116 [% w/w]	lattice	radius [nm]	standard-deviation of the radius	unit cell [nm]	radial domain [nm]	n.n.d. [nm]
10	none	8.8	0.06	-	-	
20	dis	8.8	0.05	83.1	80	58.8
30	dis	8.9	0.05	82.4	80	58.3
40	fcc	8.8	0.05	55.3	100	39.1
50	fcc	8.8	0.05	53.0	100	37.5
60	fcc	8.8	0.04	51.5	135	36.4
70	fcc	8.8	0.05	47.87	100	33.9
80	fcc	8.8	0.05	51.32	100	36.3
90	fcc	8.7	0.05	42.2	80	29.9
dry	bcc	8.7	0.05	33.2	100	28.8

5

^a Universität Bayreuth, Universitätsstrasse 30, Bayreuth, Germany. Fax: +49(0)921-55-2780; Tel: +49(0)921-55-3924;

E-mail: sara.mehdizadeh.taheri@uni-bayreuth.de, stephan foerster@uni-bayreuth.de

^b HASYLAB at DESY, Notkestrasse 85, Hamburg, Germany. Fax: +49 40 8994 2934; Tel: +49 40 8998 2934; E-mail: stephan.roth@desy.de,

jan.perlich@desy.de

7.5 Early development drug formulation on a chip: Fabrication of nanoparticles using a microfluidic spray dryer

Cite this: *Lab Chip*, 2011, **11**, 2362

www.rsc.org/loc

PAPER

Early development drug formulation on a chip: Fabrication of nanoparticles using a microfluidic spray dryer[†]

Julian Thiele,^{a,b} Maike Windbergs,^a Adam R. Abate,^a Martin Trebbin,^b Ho Cheung Shum,^{‡a} Stephan Förster^b and David A. Weitz^{*a}

Received 7th April 2011, Accepted 27th April 2011

DOI: 10.1039/c1lc20298g

Early development drug formulation is exacerbated by increasingly poor bioavailability of potential candidates. Prevention of attrition due to formulation problems necessitates physicochemical analysis and formulation studies at a very early stage during development, where the availability of a new substance is limited to small quantities, thus impeding extensive experiments. Miniaturization of common formulation processes is a strategy to overcome those limitations. We present a versatile technique for fabricating drug nanoformulations using a microfluidic spray dryer. Nanoparticles are formed by evaporative precipitation of the drug-loaded spray in air at room temperature. Using danazol as a model drug, amorphous nanoparticles of 20–60 nm in diameter are prepared with a narrow size distribution. We design the device with a geometry that allows the injection of two separate solvent streams, thus enabling co-spray drying of two substances for the production of drug co-precipitates with tailor-made composition for optimization of therapeutic efficiency.

Introduction

The development of novel pharmaceuticals is a challenging field involving cost-intensive research in combination with a high attrition rate of potential candidates.^{1,2} Due to high-throughput technologies an increasing number of new chemical entities with potential therapeutic efficiency is identified.^{3,4} Unfortunately, the molecular complexity of drugs has significantly increased over the last decade.^{5–7} Although molecular complexity usually contributes to biological activity, it often causes poor solubility of drugs.^{6,8} This limits their bioavailability in the human body, and the reason for attrition of pharmacologically promising substances can often be found in the failure to develop a suitable formulation for therapeutic application.⁹ Prevention of failure due to formulation limitations necessitates physicochemical analysis and formulation studies at a very early stage during development.^{10,11} At this stage, the availability of the drug candidate is limited to small amounts, thus hampering extensive experiments.

One suitable approach to increase the bioavailability of a drug is to reduce the particle size, which increases the specific surface

and, therefore, facilitates release and absorption of the drug.^{12–15} Furthermore, increased bioavailability can be achieved by amorphization of the sample. In this context, spray drying is a powerful technique enabling instantaneous drying of solutions, emulsions or suspensions in one step. The final product is a fine, often amorphous powder with a large surface. Pharmaceutical application of spray drying techniques are ubiquitous; their use ranges from the manufacture of dry plant extracts for avoiding decomposition of thermally degradable components, to the production of excipients for compression with improved binding characteristics.^{16–18} Furthermore, the technique is successfully used for co-precipitation of a drug and another substance to increase the drug's bioavailability.¹⁹ However unfortunately, in case of early stage formulation development the use of conventional spray drying setups is restricted. Conventional spray drying equipment requires large amounts of sample as the dead volume of the apparatus is rather large and a considerable portion of discard material is generated during the process. Furthermore, the optimization of processing parameters necessitates additional quantities of sample to receive a homogeneous product. Moreover, particle sizes below 100 nm, as often required for targeted drug delivery, are extremely hard to generate.^{20,21} An appropriate application for spray drying for early development drug formulation would require the miniaturization of the setup. These limitations can be overcome using microfluidic techniques.^{22–26} Extremely small volumes can precisely be handled on microfluidic chips enabling the controlled generation of homogeneous products as well as a fast change of process conditions. It would be highly desirable to

^aSchool of Engineering and Applied Sciences, Department of Physics, Harvard University, Cambridge, Massachusetts, USA. E-mail: weitz@seas.harvard.edu; Fax: +617-495-3275; Tel: +617-495-3275

^bPhysical Chemistry I, University of Bayreuth, Germany

[†] Electronic supplementary information (ESI) available. See DOI: 10.1039/c1lc20298g

[‡] Current address: Department of Mechanical Engineering, University of Hong Kong, Hong Kong

design a microfluidic chip which combines the versatility of microfluidics with the ability to formulate drug particles with high accuracy using spray drying techniques.

In this paper, we present the first microfluidic spray dryer on a poly(dimethylsiloxane) (PDMS) chip.^{27–29} We use the hydrophobic model drug danazol to test the new device. By controlling the collection distance of the spray, we can control the crystallinity of the product. Our microfluidic device enables fabrication of drug nanoparticles with sizes of less than 100 nm in diameter. The versatile device design also enables the formation of amorphous co-precipitates by co-spray drying two substances.

Results and discussion

In conventional spray dryers, a single liquid stream is typically vaporized by compressed air in a spray nozzle; the spray is then mixed with a heated gas stream in a drying chamber to evaporate the solvent and yield the dry product.²¹ However, this setup only allows processing of single solvent systems or mixtures of pre-mixed solvents. To process multiple separate solvent streams as required for solvent/antisolvent precipitation or rapidly reacting solvent streams, the spray dryer generally needs to be equipped with additional separate inlet channels.³⁰ In this work, we use a microfluidic device with an array of two flow-focusing cross junctions, as shown in Fig. 1.

The device enables separate injection of two solvents and provides a third inlet for compressed air to form the spray. For the formation of hydrophobic drug nanoparticles, we dissolve the hydrophobic drug danazol in an organic solvent injected into the first inlet, and inject the second fluid into the second inlet. The two solvents form a jet at the first cross junction, which extends into the second cross junction where compressed air is injected to form the spray. To process hydrophobic drugs, the PDMS device must resist fouling due to adsorption of drug crystals on the microchannel walls.^{31,32} This is especially crucial when starting up the device, as potential backflow of the drug-loaded solvent stream into the anti-solvent reservoir, and *vice versa*, can cause significant precipitation of the hydrophobic drug in the microchannels. To prevent adsorption of the drug on the microchannel walls, we treat the intrinsically hydrophobic PDMS device with oxygen plasma, as the plasma renders the walls of the device hydrophilic.³³ Although the hydrophilicity of the plasma treated device decreases over time,

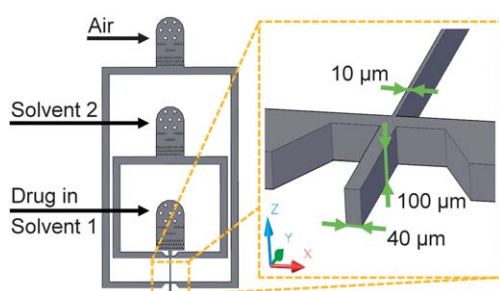


Fig. 1 Schematic of a microfluidic device for forming nanoparticles from hydrophobic drugs by spray drying. The microfluidic device is rendered hydrophilic with an oxygen plasma treatment. The device geometry enables separate injection of two solvent streams of which the spray is formed.

the channel surface can easily be regenerated in the same manner multiple times. However, for early development drug formulation, the amount of sample is extremely small thus being the limiting factor in such an experiment rather than the duration of a surface plasma treatment. In addition, we minimize the surface contact between the drug-loaded solvent stream and the channel walls. We achieve this by designing a device geometry with a high aspect ratio. The ratio h/w is 10 : 1 in the upper half of the device and 4 : 1 at the spray nozzle. Although high-aspect-ratio channel geometries are generally known to increase surface interactions,³⁴ microchannels with a high aspect ratio are less pressure-resistant than squared channels, when fabricated in the rather soft PDMS;

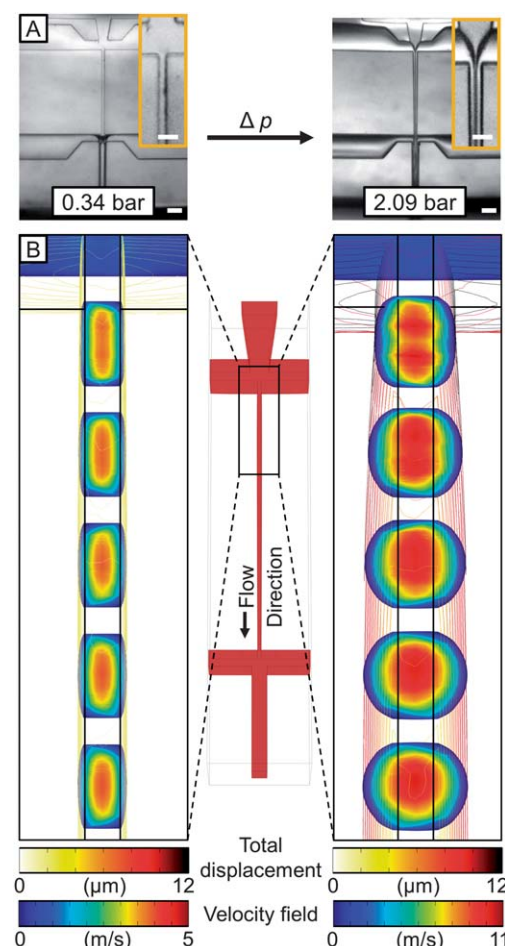


Fig. 2 Pressure-induced deformation of the microfluidic spray dryer during operation. (A) Bright-field microscopy images of the microfluidic spray dryer at low pressure (left) and operating pressure (right). The dark fields in the microchannels indicate the curvature of the channel walls causing the light to scatter. The scale bars denote 50 μm , scale bars for the magnified view are 20 μm . (B) The impact of the deformation on the flow profile is studied using CFD simulations based on the finite element method. The initial rectangular microchannels (left) expand and adopt a circular shape (right). This deformation changes the flow pattern from a two dimensional focused flow to an elliptic to coaxial flow, therefore reducing the contact between the drug-loaded solvent stream and the channels walls. To emphasize the deformation, the simulation model is viewed from an angle of approximately 30° above the second cross junction, and the original position of the microchannel walls is added as black lines to the simulation model.

thus the operating spray dryer channels easily expand, as shown in Fig. 2.

To determine the impact of the channel deformation on the flow profile, we process a typical solvent/antisolvent system in our spray dryer and compare the device deformation at low and high flow rates and air pressure, respectively. Our observations are supported by computational fluid dynamics (CFD) simulations coupled with fluid-structure interaction (FSI) using COMSOL 4.1.0.185. We design a 3D simulation model of the microfluidic spray dryer considering the solid mechanics of the device described by a linear elastic model and the fluid flow therein described by the Navier–Stokes equations. For the device building material PDMS, which is mixed from the pre-polymer and crosslinker in a ratio of 10 : 1, Young's modulus is approximately 4 MPa, the Poisson's Ratio is 0.42, and the density is 920 kg m^{-3} .^{35,36} The model consists of 62 713 finite elements with an average mesh quality of 0.8003 on a scale of 0 to 1, where 1 is the highest quality. The model is solved for 401 878 degrees of freedom. A detailed discussion of the simulation model and its mathematical background is provided in the ESI† for this publication. For the spray experiment at low flow rates and low pressure, we inject isopropyl alcohol (IPA) as the solvent, water as the anti-solvent and compressed air into the first, second and third inlet, respectively, at flow rates of 1 mL h^{-1} for the inner phase and 10 mL h^{-1} for the middle phase. The air pressure is set to 0.34 bar. For the high-flow rate/high-pressure experiment, we increase the flow rates of IPA and water to 5 mL h^{-1} and 50 mL h^{-1} , respectively, and set the air pressure to 2.09 bar. At low pressure (0.34 bar), the PDMS device demonstrates minimal deformation and we observe a two dimensional focused flow pattern between the first and second cross junction. However, as we increase the pressure, the PDMS device responds to the internal stress and expands, as shown in the magnified view of Fig. 2A. Due to the high aspect ratio, the largest expansion of the microchannels is observed in the side walls of the channels. Image analysis of microscope images shows that the microchannels widen by an average factor of two, as shown in the magnified views in Fig. 2A. This deformation strongly influences the flow profile inside the spray dryer, as shown in the corresponding simulations in Fig. 2B. As illustrated by the slice plot of the simulated velocity profile, the flow between the first and second cross junction adopts a three dimensional flow pattern, similar to that observed in microfluidic capillary devices.³⁷ Thereby, the inner phase is surrounded by a protective sheath of the middle phase, as shown in the magnified view of Fig. 2A (right). This minimizes the surface contact of the solvent in which the hydrophobic drug is dissolved with the channel walls and prevents fouling of our device.

When forming a spray, the spray shape and drop size are important factors influencing drying, particle size and morphology of the processed drug. To determine drop size and spray shape, we visualize the spray formation in our spray dryer with a high-speed camera. We inject IPA into the first and second inlet at a total flow rate of 55 mL h^{-1} . At low air pressure, the solvent stream is not dispersed into a spray; instead, a jet of liquid is ejected from the spray nozzle and breaks into large droplets due to Rayleigh–Plateau instability, as shown in Fig. 3A.³⁷ As the air pressure is increased beyond 0.5 bar, we observe the formation of a mixture of large drops and finely

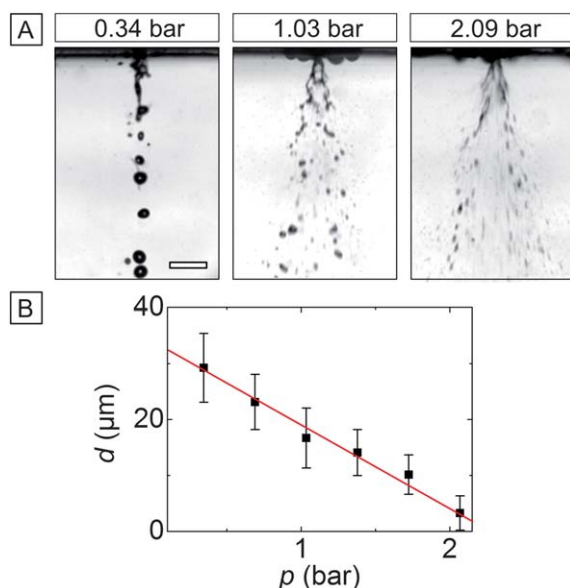


Fig. 3 (A) Spray profile of the nozzle for different air pressures. IPA is injected into the spray dryer at 55 mL h^{-1} . At low pressure, a fluid jet is ejected from the nozzle which breaks into single droplets downstream. When the pressure is increased beyond 0.5 bar, the spray profile adopts a cone-like shape. The scale bar for all panels denotes $100 \mu\text{m}$. (B) Drop diameter as a function of p . With increasing pressure, the mean size of the droplets decreases linearly. At a pressure of 2.09 bar, the droplets are approximately $4 \mu\text{m}$ in diameter. The red line is a guide to the eye.

dispersed drops at the spray nozzle; the onset of spraying can be confirmed by the round full cone pattern adopted by the droplets formed, that appears as a triangular spray pattern in the side view of the high-speed camera. This precise pattern is formed due to turbulences imparted to the liquid prior to the orifice in the short outlet channel. To quantify the spray formation process, we measure the drop size d as a function of the air pressure p , as shown in Fig. 3B. The drop size decreases linearly with increasing pressure to approximately $4 \mu\text{m}$ in diameter at 2.1 bar, which is the maximum pressure our spray dryer can withstand without delamination of the plasma-bonded PDMS.

We demonstrate the concept to form hydrophobic drug nanoparticles with our microfluidic spray dryer. Danazol is used as a model drug, which is an isoxazole derivative of testosterone and applied for the treatment of endometriosis and hereditary angioedema.²³ In general, a convenient method for processing hydrophobic drugs is liquid antisolvent precipitation (LASP), where the drug, dissolved in an alcohol, is precipitated by mixing the drug solution with water as the antisolvent.^{16,38} We dissolve danazol in isopropyl alcohol and inject it together with water into the first cross junction. As we operate our microfluidic device in the laminar flow regime, only diffusion based mixing of the solvent streams is observed at their interfaces. To evaluate the effect of microfluidic processing alone on the particle size and morphology of the hydrophobic drug, no stabilizer or surfactant is added to influence the particle growth, nor do we use common co-solvents such as DMSO and benzyl alcohol. We set the flow rates to 5 mL h^{-1} for danazol, and 50 mL h^{-1} for water, which corresponds to a volumetric ratio of 1 : 10 and has been shown to yield danazol microparticles in conventional LASP processes.²³

The spray is suspended in air, thus ensuring that the product is dried upon collection. We examine the morphology and particle size of the processed drug using scanning electron microscopy (SEM). While unprocessed danazol is composed of particles with irregular shapes ranging from approximately 2 μm to 100 μm , the particle size is reduced significantly by processing the drug using our microfluidic spray dryer. As shown in Fig. 4A, we yield danazol nanoparticles with a narrow particle size distribution (PSD) from 20 nm to 60 nm and, therefore, smaller than previously reported.^{7,23}

The formation of drug nanoparticles using LASP is driven by mixing of the drug solution with the antisolvent. Thus, the degree of supersaturation of the drug solution governs nucleation and growth of the drug nanoparticles.¹⁶ However, sufficient mixing only occurs in the short outlet channel prior to the orifice of the spray nozzle in our microfluidic device. Since we use high flow rates to form a stable spray, the delay time of the fluids in the outlet channel should be too short to enable growth of the drug nuclei by mixing. To reveal the formation process, we replace the antisolvent with the solvent, and inject a solution of danazol in IPA and pure IPA into the first and second inlet, respectively. The formation of danazol nanoparticles of identical size and morphology in the absence of the antisolvent indicates that the particle formation is primarily driven by the evaporation of the spray and not by the formation of nuclei due to supersaturation, as shown in Fig. 4B. Our hypothesis is further supported by using a microfluidic spray dryer with a longer channel between the first and second nozzle and thus increased time of diffusion, which does not have a significant influence on the particle properties.

Another crucial aspect of the spray drying process is the distance from the spray drying nozzle at which the final product is collected. While it is known that the morphology and size of hydrophobic drugs depends on the initial concentration of reactants, the choice of additives and the ratio of solvent and antisolvent,³⁹ we find a significant dependence on the collection distance by performing spatial sampling of the spray. To illustrate this, we inject danazol and IPA as described above, but this

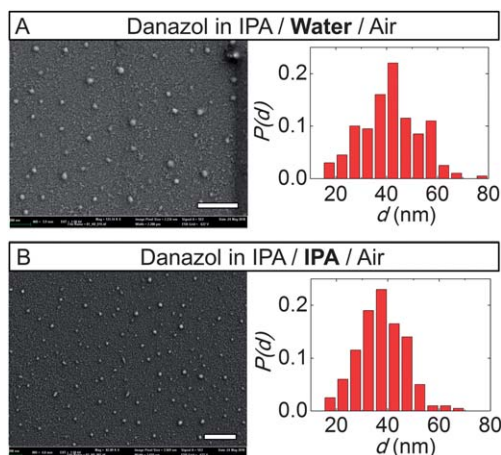


Fig. 4 Effect of the solvent system on particle size and composition. Danazol in IPA is mixed with (A) water as the antisolvent, or (B) IPA as the solvent inside the microfluidic spray dryer. In either case, nanoparticles are produced with a narrow PSD and an average diameter of 20–60 nm. Scale bars denote 300 nm.

time we collect the spray in steps of 5 cm from the spray nozzle. From our SEM analysis, two distinct product morphologies are revealed. At a collection distance of 5 cm, we observe an assembly of stacks of danazol; the thickness of each stack is about 60–80 nm, as shown in Fig. 5A. These values are in good agreement with the size of single danazol nanoparticles, as shown in Fig. 4A and 4B.

However, as the time of flight is too short to allow for complete evaporation of the spray upon collection, the remaining solvent increases the mobility of danazol particles on the collection substrate, allowing them to fuse and reach an energetically more favorable state.¹⁶ We therefore increase the collection distance to 30 cm; as the spray is completely evaporated, single nanoparticles are formed, that become densely packed over the long time of sample collection, as shown in Fig. 5B. X-ray powder diffraction analysis (XRD) is employed to determine the effect of spatial sampling on the crystallinity of danazol. We use the characteristic peaks at 20 of 15.8, 17.1 and 19.0 in the XRD pattern of unprocessed danazol as a reference. In processed danazol, the intensity of the characteristic peaks decreases as the collection distance of the spray is increased. This indicates that the initial crystallinity of the drug is not recovered, as shown in Fig. 5C. The formation of amorphous danazol is of importance, as the difference in physicochemical properties of the amorphous form significantly increases the bioavailability of danazol.²³

Another way to fabricate amorphous hydrophobic drug particles is to co-spray dry the drug and a crystallization inhibitor.⁴⁰ As a control experiment, we first co-spray dry danazol in IPA together with water and collect the spray at low distance. As shown before, the spray is not completely evaporated due to the short time of flight. This allows danazol to grow into star-shape crystalline aggregates, as shown in Fig. 6A. We use poly(vinylpyrrolidone) (PVP) as a substance for co-spray drying with

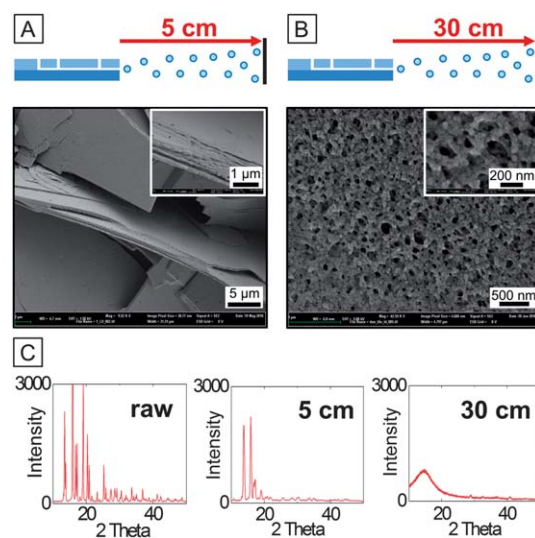


Fig. 5 Spatial sampling of processed danazol. Depending on the collection distance, various morphologies are observed; (A) assembly of stacks with a thickness of 60–80 nm, and (B) nanoparticles, approximately 20 nm to 60 nm in diameter, assembled in a dense network. (C) XRD patterns of processed danazol collected at a distance of 5 cm and 30 cm from the spray nozzle, and unprocessed danazol as a reference.

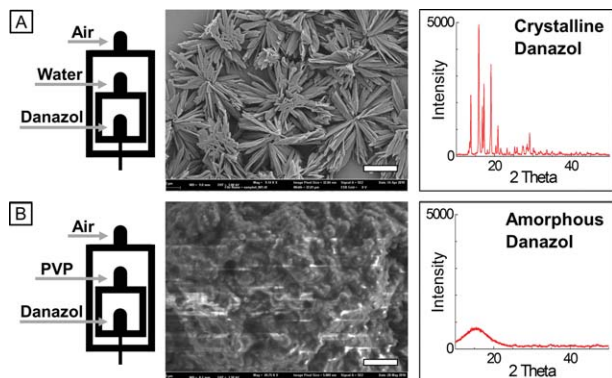


Fig. 6 Inhibition of danazol crystallization by PVP. (A) Danazol in IPA is mixed with water inside the microfluidic device; the spray is collected at a distance of 1 cm from the nozzle, allowing danazol to grow into crystalline aggregates, as indicated by the XRD pattern. The scale bar is 5 μm . (B) By processing danazol in IPA and an aqueous solution of PVP, which are injected separately into our spray dryer, amorphous co-precipitates are yielded, as indicated by the corresponding XRD pattern. The scale bar denotes 500 nm.

danazol to fabricate amorphous co-precipitates, as PVP is known to inhibit crystal growth in pharmaceutical formulations.^{41–44} We process danazol in IPA together with a 1.5 wt% solution of PVP in water at equal flow rates of 25 mL h⁻¹. Again, the spray is collected at short distance. However, as the spray is dried, danazol precipitates from the spray in a combination with PVP without crystallization, thus no characteristic peaks are observed in the XRD pattern, as shown in Fig. 6B.

To relate the performance of our microfluidic spray dryer to conventional spray dryers, we perform spray drying experiments with the same formulations and compare the results by XRD and SEM. We use the well-established and widely known Mini Spray Dryer B-191 (Buechi, Germany) with a spray rate of 10 mg min⁻¹, and process a solution of danazol in IPA without and with PVP, respectively. In both cases, we yield particles ranging from approximately 1 μm to 5 μm , which are substantially larger than the danazol particles formed with our microfluidic spray dryer. Moreover, the degree of crystallinity of the resultant danazol particles without PVP is high, as shown in Fig. 7A. We assume that the smaller drop and particle size using our microfluidic spray dryer is achieved due to the well-controllable flow conditions in the microfluidic device and the use of pulsation-free syringe pumps, which enable a degree of control over the spray formation and mixing prior to the nozzle that cannot be achieved in conventional macro-sized setups and eventually leads to the formation of particles below 100 nm, as we have observed in our studies.

However, the development of laboratory spray dryers towards benchmarking the minimal particle size is an ongoing process, though, and we expect novel equipment such as the Buechi B-90 to fabricate particles with submicron-size using our formulations. However, with the intended use for early drug formulation development, our spray drying approach exhibits several advantages, which cannot be realized in a common spray dryer. The dead volume of our chip is extremely small, thus avoiding waste of the sample and facilitating experiments with minimal sample volume. Furthermore, chip design and fabrication is easy

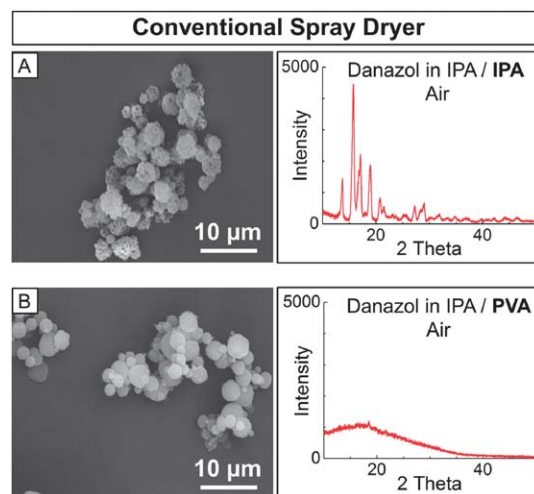


Fig. 7 Fabrication of danazol particles and danazol/PVP co-precipitates in a conventional spray dryer using the same formulations as in our microfluidic device. (A) Instead of amorphous drug nanoparticles, crystalline particles, and (B) microscopic co-precipitates are yielded.

and extremely flexible in terms of geometry, thereby allowing customized design. As drugs in their early development stage lack a complete toxicological profile, handling and cleaning of contaminated equipment has to be performed with high safety precautions. As the fabrication of our chip is inexpensive and easy, it can just be discarded after use. An additional advantage of our chip is sample collection. Due to the flexible setup the particles can directly be collected in vials or on sample holders for further characterization, thus avoiding waste and alteration of sample properties.

Experimental

Device fabrication

The PDMS microfluidic devices are fabricated using soft lithography.²⁷ All channels have a fixed height of 100 μm . The PDMS replica is bonded to a flat sheet of cured PDMS using oxygen plasma treatment. The plasma treatment renders the microchannels temporarily hydrophilic.³³ To retain the hydrophilic surface modification, suitable for handling hydrophobic drugs, the device is flushed with deionized water. The nozzle of the spray dryer is prepared by slicing the outlet channel of the stamped device with a razor blade. To achieve reproducible accuracy when slicing, we include a guide to the eye in the initial AutoCAD design of the spray dryer.

Spray drying experiments

PVP (weight-averaged molecular weight, M_w 10 000 g mol⁻¹) and all other chemicals are obtained from Sigma-Aldrich Co. unless noted otherwise. Danazol (99.9%) is obtained from Selectchemie AG. Water with a resistivity of 16.8 M Ω cm⁻¹ is prepared using a Millipore Milli-Q system. All solutions are filtered through a 0.2 μm PTFE filter (Millipore). We form danazol nanoparticles using our microfluidic spray dryer. To demonstrate long term stability of the process, each experiment is performed over a time period of 2 h. We inject a saturated

solution of danazol in IPA into the first inlet and water or IPA into the second inlet at 5 mL h⁻¹ and 50 mL h⁻¹, respectively. For the formation of co-precipitates, we inject PVP in water (1.5% w/w) at 50 mL h⁻¹ into the second inlet. We fill the PE tubing that connects the syringe pumps with the device with pure IPA to prevent precipitation of the drug in the event of back flow of the drug-loaded solvent stream into the second solvent reservoir, and *vice versa*. To form the spray, air is injected into the third inlet at 2.09 bar. The spray is ejected into air and dried at room temperature. We image the spray using a Phantom v9.1 camera (Vision Research) at 64 000 fps. The droplet size is obtained by measuring the size of at least 200 drops from high-speed camera images.

Product collection and characterization

Processed danazol is collected at distances between 5 cm and 30 cm from the spray nozzle. For SEM analysis, the spray is collected on glass slides and coated with Pd/Pt. We use an Ultra55 Field Emission SEM (Zeiss). The size distribution of the nanoparticles is determined by image analysis of SEM photographs using a public domain, Java-based image processing program, ImageJ. For XRD analysis and long-term experiments, samples are collected in an aluminum box over which the spray dryer is mounted. Due to the full-cone spray pattern, the dried product assembles in a circular pattern solely on the bottom of the collection box from which it is recovered in 70% to 95% yield. XRD analysis is performed using a Scintag XDS2000 powder diffractometer (Scintag, Cupertino, California, USA) with Cu-K α radiation at 40 kV and 30 mA. The XRD patterns are taken at room temperature in the range of 10° ≤ 2θ ≤ 50° with a scan rate of 1° min⁻¹ and a step size of 0.02°.

Conclusions

Our microfluidic spray dryer is a versatile novel tool for early formulation development of new drug candidates. Precisely controlled generation of amorphous drug nanoparticles can successfully be realized requiring only small quantities of sample. The particles exhibit narrow size distribution and low mean particle sizes. By independent injection of two solvent streams, drug co-precipitates can be prepared as well. Our approach should also be useful for forming composite nanoparticles with freely tunable composition. As the spray is dried at room temperature, our microfluidic device also enables processing of thermally degradable materials. In addition, nanosuspensions, which can greatly enhance the dissolution rate and bioavailability of hydrophobic drugs, can be easily prepared by spraying the nanoparticles into a stabilizer solution. Therefore, our approach not only enables the formation of nanoprecipitates with a small particle size, but also improves the versatility of spray drying for manipulating the composition of the resultant nanoparticles. Design and fabrication of spray drying devices is easy and inexpensive, thereby allowing customized design for each formulation and disposal of the whole chip after use. As drug candidates during their early development phase lack a complete toxicological profile, this aspect is more than valuable contributing to safety and protection during development of new pharmaceuticals.

Acknowledgements

We thank Christian Holtze and Jim Wilking for helpful discussions and COMSOL AB for technical support. This work was supported by BASF, the NSF (DMR-0602684), the Harvard MRSEC (DMR-0820484), and the Massachusetts Life Sciences Center. Experiments were performed in part at the Center for Nanoscale Systems (CNS), which is supported by the NSF (ECS-0335765). JT received funding from the Fund of the Chemical Industry (Germany) and MW was funded by the German Academic Exchange Service.

Notes and references

- J. A. Masi, R. W. Hansen and H. G. Grabowski, *J. Health Econ.*, 2003, **22**, 151–185.
- I. Kola and J. Landis, *Nat. Rev. Drug Discovery*, 2004, **3**, 711–715.
- H. Kubinyi, *Nat. Rev. Drug Discovery*, 2003, **2**, 665–668.
- X. Q. Chen, M. D. Autnan, C. Gesenberg and O. S. Gudmundsson, *AAPS PharmSciTech*, 2006, **8**, E402–208.
- X. Chen, J. M. Vaughn, M. J. Yacaman, R. O. Williams III and K. P. Johnston, *J. Pharm. Sci.*, 2004, **93**, 1867–1878.
- B. E. Rabinow, *Nat. Rev. Drug Discovery*, 2004, **3**, 785–796.
- T. Panagiotou, S. V. Mesite and R. J. Fisher, *Ind. Eng. Chem. Res.*, 2009, **48**, 1761–1771.
- A. Schuffenhauer, N. Brown, P. Selzer, P. Ertl and E. Jacoby, *J. Chem. Inf. Model.*, 2006, **46**, 525–535.
- S. Venkatesh and R. A. Lipper, *J. Pharm. Sci.*, 2000, **89**, 145–154.
- C. A. Lipinski, F. Lombardo, B. W. Dominy and P. J. Feeney, *Adv. Drug Delivery Rev.*, 1997, **23**, 3–25.
- L. F. Huang and W. Q. Tony, *Adv. Drug Delivery Rev.*, 2004, **56**, 321–334.
- P. Costa and J. M. S. Lobo, *Eur. J. Pharm. Sci.*, 2001, **13**, 123–133.
- L. Gao, D. Zhang and M. Chen, *J. Nanopart. Res.*, 2008, **10**, 845–862.
- E. Merisko-Liversidge, G. G. Liversidge and E. R. Cooper, *Eur. J. Pharm. Sci.*, 2003, **18**, 113–120.
- F. Kesisoglou, S. Panmai and Y. Wu, *Adv. Drug Delivery Rev.*, 2007, **59**, 631–644.
- R. Vehring, *Pharm. Res.*, 2008, **25**, 999–1022.
- D. Chiou, T. A. G. Langrish and R. Braham, *J. Food Eng.*, 2008, **86**, 288–293.
- Y. Gonnissen, S. I. Goncalves, J. P. Remon and C. Vervaet, *Drug Dev. Ind. Pharm.*, 2008, **34**, 248–257.
- A. Paudel, J. Van Humbeeck and G. Van den Mooter, *Mol. Pharmaceutics*, 2010, **7**, 113–1148.
- H. Gao, W. Shi and L. B. Freund, *Proc. Natl. Acad. Sci. U. S. A.*, 2005, **102**, 9469–9474.
- X. Li, N. Anton, C. Arpagaus, F. Belleteix and T. F. Vandamme, *J. Controlled Release*, 2010, DOI: 10.1016/j.jconrel.2010.07.113.
- H. S. M. Ali, P. York and N. Blagden, *Int. J. Pharm.*, 2009, **375**, 107–113.
- H. Zhao, J.-X. Wang, Q.-A. Wang, J.-F. Chen and J. Yun, *Ind. Eng. Chem. Res.*, 2007, **46**, 8229–8235.
- G. Tetradis-Meris, D. Rossetti, C. P. de Torres, R. Cao, G. Lian and R. Janes, *Ind. Eng. Chem. Res.*, 2009, **48**, 8881–8889.
- P. W. Miller, L. E. Jennings, A. J. deMello, A. D. Gee, N. J. Long and R. Vilar, *Adv. Synth. Catal.*, 2009, **351**, 3260–3268.
- A. S. Utada, E. Lorenceau, D. R. Link, P. D. Kaplan, H. A. Stone and D. A. Weitz, *Science*, 2005, **308**, 537–541.
- Y. Xia and G. M. Whitesides, *Angew. Chem., Int. Ed.*, 1998, **37**, 550–575.
- S. L. Peterson, A. McDonald, P. L. Gourley and D. Y. Sasaki, *Journal of Biomedical Materials Research Part A*, 2004, **72A**, 10–18.
- D. B. Weibel and G. M. Whitesides, *Curr. Opin. Chem. Biol.*, 2006, **10**, 584–591.
- T. Ozeki, S. Beppu, T. Mizoe, Y. Takashima, H. Yuasa and H. Okada, *Pharm. Res.*, 2006, **23**, 177–183.
- P. Mayer, W. H. J. Vaes and J. L. M. Hermens, *Anal. Chem.*, 2000, **72**, 459–464.
- M. Honest, H. K. Jin, L. Kwanseop, P. Nokyoung and H. H. Jong, *Electrophoresis*, 2003, **24**, 3607–3619.

- 33 B. Kim, E. T. K. Peterson, I. Papautsky, *Proceedings of the 26th Annual International Conference of the IEEE EMBS*, San Francisco, 2004, 5013–5016.
- 34 P. Mao and J. Han, *Lab Chip*, 2009, **9**, 586–591.
- 35 J. K. Deuschle, G. Buerki, H. M. Deuschle, S. Enders, J. Michler and E. Arzt, *Acta Mater.*, 2008, **56**, 4390–4401.
- 36 D. Armani, C. Liu, N. Aluru, *12th Int. Conf. IEEE MEMS*, 1999, 222–227.
- 37 A. S. Utada, L.-Y. Chu, A. Fernandez-Nieves, D. R. Link, C. Holtze and D. A. Weitz, *MRS Bull.*, 2007, **32**, 702–708.
- 38 J.-Y. Zhang, Z.-G. Shen, J. Zhong, T.-T. Hu, J.-F. Chen, Z.-Q. Ma and J. Yun, *Int. J. Pharm.*, 2006, **323**, 153–160.
- 39 S. D. Škapin and E. Matijević, *J. Colloid Interface Sci.*, 2004, **272**, 90–98.
- 40 S. M. Wong, I. W. Kellaway and S. Murdan, *Int. J. Pharm.*, 2006, **317**, 61–68.
- 41 H. Sekikawa, M. Nakano and T. Arita, *Chemical and Pharmaceutical Bulletin*, 1978, **26**, 118–126.
- 42 M. Yoshioka, B. C. Hancock and G. Zografi, *J. Pharm. Sci.*, 1995, **84**, 983–986.
- 43 L. S. Taylor and G. Zografi, *Pharm. Res.*, 1997, **14**, 1691–1698.
- 44 J.-H. Kim and H.-K. Choi, *International Journal of Pharmaceutics*, 2002, **236**, 81–85.

Early development drug formulation on a chip: Fabrication of nanoparticles using a microfluidic spray dryer

Julian Thiele,^{a,b} Maike Windbergs,^a Adam R. Abate,^a Martin Trebbin,^b Ho Cheung Shum,^{a,c} Stephan Förster,^b and David A. Weitz^{a‡}

^a School of Engineering and Applied Sciences/Department of Physics, Harvard University, Cambridge, Massachusetts, USA. 617-495-3275; E-mail: weitz@seas.harvard.edu

^b Physical Chemistry I, University of Bayreuth, Germany

^c Current address: Department of Mechanical Engineering, University of Hong Kong, Hong Kong

‡ Corresponding author

Supplemental Information

This supplemental information contains details of the simulation model that has been developed to study the deformation of the channel geometry of our microfluidic spray dryer and its impact on the flow profile inside the device. If you have additional questions, feel free to send an email to julian.thiele@uni-bayreuth.de.

Analysis of the flow pattern of a flow-focused aqueous solution of Rhodamine B in a microfluidic device shows that the surface contact between the dye solution and the channel walls decreases with increasing channel height, as shown in Figure S1.

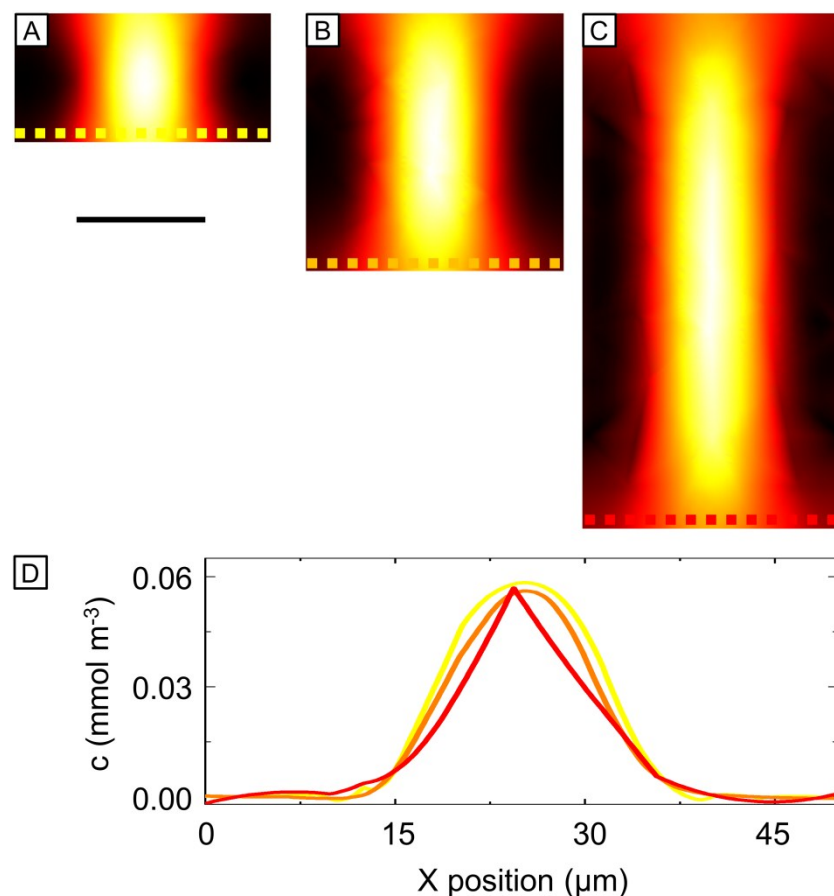


Fig. S1 Finite element simulation of a flow-focused fluid stream of Rhodamine B in water in microchannels with a constant width of 50 μm and varying heights of (A) 25 μm , (B) 50 μm and (C) 100 μm . The plane-cuts, which show the concentration profile of Rhodamine B, and (D) the corresponding line scans reveal that the surface contact between the dye solution and the microchannel walls decreases from low to high aspect ratios. The scale bar denotes 25 μm .

We analogously develop a device with a high aspect ratio to minimize the surface contact of the danazol-loaded solvent stream with the channel walls. Thus, fouling of the device due to adsorption of the hydrophobic drug on the microchannel walls can be prevented. However, PDMS microchannels with a high-aspect ratio are less pressure-resistant than squared channels and expand at high flow rates and high air pressure. To study the impact of the channel deformation on the flow profile, we use COMSOL Multiphysics v4.1.0.185, which allows simulating coupled multiphysics problems, such as the solid mechanics of PDMS that are coupled with the fluid dynamics in the case at hand. The tasks for developing the simulation model are illustrated in Figure S2.

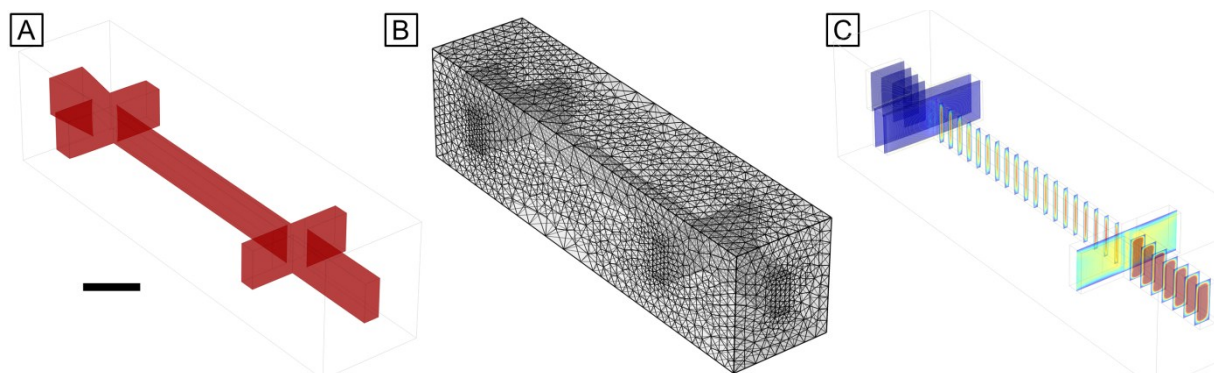


Fig. S2 Towards the simulation of the fluid flow inside the microfluidic spray dryer at low flow rates and low air pressure: (A) Import of the 3D device geometry drawn in AutoCAD 2011, (B) mesh generation and (C) solution of the model. The scale bar denotes 100 μm .

In a first step, a model of the device section of interest, which we design using AutoCAD 2011, is imported to COMSOL. Thereafter, the boundary conditions are assigned to the microchannel walls, the inlets and the outlet of the device assuming stationary conditions. Thereby, the fluid dynamics are described by the Navier-Stokes equations which can be simplified assuming incompressible fluids, thus $\rho = \text{const.}^1$

$$\rho \nabla \cdot \mathbf{u} = 0$$

$$\rho \frac{\partial \mathbf{u}}{\partial t} + \rho (\mathbf{u} \cdot \nabla) \mathbf{u} = \nabla \cdot [-p \mathbf{I} + \mu (\nabla \mathbf{u} + \nabla \mathbf{u}^T)] + \mathbf{F}$$

with the density of the fluid ρ , the pressure p , the identity matrix \mathbf{I} , the dynamic viscosity of the fluid μ , the velocity field \mathbf{u} and the volume force \mathbf{F} . The deformation of PDMS is simulated using COMSOL's linear elastic model which involves the following equations:¹

$$-\nabla \cdot \boldsymbol{\sigma} = \mathbf{F}_v$$

$$\boldsymbol{\sigma} = (\mathbf{S} \cdot (\mathbf{I} + \nabla \mathbf{u}))$$

$$\mathbf{S} - \mathbf{s}_0 = \mathbf{C} : (\boldsymbol{\varepsilon} - \alpha(T - T_{\text{Ref}}) - \boldsymbol{\varepsilon}_0)$$

$$\boldsymbol{\varepsilon} = \frac{1}{2} (\nabla \mathbf{u}^T + \nabla \mathbf{u} + \nabla \mathbf{u}^T \nabla \mathbf{u})$$

with the stress tensor \mathbf{S} , the strain tensor $\boldsymbol{\varepsilon}$, the 4th order elasticity tensor \mathbf{C} , the initial stresses \mathbf{s}_0 , the initial strains $\boldsymbol{\varepsilon}_0$, the thermal expansion tensor α and the (reference) temperature T (T_{Ref}). The specific material properties are then defined, as listed in Table S1.

Tab. S1 Material properties used in the simulation model.

Name	Value
Young's modulus (E_{PDMS}^2)	4 MPa
Poisson's ratio (ν_{PDMS}^2)	0.42
Density of PDMS (ρ_{PDMS}^3)	920 kg m ⁻³
Density of water (ρ_{water}^4)	998.2 kg m ⁻³
Dynamic viscosity (η_{Water}^4)	$1.002 \cdot 10^{-3}$ kg m ⁻¹ s ⁻¹
Main channel inlet ($v_{\text{MC,slow}}$)	0.02867 m s ⁻¹
Side channel inlet ($v_{\text{SC,slow}}$)	0.2525 m s ⁻¹
Pressure (p_{slow})	0.34 bar
Main channel inlet ($v_{\text{MC,fast}}$)	0.1434 m s ⁻¹
Side channel inlet ($v_{\text{SC,fast}}$)	1.263 m s ⁻¹
Pressure (p_{fast})	2.09 bar

The model is solved for 62713 finite elements and 401878 degrees of freedom using a multifrontal massively parallel solver (MUMPS). The average element quality of the mesh is 0.8003 on a scale from 0 to 1, where 1 is the highest quality; the minimal element quality is 0.3903. Using a Windows 7 x64 machine with two quad-core Intel® Xeon® E5440-processors operating at 2.83 GHz and an internal memory of 32 GB RAM, the less complex model of the microfluidic spray dryer at low flow rates and low pressure is solved in 1307 s, and the model of the microfluidic device operating at high flow rates and high air pressure is solved in 2700 s.

References

- [1] MEMS Module User's Guide for COMSOL v4.1, COMSOL AB, 2010, 174-184; 279-321.
- [2] J. K. Deusdle, G. Buerki, H. M. Deusdle, S. Enders, J. Michler, E. Arzt, *Acta Mater.*, 2008, **56**, 4390-4401.
- [3] D. Armani, C. Liu, N. Aluru, *12th Int. Conf. IEEE MEMS*, 1999, 222-227.
- [4] R. Weast, M. Astle, *Handbook of Chemistry and Physics*, 60th edition, CRC Press, Boca Raton, 1979, F-11, F-49.

7.6 Freestanding films of crosslinked gold nanoparticles prepared via layer-by-layer spin-coating

Freestanding films of crosslinked gold nanoparticles prepared via layer-by-layer spin-coating

Hendrik Schlicke^{1,2}, Jan H Schröder², Martin Trebbin³,
Alexey Petrov, Michael Ijeh, Horst Weller and Tobias Vossmeyer⁴

Institute of Physical Chemistry, University of Hamburg, Grindelallee 117, 20146 Hamburg,
Germany

E-mail: tobias.vossmeyer@chemie.uni-hamburg.de

Received 1 April 2011, in final form 27 May 2011

Published 27 June 2011

Online at stacks.iop.org/Nano/22/305303

Abstract

A new, extremely efficient method for the fabrication of films comprised of gold nanoparticles (GNPs) crosslinked by organic dithiols is presented in this paper. The method is based on layer-by-layer spin-coating of both components, GNPs and crosslinker, and enables the deposition of films several tens of nanometers in thickness within a few minutes. X-ray diffraction and conductance measurements reveal the proper adjustment concentration of the crosslinker solution of the critical is in order to prevent the destabilization and coalescence of particles. UV/vis spectroscopy, atomic force microscopy, and conductivity measurements indicate that films prepared via layer-by-layer spin-coating are of comparable quality to coatings prepared via laborious layer-by-layer self-assembly using immersion baths. Because spin-coated films are not bound chemically to the substrate, they can be lifted-off by alkaline underetching and transferred onto 3d-electrodes to produce electrically addressable, freely suspended films. Comparative measurements of the sheet resistances indicate that the transfer process does not compromise the film quality.

 Online supplementary data available from stacks.iop.org/Nano/22/305303/mmedia

(Some figures in this article are in colour only in the electronic version)

1. Introduction

The chemical and physical properties of thin films comprised of two- and three-dimensionally crosslinked metal nanoparticles have attracted enormous attention over the past decade. Several research groups demonstrated that these films can be used for numerous applications, such as vapor [1–4] or gas sensors [5], selective coatings for electrochemical sensors [6, 7], strain gauges [8, 9], and substrates for surface enhanced Raman scattering (SERS) [10]. Recently, the preparation and characterization of freestanding films of

gold nanoparticle (GNP) monolayers [11–13] and multilayers [14, 15] have been reported. Freestanding films are of major interest, because they enable the investigation of their properties, e.g. mechanical properties, without disturbance by a supporting substrate. Moreover, applications of freely suspended films from GNP/polymer layers as highly sensitive pressure sensors [16] and IR-microimagers [17] have been demonstrated.

In this study we are interested in the facile fabrication of freestanding and electrically conductive films from crosslinked GNPs. Such conductive films are especially interesting, because their charge transport is sensitively affected by mechanical deformation, coming from e.g. pressure variations or chemical reaction. Although the preparation of crosslinked GNP films on solid supports has been described in numerous publications, the efficient preparation of freely suspended, crosslinked GNP films remains challenging. Substrate

¹ Present address: Department of Chemistry, University of California, Berkeley, CA 94720, USA.

² The first two authors contributed equally to this study.

³ Present address: Bayreuth Center for Colloids and Interfaces, University of Bayreuth, Universitätsstraße 30, 95440 Bayreuth, Germany.

⁴ Author to whom any correspondence should be addressed.

supported crosslinked GNP films are usually fabricated via layer-by-layer self-assembly (LbL-SA). This method is based on the functionalization of a substrate surface with functional groups to bind GNPs, followed by alternating immersion of the substrates into solutions of GNPs and the crosslinker [18, 19]. The major advantages of LbL-SA are the precise control of film thickness, film homogeneity, the high degree of crosslinking, applicability to curved substrates, and the ability for the combinatorial design of multilayered coatings. However, because LbL-SA involves laborious substrate handling with intensive washing steps after every GNP and linker deposition, the method is extremely time consuming and requires significant amounts of solvent. Additionally, the obtained films are chemically attached to the substrate. Thus, it is difficult detaching them without damage from the substrate to produce freely suspended films.

In order to provide a more facile route to crosslinked GNP films some alternative methods have been proposed, including precipitation and solvent evaporation [20], spray coating [21], and ink jet printing [22]. Recently, Grzybowsky and co-workers [23] described the preparation of GNP films on glass substrates via solvent evaporation followed by immersing the films into crosslinker solution. Afterward, GNP films with square centimeter dimensions could be lifted-off the substrate by underetching in alkaline solution and transferred onto various other substrates. Tsukruk and co-workers developed a very efficient method for producing multilayer GNP/polymer composite films via spin-assisted layer-by-layer assembly (SALBL) [24]. The method is based on the combination of repetitive GNP self-assembly and spin-coating of the polymer acting as crosslinker. By using a sacrificial layer of cellulose acetate between the substrate and the GNP/polymer film it was possible to lift-off the films after their assembly by immersion into acetone [15, 25]. Subsequently the films could be transferred onto holey substrates for producing freely suspended membranes. Nevertheless, to our knowledge, the electric conductivity of these suspended films has not been reported.

Here, we present an extremely efficient method for the well-controlled layer-by-layer preparation of conductive and covalently crosslinked GNP films. The use of alkylamine-stabilized GNPs and alkyleneedithiol (ADT) crosslinkers enabled a fast ligand/linker exchange and allowed for depositing both film components onto glass substrates via repetitive spin-coating. Choosing the right concentration of ADT made intermediate washing steps unnecessary. The deposition of films several tens of nanometers in thickness took only a few minutes, compared to several hours needed for traditional LbL-SA. As these films are not bound chemically to the substrates they can easily be detached and transferred onto electrodes to form electrically addressable freestanding films.

2. Experimental details

2.1. Materials

Chemicals were purchased from Merck, Chemsolute, Honeywell Speciality Chemicals Seelze GmbH, Prolabo, and

Aldrich. All chemicals and solvents were reagent grade or of higher quality and used as received. Deionized water was purified with a Millipore Simplicity system (resistivity 18.2 MΩ cm). 1,6-hexanedithiol (HDT) and 1,9-nanonanedithiol (NDT) were purchased from Aldrich, and 1,12-dodecanedithiol (DDT) was synthesized as described elsewhere [19]. 1-dodecylamine-stabilized GNPs with a size of ~3 nm were synthesized following the method of Leff *et al* [19, 26] and stored at -18 °C. Microscope coverslips (borosilicate glass, thickness: 0.17 mm) were purchased from Carl Roth GmbH.

2.2. Methods and apparatus

2.2.1. Preparation of 3d-electrode structures. The preparation of microstructures was performed under clean room conditions. A silicon wafer (Rockwood Electronic Materials) was cleaned with isopropanol and dried at 150 °C. The blank wafer was spin-coated (Laurell Technologies Corporation) at 1000 rpm with a layer of SU-8 50 negative photoresist (Micro Resist Technology GmbH). Using a mask aligner (Süss MicroTec AG) the photoresist was selectively exposed to UV light. For this step a lithography transparency with a stripe-pattern and a resolution of 64 kdpi (Zitzmann GmbH) served as a template. The exposed photoresist was developed (mr-Dev 600, Micro Resist Technology GmbH), rinsed with isopropanol and dried with a gentle stream of air.

The wafer covered with the resist material, patterned with trenches (gap: 100 μm, depth: ~100 μm, width: several centimeters), was coated with a 60 nm thick gold layer by vacuum evaporation (Pfeiffer Classic 250). In this process the wafer was tilted 45° with respect to the sample-source axis. Thus, the trenches served as shadow masks resulting in electrically separated electrodes on each side of a trench.

2.2.2. Determination of GNP sizes and concentration. After purifying the GNPs by fractionated precipitation they were dissolved in n-heptane to give a stock solution, which had an absorbance of ~0.45 (1 cm path length) at 450 nm after diluting by a factor of 1/500. To 50 μL stock solution 10 μL (42 μmol) 1-dodecanethiol and 500 μL n-heptane were added. After 35 min 1000 μL ethanol were added and the obtained precipitate was separated by centrifugation (2291g). The precipitate was resuspended in 1000 μL ethanol and again separated by centrifugation. Afterward the precipitate was dried under nitrogen flow and redissolved in 2000 μL n-heptane. This solution was used to transfer the nanoparticles onto a carbon coated TEM copper grid for TEM analysis (Jeol JEM-1011, LaB₆, 100 kV). Statistical analysis of the acquired micrographs revealed a GNP core size of ~3 nm (±14%) (supplementary data available at stacks.iop.org/Nano/22/305303/mmedia). Taking into account the average particle size and the optical density at 450 nm the GNP concentration of the stock solution was estimated to be ~0.14 mM, according to Haiss *et al* [27].

2.2.3. Preparation of GNP films. Microscope coverslips were first cleaned with acetone in an ultrasonic bath (Bandelin Sonorex), rinsed with water and dried under nitrogen flow.

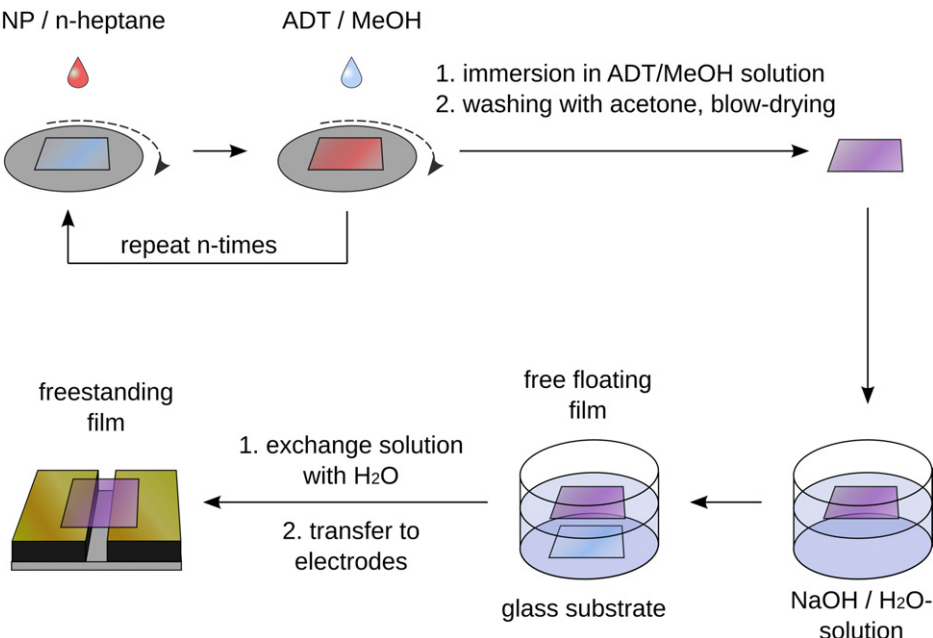


Figure 1. Preparative route to freestanding films of crosslinked gold nanoparticles (GNPs). First, GNPs and alkylenedithiol (ADT) crosslinkers were deposited onto a glass substrate via spin-coating. After immersion into ADT solution and washing, the GNP film was detached from the substrate in alkaline solution and transferred onto electrode structures.

The coverslips were then rotated at 3000 rpm using a spin-coater (Specialty Coating Systems Inc., Model P6700 Series). 8 μ L of GNP stock solution and 2 \times 10 μ L alkylene dithiol solution (HDT, NDT, DDT, \sim 7.4 mM, in methanol) were alternately dropped into the center of the rotating substrate until the desired thickness was obtained. Between applications a waiting time of 30 s was kept, while continuing to rotate the substrate. After finishing the final deposition cycle the substrate was immersed into a solution of ADT (\sim 7.4 mM, in methanol) overnight. Finally the substrates were washed with acetone and dried under gentle nitrogen flow or at air.

GNP films could be lifted-off the substrate by floating the glass substrate onto a 0.1 M NaOH solution. After a while the glass substrate settled to the bottom of the beaker, while the film floated on top of the solution. The NaOH solution was then exchanged by purging with water. Finally, the free floating film was transferred onto the electrode structures and allowed to dry at ambient conditions. We note that cleaning the glass substrates with Caro's acid (CAUTION: Caro's acid reacts explosively with organics!), rinsing them with water, and then treating them with alkyl carboxylic acids before film deposition facilitated the lift-off process. However, this treatment of the coverslips was not essential.

2.2.4. Characterization of GNP films. The UV/vis spectra were recorded using a Varian Cary-50 spectrometer. Light microscopy (LM) was done using a Zeiss Axiovert S 100 or an Olympus BX 51 microscope equipped with a UC 30 CCD camera, which allowed for 3d reconstruction of acquired image stacks. The surface topography of the films was investigated using a DI (Digital Instruments) Multimode atomic force microscope (AFM), equipped with a Nanoscope

IV controller, and a 100 μ m scanner, and operated with a Veeco RTESPW-tip. Alternatively, a JPK NanoWizard 3 AFM was used, equipped with a 100 μ m scanner, and operated with an AppNano HYDRA6V-100NG tip. All images were acquired in tapping-mode™ or contact mode with low force setting. Step profiles were measured for determining the thicknesses of the films. The average roughness of the films was determined using the Gwyddion V2.x software package. X-ray diffractograms were measured using a PANalytical X'PERT Pro diffractometer equipped with a copper anode operated at 45 kV, 40 mA. For these measurements the films were deposited onto silicon (911) wafers. Current-voltage (IV-) measurements were done using an Agilent 4156C parameter analyzer. The GNP films were contacted with gold electrodes (individual widths in the range of 7.0–10.1 mm, gap: 400 μ m, thickness: \sim 60 nm), which were deposited onto the films using a Pfeiffer Classic 250 vacuum evaporation system. The gap was defined using a shadow mask.

3. Results and discussion

3.1. Preparation process

The process of GNP film preparation is schematically shown in figure 1. First, a layer of nanoparticles was deposited onto a glass substrate by spin-coating GNPs from their solution in n-heptane. Dodecylamine-stabilized GNPs were used because the alkylamines are only weakly bound to the particles and are efficiently replaced by thiols [19]. Second, a solution of the ADT crosslinker was spin-coated. To avoid removal of particles from the substrate, the ADT was applied as a solution in methanol, which does not dissolve the GNPs. However, methanol dissolved the weakly bound dodecylamine

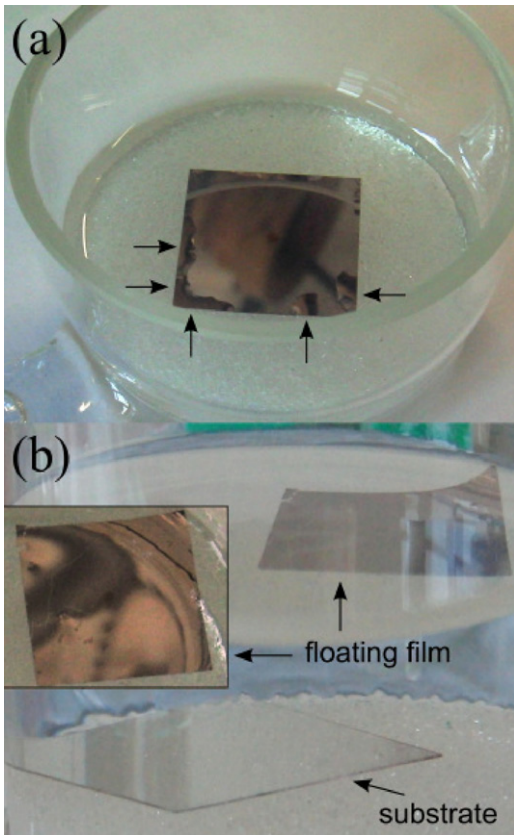


Figure 2. (a) Crosslinked GNP/NDT film deposited onto a glass substrate floating on NaOH solution. As indicated, the lift-off process started at the rim of the substrate. (b) Free floating film on water after complete detachment (inset: top view).

capping ligands and thereby destabilized the nanoparticles, as clearly evidenced by the XRD results presented below. In order to avoid destabilization and coalescence of GNPs it was necessary to supply ADT in a sufficiently high concentration. Thus, the ADT served as a crosslinker but additionally to (re)stabilizing the particles. Adjusting the right concentration of the ADT solution turned out to be critical for the whole assembly process. As indicated by conductance measurements

(see below) too low a concentration of ADT was insufficient to stabilize the particles, while an excess of ADT deposited onto the film making the formation of homogeneous coatings laborious or impossible. After spin-coating the ADT solution, the deposition of GNPs and crosslinker was repeated until a film of desired thickness was obtained. Notably, with the ADT concentration properly adjusted washing steps were not necessary. The films were finally treated with ADT solution, washed, and dried under nitrogen flow or at air. As reported previously by Grzybowski and co-workers [23], we could detach the films from their substrates by underetching with sodium hydroxide solution, as shown in figure 2. After this, the films floated on the surface of the alkaline solution, which was exchanged by purging carefully with water. The floating films could easily be transferred onto three-dimensionally patterned electrodes to obtain electrically addressable, freestanding GNP films.

3.2. Determination of nanoparticle sizes

Dodecylamine-stabilized GNPs were synthesized as reported previously [19, 26]. While investigating the as-prepared samples by TEM it was observed that the particles easily fused and formed larger aggregates due to their weak stabilization. Therefore, we exchanged the dodecylamine ligands with dodecanethiol ligands before determining the particle sizes by TEM. UV/vis spectra of the particles recorded before and after ligand exchange were almost identical, indicating that their sizes were not affected by the ligand exchange reaction. After ligand exchange, the stability of the particles during TEM imaging was significantly improved and particle sizes of ~ 3 nm ($\pm 14\%$) were determined without difficulties. Notably, very similar sizes were determined by TEM investigations of the as-prepared GNPs if only those particles were counted, which were well-separated from aggregated and fused particles.

3.3. UV/vis-absorption spectroscopy

The deposition of GNPs and ADT crosslinkers was investigated by recording the UV/vis spectrum after each spin-coating step. Figure 3(a) exemplarily shows a set of UV/vis

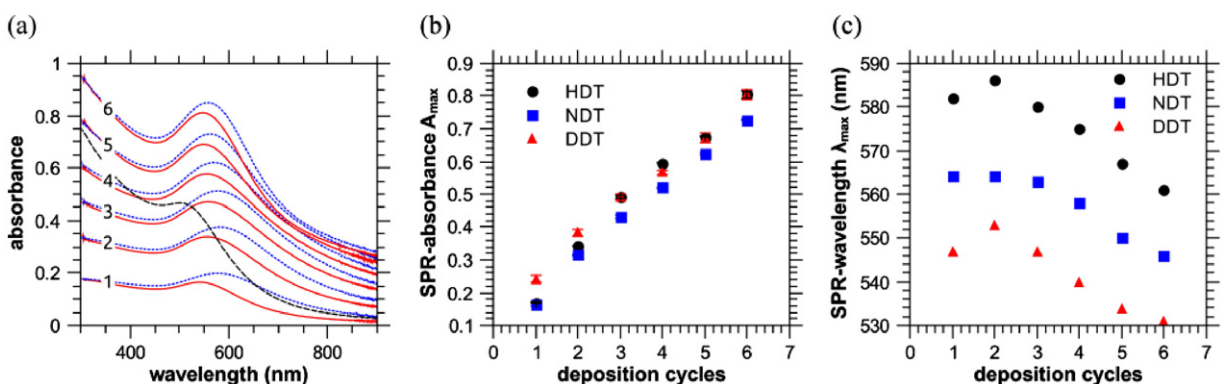


Figure 3. (a) Absorption spectra of GNP solution in n-heptane (dashed black line) and of GNP films after alternating deposition of GNPs (solid red lines) and HDT (dotted blue lines). (b) Plasmon absorbance and (c) spectral position of plasmon band plotted versus number of deposition cycles. HDT, NDT, and DDT were used as the crosslinker, as indicated.

spectra recorded of films crosslinked with 1,6-hexanedithiol (HDT). Spectra of films crosslinked with longer ADTs, i.e. 1,9-nonenedithiol (NDT) and 1,12-dodecanedithiol (DDT) are qualitatively very similar (supplementary data available at stacks.iop.org/Nano/22/305303/mmedia). For comparison the spectrum of the GNP solution is also presented in figure 3(a).

After depositing the GNPs from their solution onto the glass substrate, the maximum of their surface plasmon resonance (SPR) band red-shifted from ~ 500 to ~ 540 nm. This red-shift is explained by changes of the effective dielectric function, which strongly depends on the number density of particles, as described by Maxwell-Garnett Theory and confirmed experimentally [28, 29]. Additionally, the plasmon coupling of neighboring GNPs becomes important at very small particle distances. After spin-coating the crosslinker onto the first layer of GNPs, the SPR-band was further red-shifted to ~ 580 nm. This additional red-shift along with a slight increase in absorbance is attributed to a decrease of average particle distances after crosslinking, resulting in enhanced coupling between neighboring GNPs. Accordingly, decreasing the length of the ADT crosslinker further red-shifted the position of the SPR-band, as discussed in detail below.

After completing the first deposition cycle, alternating spin-coating of GNPs and crosslinker was repeated until a film of the desired thickness was obtained. The stepwise growth of the films was recognized by an increase in SPR-absorbance after each completed deposition cycle, as shown in figure 3(b). Obviously, the increase in absorbance was rather independent of the crosslinkers' chain length. In figure 3(c) the spectral position λ_{max} of the plasmon band is plotted versus the number of deposition cycles for all three film materials investigated. In agreement with previously published data [19], referring to GNP/ADT films prepared via traditional LbL-SA, we observed a red-shift of the plasmon band after the second deposition cycle for films crosslinked with HDT and DDT. We note that in the previously published study the maximum thickness of the films corresponded to the thickness obtained after the second deposition cycle in our present work. With increasing cycle number a significant blue-shift of the plasmon band was observed. We assign this finding to changes of both scattering background and reflectivity with increasing film thickness.

As mentioned above, the position of the SPR-maximum depended on the alkylene chain length of the crosslinker and was significantly red-shifted with decreasing length of the linker, as apparent in figure 3(c). This finding indicates that the electronic coupling between the particles was controlled by the size of the crosslinker, similar as observed previously in the case of ADT crosslinked GNP films assembled via the traditional LbL-SA immersion bath method [19]. The control of particle distances by the length of the crosslinker was confirmed by the conductivity measurements presented below.

3.4. Microscopy

A representative LM-micrograph of a substrate supported GNP/NDT film is shown in figure 4(a). Both, the NDT as well as the HDT crosslinked film had a smooth

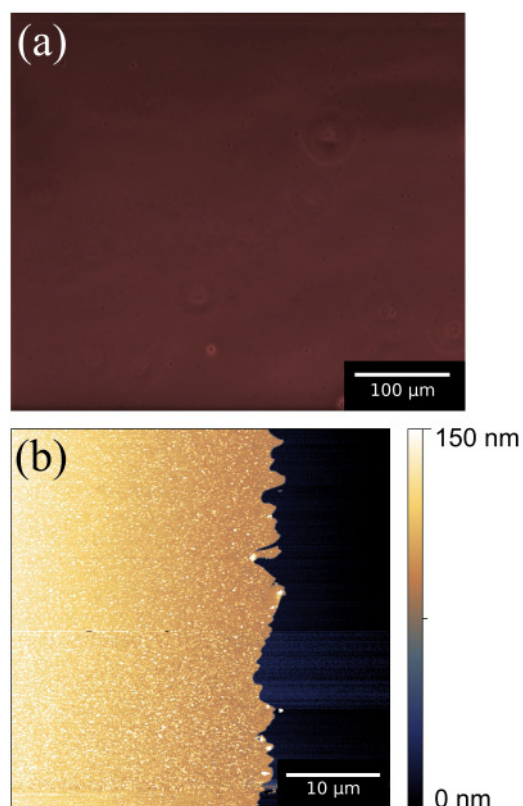


Figure 4. (a) LM-micrograph of a GNP/NDT film recorded in transmission mode. (b) AFM-Micrograph of the same film acquired in tapping-mode™. The AFM image was taken at the edge of a scratch. Height profiles measured at the edge were used to determine the film thickness (supplementary data available at stacks.iop.org/Nano/22/305303/mmedia).

appearance, whereas the DDT crosslinked film appeared somewhat inhomogeneous (supplementary data available at stacks.iop.org/Nano/22/305303/mmedia). Most likely, the solubility of the linker in methanol, which decreased with increasing chain length, was important for homogeneous film formation. We assume that solvent evaporation during the spin-coating process lead to the precipitation of excess DDT, causing inhomogeneous film deposition. Currently, we are working on protocols to improve the homogeneity of the DDT crosslinked film by applying solvent mixtures, such as THF/methanol, instead of pure methanol for dissolving the linker.

The surface topography of the films was characterized by AFM operated in tapping-mode™ or contact mode with a low force setting. A representative image of the GNP/NDT film is shown in figure 4(b). Step profiles recorded at the edges of scratches in the film were used to determine the film thicknesses. The measured values for films prepared by five deposition cycles are presented in table 1. Plots of film thicknesses versus the number of deposition cycles are shown in figure 5. All three film materials showed a linear increase in film thickness with increasing number of deposition cycles. This observation indicates that the same amount of GNPs was deposited with each spin-coating cycle. As expected, figure 5 shows that with increasing length of the linker the incremental

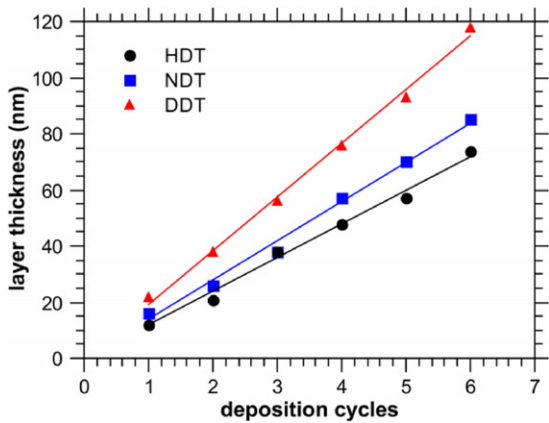


Figure 5. Increase in film thickness with increasing number of deposition cycles.

Table 1. Thickness, average roughness, and conductivity of differently crosslinked GNP/ADT films. In each case the standard deviation of the film thickness refers to ten graphically averaged values determined from step profiles (supplementary data available at stacks.iop.org/Nano/22/305303/mmedia). Values for the average roughness R_a were determined from AFM images measured over an area of $5 \mu\text{m} \times 5 \mu\text{m}$ (supplementary data available at stacks.iop.org/Nano/22/305303/mmedia). Conductivities given in parenthesis are taken from [19].

Linker	Cycle #	Thickness δ (nm)	Average roughness R_a (nm)	Conductivity $\sigma (\Omega^{-1} \text{cm}^{-1})$
HDT	5	57 ± 1	0.44	4.2×10^{-2} (3.73×10^{-2})
NDT	5	70 ± 2	0.47	1.5×10^{-3} (2.06×10^{-3})
DDT	5	93 ± 3	2.10	4.1×10^{-5} (2.30×10^{-4})

increase in film thickness became larger. The same trend was observed previously for GNP/ADT films assembled via the traditional LbL-SA method using immersion baths [19].

Table 1 gives typical values for the average roughness R_a of the films, acquired from samples prepared by five

deposition cycles. Consistent with LM images (supplementary data available at stacks.iop.org/Nano/22/305303/mmedia) the DDT crosslinked film had a significantly higher roughness than HDT and NDT crosslinked films. Analyzing the AFM images of films prepared by 1, 3 and 5 deposition cycles revealed that for HDT and DDT crosslinked films the roughnesses decreased somewhat after the third deposition cycle (supplementary data available at stacks.iop.org/Nano/22/305303/mmedia).

3.5. Conductivity measurements

The charge transport through multilayered GNP films has been studied extensively and described by an activated tunneling model [30, 31]. Usually these films show Ohmic current-voltage (IV -) characteristics. A representative set of IV -curves referring to NDT crosslinked films with various thicknesses is shown in figure 6(a). For comparison the IV -curves of HDT, NDT, and DDT crosslinked films, obtained after the fifth spin-coating cycle, are presented in figure 6(b) on a log-scale.

The reciprocal sheet resistances plotted versus deposition cycle number showed an approximately linear correlation, irrespective of the crosslinker used for film assembly. Figure 6(c) shows representative results obtained with NDT crosslinked films. Results referring to other film materials are provided as supplementary data (available at stacks.iop.org/Nano/22/305303/mmedia). The linear increase in conductance with increasing cycle number is in agreement with the linear increase in film thickness (figure 5) and confirms a well-controlled deposition of crosslinked nanoparticles with each spin-coating cycle. The conductivities of all films investigated were calculated by dividing the sheet resistances by the film thicknesses. In figure 7 the conductivities are plotted versus the corresponding film thickness. After the second deposition cycle the conductivities of the films did not depend significantly on their thickness. The conductivities of films obtained after five deposition cycles are presented in table 1. For HDT and the NDT crosslinked films the conductivities fall into the same range as the values reported earlier for films prepared via the traditional LbL-SA method using

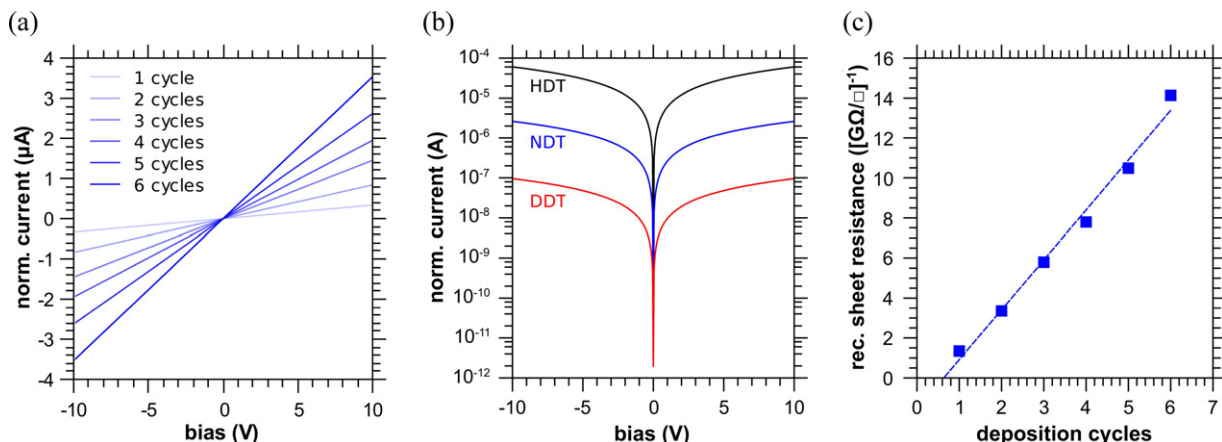


Figure 6. (a) IV -curves of GNP/NDT films measured after each deposition cycle. (b) IV -curves of the three film materials prepared by five deposition cycles plotted on the log-scale. (c) Reciprocal sheet resistance of GNP/NDT films plotted versus cycle number. The currents displayed graphically in (a) and (b) were normalized to a common electrode width of 1.0 cm.

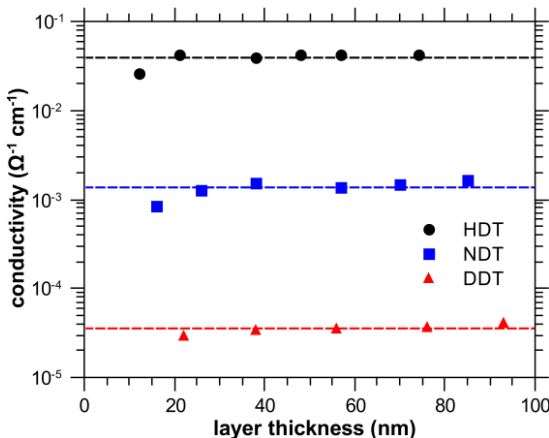


Figure 7. Conductivity of the three materials investigated plotted versus film thickness, crosslinker used as indicated.

GNPs of similar sizes [19]. This finding indicates that the internal structure of the films was similar regardless of which preparation method was used. However, the conductivity of the DDT crosslinked films reported previously was ~ 6 times higher than the value measured here. We assume that the lower conductivity determined in our present study for the DDT crosslinked film is due to its inhomogeneous morphology observed by light microscopy and AFM (supplementary data available at stacks.iop.org/Nano/22/305303/mmedia).

3.6. Characterization of substrate supported films by XRD

Two parallel processes are important for GNP deposition during the LbL-spin-coating process. One is the destabilization of GNPs by the removal of dodecylamine ligands when applying the methanolic linker solution. The other is the (re)stabilization and crosslinking of particles by reaction with ADT. Figure 8 shows XR-diffractograms of a drop-coated film from dodecylamine-stabilized AuNPs before and after immersion into pure methanol. The pronounced sharpening of the reflexes after treatment with methanol clearly reveals destabilization and coalescence of GNPs. In contrast, films which were LbL-spin-coated using a ~ 7.4 mM solution of NDT in methanol did not show any narrowing of XRD reflexes. We conclude that the fusion of AuNPs by the removal of dodecylamine ligands is efficiently suppressed by the presence of the crosslinker, which serves both to interlink and to stabilize the particles via a fast ligand-linker exchange reaction.

By applying the Scherrer-equation [32] the coherent crystalline domain size was calculated using the width of the reflexes at half maximum. For as-prepared particles as well as for particles within the NDT crosslinked film we calculated a coherent crystalline domain size of ~ 1.5 nm, while the domain size of the fused particles, obtained after treatment with methanol, was ~ 15.0 nm.

3.7. Influence of GNP and crosslinker concentration on the assembly process

The adjustment of the ADT concentration was critical for successful film assembly. In a first set of experiments

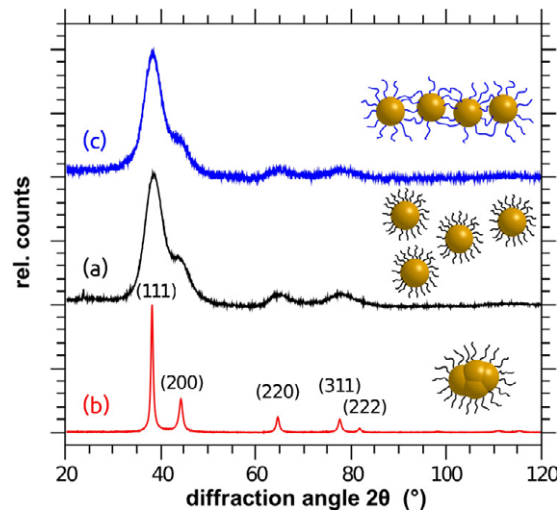


Figure 8. (a) XR-Diffractograms of a drop-coated film of dodecylamine-stabilized GNPs, (b) of the drop-coated film after immersion in methanol (MeOH) for several hours, and (c) of an LbL-spin-coated GNP film assembled with NDT as the crosslinker. Reflexes are assigned to the face-centered cubic lattice of gold, as indicated.

it was found that a crosslinker concentration of ~ 5 mM enabled a well-controlled and reproducible LbL growth of homogeneous films. Significantly higher concentrations led to the deposition of droplets of excess linker and resulted in inhomogeneous film growth. Significantly lower concentrations of crosslinker did not enable the reproducible deposition of GNPs with increasing cycle number, because GNPs were only insufficiently bound and removed while repeatedly applying the GNP solution. Therefore, we investigated how a variation of ADT concentration in the range 0.5–15 mM influenced the film deposition. Figure 9 shows how the reciprocal sheet resistance of films obtained after four deposition cycles varied with the concentration of NDT. It is seen that diluting the linker concentration below ~ 4 mM resulted in a significant increase in conductance. Taking into account the XRD results discussed above, we attribute this finding to insufficient GNP stabilization at ADT concentrations below ~ 4 mM, resulting in reduced average interparticle distances and GNP coalescence. However, at concentrations above ~ 4 mM the reciprocal sheet resistance was rather constant at ~ 10 ($\text{G}\Omega/\text{square}$) $^{-1}$. Therefore, in order to avoid destabilization of GNPs on the one hand and deposition of excess ADT on the other hand we have chosen ~ 7.4 mM as the standard concentration of the crosslinker throughout this study.

We note that in figure 6(c) the corresponding value of the reciprocal sheet resistance of the GNP film obtained after four deposition cycles, ~ 8 ($\text{G}\Omega/\text{square}$) $^{-1}$, was somewhat below 10 ($\text{G}\Omega/\text{square}$) $^{-1}$. Taking into account that different batches of GNP preparations were used in both experiments, these values are in reasonable agreement. Slight deviations in GNP size distribution and concentration can easily influence the conductivity of the prepared films and, thus, explain the observed difference.

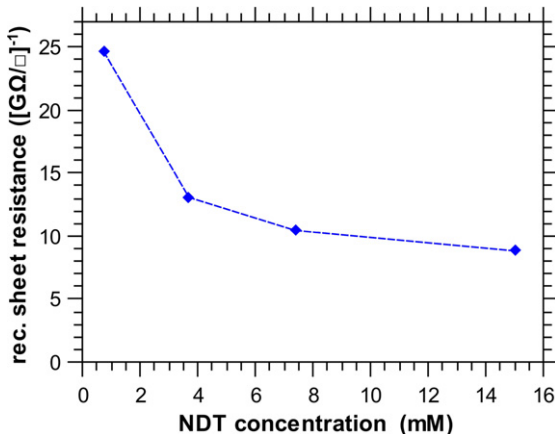


Figure 9. Reciprocal sheet resistances of GNP/NDT films obtained after completing the fourth spin-coating cycle versus NDT concentration used for film assembly.

Throughout this study we used a ~ 0.14 mM solution of GNPs as the standard GNP concentration. With this GNP concentration it was possible to quickly grow films with several tens of nanometers in thickness. Notably, these films were deposited within a few minutes. In contrast, the deposition of GNP/ADT films via the traditional LBL-SA method, with thicknesses of only 20–30 nm, takes several hours [19].

The data presented in figure 5 show that with each spin-coating cycle films with thicknesses of ~ 10 – 25 nm, corresponding to a few GNP monolayers, were deposited. By varying the GNP concentration the amount of GNPs deposited in every spin-coating cycle could be controlled. For example, reducing the GNP concentration by a factor of 0.5 reduced the absorbance measured after the first and fourth deposition cycle by a factor of ~ 0.65 (supplementary data available at stacks.iop.org/Nano/22/305303/mmedia).

3.8. Electrically addressable freestanding GNP films

Figure 10 shows the LM-micrograph (a) and a three-dimensionally reconstructed image (b) of a freestanding GNP/NDT film. The membrane was ~ 100 nm thick and bridged a trench of $100\ \mu\text{m}$ width between two gold electrodes. The length of the bridged trench was almost ~ 4 mm (supplementary data available at stacks.iop.org/Nano/22/305303/mmedia). The *IV*-curve of the freestanding film was linear, as in the case of substrate supported films. In order to investigate if the transfer of the film onto the electrodes affected its integrity, we measured the sheet resistances of one part of the film left on the original substrate and another part transferred onto the electrodes. These measurements gave $61.3\ \text{M}\Omega/\text{square}$ and $57.4\ \text{M}\Omega/\text{square}$, respectively. The difference of only 6% is within the accuracy of these comparative measurements, and indicates that the membrane was transferred without significant damage. Folding of the membrane, as seen in figure 10, most likely results from the drying process required after transferring the membrane from the water surface onto the electrodes. Thus, we attribute the observed folding to local strain caused by capillary forces during film transfer and the drying process. The similar

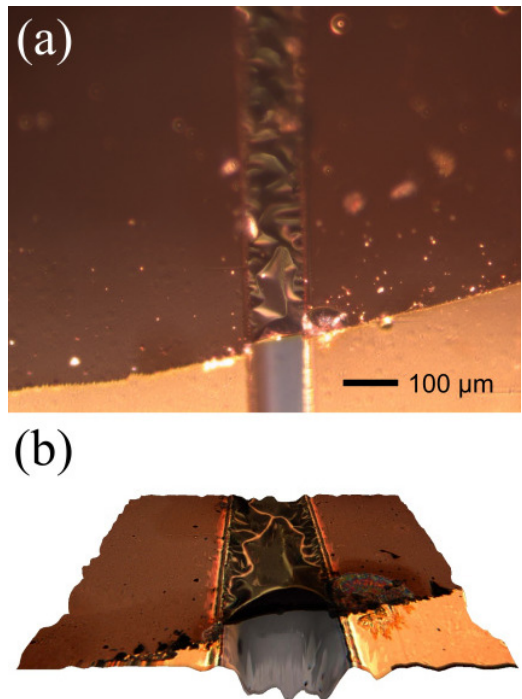


Figure 10. LM images of a freestanding GNP/NDT film on gold electrodes bridging a trench of $100\ \mu\text{m}$ width. (a) Top view, (b) 3d-reconstructed image.

sheet resistances of both the substrate supported film and the freestanding film suggest that folding did not significantly affect the electronic transport properties. In order to reduce folding of the membrane we are currently working on improved protocols for membrane transfer and drying.

4. Conclusions

In this study we developed a new, very efficient method for the preparation of crosslinked GNP films using alkylamine-stabilized GNPs and alkylene dithiols as the starting materials. The deposition of both, GNPs and crosslinker, is based on spin-coating. Adjusting the concentrations of GNP and crosslinker solutions made intermediate washing steps unnecessary. Thus, the spin-coating process requires only several μL of solvents whereas traditional LbL-SA using immersion baths requires significant amounts of solvents. Further, depositing films of ~ 100 nm thickness took only a few minutes, compared to several hours required for laborious LbL-SA using immersion baths. Nevertheless, our results indicate that the optical and electrical properties of films assembled via spin-coating are of comparable quality as previously described LbL-self-assembled films [19]. Because the spin-coated films were chemically not attached to the substrate, they could be lifted-off and transferred as freely suspended films onto three-dimensionally patterned electrodes. Measuring their sheet resistances indicated that the transfer process did not affect the film integrity.

Freestanding and electrically addressable films are of major interest, because they enable a simple readout of stress-induced deformations, which can be brought about

by e.g. pressure fluctuations, sorption of guest molecules, or chemical reactions. Therefore, these freestanding films are interesting new materials for developing physical and chemical sensors with simple electric signal transduction. Currently, we are investigating the mechanical properties of these freestanding films as well as their potential application as pressure sensors and chemical sensors.

Acknowledgments

We thank Oliver Frank, Mazlum Yesilmen, Tobias Grünzel, Anika Juhl, and Elisabeth Leib for their contributions regarding some experimental procedures. OF investigated methods for detaching self-assembled GNP films from glass substrates during his bachelor research project. MY, TG, AJ and EL contributed to this project while completing an advanced practical research placement as part of their degree program.

References

- [1] Wang L, Shi X, Kariuki N N, Schadt M, Wang G R, Rendeng Q, Choi J, Luo J, Lu S and Zhong C-J 2007 *J. Am. Chem. Soc.* **129** 2161–70
- [2] Zamborini F P, Leopold M, Hicks J F, Kulesza P J, Malik M A and Murray R W 2002 *J. Am. Chem. Soc.* **124** 8958–64
- [3] Joseph Y, Peic A, Chen X, Michl J, Vossmeyer T and Yasuda A 2007 *J. Phys. Chem. C* **111** 12855–9
- [4] Krasteva N, Fogel Y, Bauer R E, Müllen K, Joseph Y, Matsuzawa N, Yasuda A and Vossmeyer T 2007 *Adv. Funct. Mater.* **17** 881–8
- [5] Joseph Y, Guse B, Yasuda A and Vossmeyer T 2004 *Sensors Actuators B* **98** 188–95
- [6] Shipway A N, Katz E and Willner I 2000 *ChemPhysChem.* **1** 18–52
- [7] Shipway A N, Lahav M, Blonder R and Willner I 1999 *Chem. Mater.* **11** 13–5
- [8] Herrmann J, Müller K-H, Reda T, Baxter G R, Raguse B, de Groot G J J, Chai R, Roberts M and Wieczorek L 2007 *Appl. Phys. Lett.* **91** 183105
- [9] Vossmeyer T, Stolte C, Ijeh M, Kornowski A and Weller H 2008 *Adv. Funct. Mater.* **18** 1–6
- [10] Musick M D, Keating C D, Lyon L A, Botsko S L, Pena D J, Hollaway W D, McEvoy T M, Richardson J N and Natan M J 2000 *Chem. Mater.* **12** 2869–81
- [11] Mueggenburg K E, Lin X-M, Goldsmith R H and Jaeger H M 2007 *Nat. Mater.* **6** 656–60
- [12] He J, Kanjanaboos P, Frazer N L, Weis A, Lin X-M and Jaeger H M 2010 *Small* **13** 1449–56
- [13] Cheng W, Campolongo M J, Cha J J, Tan S J, Umbach C C, Muller D A and Luo D 2009 *Nat. Mater.* **8** 519–25
- [14] Endo H, Kado Y, Mitsuishi M and Miyashita T 2006 *Macromolecules* **39** 5559–63
- [15] Jiang C, Markutsya S and Tsukruk V V 2004 *Adv. Mater.* **16** 157–61
- [16] Jiang C, Markutsya S, Pikus Y and Tsukruk V V 2004 *Nat. Mater.* **3** 721–8
- [17] Jiang C, McConney M E, Singamaneni S, Merrick E, Chen Y, Zhao J, Zhang L and Tsukruk V V 2006 *Chem. Mater.* **18** 2632–4
- [18] Bethell D, Brust M, Schiffrin D J and Kiely C J 1996 *J. Electroanal. Chem.* **409** 137–43
- [19] Joseph Y et al 2003 *J. Phys. Chem. B* **107** 7406–13
- [20] Leibowitz F L, Zheng W, Maye M M and Zhong C-J 1999 *Anal. Chem.* **71** 5076–83
- [21] Lu C, Döñch I, Nolte M and Fery A 2006 *Chem. Mater.* **18** 6204–10
- [22] Andres C M and Kotov N A 2010 *J. Am. Chem. Soc.* **132** 14496–502
- [23] Kowalczyk B, Apodaca M M, Nakanishi H, Smoukov S K and Grzybowski B A 2009 *Small* **5** 1970–3
- [24] Jiang C, Markutsya S and Tsukruk V V 2004 *Langmuir* **20** 882–90
- [25] Mamedov A A and Kotov N A 2000 *Langmuir* **16** 5530–3
- [26] Leff D V, Brandt L and Heath J R 1996 *Langmuir* **12** 4723–30
- [27] Haiss W, Thanh N T K, Aveyard J and Fernig D G 2007 *Anal. Chem.* **79** 4215–21
- [28] Kreibig U and Vollmer M 1995 *Optical Properties of Metal Clusters (Series in Materials Science vol 25)* ed J P Toennies et al (Berlin: Springer)
- [29] Ung T, Liz-Marzan L M and Mulvaney P 2001 *J. Phys. Chem. B* **105** 3441–52
- [30] Terrill R H et al 1995 *J. Am. Chem. Soc.* **117** 12537–48
- [31] Wuelfing W P, Green S J, Pietron J J, Cliffel D E and Murray R W 2000 *J. Am. Chem. Soc.* **122** 11465–72
- [32] Guinier A 1994 *X-Ray Diffraction—In Crystals, Imperfect Crystals and Amorphous Bodies* (New York: Dover)

Supplementary Data

Freestanding films of crosslinked gold nanoparticles prepared via layer-by-layer spin-coating

By Hendrik Schlicke¹, Jan H. Schröder, Martin Trebbin², Alexey Petrov, Michael Ijeh, Horst Weller, and Tobias Vossmeyer

Institute of Physical Chemistry, University of Hamburg, Grindelallee 117, 20146 Hamburg, Germany

E-mail: tobias.vossmeyer@chemie.uni-hamburg.de

¹ current address: Department of Chemistry, University of California, Berkeley, California 94720, USA

² current address: Bayreuth Center for Colloids and Interfaces, University of Bayreuth, Universitätsstr. 30, 95440 Bayreuth, Germany

1. TEM Characterization

Figure S1 shows a TEM image taken of the particles immobilized on a TEM grid. The image shows a quite narrow size distribution of the obtained GNPs. As well does the corresponding size histogram of the statistical analysis of the particle core size.

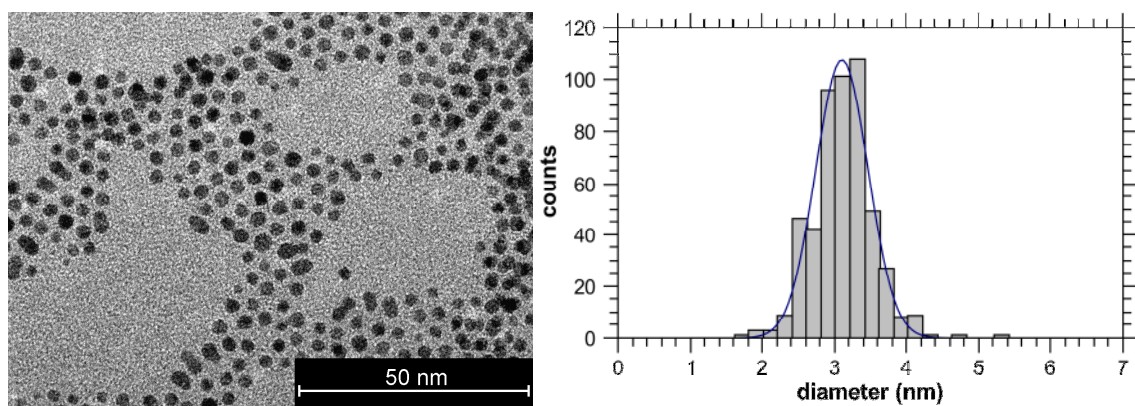


Figure S1 TEM image and size histogram of the GNPs.

2. UV/vis Characterization

After each deposition cycle a UV/vis spectrum was recorded. Figure S2 shows the qualitatively similar absorption spectra of the three different GNP films. Each spectrum was recorded after depositing the linker compound.

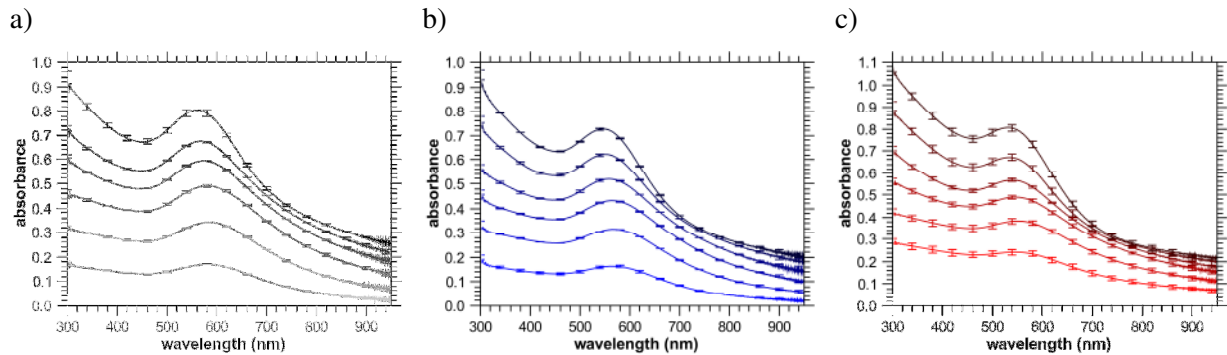


Figure S2 Absorption spectra of GNP films prepared with different linker solutions: a) HDT, b) NDT, c) DDT.

3. Light microscope characterization

LM-micrographs of every substrate supported GNP film were recorded in transmission mode to inspect the homogeneity of the obtained films. Figure S3a shows one of the GNP films crosslinked by HDT and Figure S3b shows a GNP film crosslinked by NDT. Both films show a good homogeneity over a large area. In comparison, the GNP film crosslinked by DDT shown in Figure S4a has a rougher surface. We were able to improve the homogeneity of the DDT crosslinked GNP film by using a solvent mixture (20% THF in methanol) for dissolving the DDT linker. The LM-micrograph of one of those films is shown in Figure S4b.

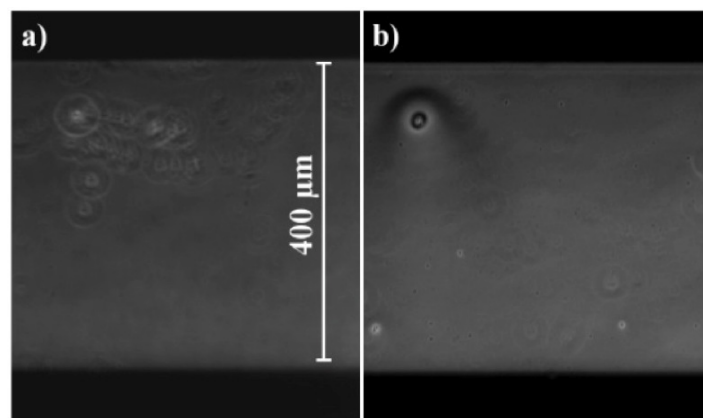


Figure S3 LM-Micrographs of GNP-films prepared with (a) HDT and (b) NDT.

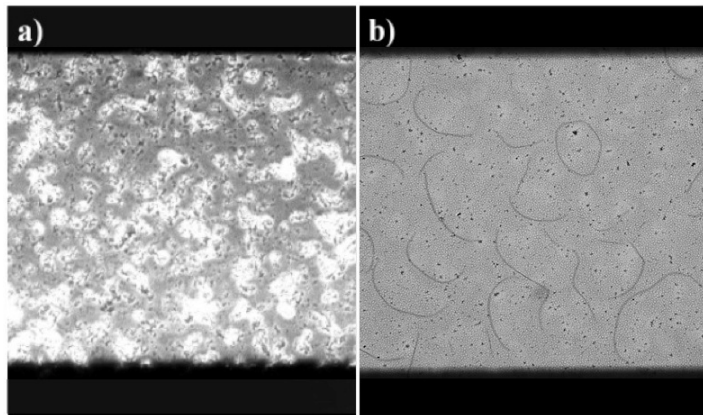


Figure S4 LM-Micrographs of GNP-films with DDT. The GNP films were prepared with DDT dissolved in a) methanol and b) in methanol 8:2 THF. Same scale as Figure S3.

4. AFM Characterization

Figure S5 shows an AFM image taken of a NDT-linked GNP film deposited onto a glass coverslip. The film was scratched using a 0.4 mm cannula with very low force and therefore without scratching the surface of the glass. The extracted profiles like one in Figure S6 show the step height of the films on top of the coverslip. 10 profiles were taken equally selected over the distance of 50 μm and the mean value was calculated. The measurements of the other samples were done using the same procedural manner. Figure S7 shows the AFM images of the 6-layer samples of the GNP films crosslinked by HDT and DDT. As one can see, the homogeneity of the GNP film prepared using DDT is not comparable to the others.

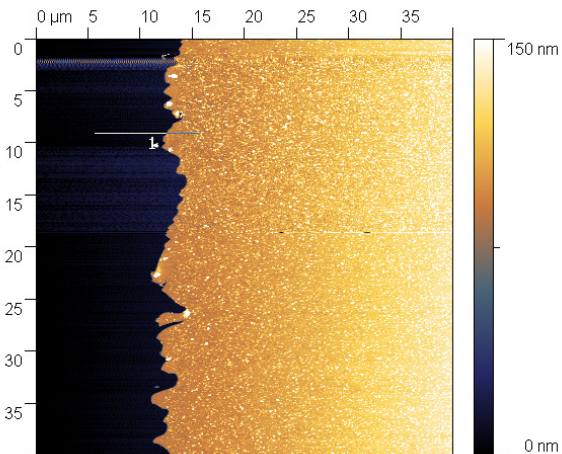


Figure S5 AFM image of the 6-Layer sample of GNPs crosslinked by NDT.

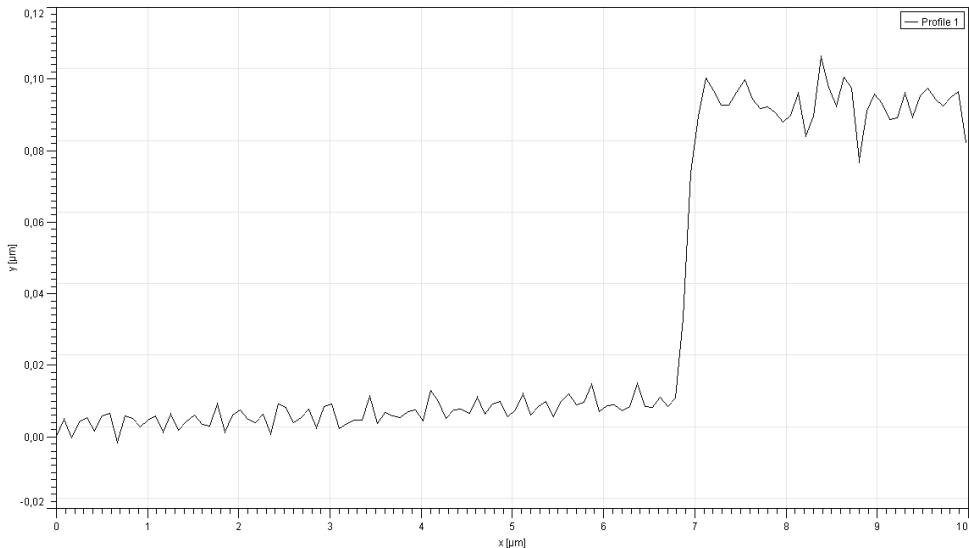


Figure S6 Height profile 1 taken from AFM-image of GNP film crosslinked by NDT shown in Figure S5.

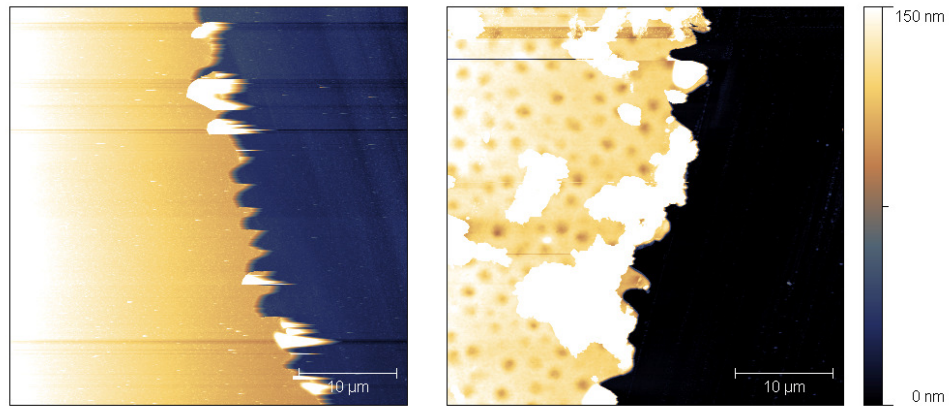


Figure S7 AFM images of the 6-layer samples of GNP films crosslinked by HDT (left) and DDT (right).

5. Surface roughness

The roughness of the films was calculated using data acquired over an area of 5 x 5 μm. R_a , the average roughness, is the value of the height irregularities and calculated as follows:

$$R_a = \frac{1}{N} \sum_{j=1}^N |r_j|$$

$$r_j = z_j - \bar{z}$$

Figures S8 to S16 show the AFM images of crosslinked GNP films with different linkers and different thicknesses.

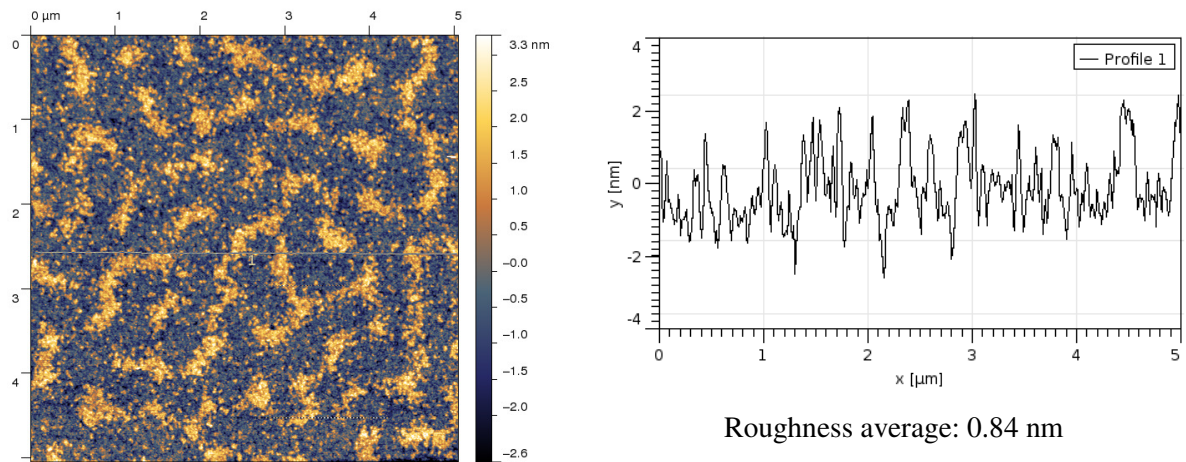


Figure S8 AFM image of a 1-layer sample of a GNP film crosslinked by HDT with corresponding linescan.

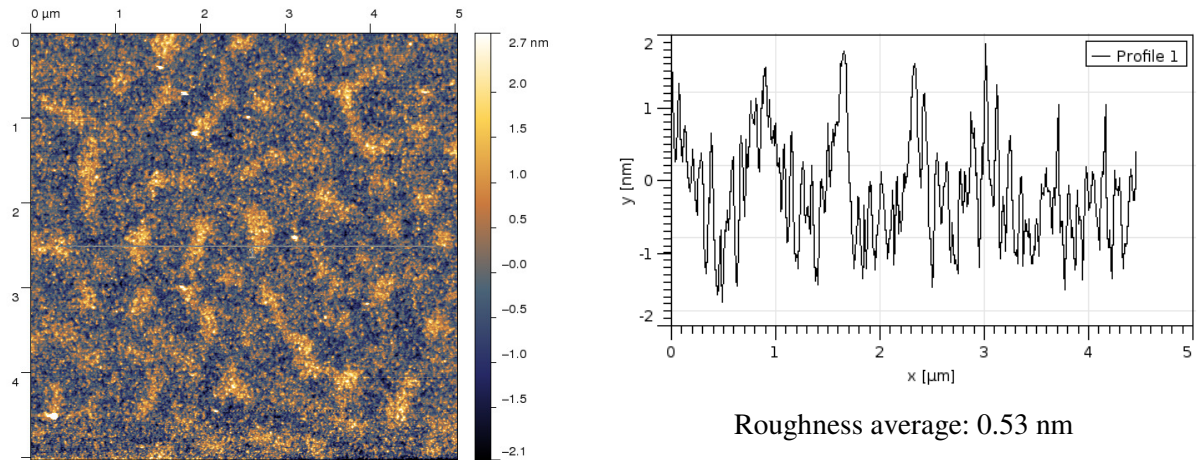


Figure S9 AFM image of a 3-layer sample of a GNP film crosslinked by HDT with corresponding linescan.

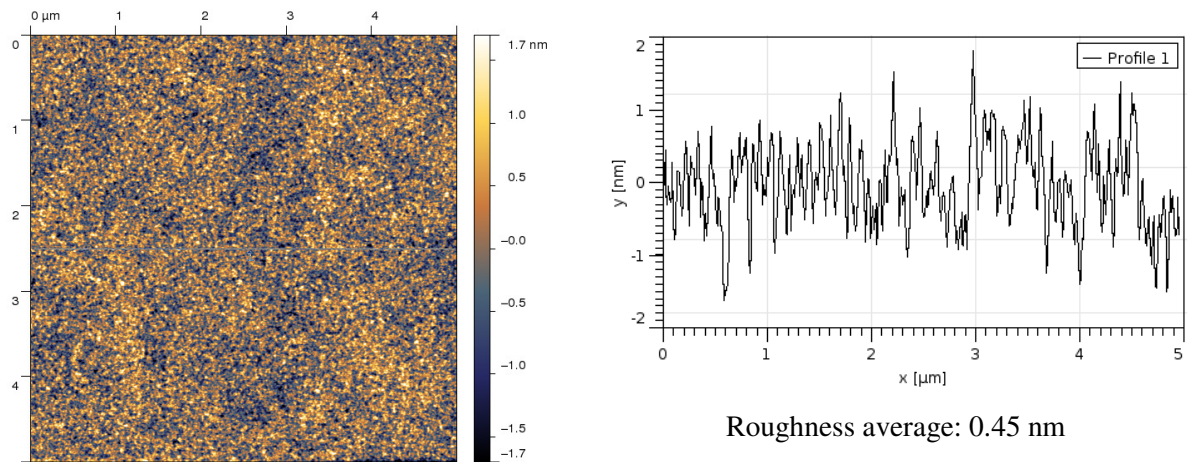


Figure S10 AFM image of a 5-layer sample of a GNP film crosslinked by HDT with corresponding linescan.

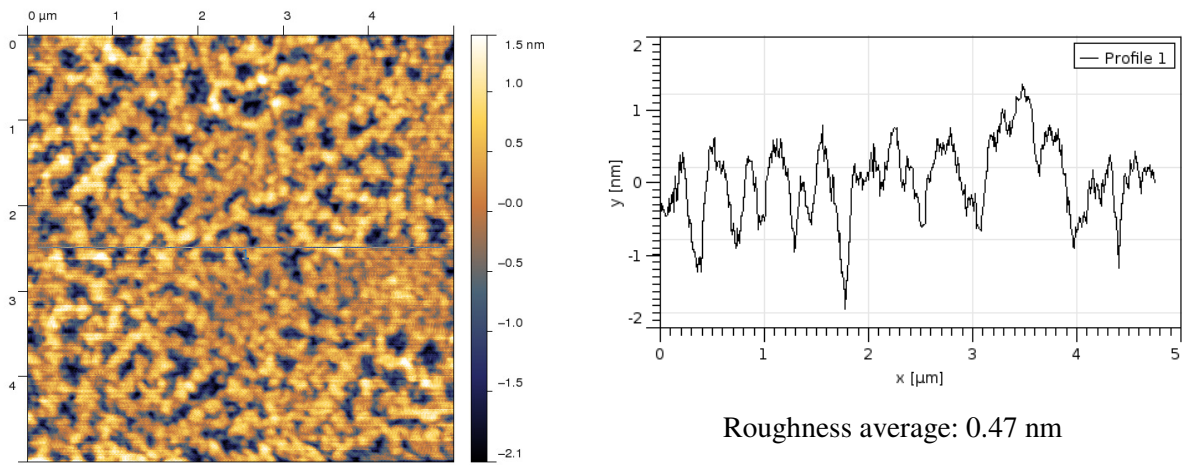


Figure S11 AFM image of a 1-layer sample of a GNP film crosslinked by NDT with corresponding line scan.

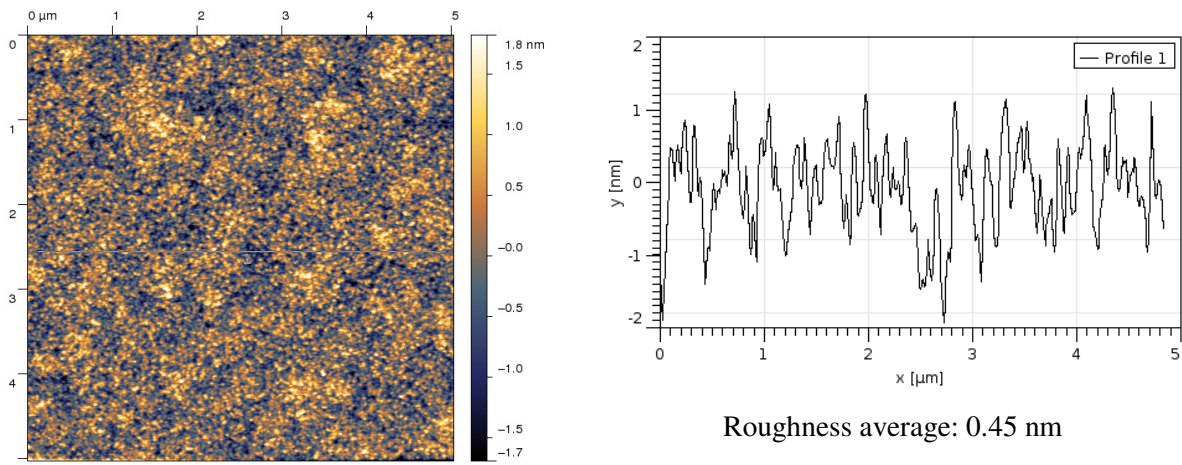


Figure S12 AFM image of a 3-layer sample of a GNP film crosslinked by NDT with corresponding linescan.

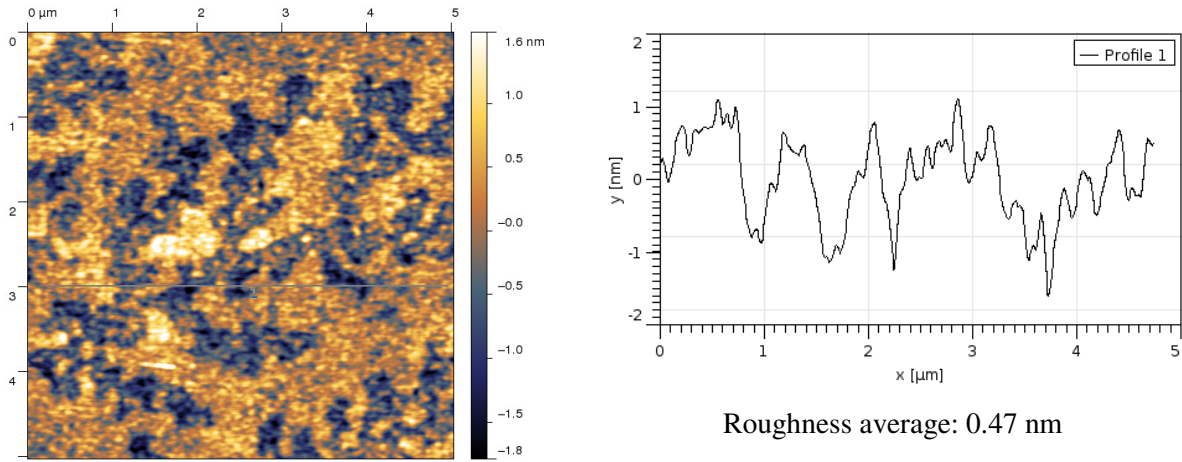


Figure S13 AFM image of a 5-layer sample of a GNP film crosslinked by NDT with corresponding linescan.

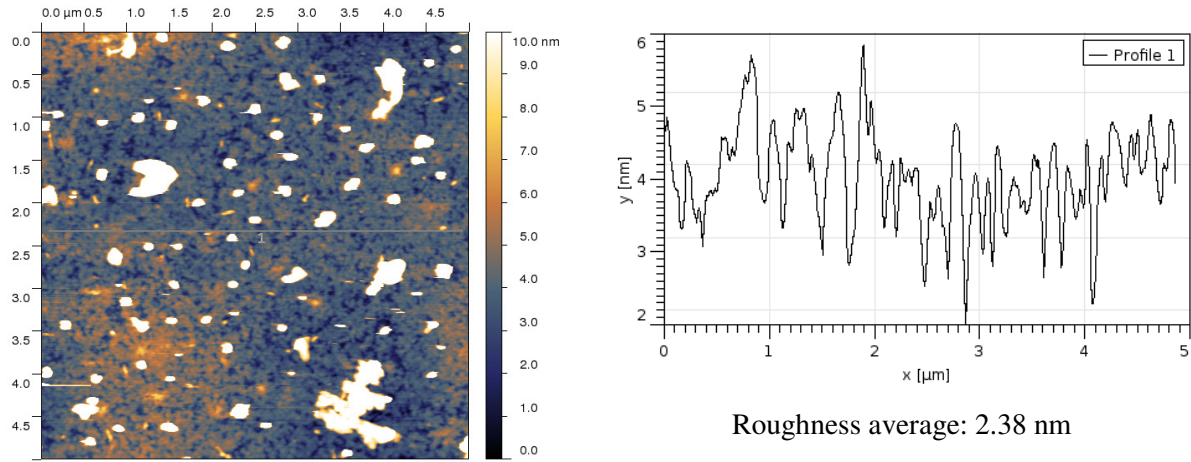


Figure S14 AFM image of a 1-layer sample of a GNP film crosslinked by DDT with corresponding linescan.

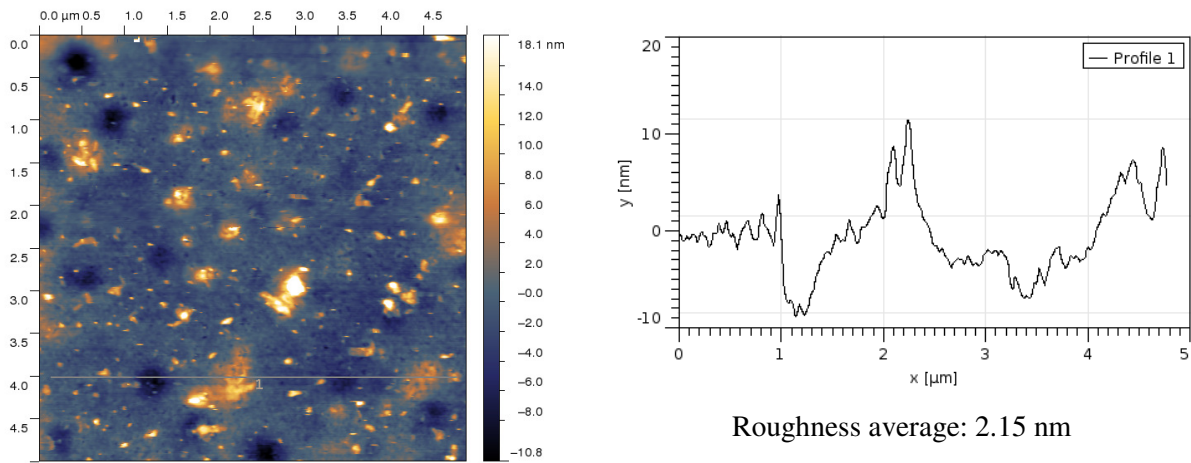


Figure S15 AFM image of a 3-layer sample of a GNP film crosslinked by DDT with corresponding linescan.

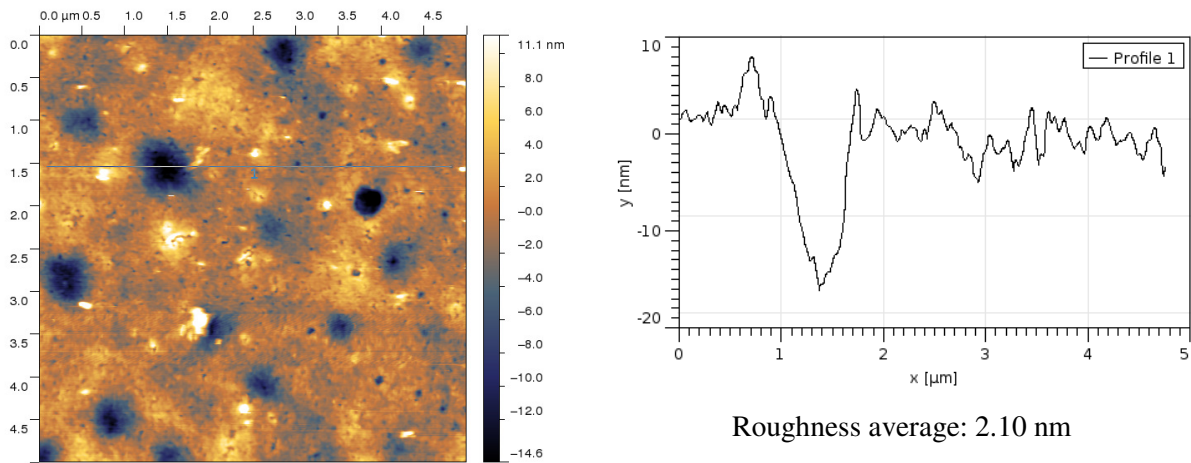


Figure S16 AFM image of a 5-layer sample of a GNP film crosslinked by DDT with corresponding linescan.

6. Conductivity measurements

Figure S17 shows IV-curves referring to HDT and DDT crosslinked films measured after up to 6 deposition cycles.

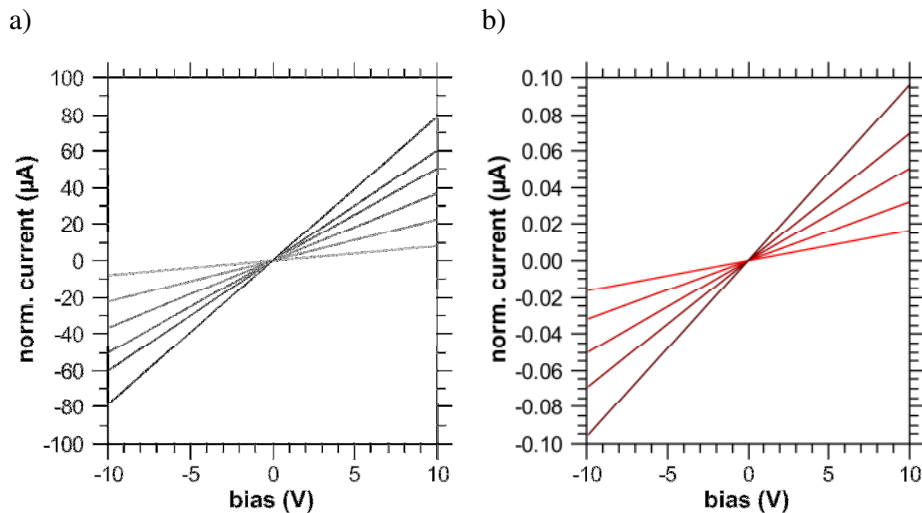


Figure S17 IV-curves of a) GNP/HDT and b) GNP/DDT measured after each deposition cycle. The slope of the curves increases with increasing number of deposition cycles.

Figure S18 shows the reciprocal sheet resistance plotted vs. the deposition cycle number for GNP films crosslinked by HDT and DDT. Both show an approximately linear correlation.

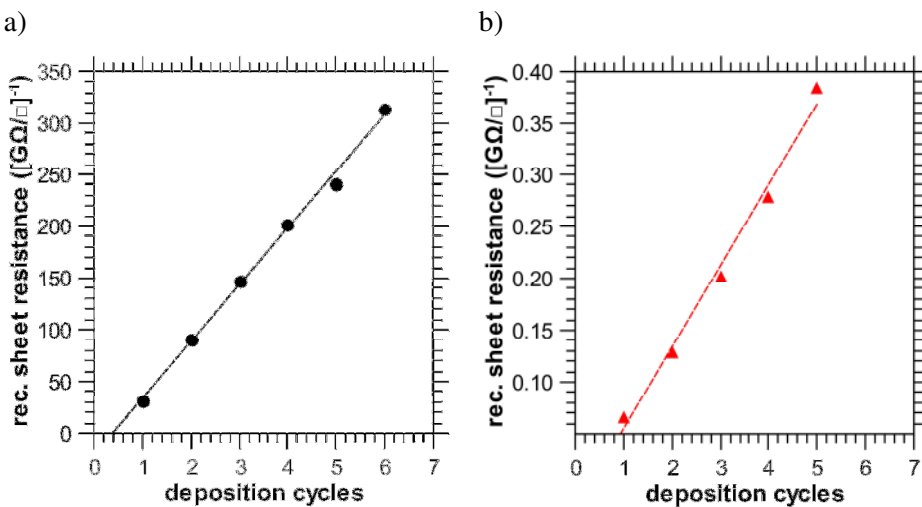


Figure S18 Reciprocal sheet resistance of a) GNP/HDT and b) GNP/DDT films plotted vs. cycle number.

7. Concentration variation

Figure S19 shows the absorbance of GNP/NDT films prepared with GNP solutions of different concentration. These films were obtained after completing 1 and 4 deposition cycles. Reducing the GNP concentration by a factor of 0.5 resulted in a decrease in the absorbance of the GNP film by a factor of ~ 0.65 .

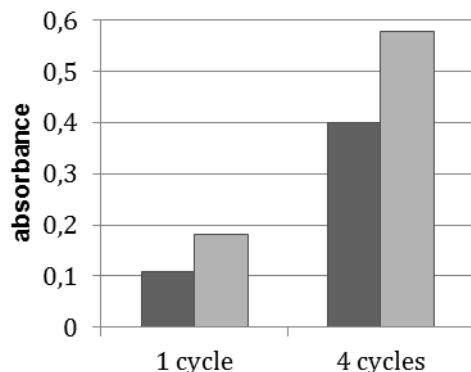


Figure S19 Absorption maxima of GNP films prepared with NDT with reduced GNP concentration (0.07 mM; dark) and usual concentration (0.14 mM; light).

8. Freestanding GNP films

Figure S20 shows jointed LM-micrographs of a free-standing GNP/NDT film. The membrane bridged a trench with a 100 μm gap over a length of 3723 μm .



Figure S20 LM-micrograph of the freestanding GNP-film with an overall length of 3723 μm and 100 μm width.

7.7 Adsorption of spherical polyelectrolyte brushes: from interactions to surface patterning

Adsorption of Spherical Polyelectrolyte Brushes: from Interactions to Surface Patterning

By Christoph Hanske¹, Johann Erath¹, Christin Kühr², Martin Trebbin²,
Christian Schneider^{2,3}, Alexander Wittemann⁴, and Andreas Fery^{1,*}

¹ Physical Chemistry II, University of Bayreuth, 95440 Bayreuth, Germany

² Physical Chemistry I, University of Bayreuth, 95440 Bayreuth, Germany

³ F-I2 Soft Matter and Functional Materials, Helmholtz-Zentrum Berlin, 14109 Berlin, Germany

⁴ Department of Chemistry, University of Constance, 78464 Konstanz, Germany

Dedicated to Matthias Ballauff on the occasion of his 60th birthday

(Received April 30, 2012; accepted in revised form July 6, 2012)

(Published online August 6, 2012)

Spherical Polyelectrolyte Brushes / Adsorption / Particles / Colloidal Probe / AFM / Microcontact Printing / Surface Patterning

Adsorption of colloidal particles constitutes an attractive route to tailor the properties of surfaces. However, for efficient material design full control over the particle-substrate interactions is required. We investigate the interaction of spherical polyelectrolyte brushes (SPB) with charged substrates based on adsorption studies and atomic force spectroscopy. The brush layer grafted from the colloidal particles allows a precise adjustment of their adsorption behavior by varying the concentration of added salt. We find a pronounced selectivity between oppositely and like-charged surfaces for ionic strengths up to 10 mM. Near the transition from the osmotic to the salted brush regime at approximately 100 mM attractive secondary interactions become dominant. In this regime SPB adsorb even to like-charged surfaces. To determine the adhesion energy of SPB on charged surfaces directly, we synthesize micrometer-sized SPB. These particles are used in colloidal probe AFM studies. Measurements on oppositely charged surfaces show high forces of adhesion for low ionic strengths that can be attributed to an entropy gain by counterion release. Transferring our observations to charge patterned substrates, we are able to direct the deposition of SPB into two-dimensional arrays. Considering that numerous chemical modifications have been reported for SPB, our studies could open exiting avenues for the production of functional materials with a hierarchical internal organization.

1. Introduction

The physisorption of components from solution constitutes a versatile and easily up-scalable alternative to surface modifications based on covalent chemical coupling, since coupling by physisorption does not require specific chemical reactions to occur.

* Corresponding author. E-mail: andreas.fery@uni-bayreuth.de

A prominent example for this approach is the layer-by-layer (LbL) deposition of oppositely charged polyelectrolytes [1–4]. Multilayers can be applied to large substrates by simple dip or spray coating and the non-covalent nature of the underlying interactions allows for a broad spectrum of molecular components [5–8]. Other examples are the physisorption of microgel-particles [9] which can be used as temperature-responsive cell substrates [10] or the adsorption of responsive block-copolymer micellar aggregates [11] for controlled release and cellular response.

Indeed often colloidal building blocks are integrated in such physisorption-layers [12–16], since they carry functions (optical, electronic, catalytic, magnetic properties or responsiveness towards various stimuli), but also because the size of colloidal particles increases the adsorption energy as compared to single (macro-)molecules while still ensuring that interfacial interactions are dominant over inertia or other forces governing the macro-scale. The efficiency of these materials depends on both the physical properties of the colloids and their spatial arrangement on the substrate.

Modification of the colloidal building blocks by grafting polymer chains prior to physisorption is a promising strategy for optimizing these aspects inasmuch as the surface layer moderates the interaction with the substrate independent of the type of particles. Such an approach can be applied to any type of colloids including inorganic and polymer particles. If the packing of the chains is sufficiently dense, *i.e.* the lengths of the chains tethered with one end to the particle must be considerably larger than the distance between two neighboring chains, a polymer brush results [17]. Moreover, if the brush is made from polyelectrolytes, it adds electrosteric stabilization, stimuli-responsiveness and compatibility as well as adhesiveness or non-adhesiveness to particles that could exhibit special optical, mechanical or magnetic features, thus establishing multi-functional building blocks [18–21]. Because of the spherical geometry of the colloidal support, such particles are denoted as “spherical polyelectrolyte brushes” (SPB). The core–shell morphology of SPB is schematically depicted in Fig. 1A.

The properties of SPB in solution are widely determined by the confinement of the counterions of the polyelectrolyte chains. Approximately 95% of the counterions of the polyelectrolyte chains are trapped within the brush at low concentrations of added salt [22]. This creates a huge osmotic pressure resulting in a marked stretching of the polyelectrolytes [23,24]. The responsiveness of the SPB towards external stimuli such as the ionic strength and pH allows precise control over the spatial dimensions of the particles and their mutual interaction [25–28].

Functionalization of the core–shell colloids can be accomplished by loading the core with hydrophobic substances, including many drugs. Moreover, the surrounding brush layer may serve as a carrier for active nanostructures, namely for metal nanoparticles, enzymes and conductive polymers yielding functional colloids with tailored biological, catalytic or electronic properties [29–32]. This opens up avenues for multi-functional responsive mesoscopic building units that are stable against coagulation and can be easily handled [33].

Understanding the interaction of SPB with solid substrates is a prerequisite for their technological application in functional coatings. Studies with mica surfaces demonstrated distinct differences in the adsorption behavior of cationic and anionic SPB [34, 35]. While anionic SPB exhibited a high lateral mobility on the negative substrates and

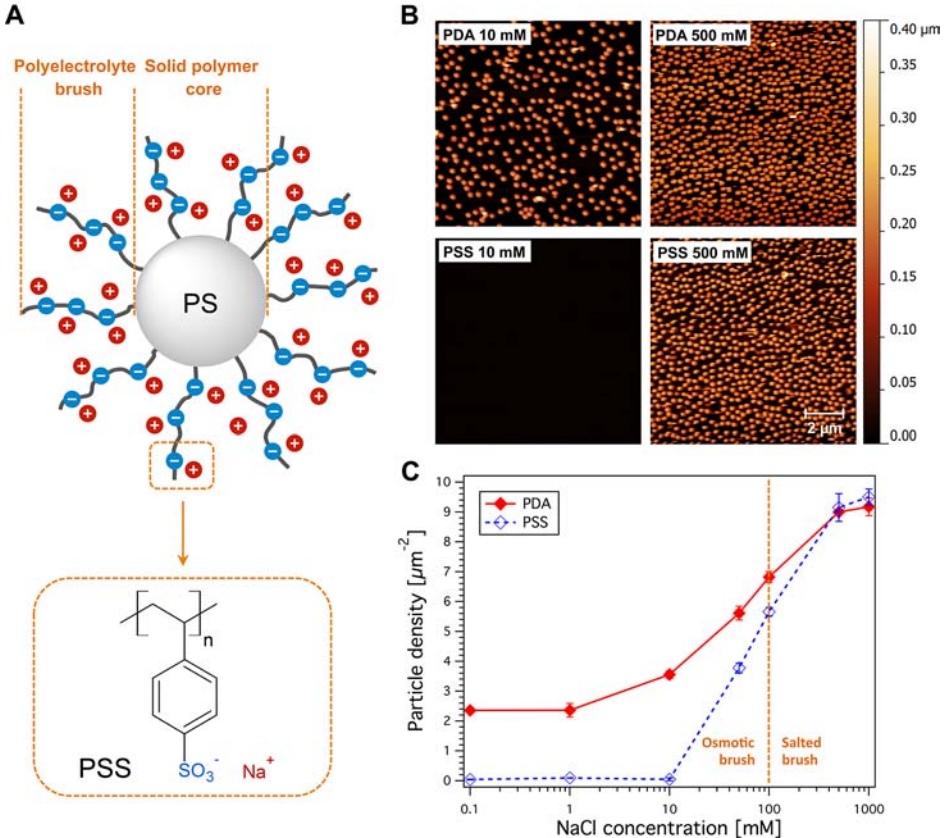


Fig. 1. Influence of substrate charge and ionic strength on SPB adsorption. For this study anionic SPB consisting of a PS core and attached PSS chains were used (A). Before drying, the films exhibit a liquid-like particle ordering indicating a random adsorption process (B). At 10 mM of added salt the particles bind only to oppositely charged surfaces, whereas particle deposition at 500 mM results in a high surface coverage on both types of substrates. The equilibrium particle density plotted against the ionic strength shows that the loss of substrate selectivity coincides with the transition from the osmotic to the salted brush regime near 100 mM (C).

formed hexagonally packed arrangements during drying, cationic SPB were strongly affixed to the surface resulting in network-like structures. Recently, we investigated SPB adsorption onto polyelectrolyte multilayers focusing on the kinetics [36]. We found that after an initial diffusion-limited stage SPB adsorption slows down and finally ceases with the formation of a particle monolayer.

In this work we investigate the interaction of anionic SPB and polyelectrolyte multilayers consisting of polystyrene sulfonate (PSS) and poly(diallyldimethylammonium chloride) (PDA). In addition to adsorption studies covering a wide range of ionic strengths [36], we present a direct assessment of the force of adhesion *via* atomic force microscopy (AFM). We utilize the colloidal probe (CP) technique, in which force-distance curves are recorded with an AFM cantilever bearing a micrometer-sized

spherical particle [37]. This method was developed independently by Butt and Ducker and allows a normalization of the measured forces over the contact area by the Derjaguin approximation [38,39]. Another advantage of CP-AFM is the possibility to use functionalized particles and measure the interaction between arbitrary surfaces including polyelectrolyte brushes [40–43]. Building upon the synthetic route to submicron SPB originally developed by Ballauff and co-workers [24,25], we attach PSS chains to micrometer-sized polystyrene particles. These SPB microparticles are then used to measure the interaction of SPB with charged surfaces. Finally, we demonstrate that under appropriate deposition conditions SPB can be arranged into well-defined arrays on charge patterned substrates. For this purpose we utilize microcontact printing, which is a prominent technique to facilitate surface patterning and guided adsorption [44–46].

2. Experimental section

2.1 Materials

Styrene was passed through a catechol inhibitor remover column before use. Irgacure 2959 was kindly supplied by Ciba Specialty Chemicals and transferred into the copolymerizable photoinitiator (HMEM) by a Schotten-Baumann reaction of Irgacure 2959 and methacrylic acid hydrochloride along the lines given in Ref. [24]. Purification was accomplished by column chromatography on silica gel. The purity of the product was verified through NMR spectroscopy (AC 250, Bruker). Deionized water obtained from a reverse osmosis water purification system (Millipore Academic A10) was used throughout the entire studies. All latexes were purified by exhaustive ultrafiltration against deionized water. The other chemicals and solvents were of analytical grade and were used as received.

2.2 Nanoparticles synthesis

The synthesis and characterization of submicron SPB following the approach of Ballauff and coworkers are described in Ref. [47]. Briefly, polystyrene cores bearing covalently anchored photoinitiator moieties were produced by soap-free emulsion polymerization in the presence of a UV sensitive comonomer. From the particle surfaces PSS chains were grafted by UV induced polymerization of sodium styrene sulfonate. The PS cores display a narrow size distribution with an average radius of 126 ± 2 nm as measured by dynamic light scattering (DLS). The hydrodynamic thickness of the PSS brush is 74 ± 3 nm in deionized water. The PSS chains were cleaved from the PS cores and analyzed by size exclusion chromatography. The molecular weight of the longest PSS chains that govern the spatial extension of the brush layer was determined as $67\,600 \pm 4950$ g/mol, which corresponds to a contour length of 82 ± 6 nm [47]. The polydispersity of the chains (weight averaged molecular weight by number averaged molecular weight) was calculated as 2.1, which is a common value for polymers prepared by free radical polymerization. The chain grafting density is 0.03 ± 0.01 chains per nm^2 [47].

2.3 Microparticles synthesis

PSS brushes were grafted from monodisperse cross-linked PS microparticles with a diameter of 4.8 μm (SX-500 H) which were kindly supplied from Soken Chemical & Engineering Co.

The photoinitiator layer surrounding the microparticles was formed in a seeded growth polymerization. Briefly, 15 g of the microparticle powder was dissolved in 14 g ethanol yielding a homogeneous suspension after sonication for 2 min. 143 g deionized water was added dropwise under continuous stirring followed by further sonication to minimize agglomeration. The PS seeds were swollen with 1.13 g styrene (injection rate 0.02 g/ml) and stirred for a period of 15 h at 130 rpm. The polymerization was performed at 70 °C under a nitrogen atmosphere and continuous stirring (300 rpm). To initiate the reaction, 0.284 g potassium persulfate was added. After 15 min, 2.098 g of a 69.6 wt % solution of the copolymerizable photoinitiator HMEM in acetone was injected into the suspension (rate 0.05 g/min). The reaction was allowed to proceed for 2 h. The microparticles were isolated from the dispersant, redispersed in ethanol and stored in a 1 : 1 ethanol-water mixture for further use.

Grafting of the polyelectrolyte brushes was carried out in a closed reaction chamber containing a UV emitter with a focusable reflector (Hoenle UV Technology UV-F 400 F). An iron doped metal halogenide lamp with a power of 400 W was used in combination with a blue filter (transmission window: 320–450 nm). 44 mg of sodium styrene sulfonate was added to suspensions of 217 mg photoinitiator-coated microparticles dispersed in 4.8 g of a 1 : 1 ethanol-water solution. The reaction mixtures were irradiated with UV for 30 min at r.t. under permanent stirring. Purification of the suspension was accomplished by exhaustive ultrafiltration against deionized water.

2.4 Polyelectrolyte solutions

All polyelectrolytes were used as aqueous solutions containing 1 g/l and varying amounts of NaCl (99.88%, Fisher Scientific). Multilayer coatings were produced with the following polyelectrolytes (Aldrich): PEI (poly(ethylene imine), MW = 25 000 g/mol), PSS (poly(sodium-4-styrene sulfonate), MW = 70 000 g/mol, 50 mM NaCl), PDA (poly(diallyldimethylammonium chloride), MW = 100 000–200 000 g/mol, 50 mM NaCl). For microcontact printing we used fluorescently labeled PDA-TRITC (Surflay, MW = 70 000 g/mol, 500 mM NaCl).

2.5 Substrate preparation

Glass slides and silicon wafers were cut into pieces of 10 mm × 25 mm and cleaned by the RCA method using analytical grade chemicals (2-propanol, NH₃, H₂O₂ from VWR) [48]. Functionalization of the wafers with 3-aminopropyltrimethoxysilane (97%, Sigma Aldrich) was achieved by vapor phase silanization under reduced pressure (10 mbar, 24 h) followed by rinsing with EtOH (VWR) to remove excess molecules.

Prior to the multilayer coating the substrates were immersed in PEI solution for 30 min to deposit an adhesion promoting layer. The build-up of (PSS/PDA)₅ and (PSS/PDA)_{5,5} multilayers by spray coating followed the procedure reported in Ref. [5].

Multilayers terminated with PSS were charged patterned by microcontact printing of PDA-TRITC following established protocols [49,50]. For this purpose we used polydimethylsiloxane (PDMS) stamps cast from lithographically patterned silicon masters.

On homogeneous substrates SPB were deposited by immersion in suspensions of varying ionic strength (0.1 mM to 1 M, 0.1 wt % particles) for 60 min. Deposition of SPB on charge patterned surfaces was facilitated by drop casting in a humidified desiccator. The suspensions contained 0.1 wt % particles and NaCl concentrations of 1 mM and 100 mM respectively and were left on the substrates for at least 24 h. Before drying, the non-adsorbed particles were removed by thorough washing. In-situ AFM imaging of wet samples showed that the amount of adsorbed particles did not change during this step.

2.6 AFM imaging

Imaging of the SPB assemblies was performed with a Nanowizard I AFM (JPK Instruments) operating in the Intermittent Contact Mode. We used soft cantilevers (0.15 N/m, 12 kHz, CSC-17, MikroMasch Estonia) for in-situ imaging and stiff cantilevers (42 N/m, 300 kHz, OMCL-AC160TS-W2, Olympus) for imaging in air. To estimate the surface coverage in dependence on the ionic strength $100 \mu\text{m}^2$ scans were recorded on at least three positions per sample using a Dimension IIIa AFM (Bruker). The particle density was determined by the automated counting procedure implemented in ImageJ.

2.7 Force spectroscopy

The colloidal particles were attached to calibrated, tipless AFM cantilevers (NSC12, Mikromasch) using a commercial epoxy glue (UHU Endfest 300) and a micromanipulator. The force constants as detected by the thermal noise method [37] ranged from 0.25 N/m to 0.7 N/m. Force-distance curves were recorded in liquid using a Nanowizard I AFM. All solutions were adjusted to pH 4 with HCl (Grüssing). Salt concentrations of 1 mM and 100 mM were obtained by addition of NaCl.

2.8 Electrophoretic mobility measurements

Double-layer potential measurements of the microparticles were performed with a ZETAVIEW laser scattering video microscope (Particle Metrix GmbH). From the electrophoretic mobilities determined by the implemented image analysis algorithm, zeta potential values were calculated using the Smoluchowski equation [51]. All samples were strongly diluted in 1 mM NaCl solution. Their pH was adjusted by addition of HCl.

2.9 Field emission scanning electron microscopy (FESEM)

FESEM specimen were prepared by drying one drop of a highly diluted suspension on a clean silicon wafer (CrysTec) at room temperature and coating with a platinum layer

of 2 nm thickness using a sputter coater (Cressington 208HR) to make the specimen conductive. Micrographs were recorded on a LEO Gemini microscope (Zeiss) equipped with a field emission cathode operating at 3–5 kV, which corresponds to a lateral resolution of 2 nm.

2.10 Cryogenic transmission electron microscopy (cryo-TEM)

Cryo-TEM sample were contrast enhanced in accordance to Ref. [52] by counterion exchange with CsCl and subsequent adsorption of bovine serum albumin (BSA). The SPB suspension was spread on a hydrophilized lacey carbon TEM grid (mesh size 200, Plano GmbH) and vitrified with liquid ethane. Imaging was performed with a Zeiss EM922 OMEGA EFTEM (Zeiss NTS GmbH) at a temperature of 90 K and an acceleration voltage of 200 kV.

2.11 Differential centrifugal sedimentation (DCS)

The average size of the microparticles and their size distribution were measured using an analytical disc centrifuge (CPS Instruments CPS-24000) [53]. Within a hollow disc rotating at 5050 rpm a gradient was prepared by layering eight sucrose solutions of decreasing density (8 to 3 wt %) upon one another. 0.1 ml of a dilute suspension of microparticles was placed on top of the gradient. The distribution of the microparticles was obtained by measuring the time required for the different species to reach a known position within the gradient. The concentration at this position and time was measured by light absorption at 405 nm.

3. Results and discussion

Analysis of the adsorption behavior is an established methodology for investigating the interaction between particles and solid interfaces. Both the adsorption kinetics and the final surface coverage provide insights in this respect. In a recent study we found that SPB adsorption kinetics is diffusion-limited in the low surface coverage regime. After extended adsorption times the process runs into a jamming limit which always results in the formation of a SPB monolayer [36].

The saturation coverage of adsorbed SPB depends on both the surface charge and the ionic strength in solution. Figure 1B shows layers formed by the adsorption of particles carrying a PSS brush onto PDA and PSS terminated multilayers. While the SPB adsorb exclusively on the oppositely charged surface at low ionic strength, selectivity vanishes at high concentrations of added salt. The AFM images were recorded *in-situ* directly after excess particles had been removed by gentle washing. In the absence of attractive capillary forces a liquid-like ordering is preserved, indicating a random sequential adsorption of SPB. Obviously, the characteristic interparticle distance is strongly reduced by the addition of salt, which induces screening of the repulsive electrostatic interaction between the SPB. In Fig. 1C the saturation surface coverage on both oppositely and like-charged substrates is plotted as a function of the ionic strength. On PDA the surface coverage increases monotonically with the ionic strength, whereas

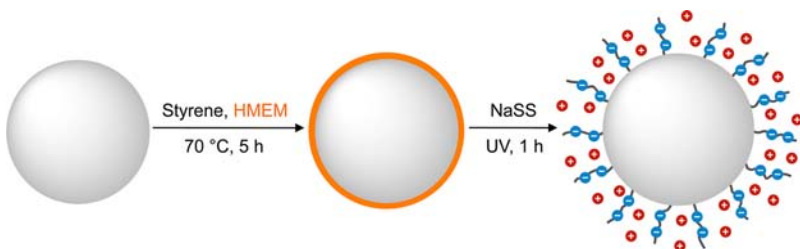


Fig. 2. Synthesis of micrometer-sized SPB: Microparticles bearing photocleavable groups at their surface were prepared by seeded growth polymerization of styrene and the polymerizable photoinitiator HMEM onto narrowly dispersed polystyrene seeds. Sodium styrene sulfonate (NaSS) was added and the suspension was irradiated by UV light. Covalently bound surface radicals thus generated initiated the polymerization of the water-soluble monomer resulting in polyelectrolyte brushes attached to the microparticles.

virtually no adsorption is observed on PSS terminated substrates below 10 mM of added salt. Even higher salt concentrations lead to a gradual loss of the substrate selectivity. Matching surface coverage on both oppositely and like-charged substrates is found at salt concentrations above 100 mM. Interestingly, this value corresponds to the transition from the osmotic brush to the salted brush regime, which is known to have also a pronounced influence on the binding of proteins to SPB [54,55].

It is reasonable to assume that electrosteric forces dominate the interaction between SPB and charged surfaces in the osmotic brush regime. At low ionic strength SPB attachment to oppositely charged substrates is entropically favored due to counterion release, whereas electrostatic and steric repulsion suppress adsorption onto like-charged surfaces. In the salted brush regime, the polyelectrolyte corona is strongly collapsed due to screening rendering electrosteric interactions insignificant. Instead, attractive forces such as van der Waals or hydrophobic interactions become dominant facilitating SPB adsorption independent of the substrate type.

To assess the forces governing the interaction of SPB with charged surfaces directly, we chose the colloidal probe technique, where single colloidal particles are attached to AFM cantilevers. Due to the well-defined geometry a normalization of the measured force data by the Derjaguin approximation is possible. In order to perform such experiments, it was fundamental to modify micrometer-sized particles of suitable dimensions to be used as colloidal probes by grafting polyelectrolyte brushes. For this purpose, we selected cross-linked polystyrene microparticles, which were supplied from Soken Chemical & Engineering Co.. Measurements of the distribution of the particle diameters by differential centrifugal sedimentation showed that the particles are narrowly dispersed with an average diameter of 4.8 μm . Their polydispersity defined as the weight-averaged diameter divided by the number-averaged diameter is as low as 1.001. Moreover, scanning electron micrographs revealed that the particles exhibit a uniform spherical shape with a smooth surface, which was essential to obtain a well-defined core–shell morphology after grafting the polyelectrolyte brush.

As illustrated in Fig. 2 the surface modification was carried out in two steps, beginning with coating the microparticles with a thin layer of photoinitiator. In the second step, surface-bound radicals, formed upon irradiation with UV light, initiated

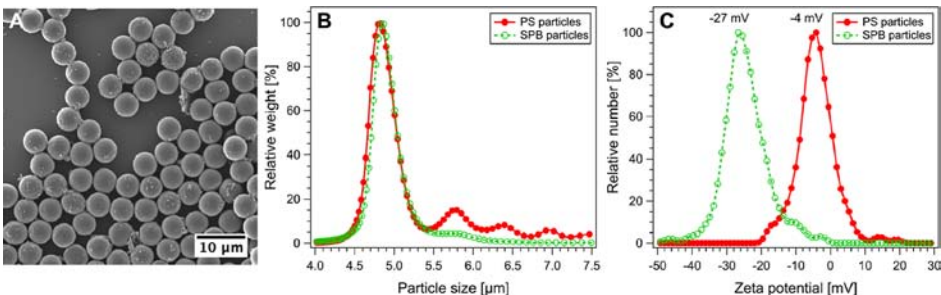


Fig. 3. Characterization of SPB microparticles. Size and shape of the microparticles are preserved during grafting of the brushes (A). In comparison to the PS seeds the brush decorated SPB microparticles show a significantly reduced amount of aggregates in differential centrifugal sedimentation measurements (B). The zeta potential at pH 4 is clearly shifted to more negative values due to the grafted PSS chains (C).

the polymerization of the water-soluble monomer sodium styrene sulfonate resulting in covalently attached polyelectrolyte brushes. This method is well-established for the synthesis of SPB with submicron dimensions [24,56], but has to the best of our knowledge not been adapted to larger particles. While the general concept is similar to the one developed by Ballauff and co-workers for nanoparticles, special attention had to be paid to prevent aggregation of the micrometer-sized particles until the brush layer could add electrosteric stabilization.

Careful preparation was necessary to obtain homogeneous suspensions of the microparticles. For this purpose, the particles that were supplied as a freeze-dried powder were at first suspended in ethanol before an aliquot of water was added dropwise. Homogenization was accomplished by sonication. The photoinitiator layer was generated by swelling the cross-linked micrometer-sized seeds with a defined amount of styrene and then initiating the polymerization by addition of potassium persulfate. A water-soluble initiator was chosen to facilitate the polymerization at the surface of the particles. After a time given to form a “fresh” layer of polystyrene, a polymerizable photoinitiator was added under starved conditions resulting in a copolymer shell on the seeds. It has to be noted that the microparticles kept their uniform spherical shape during the polymerization as corroborated by electron micrographs (Fig. 3A). This finding is not trivial, because given appropriate experimental conditions seeded growth polymerization from cross-linked particles can be used to prepare particles that exhibit defined anisotropic shapes, e.g. dumbbell-shaped particles [57,58]. In the final step, the water soluble monomer sodium styrene sulfonate was added and the suspension of the modified microparticles bearing covalently attached photoinitiator moieties at their surface was irradiated by UV light in a closed reaction chamber. As shown in earlier studies, multiple elastic scattering of the UV light within the turbid suspension enables the decomposition of the surface-bound photoinitiator. These radicals initiate the polymerization of the water-soluble monomer resulting in polyelectrolyte brushes covalently attached to the particles [24,56]. The decomposition of the applied photoinitiator results both in surface-bound radicals and free radicals in solution. The free polyelectrolyte chains in solution thus formed were removed by ultrafiltration against water.

Manifold analytical techniques such as small-angle X-ray scattering [59], dynamic light scattering [24], cryogenic transmission electron microscopy [52] and electrophoretic measurements [60] have been used to comprehensively investigate the core-shell character of submicrometer-sized SPB. While such techniques are well-suited to study submicrometer-sized particles, they can be hardly applied on microscale objects. In order to estimate the brush thickness, a reference experiment with PS seeds of 169 nm in diameter was carried out in parallel to the photopolymerization onto the microscale seeds in the UV chamber. A brush thickness of 30 nm was obtained by DLS measurements of the hydrodynamic radii before and after the photopolymerization. As a first indication that a brush layer also formed on the microparticles may serve their significantly enhanced stability when dispersed in water. This was already evident from visual inspection. While the unmodified core particles showed rapid sedimentation in water and had thus to be kept in water/ethanol mixtures during surface modification, sedimentation of the brush coated microparticles proceeded much slower. This observation was quantitatively corroborated when measuring the size distribution of the particles by DCS (Fig. 3B). Considerable amounts of particle dimers, trimers and tetramers were found in freshly prepared aqueous suspensions of the PS seeds, which is in accord with their high sedimentation rate. Only a small portion of dimer ensembles are found after modification of the microparticles indicating the stabilization effected by the surrounding polyelectrolyte layer. This is further documented by optical measurements of the electrophoretic mobilities of individual microparticles before and after grafting the surface layer. The experiments were carried out at pH 4 to exclude the influence of the carboxylic groups of the PS seeds on the mobility. Calculations of zeta potentials for hairy particles from electrophoretic mobilities are non-trivial [61]. In contrast to submicrometer-sized SPB, the influence of a 30 nm thick surface layer on the mobility of the 4.8 μm SPB microparticles can be widely restricted to the effective charge of the particles. For this reasons, zeta potentials were calculated based on the Smoluchowski equation [51]. The low zeta potential of -4 mV of the PS seeds is in full accord with the modest stability of aqueous suspensions of these particles. There was a significant increase of the absolute value of the zeta potential (-27 mV) after the photopolymerization again indicating the successful formation of the polyelectrolyte layer and the improved stability of the suspensions.

While the standard characterization methods all indicate a successful modification of the PS microparticles, they reflect the averaged properties of a large ensemble of particles. To investigate the single particles by CP-AFM we attached PS core particles and PSS modified particles to tipless cantilevers. In analogy to the zeta potential measurements all AFM experiments were conducted at pH 4 to screen contributions stemming from the carboxyl moieties of the core particles. Figure 4A,B displays typical force-distance curves obtained on amino-functionalized Si wafers, which carry a positive net charge under acidic conditions. Independent of the ionic strength the PS core particles show a hard repulsive interaction without noticeable adhesion upon retraction. Retract curves of the modified particles on the other hand display a strongly adhesive interaction most pronounced at low ionic strength. Despite the fact that SPB adsorption is promoted by the addition of salt, electrostatic screening results in significantly decreased binding strengths. Similar trends apply to PDA terminated polyelectrolyte multilayers as substrates with the qualitative difference that we often observe a less

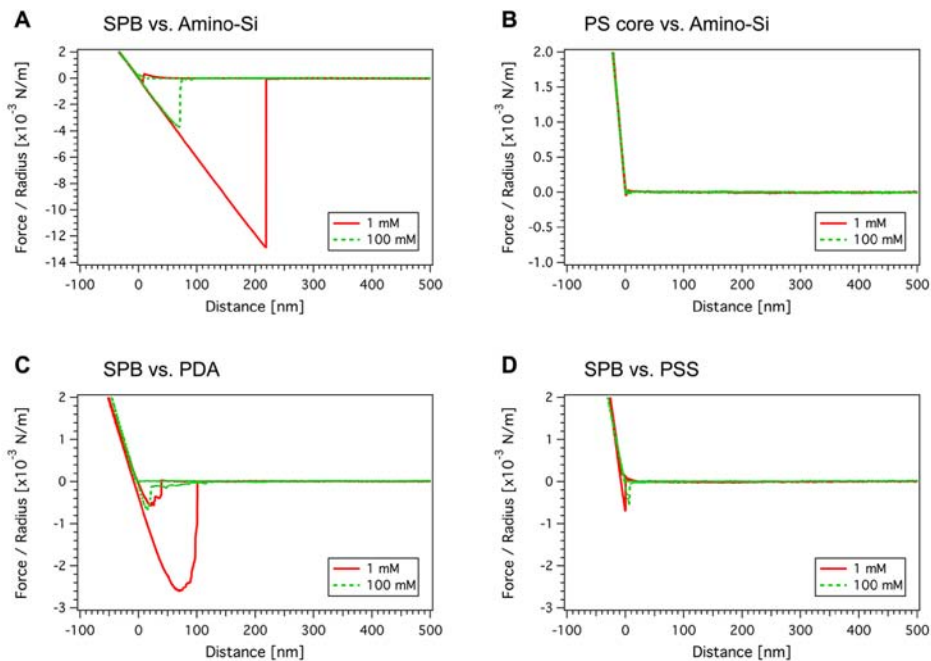


Fig. 4. Force curves of PS microparticles and SPB microparticles. While the SPB microparticle shows strong adhesion to the oppositely charged, amino-functionalized substrate (A), little adhesion is found for the PS reference particle (B). The strength of the attractive interaction can be controlled by the ionic strength and the charge of the substrate as shown for PDA (C) and PSS (D) terminated multilayers. All data was obtained at pH 4.

rapid, stepwise detachment upon retraction of the cantilever (Fig. 4C). Measurements in the presence of PSS terminated multilayers (Fig. 4D) on the other hand displayed small forces of adhesion, which were independent of the ionic strength and can be attributed to secondary interactions and chain entanglements [62].

We have to note that only about half of the probed SPB microparticles showed significant differences from the bare PS cores indicating an incomplete conversion during photopolymerization. Also with an increasing number of measurements the force of adhesion decreased steadily indicating that PSS chains are partially torn out of the brush. Considering the charged surface as a multivalent counterion very strong binding is expected [35]. In our measurements the retract speeds (500 nm/s) were rather high possibly preventing a stepwise detachment of single charged polymer groups. Whereas more quantitative investigations will have to take these aspects into account, we were primarily interested in a qualitative assessment of the strength of SPB adhesion at high and low ionic strengths.

Both the adsorption study and the single particle study demonstrated the pronounced substrate selectivity of SPB, which is a prerequisite for the construction of SPB surface assemblies on charge patterned substrates. To create substrates with well-defined positive and negative regions we printed labeled PDA-TRITC onto PSS termi-

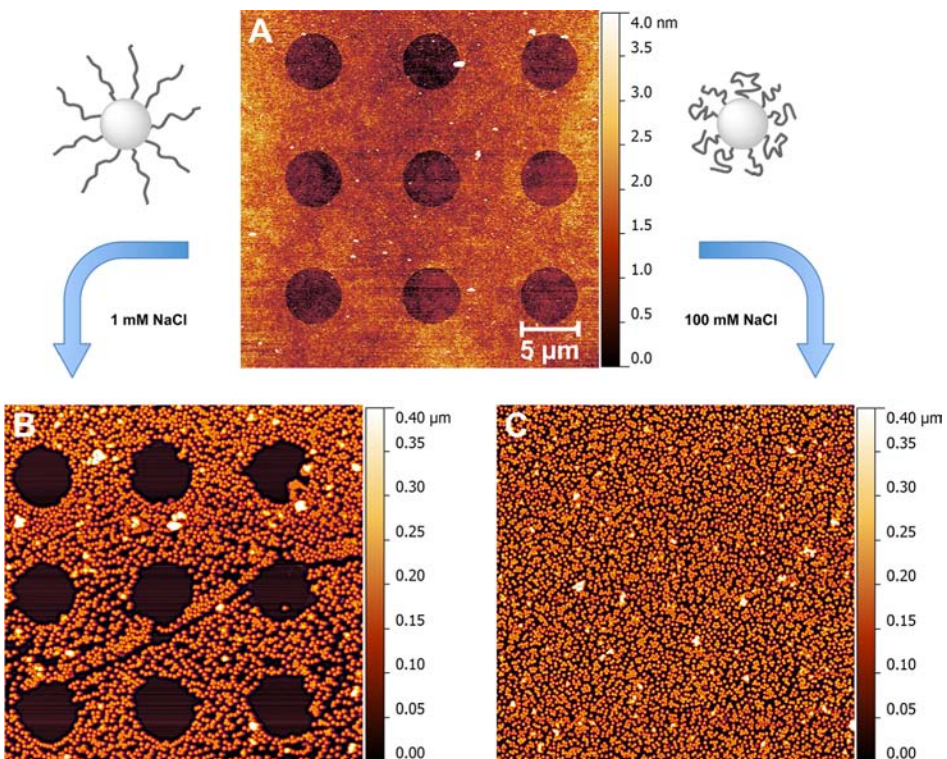


Fig. 5. SPB adsorption onto charge patterned substrates. The AFM image shows negatively charged areas as dark circles surrounded by a positively charged matrix (A). At low ionic strength the particles adsorb selectively onto the oppositely charged regions (B). Substrate selectivity is completely suppressed at high concentrations of added salt (C).

nated multilayers using hydrophilized PDMS stamps. Successful pattern reproduction was proven by fluorescence microscopy and AFM imaging. A typical microcontact print consisting of negative circles and a surrounding positive matrix is displayed in Fig. 5A. Onto the patterned region we applied droplets of SPB suspensions containing 1 mM and 100 mM of NaCl. These samples were stored in a humidified desiccator for at least 24 h before washing with water and drying in a nitrogen stream. As shown in Fig. 5B the SPB adsorbed only onto oppositely charged areas at low ionic strength leading to excellent pattern reproduction. Increasing the ionic strength to 100 mM on the other hand resulted in a complete loss of substrate selectivity (Fig. 5C). As confirmed by fluorescence microscopy the pattern fidelity was unaffected by the deposition process. The observed non-selectivity can therefore be attributed to attractive secondary interactions, such as van der Waals forces or hydrophobic interaction, dominating the SPB adsorption in the salted brush regime.

As further demonstrated in Fig. 6, charge patterning is a powerful tool for controlling surface order as well as the patterning of sub-micrometer SPB on the micrometer scale and even up to macroscopic dimensions.

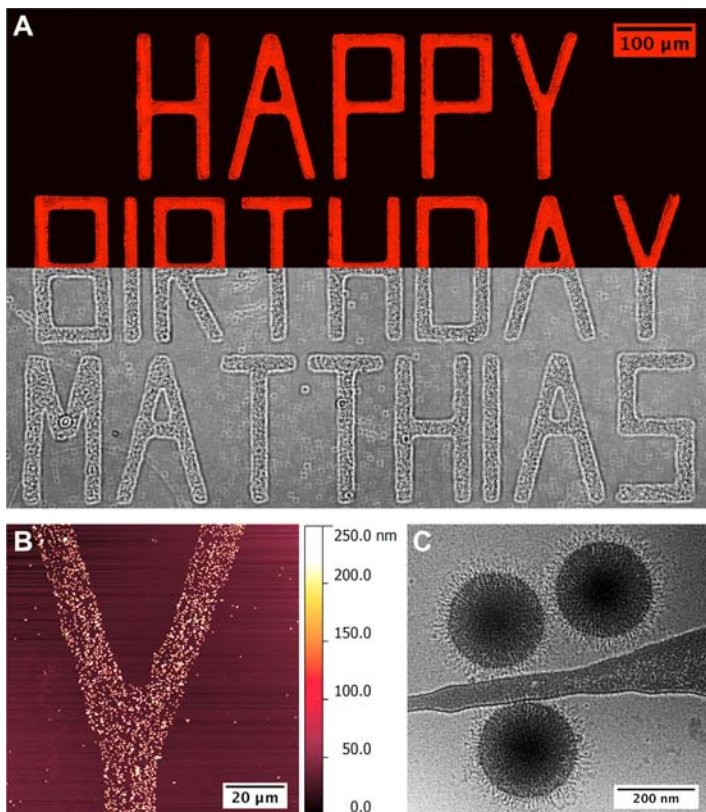


Fig. 6. Hierarchical structuring by selective SPB adsorption: Millimeter-sized patterned areas were produced by microcontact printing with a custom PDMS stamp (top: fluorescence image, bottom: phase contrast micrograph after SPB deposition) (A). Micron-sized particle arrays are formed upon the adsorption of SPB (AFM) (B). The Cryo-TEM image of individual SPB contrasted by the adsorption of bovine serum albumin demonstrates the core-shell architecture (C).

4. Conclusions

We investigated the interaction of spherical polyelectrolyte brushes with charged surfaces. Particle monolayers prepared by SPB adsorption onto positively and negatively charged polyelectrolyte multilayers showed a distinct dependence of the surface coverage on the concentration of added NaCl. The particles adsorbed exclusively onto oppositely charged surfaces at ionic strengths up to 10 mM, whereas higher salt concentrations resulted in a gradual loss of substrate selectivity. While counterion release and electrosteric repulsion govern the interaction between SPB and charged surfaces in the osmotic brush regime, attractive secondary interactions become dominant in the salted brush regime.

The strength of the interaction forces can be assessed on a single particle level by colloidal probe AFM. For this purpose we equipped cross-linked polystyrene mi-

croparticles with UV sensitive moieties and grafted chains of polystyrene sulfonate from the particle surfaces. This modification lead to significantly enhanced colloidal stability in water. Further, the PSS grafted microparticles displayed a strongly negative zeta potential even under acidic conditions, where the bare core particles carrying only carboxyl groups are mostly neutral. In analogous single particle AFM measurements the presence of grafted PSS chains resulted in a massively altered interaction with positively charged surfaces. Whereas the bare cores show no attraction towards the substrate under acidic conditions, the modified particles adhere strongly. The force of adhesion can be regulated *via* the ionic strength in the surrounding medium.

Further, we used charge patterned substrates produced by polymer-on-polymer stamping to arrange SPB into patterned arrays. As expected from the experiments with homogenous surfaces site-selective SPB attachment occurred only at low ionic strength. While this has been demonstrated with hard particles [45], the stimuli-responsive nature of the brush layer avoids an irreversible hit-stick behavior and could therefore allow us to remove structural defects by annealing. Considering the numerous chemical modifications which have been reported for SPB [29,33,63], our study opens exiting avenues for the production of stimuli-responsive materials with a hierarchical internal organization.

Figure 6 shows a particular example of such a hierarchical structure containing two levels of hierarchy: the internal core–shell character of the particles and their positional order on the printed micropattern. As one can clearly see, completely novel functionalities arise, like the use of nanoparticles for communication, which brings us to the main aim of this manuscript:

Lieber Matthias, wir wünschen Dir alles Gute zu Deinem Geburtstag! Es ist uns eine Freude und ein Privileg mit diesem Manuskript einen wissenschaftlichen Beitrag zu Deiner Geburtstagsfeier leisten zu können! Herzliche Gratulation!

Acknowledgement

This work has been conducted within the special collaborative research project SFB 840 (project B5) and was funded by the German Science Foundation (DFG). The authors would like to acknowledge Carmen Kunert and Dr. Simone Wagner for FESEM imaging as well as Dr. Markus Drechsler for cryo-TEM imaging. We also thank Nicolas Helfricht for his assistance with the colloidal probe preparations.

References

1. G. Decher, *Science* **277** (1997) 1232.
2. G. Decher, J. D. Hong, and J. Schmitt, *Thin Solid Films* **210** (1992) 831.
3. S. T. Dubas and J. B. Schlenoff, *Macromolecules* **32** (1999) 8153.
4. D. Yoo, S. S. Shiratori, and M. F. Rubner, *Macromolecules* **31** (1998) 4309.
5. A. Izquierdo, S. S. Ono, J.-C. Voegel, P. Schaaf, and G. Decher, *Langmuir* **21** (2005) 7558.
6. C. H. Porcel, A. Izquierdo, V. Ball, G. Decher, J.-C. Voegel, and P. Schaaf, *Langmuir* **21** (2005) 800.
7. J. B. Schlenoff, S. T. Dubas, and T. Farhat, *Langmuir* **16** (2000) 9968.

8. J. E. Wong, H. Zastrow, W. Jaeger, and R. von Klitzing, *Langmuir* **25** (2009) 14061.
9. S. Schmidt, H. Motschmann, T. Hellweg, and R. von Klitzing, *Polymer* **49** (2008) 749.
10. S. Schmidt, M. Zeiser, T. Hellweg, C. Duschl, A. Fery, and H. Möhwald, *Adv. Funct. Mater.* **20** (2010) 3235.
11. J. Gensel, T. Borke, N. Pazos-Pérez, A. Fery, D. V. Andreeva, E. Betthausen, A. H. E. Müller, H. Möhwald, and E. V. Skorb, *Adv. Mater.* **24** (2012) 985.
12. O. D. Velev and S. Gupta, *Adv. Mater.* **21** (2009) 1897.
13. Y. Xia, B. Gates, Y. Yin, and Y. Lu, *Adv. Mater.* **12** (2000) 693.
14. W. S. Tan, Z. Zhu, S. A. Sukhishvili, M. F. Rubner, and R. E. Cohen, *Macromolecules* **44** (2011) 7767.
15. C. H. Lu, H. Möhwald, and A. Fery, *Soft Matter* **3** (2007) 1530.
16. A. Schweikart, N. Pazos-Pérez, R. A. Alvarez-Puebla, and A. Fery, *Soft Matter* **7** (2011) 4093.
17. S. T. Milner, *Science* **251** (1991) 905.
18. M. Ballauff and O. Borisov, *Curr. Opin. Colloid Interface Sci.* **11** (2006) 316.
19. M. A. C. Stuart, W. T. S. Huck, J. Genzer, M. Müller, C. Ober, M. Stamm, G. B. Sukhorukov, I. Szleifer, V. V. Tsukruk, M. Urban, F. Winnik, S. Zauscher, I. Luzinov, and S. Minko, *Nat. Mater.* **9** (2010) 101.
20. M. Biesalski, D. Johannsmann, and J. Rühe, *J. Chem. Phys.* **117** (2002) 4988.
21. T. Chen, R. Ferris, J. M. Zhang, R. Ducker, and S. Zauscher, *Prog. Polym. Sci.* **35** (2010) 94.
22. G. Lagaly (Ed.), *Molecular Organisation on Interfaces*, Springer Berlin/Heidelberg (2002), p. 34.
23. A. Jusufi, C. N. Likos, and M. Ballauff, *Colloid Polym. Sci.* **282** (2004) 910.
24. X. Guo and M. Ballauff, *Langmuir* **16** (2000) 8719.
25. X. Guo and M. Ballauff, *Phys. Rev. E* **64** (2001) 051406.
26. Y. Mei, K. Lauterbach, M. Hoffmann, O. V. Borisov, M. Ballauff, and A. Jusufi, *Phys. Rev. Lett.* **97** (2006) 158301.
27. G. Dominguez-Espinoza, A. Synytska, A. Drechsler, C. Gutsche, K. Kegler, P. Uhlmann, M. Stamm, and F. Kremer, *Polymer* **49** (2008) 4802.
28. C. Gutsche, M. M. Elmahdy, K. Kegler, I. Semenov, T. Stangner, O. Otto, O. Ueberschär, U. F. Keyser, M. Krueger, M. Rauscher, R. Weeber, J. Harting, Y. W. Kim, V. Lobaskin, R. R. Netz, and F. Kremer, *J. Phys.-Condens. Matter* **23** (2011) 17.
29. A. N. Korovin, V. G. Sergeyev, O. A. Pyshkina, C. Hanske, A. Fery, A. Wittemann, and L. Tsarkova, *Macromol. Rapid Commun.* **32** (2011) 462.
30. M. Schrinner, M. Ballauff, Y. Talmon, Y. Kauffmann, J. Thun, M. Möller, and J. Breu, *Science* **323** (2009) 617.
31. A. Wittemann and M. Ballauff, *Phys. Chem. Chem. Phys.* **8** (2006) 5269.
32. F. Schacher, E. Betthausen, A. Walther, H. Schmalz, D. V. Pergushov, and A. H. E. Müller, *AC Nano* **3** (2009) 2095.
33. Y. Lu, A. Wittemann, and M. Ballauff, *Macromol. Rapid Commun.* **30** (2009) 806.
34. H. Gliemann, Y. Mei, M. Ballauff, and T. Schimmel, *Langmuir* **22** (2006) 7254.
35. Y. Mei, A. Wittemann, G. Sharma, M. Ballauff, T. Koch, H. Gliemann, J. Horbach, and T. Schimmel, *Macromolecules* **36** (2003) 3452.
36. C. Hanske, C. Schneider, M. Drechsler, A. Wittemann, and A. Fery, *Phys. Chem. Chem. Phys.* **14** (2012) 4196.
37. H.-J. Butt, B. Capella, and M. Kappl, *Surf. Sci. Rep.* **59** (2005) 1.
38. H.-J. Butt, *Biophys. J.* **60** (1991) 1438.
39. W. A. Ducker, T. J. Senden, and R. M. Pashley, *Nature* **353** (1991) 239.
40. E. Spruijt, M. A. Cohen Stuart, and J. van der Gucht, *Macromolecules* **43** (2010) 1543.
41. J. Bünsow, J. Erath, P. M. Biesheuvel, A. Fery, and W. T. S. Huck, *Angew. Chem.-Int. Ed.* **50** (2011) 9629.
42. S. Block and C. A. Helm, *Macromolecules* **42** (2009) 6733.
43. V. Bosio, F. Dubreuil, G. Bogdanovic, and A. Fery, *Colloid Surf. A-Physicochem. Eng. Asp.* **243** (2004) 147.
44. Q. Chen, G. W. de Groot, H. Schönher, and G. J. Vancso, *Eur. Polym. J.* **47** (2011) 130.
45. H. Zheng, M. F. Rubner, and P. T. Hammond, *Langmuir* **18** (2002) 4505.

46. T. Chen, R. Jordan, and S. Zauscher, *Small* **7** (2011) 2148.
47. M. Hoffmann, A. Jusufi, C. Schneider, and M. Ballauff, *J. Colloid Interface Sci.* **338** (2009) 566.
48. W. Kern and D. A. Puotinen, *RC. Rev.* **31** (1970) 187.
49. X. P. Jiang, H. P. Zheng, S. Gourdin, and P. T. Hammond, *Langmuir* **18** (2002) 2607.
50. M. Pretzl, A. Schweikart, C. Hanske, A. Chiche, U. Zettl, A. Horn, A. Böker, and A. Fery, *Langmuir* **24** (2008) 12748.
51. M. von Smoluchowski, *Z. Phys. Chem.* **92** (1917) 129.
52. A. Wittemann, M. Drechsler, Y. Talmon, and M. Ballauff, *J. Am. Chem. Soc.* **127** (2005) 9688.
53. D. J. Scott, S. E. Harding, and A. J. Rowe (Eds.), *Analytical Ultracentrifugation: Techniques and Methods*, The Royal Society of Chemistry, Cambridge (2005), p. 270.
54. A. Wittemann, B. Haupt, and M. Ballauff, *Phys. Chem. Chem. Phys.* **5** (2003) 1671.
55. A. Wittemann, B. Haupt, and M. Ballauff, *Z. Phys. Chem.-Int. J. Res. Phys. Chem. Chem. Phys.* **221** (2007) 113.
56. M. Schrinner, B. Haupt, and A. Wittemann, *Chem. Eng. J.* **144** (2008) 138.
57. J.-W. Kim, R. J. Larsen, and D. A. Weitz, *Adv. Mater.* **19** (2007) 2005.
58. E. B. Mock, H. D. Bruyn, B. S. Hawkett, R. G. Gilbert, and C. F. Zukoski, *Langmuir* **22** (2006) 4037.
59. M. Ballauff, *Prog. Polym. Sci.* **32** (2007) 1135.
60. M. L. Jiménez, A. V. Delgado, S. Ahualli, M. Hoffmann, A. Witteman, and M. Ballauff, *Soft Matter* **7** (2011) 3758.
61. H. Ohshima and K. Makino, *Colloids Surf. A* **109** (1996) 71.
62. R. Pericet-Camara, G. Papastavrou, S. H. Behrens, C. A. Helm, and M. Borkovec, *J. Colloid Interface Sci.* **296** (2006) 496.
63. Y. Lu, Y. Mei, R. Walker, M. Ballauff, and M. Drechsler, *Polymer* **47** (2006) 4985.

8 List of Publications

published:

1. Trebbin, M.; Steinhauser, D.; Perlich, J.; Buffet, A.; Roth, S. V.; Zimmermann, W.; Thiele, J.; Förster, S.; *PNAS* **2013**, *110*, 6706–6711.
"Anisotropic particles align perpendicular to the flow direction in narrow microchannels".
2. Pillai, S. K. T.; Kretschmer, W. P.; Denner, C.; Motz, G.; Hund, M.; Fery, A.; Trebbin, M.; Förster, S.; Kempe, R.; *Small* **2012**, *9*, 984–989.
"SiCN nanofibers with a diameter below 100 nm synthesized via concerted block copolymer formation, microphase separation, and crosslinking".
3. Pillai, S. K. T.; Kretschmer, W. P.; Trebbin, M.; Förster, S.; Kempe, R.; *Chem. Eur. J.* **2012**, *18*, 13974–13978.
"Tailored nanostructuring of end-group-functionalized high-density polyethylene synthesized by an efficient catalytic version of Ziegler's 'Aufbaureaktion'".
4. Hanske, C.; Erath, J.; Kühr, C.; Trebbin, M.; Schneider, C.; Wittemann, A.; Fery, A.; *Z. Phys. Chem.* **2012**, *226*, 569–584.
"Adsorption of spherical polyelectrolyte brushes: from interactions to surface patterning".
5. Taheri, S. M.; Fischer, S.; Trebbin, M.; With, S.; Schröder, J. H.; Perlich, J.; Roth, S. V.; Förster, S.; *Soft Matter* **2012**, *8*, 12124.
"Lyotropic phase behavior of polymer-coated iron oxide nanoparticles".
6. Schlicke, H.; Schröder, J. H.; Trebbin, M.; Petrov, A.; Ijeh, M.; Weller, H.; Vossmeyer, T.; *Nanotechnology* **2011**, *22*, 305303.
"Freestanding films of crosslinked gold nanoparticles prepared via layer-by-layer spin-coating".
7. Thiele, J.; Windbergs, M.; Abate, A. R.; Trebbin, M.; Shum, H. C.; Förster, S.; Weitz, D. A.; *Lab Chip* **2011**, *11*, 2362.
"Early development drug formulation on a chip: fabrication of nanoparticles using a microfluidic spray dryer".
8. Rosenberg, M. L.; Aasheim, J. H. F.; Trebbin, M.; Uggerud, E.; Hansen, T.; *Tetrahedron Lett.* **2009**, *50*, 6506–6508.
"Synthesis of a 1,3,4,5-tetrahydrobenzindole beta-ketoester".

submitted:

9. Trebbin, M.; Krüger, K.; DePonte, D.; Schulz, J.; Roth, S. V.; Chapman, H. N.; Förster, S.; *Lab Chip, manuscript in revision*.
"Microfluidic Liquid Jet System with compatibility for atmospheric and high-vacuum conditions".
10. Benecke, G.; Wagermaier, W.; Schwartzkopf, M.; Hoerth, R.; Li, C.; Zizak, I.; Burghammer, M.; Metwalli, E.; Muller-Buschbaum, P.; Trebbin, M.; Förster, S.; Paris, O.; Roth, S. V.; Fratzl, P., *J. Appl. Cryst., submitted*.
"DPDAK (directly programmable data analysis kit) - a customizable software for automated reduction and analysis of large X-ray scattering data sets".

manuscript ready for submission:

11. Trebbin, M.; With, S.; Mark, A.; Hankse, C.; Buffet, A.; Santoro, G.; Yu, S.; Perlich, J.; Roth, S. V.; Zimmermann, W.; Förster, S.; *manuscript ready for submission*.
"Microfluidic SAXS for the high-throughput screening and correlation of complex fluid behavior with structural information".

in preparation:

12. Trebbin, M.; Hofmann, E.; Blüm, C.; Heidebrecht, A.; Lang, G.; Bargel, H.; Scheibel, T.; Förster, S.; *in preparation*.
"Recombinant spider silk fiber formation in microfluidic devices".
13. Trebbin, M.; Schlenk, M.; Laumann, M.; Zimmermann, W.; Förster, S.; *in preparation*.
"Elasto-inertial effects of non-Newtonian fluids for the continuous separation of colloids in microfluidic devices".
14. DeJong, F. J.; Buffet, A.; Herzog, G.; Schwartzkopf, M.; Gonzalo, S.; Yu, S.; Perlich, J.; Mecklenburg, M.; Schnoor, T.; Koerstgens, V.; Trebbin, M.; Foerster, S.; Schulte, K.; Müller-Buschbaum, P.; Roth, S. V.; Schlüter, M.; *in preparation*.
"Droplet impact and resulting flow within a multi-walled carbon nanotube thin film".

Non-peer-reviewed publications

15. Roth, S. V.; Benecke, G.; Bommel, S.; Buffet, A.; Heidmann, B.; Herzog, G.; Schwartzkopf, M.; Yu, S.; Trebbin, M.; Förster, S.; *HASYLAB annual report 2013, submitted*.
"Installing micellar thin films via spray coating".
16. With, S.; Trebbin, M.; Körstgens, V.; Buffet, A.; Kashem, M. A.; Roth, S. V.; Müller-Buschbaum; P.; Förster, S.; *HASYLAB annual report 2012, submitted*.
"In-situ lyotropic phase mapping combining microfluidics and microfocus SAXS at MiNaXs beamline/PETRA III".
17. Trebbin, M.; Thiele, J.; With, S.; Körstgens, V.; Rawolle, M.; Benecke, G.; Herzog, G.; Schwartzkopf, M.; Buffet, A.; Perlich, J.; Müller-Buschbaum, P.; Roth, S. V.; Förster, S.; *DESY Photon Science 2011*, 111.
"P03/MiNaXS at PETRA III - Technical highlight: microfluidics at the microfocus SAXS beamline - in-situ investigations with short residence times".
(http://www.desy.de/sites2009/site-www-desy/content/e410/e84441/e100769/PHOTONSCIENCE2011_ger.pdf)
18. Thiele, J.; Trebbin, M.; With, S.; Körstgens, V.; Rawolle, M.; Benecke, G.; Herzog, G.; Schwartzkopf, M.; Buffet, A.; Perlich, J.; Müller-Buschbaum, P.; Roth, S. V.; Förster, S.; *HASYLAB annual report 2010*.
"Shear orientation in microfluidic channels investigated at the microfocus beamline MiNaXS/P03 at PETRA III".
(http://photon-science.desy.de/annual_report/files/2010/20101275.pdf)
19. Rawolle, M.; Körstgens, V.; Ruderer, M.A.; Metwalli, E.; Guo, S.; Trebbin, M.; With, S.; Thiele, J.; Herzog, G.; Benecke, G.; Schwartzkopf, M.; Buffet, A.; Perlich, J.; Roth, S. V.; Lellig, P.; Gutmann, J. S.; Müller-Buschbaum, P.; *HASYLAB annual report 2010*.
"Comparison of grazing incidence small angle X-ray scattering of a titania thin film sponge structure at BW4 (DORIS III) and P03 (PETRA III)".
(http://photon-science.desy.de/annual_report/files/2010/20101004.pdf)
20. Körstgens, V.; Rawolle, M.; Buffet, A.; Benecke, G.; Herzog, G.; Perlich, J.; Schwartzkopf, M.; Trebbin, M.; Thiele, J.; With, S.; DeJong, F. J.; Schlüter, M.; Roth, S. V.; Förster, S.; Müller-Buschbaum, P.; *HASYLAB annual report 2010*.
"Flow induced surface attachment of gold nanoparticles - an in situ x-ray investigation with micro-fluidic cell".
(http://photon-science.desy.de/annual_report/files/2010/20101007.pdf)

21. Benecke , G.; Li, C.; Roth, S. V.; Körstgens, V.; Müller-Buschbaum, P.; Gehrke, R.; Rothkirch, A.; Kracht, T.; Paris, O.; Aichmayer, B.; Gourrier, A.; Burghammer, M.; Thiele, J.; Trebin, M.; With, S.; Körstgens, V.; Rawolle, M.; Herzog, G.; Schwartzkopf, M.; Buffet, A.; Perlich, J.; Müller-Buschbaum, P.; Förster, S.; Riekel; C.; Fratzl, P.; *HASYLAB annual report 2010*.
"DPDAK: directly programmable data analysis kit for online analysis of 2D scattering data - First results from MiNaXS (P03)".
(http://photon-science.desy.de/annual_report/files/2010/20101305.pdf)
22. Rawolle, M.; Körstgens, V.; Trebin, M.; With, S.; Thiele, J.; Herzog, G.; Benecke, G.; Schwartzkopf, M.; Buffet, A.; Perlich, J.; Roth, S. V.; Fröschl, T.; Hüsing, N.; Müller-Buschbaum, P.; *HASYLAB annual report 2010*.
"In-situ sol-gel templating in a micro-fluidic cell probed at beamline P03 (PETRA III)".
(http://photon-science.desy.de/annual_report/files/2010/20101003.pdf)

9 Conference presentations

Oral presentations:

1. Trebbin, M.; Krüger, K.; DePonte, D.; Steinhauser, D.; Perlich, J.; Buffet, A.; Roth, S. V.; Müller-Buschbaum, P.; Zimmermann, W.; Thiele, J.; Schulz, J.; Chapman, H. N.; Förster, S.
22nd International Congress on X-ray Optics and Microanalysis (ICXOM),
University of Hamburg, September 2.-6., 2013.
"Microfluidics at high-intensity X-ray sources: from microflow chips to microfluidic liquid jet systems".
2. Trebbin, M.; Krüger, K.; DePonte, D.; Steinhauser, D.; Perlich, J.; Buffet, A.; Roth, S. V.; Müller-Buschbaum, P.; Zimmermann, W.; Thiele, J.; Schulz, J.; Chapman, H. N.; Förster, S.
Invited talk, Laboratoire Interdisciplinaire de Physique, Université Joseph Fourier, *Grenoble*, February 11., 2013.
"Versatile Microfluidics: on microfocus SAXS, perpendicular colloid alignment and liquid jets".
3. Trebbin, M.; Krüger, K.; DePonte, D.; Roth, S. V.; Schulz, J.; Chapman, H. N.; Förster, S.
HASYLAB User's Meeting 2013 - Satellite Meeting: Status and Perspectives of Small Angle X-ray Scattering at DESY, *DESY Hamburg*, January 23.-25., 2013.
"Microfluidics at P03/MiNaXS: The latest results".
4. Trebbin, M.; Krüger, K.; DePonte, D.; Roth, S. V.; Schulz, J.; Chapman, H. N.; Förster, S.
XFEL User's Meeting 2013 - Satellite Meeting: Challenges for sample delivery at the European XFEL Facility, *DESY Hamburg*, January 23.-25., 2013.
"Microfluidic liquid jet systems".
5. Trebbin, M.; Hofmann, E.; Blüm, C.; Heidebrecht, A.; Lang, G.; Albrecht, G.; Küttner, M.; Freytag, A.-S.; Bargel, H.; Scheibel, T.; Förster, S.
4th Scientific Seminar of the North-Bavaria Biomaterials Alliance (NBBA),
University of Erlangen, November 27., 2012.
"Spider silk fiber formation in microfluidic devices".
6. Trebbin, M.; With, S.; Benecke, G.; Steinhauser, D.; Perlich, J.; Roth, S. V.; Zimmermann, W.; Thiele, J.; Förster, S.
17th Fall Seminar on Nonlinear Dynamics 2012, *University of Bayreuth*, October 7.-10., 2012.
"Anisotropic particles align perpendicular to flow-direction in narrow microchannels".

7. Trebbin, M.; Thiele, J.; With, S.; Benecke, G.; Buffet, A.; Abul Kashem, M.; Perlich, J.; Müller-Buschbaum, P.; Roth, S. V.; Förster, S.
 HASYLAB User's Meeting 2012 - Satellite Meeting: Status and Perspectives of Small Angle X-ray Scattering at DESY, *DESY Hamburg*, January 25.-27., 2012.
 "Status of the microfluidic T-SAXS Project at P03/MiNaXS".
8. Trebbin, M.; Thiele, J.; With, S.; Buffet, A.; Perlich, J.; Benecke, G.; Müller-Buschbaum, P.; Roth, S. V.; Förster, S.
 25th ECIS Conference (European Colloid and Interface Society) & 45th Biennial Meeting of the German Colloid Society, *Technical University of Berlin*, September 4.-9., 2011.
 "Particle-orientation control in microfluidic devices".
9. Trebbin, M.; Buffet, A.; Perlich, J.; Benecke, G.; Thiele, J.; With, S.; Körstgens, V.; Rawolle, M.; Herzog, G.; Müller-Buschbaum, P.; Roth, S. V.; Förster, S.
 HASYLAB User's Meeting 2011 - Satellite Meeting: Status and Perspectives of Small Angle X-ray Scattering at DESY, *DESY Hamburg*, January 26.-28., 2011.
 "Latest results from microfluidics at MiNaXS".
10. Trebbin, M.; Fischer, S.; Taheri, S.; Meyer, A.; With, S.; Thiele, J.; Förster, S.
 2nd TUM-HASYLAB Colloquium "The metal-polymer interface", *DESY Hamburg*, November 2.-3., 2010.
 "A microfluidic sample environment at a microfocus beamline - basics and perspectives".

Poster presentations:

11. Trebbin, M.; Krüger, K.; DePonte, D.; Roth, S. V.; Schulz, J.; Chapman, H. N.; Förster, S.
 XFEL User's Meeting 2013, *DESY Hamburg*, January 23.-25., 2013.
 "Microfluidic liquid jet systems".
12. With, S.; Fürst, C.; Trebbin, M.; Chen, X.; Bartz, C.; Roth, S. V.; Förster, S.
 HASYLAB User's Meeting 2013, *DESY Hamburg*, January 23.-25., 2013.
 "Scanning structural evolution of lyotropic phases with microfluidics & microfocus SAXS".
13. Trebbin, M.; Hofmann, E.; Blüm, C.; Heidebrecht, A.; Lang, G.; Albrecht, G.; Küttner, M.; Freytag, A.-S.; Bargel, H.; Scheibel, T.; Förster, S.
 4th Scientific Seminar of the North-Bavaria Biomaterials Alliance (NBBA), *University of Erlangen*, November 27., 2012.
 "Spider silk fiber formation in microfluidic devices".

14. Trebbin, M.; With, S.; Steinhauser, D.; Perlich, J.; Roth, S. V.; Zimmermann, W.; Thiele, J.; Förster, S.
Microfluidics 2012, EMBL Heidelberg, July 25.-27., 2012.
 "Microfluidics meets microfocus SAXS: fast screening and correlation of complex fluid behavior with structural information".
15. Trebbin, M.; Thiele, J.; With, S.; Benecke, G.; Steinhauser, D.; Koerstgens, V.; Buffet, A.; Kashem, M. A.; Perlich, J.; Müller-Buschbaum, P.; Roth, S. V.; Förster, S.
HASYLAB User's Meeting 2012, DESY Hamburg, January 25.-27., 2012.
 "Microfluidics meets microfocus SAXS: particle-orientation control studied *in-situ*".
16. Trebbin, M.; Thiele, J.; Steinhauser, D.; Perlich, J.; Roth, S. V.; Förster, S.
1st Bonn Humboldt Award Winners' Forum of the Alexander von Humboldt Foundation - "Frontiers in Macromolecular and Material Science", Bonn, October 12.-16., 2011.
 "Microfluidics meets microfocus SAXS: particle-orientation control studied *in-situ*".
17. Trebbin, M.; Thiele, J.; With, S.; Perlich, J.; Roth, S. V.; Förster, S.
Bayreuth Polymer Symposium '11, University of Bayreuth, September 11.-13., 2011.
 "Particle-orientation control in microfluidic devices".
18. Thiele, J.; Trebbin, M.; With, S.; Perlich, J.; Förster, S.
Makromolekulares Kolloquium, University of Freiburg, February 24.-26., 2011.
 "Shear orientation in microfluidic channels".
19. Thiele, J. ; Trebbin, M.; Förster, S.
44th Biennial Meeting of the German Colloid Society, University of Hamburg, September 28.-30, 2009.
 "Preparation of monodisperse block copolymer vesicles via flow focusing in microfluidics".

10 Acknowledgements

I would like to express my deepest gratitude to my supervisor **Prof. Dr. Stephan** who gave me the opportunity to work on both exciting and challenging research topics whilst continuously supporting me in every imaginable aspect. Stephan, I thank you from my heart.

I would also like to thank all my friends, colleagues and coworkers at the University of Bayreuth, the University of Hamburg and at DESY.

I would like to thank all the people who contributed to this work, especially all my students who worked with me on many research projects and who contributed greatly to the research in the Förster group.

Lastly, I would like to thank **my family** and friends for their ongoing support and wisdom.
I can't tell how much I appreciate what you have done for me.

11 (Eidesstattliche) Versicherungen und Erklärungen

(§ 5 Nr. 4 PromO)

Hiermit erkläre ich, dass keine Tatsachen vorliegen, die mich nach den gesetzlichen Bestimmungen über die Führung akademischer Grade zur Führung eines Doktorgrades unwürdig erscheinen lassen.

(§ 8 S. 2 Nr. 5 PromO)

Hiermit erkläre ich mich damit einverstanden, dass die elektronische Fassung meiner Dissertation unter Wahrung meiner Urheberrechte und des Datenschutzes einer gesonderten Überprüfung hinsichtlich der eigenständigen Anfertigung der Dissertation unterzogen werden kann.

(§ 8 S. 2 Nr. 7 PromO)

Hiermit erkläre ich eidesstattlich, dass ich die Dissertation selbständig verfasst und keine anderen als die von mir angegebenen Quellen und Hilfsmittel benutzt habe.

Ich habe die Dissertation nicht bereits zur Erlangung eines akademischen Grades anderweitig eingereicht und habe auch nicht bereits diese oder eine gleichartige Doktorprüfung endgültig nicht bestanden.

(§ 8 S. 2 Nr. 9 PromO)

Hiermit erkläre ich, dass ich keine Hilfe von gewerblichen Promotionsberatern bzw. -vermittlern in Anspruch genommen habe und auch künftig nicht nehmen werde.

..... Ort, Datum, Unterschrift